

Heterogeneous CuMn_2O_4 , Pt, Pd and SnO_2 Catalysts for Ambient Temperature Oxidation of Carbon Monoxide



JAMES K W ALDRIDGE

Ph.D Thesis

December 2011

Supervisors:

Prof. Graham Hutchings

Dr. Stuart Taylor

Dr. Mandy Crudace

Declaration

This work has not previously been accepted in substance for any degree and is not concurrently submitted in candidature for any degree.

Signed (candidate) Date

STATEMENT 1

This thesis is being submitted in partial fulfilment of the requirements for the degree of PhD.

Signed (candidate) Date

STATEMENT 2

This thesis is the result of my own independent work/investigation, except where otherwise stated. Other sources are acknowledged by explicit references.

Signed (candidate) Date

STATEMENT 3

I hereby give consent for my thesis, if accepted, to be available for photocopying and for inter-library loan, and for the title and summary to be made available to outside organisations.

Signed (candidate) Date

Abstract/Summary

Ambient temperature oxidation of carbon monoxide is a vital reaction for life support in enclosed atmospheres such as submarines and spacecraft. This reaction is usually achieved through the use of two classes of catalyst. Firstly, mixed copper and manganese oxides designated 'Hopcalite' or CuMn_2O_4 . Secondly, high surface area noble metal catalysts deposited on durable metal oxide supports. Both of these classes of catalyst are investigated in this thesis, with the aim of producing novel, reproducible, robust and active ambient temperature carbon monoxide oxidation catalysts.

In this thesis, CuMn_2O_4 is sequentially doped and/or impregnated with low weightings (1-10%) of the transition metals V and Ce, noble metals Pd and Pt and metalloid Si in an attempt to improve activity and moisture resistance. It was observed that doped V, Ce, Pd and Si are catalytic poisons toward CuMn_2O_4 . This is likely due to their interference in the $\text{Cu} \leftrightarrow \text{Mn}$ redox mechanism. XRD investigations infer doped Pd is a structural promoter toward CuMn_2O_4 , increasing surface area and decreasing catalyst crystallinity. Impregnation of noble metals Pt and Pd onto CuMn_2O_4 surface causes deactivation of the noble metals, most likely due to the oxidation of Pt and Pd by Mn. No novel catalyst tested in this thesis displayed increased resistance to moisture deactivation.

Noble metals Pt and Pd were impregnated upon 3 mm diameter Al_2O_3 spheres and tested for ambient temperature CO oxidation activity. The positive synergy between the two metals is measured, and the most efficient Pt:Pd ratio is discovered to be ~ 1:4.

A novel, atom efficient method, for synthesising Pt/Pd/ SnO_2 / Al_2O_3 catalysts using tin oxalate was conceived of and investigated. Compared to existing reference catalysts, oxalate derived catalysts performed favourably and can be described as equivalently active.

Acknowledgements

Primary acknowledgements go to my supervisors, Stuart Taylor and Graham Hutchings, without whom I would not have made it past week one, let alone submitted. Also well appreciated was the support of Stan Golunski. Thanks guys.

Much support was offered by Mandy Crudace and Mike Clarke of Molecular Products. This organization was also kind enough to fund half my budget across the three years, alongside the EPSRC. I am in your debt.

To my chemistry colleagues from the last 7 years - Tom, Simon, Dave, Cat, Pete, Ewa, James H, James P, Sarwat, Heather, Carl, Courtney, Terri, Sarah and Allison. I couldn't have done it without you.

To my Cardiff based non-scientific friends - Clare, Rach O, Rach A and Rach B, Jodie, Cerys, Dave, Paddy, Elin, Hannah, Manon, Lowri, Dan, Alex, Annie, Sarah, Anna, Chris, Nikki, Becky, Pete, Paul, Ali, John, Ceris, Andy, Jay, Caleb, Faye, Ciaran, Henry, Zoë, Liz and Jayne. I probably could have done it without you, but both Cardiff and my life would have been a much more unfulfilling place.

I'd like to thank my Dad for caring enough to work three jobs simultaneously, which allowed me the opportunity to go to university. My family have been inspirational, all of them.

Most of all I'd like to thank my Mum, who sadly passed away as I was proofreading my final thesis draft. She taught me the most important lesson I have ever learnt – 'You'll be surprised what you can achieve when you have no option to quit'.

Contents

Chapter 1 - Introduction	1
1.1 Aims of Thesis	1
1.2 Carbon Monoxide	2
1.3 CO Oxidation over Transition Metal Oxide Surfaces	4
1.4 Copper-Manganese Oxide - Hopcalite	8
1.4.1 Structure of Copper-Manganese Oxides	9
1.4.2 Preparation Conditions of Copper-Manganese Oxides	10
1.4.3 Activity of Copper-Manganese Oxides	14
1.4.4 Deactivation of Copper-Manganese Oxides	16
1.4.5 Promotion of Copper-Manganese Oxides	18
1.5 CO Oxidation over Supported Precious Metals	23
1.5.1 Catalyst Supports	26
1.6 Chapter 1 References.....	34
Chapter 2 - Experimental	40
2.1 Preparation of CuMn ₂ O ₄ Hopcalite Catalyst.....	41
2.1.1 Preparation of doped co-precipitate CuMn ₂ O ₄ catalyst	41
2.1.2 Incipient Wetness (IW) onto CuMn ₂ O ₄ Catalyst Support	43
2.1.3 Deposition Precipitation (DP) onto CuMn ₂ O ₄ Catalyst Support	43
2.1.4 Hopcalite Reduction.....	43
2.2 Preparation of Impregnated Alumina Sphere Catalysts	44
2.2.1 Silicon Deposition on Alumina Spheres	45
2.2.2 Tin Oxide Impregnated Alumina Spheres	46
2.3 Catalyst CO Activity Testing.....	47
2.3.1 Calculation of Surface Area Normalised Activities (SANA)	49
2.4 Activity Measurement by Gas Chromatography	49
2.5 BET Surface Area Analysis	53
2.6 Powder X-Ray Diffraction (XRD)	55

2.7 Thermogravimetric Analysis (TGA).....	56
2.8 Scanning Electron Microscopy (SEM).....	57
2.9 Energy Dispersive X-Ray Spectroscopy (EDX).....	58
2.10 X-Ray Photoelectron Spectroscopy (XPS).....	60
2.11 Ultraviolet Visible Spectroscopy (UV-Vis).....	61
2.12 Chapter 2 References.....	62
Chapter 3 – Transition Metal Doped Hopcalite	63
3.1 V-doped CuMn ₂ O ₄ – Mn Replacement.....	64
3.1.1 CO Oxidation Activity	64
3.1.2 BET Surface Area, SANA and EDX Molar Ratio	65
3.1.3 Powder X-Ray Diffraction.....	67
3.1.4 SEM Analysis	68
3.2 V-doped CuMn ₂ O ₄ – Cu Replacement	72
3.2.1 CO Oxidation Activity	72
3.2.2 BET Surface Area, SANA and EDX Molar Ratio	73
3.2.3 Powder X-Ray Diffraction.....	74
3.2.4 SEM Analysis	75
3.3 V-doped CuMn ₂ O ₄ – Dual Cu and Mn Replacement.....	78
3.3.1 CO Oxidation Activity	78
3.3.2 BET Surface Area, SANA and EDX Molar Ratio	79
3.3.3 Powder X-Ray Diffraction.....	80
3.3.4 SEM Analysis	81
3.4 Cerium Doping	84
3.4.1 CO Oxidation Activity	84
3.4.2 BET Surface Area, SANA and EDX Molar Ratio	85
3.4.3 Powder X-Ray Diffraction.....	87
3.4.4 SEM Analysis	88
3.5 Silicon Doping.....	91
3.5.1 CO Oxidation Activity	91
3.5.2 EDX Molar Ratio and BET Surface Area	92

3.5.3 Powder X-Ray Diffraction	92
3.6 Discussion	94
3.6.1 Vanadium Doping	94
3.6.2 Cerium Doping	98
3.6.3 Silicon Doping	99
3.7 Conclusions	101
3.8 Chapter 3 references.....	102
Chapter 4 – Noble Metal Modified Hopcalite.....	104
4.1 Palladium Doping	104
4.1.1 CO Oxidation Activity	104
4.1.2 BET Surface Area, SANA and EDX Molar Ratio	105
4.1.3 Powder X-Ray Diffraction	106
4.1.4 SEM Analysis	107
4.2 Palladium Impregnation	110
4.2.1 Catalyst Reduction	110
4.2.2 CO Oxidation Activity	111
4.2.3 BET Surface Area, SANA and EDX Molar Ratio	112
4.2.4 Powder X-Ray Diffraction	113
4.2.5 SEM Analysis	114
4.3 Deposition Precipitation of Noble Metals	117
4.3.1 Catalyst Reduction	117
4.3.2 CO Oxidation Activity	118
4.3.3 BET Surface Area, SANA and EDX Molar Ratio	119
4.3.4 Powder X-Ray Diffraction	120
4.3.5 SEM Analysis	121
4.4 Discussion	126
4.4.1 Effects of Pd-Doping on CuMn_2O_4	126
4.4.2 Effects of Pd-Impregnation on CuMn_2O_4	130
4.4.3 Effects of Pt and Pd Deposition on CuMn_2O_4	132
4.4.4 Effects of Reduction of Pt and Pd on CuMn_2O_4	134

4.5 Conclusions	136
4.6 Chapter 4 References	137
Chapter 5 – Bimetallic Pt-Pd Impregnated γ-Alumina	139
5.1 Investigations in Pt/Pd/ Al_2O_3 synergy	140
5.1.1 CO Oxidation Activity	140
5.1.2 Ultraviolet Visible Spectra	147
5.1.3 EDX Molar Ratio	150
5.2 Investigations into Optimum Pt/Pd ratio	151
5.2.1 CO Oxidation Activity	152
5.2.2 Ultraviolet Visible Spectra	154
5.2.3 EDX Molar Ratio	156
5.2.4 X-Ray Photoelectron Spectroscopy	158
5.3 Deposition of Pt/Pd on Si/ Al_2O_3	160
5.3.1 CO Oxidation Activity	160
5.3.2 BET Surface Area and XPS	162
5.3.3 EDX Molar Ratio	162
5.3.4 Thermogravimetric Analysis.....	163
5.4 Discussion	164
5.4.1 Effective ratio towards synergy between Pt/Pd/ Al_2O_3	164
5.4.2 Effect of Silicon on CO oxidation over Pt/Pd/ Al_2O_3	168
5.5 Conclusions	171
5.6 Chapter 5 References	172
Chapter 6 – Noble Metal Modified Alumina/Tin Oxide	174
6.1 Preparation of Pt/Pd/Sn/ Al_2O_3 spheres from SnO_2	175
6.1.1 CO Oxidation Activity	175
6.1.2 X-Ray Photoelectron Spectroscopy	176
6.1.3 EDX Molar Ratio	179
6.2 Preparation of Pt/Pd/Sn/ Al_2O_3 spheres from Na_2SnO_3	180
6.2.1 CO Oxidation Activity	180

6.2.2 X-Ray Photoelectron Spectroscopy	181
6.2.3 EDX Molar Ratio	184
6.3 Preparation of Pt/Pd/Sn/Al ₂ O ₃ spheres from Sn(C ₂ O ₄).....	185
6.3.1 CO Oxidation Activity	185
6.3.2 Thermogravimetric Analysis.....	186
6.3.3 X-Ray Diffraction	186
6.3.4 X-Ray Photoelectron Spectroscopy	187
6.3.5 EDX Molar Ratio	190
6.4 Discussion	191
6.5 Conclusions	193
6.6 References	194
Chapter 7 – Conclusions & Further Work	195
7.1 Hopcalite Modification.....	195
7.2 Noble Metals Supported on Alumina and Tin Oxide	197
7.3 References	198

1

Introduction

1.1 Aims of the Thesis

This research is intended to develop, investigate and report on novel ambient temperature carbon monoxide oxidation catalysts. Developing on previous studies in published literature, a series of reproducible catalysts will be prepared from a range of current synthesis methods.

Continuing current work at Cardiff, pre-optimised hopcalite synthesis will be doped with a range of transition metals in an effort to promote ambient temperature CO oxidation activity. Hopcalite surface will also be impregnated with a series of noble metals and metalloids in an attempt to influence activity and moisture resistance.

Pt/Pd/Al₂O₃ catalysts, known to be active for ambient temperature CO oxidation, will be studied to determine the extent of bimetallic synergy. The most efficient Pt:Pd ratio will be investigated.

Previously studied Pt/Pd/SnO₂/Al₂O₃ catalysts, reported to be active for ambient temperature CO oxidation, will be synthesised in an atom efficient process from novel oxalate reagents. These catalysts will be compared to reference catalysts synthesised from existing methods.

These novel and reference catalysts will be probed with a range of analysis methods, including BET, XPS, EDX, SEM, UV-Vis, XRD and TGA. This data will be used to infer the chemical reactions driving increased or decreased activity in novel catalysts.

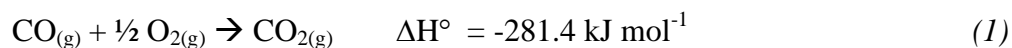
1.2 Carbon Monoxide

Carbon monoxide, or CO, is a colourless, odourless and tasteless gas. It is known to be highly toxic to the respiratory system of vertebrates. It is especially dangerous to humans due to our inability to detect it with conventional senses¹. CO is normally produced during an oxidation reaction with an excess of carbon compared to oxygen. This is typically partial oxidation of organic compounds in a closed system. A widespread number of modern day processes produce CO. This includes all forms of combustion engine, as well as firearms, indoor heaters and contained ovens. Humans also exhale CO in parts per million (ppm) quantities². In a long-term enclosed system, such as a spaceship or submarine, this CO will eventually accumulate to lethal levels. Omota *et al.*³ reports carbon monoxide poisoning may be the most common type of fatal poisoning in many countries. The UK Health and Safety Executive dictates safe CO exposure levels of below 30ppm for periods of over 8 hours⁴. The toxicity of CO is due to its affinity for haemoglobin in the bloodstream. Haemoglobin carries oxygen molecules from the lungs to most cells in the body. CO is 210 times as affinitive for haemoglobin as O₂¹. CO irreversibly binds to the haemoglobin molecule, rendering it useless as carboxyhaemoglobin. Moderate exposure of 200ppm CO can produce a slight headache after 3 hours. Exposure of 800ppm causes severe symptoms including headaches, vomiting, nausea and fainting. Prolonged exposure to CO of more than 1600ppm results in death by asphyxiation⁵.

At standard conditions, CO is a gas containing one carbon atom bound to one oxygen atom via a triple bond. This bond consists of two covalent bonds and one dative covalent bond. The dative bond is dipolar, resulting in a small negative charge on the carbon atom and a small positive charge on the oxygen atom. This imbalance allows CO to attract towards charged molecules. Studies have reported on the behaviour of CO when approaching positively charged molecules. Lupinetti *et al.*⁶ reports that CO will always bond with metal cations in the form of M-C≡O. He theorises that the C≡O bond will shorten on approach to a metal cation. This bond will then lengthen as M⁺ distance approaches zero due to M⁺ → CO back-donation. This effect is seen in Ag and Li, but not in Cu or Au.

Oxidation of Carbon Monoxide

Oxidation of CO in excess oxygen occurs readily at high temperatures, burning with a blue flame in an exothermic reaction (1). The low ΔH° value of $-281.4 \text{ kJ mol}^{-1}$ ensures that $-\Delta G^\circ$ for the reaction is $-256.9 \text{ kJ mol}^{-1}$ ⁷. This reaction is thermodynamically irreversible at most temperatures without side reactions. This reaction has an auto-ignition temperature in air at ambient temperature of 620°C ⁸. CO oxidation by combustion presents a problem in sensitive environments. An open, potentially explosive flame cannot be used in an enclosed atmosphere such as a deep mine or submersible vehicle. In addition, cold start technologies such as combustion engines will not reach high temperatures until sometime after they are ignited. A catalyst can be introduced to allow oxidation at ambient temperature.



Ambient Temperature CO Oxidation by Catalysis

Heterogeneous oxidation of carbon monoxide has been extensively studied for most of the last century. Langmuir⁹ first observed adsorption of gases over heated platinum sponge in 1918. Investigations into CO oxidation for practical uses has led to an excellent understanding of gas adsorption theory. CO is also a classic laboratory reductant. CO oxidation on novel surfaces is a model reaction reported in hundreds of scientific papers across surface science and heterogeneous catalysis. This has contributed to discoveries in photoactive TiO_2 catalysts¹⁰ and catalyst deactivation¹¹ amongst many others. CO oxidation is also still of great interest to fuel cell technologies¹², where CO can poison vital Pt electrodes.

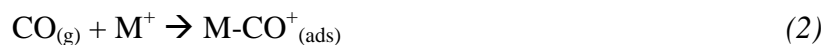
In the early 20th century, advances in chemical warfare made CO poisoning a credible battlefield hazard. Although it was discarded as an intentional weaponised gas, the increasing use of bunkers, battleships and submersibles combined with CO-producing technologies such as heavy calibre naval guns and motorized armoured transport made CO “*a source of serious danger both in marine and land warfare*”¹³. In peace, increased use of both mining explosives and CO as a

fuel gas produced regular casualties. A chemical capable of absorbing, oxidizing or otherwise removing CO at ambient temperature was needed. CO oxidation was problematic at ambient temperature in 1920. Existing methods involved powerful acids such as gold chloride, reactions with expensive ozone in a 1:1 CO:O₃ molar ratio, or oxidation with rare palladium catalysts. Mixed metal oxide catalysts, such as CuO-AgO and MgO-AgO, were known, but were impractical. The first practical example of a CO oxidation catalyst was developed in a joint effort between John Hopkins University and California Institute of Technology, and published by the US naval department¹³. It was designated ‘*Hopcalite*’ after these two institutes.

Since 1920, two main classes of catalyst for practical CO oxidation at ambient temperature have been developed. The first class predominately describes reactions on high surface area precious metal catalysts including Pt⁹, Pd¹⁴ and, more recently, Au¹⁵. These are typically in the form of nanoparticles distributed on oxide or carbon supports¹⁶, or porous, high surface area sponges. These are discussed in Part 1.5. The second class describes oxidation on transition metal oxides¹⁷ including Co₂O₃¹⁸, MnO₂¹⁹, Co₃O₄²⁰ and CuO²¹. Previous work at Cardiff by Jones *et al.*⁷ and Cole *et al.*²² have been predominately performed on mixed metal oxides.

1.3 CO Oxidation over Transition Metal Oxide Surfaces

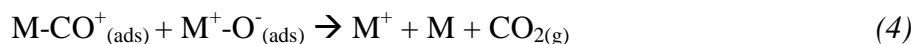
Transition metal oxide surfaces are described as catalysts for oxidation²³. There are several proposed mechanisms. The first is an associative mechanism. This begins with the rate determining step for CO oxidation, CO chemisorption (Equation 2).



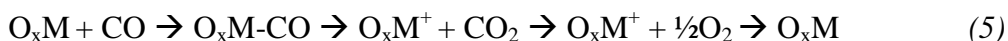
Simultaneously, the chemisorption of O₂ is comparatively fast. (Equation 3)



The final step, a Langmuir-Hinshelwood mechanism, (Equation 4), involves the formation and desorption of CO₂ from the adsorbates.



Another mechanism for CO oxidation involves a redox mechanism and lattice oxygen (Equation 5). Metal ions are reduced by CO and reoxidised by atmospheric oxygen, which may be donated via an adjacent metal ion²⁴. This reaction is normally described as a Mars-van Krevelen mechanism.



CO oxidation over transition metal oxides correlates with the bonding energy of CO, O₂ and CO₂ on the catalyst surface. Catalyst morphology, surface area, impurities and surface structure must also be considered. Cobalt, manganese, copper and tin oxides have all been described as CO oxidation catalysts.

Cobalt oxide has been described by Jansson *et al.*¹⁸ as an active CO oxidation catalyst at ambient temperature. Co₃O₄ was shown to have high initial activity which decreased with time. Jansson proposes that lightly reduced Co active sites can be reoxidised by O₂, but more deeply reduced Co sites are unoxidisable at temperatures below 150°C. This phenomena gradually reduces the active catalyst surface area. Jansson also links rapid deactivation to water poisoning. This is a common problem with transition metal oxide catalysts²⁵. In a supporting study using TPD, Taktita *et al.*²⁶ identify three types of adsorbed oxygen and four types of adsorbed water on the Co₃O₄ surface. He reports that water on the surface of Co₃O₄ strongly affects the catalysts ability to absorb oxygen. Water in sufficient quantity can completely deactivate the Co₃O₄ surface. Other poisons are also known; Jansson has proposed that CO₂ may adsorb onto the surface to form carbonate species, blocking active sites. The generally accepted model for CO oxidation over Co₃O₄ begins with CO adsorbing onto the Co₃O₄ surface. CO_(ads) removes lattice oxygen from Co, and dissociates as CO₂. Reduced cobalt is reoxidised by atmospheric oxygen.

Xie *et al.*²⁰ reported that Co_3O_4 activity can be increased by preferentially exposing the (110) plane of the lattice. This was achieved by formation of cobalt oxide nanorods. The rods preferentially expose the Co^{3+} ion on the surface. Xie correlates the activity increase to the increase in Co^{3+} sites. The nanorod catalysts are observed to be active at 196 K.

Manganese oxides were noted as catalytically active for ambient temperature CO oxidation by Whitesell and Frazer in 1923²⁷. The preparation involved combining sulphuric and nitric acids with potassium permanganate. They were quick to notice both the activity of the catalyst at temperatures as low as -20°C , and its intolerance to water.

The mechanism for CO oxidation over MnO_2 was investigated by Kanungo¹⁹. He begins by reporting that H_2O_2 decomposition activity in nonstoichiometric manganese oxide is due to the presence of Mn^{3+} . Mn^{3+} is present as MnOOH , and catalyst activity is based upon electron transfer between Mn^{3+} and Mn^{4+} . He then reports that CO oxidation activity is poisoned by surface hydroxyl groups. Loss of compositional water creates lattice defects responsible for increased catalytic activity.

Kobayashi *et al.*²⁸ used sophisticated equipment to measure changes in outlet gases over a continuous flow MnO_2 catalytic reactor. Based on their results, they suggest the existence of two separate types of surface oxygen – one dependant on CO partial pressure and the other independent. The involved oxygen species was demonstrated to be negatively charged O^- or O^{2-} . In a later study, Kobayashi & Kobayashi²⁹⁻³¹ used their transient-response method to define two types of oxygen present on the catalyst surface. The first is a low oxidising power species present on a high percentage of the surface, and the second a high oxidising power species present on a low percentage of the surface. They also reported that CO_2 desorption was one of the slower steps of the catalytic process.

Copper oxide has never been described as an ambient temperature CO catalyst. At higher temperatures, CuO is an effective catalyst. It is of interest in emission control technology and is used in catalytic converters. Huang and Tsai²¹ investigated the behaviour of CuO and Cu_2O as CO oxidation catalysts at $140\text{-}205^\circ\text{C}$. They discovered that Cu_2O was a more effective catalyst

under excess oxygen conditions. Under low oxygen conditions, however, CuO was a more effective catalyst. They correlated activity to the formation of metastable non-stoichiometric CuO clusters.

The exact mechanism of CO oxidation over copper (II) was once unknown due to the change in copper oxidation states during the reaction. Labinger and Ott³² support the idea of a redox mechanism involving lattice oxygen, which is replaced by atmospheric oxygen the last stage of the reaction. The mechanism of CO oxidation over CuO, Cu₂O and Cu was investigated by Jernigan and Somorjai³³. CO at 100 Torr and 200-350°C was passed over copper and oxidic copper catalysts. By controlling the partial pressures of CO and O₂, they isolated Cu in oxidation states of 0, +1 and +2. Cu⁰ was the most active catalyst followed by Cu⁺ and Cu²⁺. The trend in activation energy was reversed, increasing with oxidation state. Their proposed mechanism for CO oxidation over CuO supports the redox theory, with a mechanism between Cu²⁺ and Cu¹⁺. They also postulate that the rate limiting step for the reaction is the reduction of CuO by CO.

Tin oxide can be broadly separated into stannous oxide, SnO, and stannic oxide, SnO₂. Both were discovered by B.Pelletier in 1792³⁴. No form of tin oxide has ever been reported as exhibiting ambient temperature CO oxidation activity. Fuller³⁵ reports activity at no lower than 150°C. Tin (IV) oxide has been described as a CO oxidation catalyst via a redox mechanism³⁵. Hagemeyer *et al.*³⁶ prepared tin oxide by over a hundred synthesis procedures using different reagents. He reports that high surface areas can be synthesised by calcinations between 300-500°C. Hydrazine synthesis was reported as one of the most efficient procedures in regard to high surface area and sintering resistance. The highest surface area (>200 m² g⁻¹) was reported after synthesis using aqueous glyoxylic acid and Sn(IV) acetate.

Stannic oxide is normally promoted with dopant elements to enhance its activity. Stannic oxide modified by rare earth metals was reported by Harrison *et al.*³⁷. Coprecipitation of La, Pr, Nd, Sm and Gd onto SnO₂ surface displayed no significant enhancement of catalytic activity against standard stannic oxide. He has previously reported that impregnation by chromium and copper increases catalyst activity.

Low temperature CO oxidation by stannic oxide is normally achieved by impregnation of tin (IV) oxide with noble metals. Grass and Lintz³⁸ observed a synergetic effect between SnO₂ and Pt/Pd, which they attributed to the spillover of oxygen. They measured the rate limiting step for the reaction to be migration of adsorbed oxygen. They also reported that increasing the catalyst calcination temperature above 350°C, or prolonging the calcination time at 350°C, results in loss of tin oxide surface area.

1.4 Copper-Manganese Oxide – Hopcalite

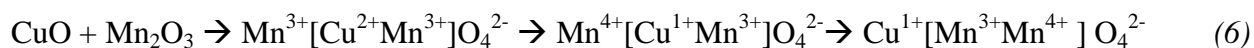
Hopcalite was originally developed as a mixture of 50% MnO₂, 30% CuO, 15% Co₂O₃ and 5% Ag₂O¹³. The individual components of this composite are each active for CO oxidation, though copper oxide is not active at ambient temperature. Hopcalite was originally selected over other chemicals to fulfil a number of criteria, including cost, activity, longevity and robustness. Over time, the formula has been refined. Commercial and academic Hopcalite in 2012 can vary depending on supplier. CaruliteTM comprises of 30% Copper Oxide and 70% Manganese Dioxide³⁹; while Purelyst⁴⁰ is 13% Copper Oxide, 76+% Manganese Dioxide and balance Al₂O₃. At Cardiff, work by Hutchings *et al.*⁴¹ discovered a 1:2 [Cu]:[Mn] molar ratio produced the most efficient CO oxidation catalyst. Hopcalite is also used for oxidation of ozone, VOC's and NO_x. In some older publications, 'hopcalite' is defined as manganese and silver oxide⁴². This may explain the lack of consensus on the optimum formula.

Despite its additional components, in terms of this thesis, hopcalite is defined by its combination of copper and manganese oxides. It will henceforth be referred to as either CuMn₂O₄ or 'hopcalite'.

The kinetics of CO oxidation over hopcalite were studied by Li *et al.*⁴³. The activation energy for the reaction was discovered to be 64.08 kJ mol⁻¹ between 0°C and 40°C. This drops to 12.15 kJ mol⁻¹ between 60°C and 100°C. The reaction was proved to be first order in respect to CO.

1.4.1 Structure of Copper-Manganese Oxides

The exact structure of CuMn_2O_4 was unresolved for many decades following its discovery. Catalyst morphology can vary depending on preparation. Early studies⁴⁴ predicted the presence of two Jahn-Teller ions, Mn^{3+} and Cu^{2+} , would lead to interesting crystallographic properties. It has previously been assumed that CuMn_2O_4 would follow the pattern established by CuFe_2O_4 and CuCr_2O_4 and have a 'tetragonal pseudo-spinel structure'⁴⁵. A spinel structure is defined as a $\text{A}^{2+}\text{B}_2^{3+}\text{O}_4^{2-}$, with the oxide anions arranged in a close packed cubic lattice and the cations A & B occupying some or all of the octahedral and tetrahedral sites. Sinha *et al.*⁴⁵ reported that CuMn_2O_4 had a cubic structure. This was unexpected, as either a normal or inverse cubic structure would theoretically become unstable. The theory postulates that a cubic structure will become unstable when a certain proportion of distortive ions occupy a particular site. In this case, the limit was set at 55%⁴⁶. To account for the formation of a stable cubic structure by two unstable ions, Sinha investigated x-ray intensities and bonding rules. He proposed $\text{Cu}^+[\text{Mn}^{3+}\text{Mn}^{4+}]\text{O}_4$ as the structure, with manganese cations present in an octahedral environment. Also proposed was an electron transfer system described in Equation (6).



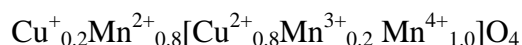
Miyahara⁴⁷ disagreed and investigated the Jahn-Teller distortions of both Mn^{3+} and Cu^{2+} . He postulated that the two distortions caused by octahedral and tetragonal Cu^{2+} were cancelling each other out, and proposed $\text{Cu}^{2+}[\text{Mn}^{3+}]\text{O}_4$ configuration. However, Dollimore and Tonge⁴⁸ supported Sinha and reported the presence of Mn^{4+} (although no MnO_2 was detected) in the presence of Cu^+ . The high electrical conductivity⁴⁶ of CuMn_2O_4 is evidence of the presence of mixed valance states. The electron transfer proposed by Sinha can be summarised more simply in Equation (7). This theory indicates that four distinct ions would always be present in the spinel lattice.



Many investigations faced difficulties preparing pure CuMn_2O_4 . Buhl *et al.*⁴⁹ reported his synthesised cubic spinels normally contained significant impurities⁴⁹. Pure tetragonal CuMn_2O_4

could be formed only by heating to 940°C. The preparation of pure CuMn₂O₄ was believed to be impossible at room temperature. This was supported by Vandenberghe⁵⁰, who found that cubic configuration would only arise with a change in catalyst stoichiometry to Cu_{1.05}Mn_{1.95}O₄.

Gillot *et al.*⁵¹ supports Sinha in his study on ionic configuration and oxidation mechanism of CuMn₂O₄ spinels prepared at 850-930°C. He reported that octahedral sites were more likely to be occupied by Cu²⁺, Mn³⁺ and Mn⁴⁺, while tetrahedral sites were more likely to be occupied by Mn²⁺ and Cu⁺ ions. Wařkowska *et al.*⁴⁶ reports a concise study detailing the behaviour of CuMn₂O₄ under a pressure of 30GPa. He reports the ambient pressure crystal as cubic with a partially inverse spinel structure:



He explains that the Cu²⁺ ions have occupied the octahedral sites, allowing Mn²⁺ ions to occupy the majority of the tetrahedral sites. This configuration allows the molecule to retain cubic structure, as the number of distortive ions occupying each site is below 55%.

1.4.2 Preparation Conditions of Copper-Manganese Oxides

Preparation of mixed oxide catalysts is most commonly achieved by a co-precipitation in solution of a precursor. This precursor normally takes the form of an oxide, hydroxide or other insoluble salt. Koleva *et al.*⁵² reports that hopcalite precipitations typically involve the use of nitrate precursors. This is due to their high solubility and the ease of removal of the nitrate anion during calcination. The alternatives, chlorides or sulphates, leave residue that can interfere with catalyst structure. Used occasionally are metal formates⁵³, which decompose upon heating to the oxides at ~400°C. Catalyst precipitation is normally induced by the introduction of a base. The identity of the basic salt is important, as it has been shown that alkali metals can segregate and block surface sites of CuMn₂O₄⁵⁴.

Precipitation normally takes place in two stages⁷. During nucleation, small unstable crystals form where the free energy of formation is less than the surface energy. The crystals have high surface area and free energy. The second stage, growth, occurs when particles are above this

critical size. Growth is primarily limited by diffusion. Nucleated crystals are normally preferable to growth crystals due to their larger surface area. Certain parameters can be adjusted during the precipitation process to influence product morphology. Vigorous stirring during addition of the precipitating agent favours crystal nucleation over growth. This maximises contact with equipment surfaces, which lower the free energy of particles and stabilise them. The fastest practical addition of precipitate salt also favours nucleation. Lowering the temperature reduces diffusion and thus reduces rates of crystallite growth.

It has been reported by various researchers that in regard to low temperature CO oxidation, amorphous hopcalite spinel is more active than its crystalline counterpart^{55, 56}. Porta *et al.*⁵⁷ reported that decomposition conditions of CuMn_2O_4 precursor could manipulate catalyst morphology and activity. Porta coprecipitated nitrates and found the precipitate catalyst precursor to consist of hydroxycarbonates; Mn-containing malachite and Cu-containing rhodochrosite. Precursors were calcined in both air and N_2 . He discovered the $\text{Cu}^{2+} + \text{Mn}^{3+} \leftrightarrow \text{Cu}^{1+} + \text{Mn}^{4+}$ redox system was shifted to the left for N_2 calcined samples. In air-calcined samples the system shifted to the right. In another study, Porta *et al.*⁵⁸ reported that the composition of the hydroxycarbonate catalyst precursor was crucial in determining final catalyst activity. This discovery led to extensive research into catalyst preparation by Hutchings and colleagues.

Hutchings *et al.*⁵⁹ investigated the structure of co-precipitated hopcalite catalyst in regard to aging. They discovered that catalyst aging is crucial to final catalyst morphology and activity. The reaction brew upon the conclusion of reagent introduction was comprised mostly of crystalline copper hydroxynitrate and manganese carbonate. Upon aging, the copper complex dissolved and the manganese complex remained insoluble. This would suggest that upon filtration, copper would be removed from the catalyst. In a later study, Hutchings *et al.*⁴¹ investigated several preparation conditions involved in hopcalite coprecipitation. The optimum conditions reported were:

- [Cu]:[Mn] ratio of [1]:[2]
- pH of precipitation maintained at 9.0
- Temperature of precipitation maintained at 80°C
- Precipitate aging time of 12 h
- Temperature and duration of calcination of 500°C for 17 h

These produced an amorphous catalyst with the highest measured CO conversion. The 1:2 [Cu]:[Mn] ratio produced the highest activity catalyst, and also contained the largest quantity of highly active CuMn_2O_4 catalyst. In a similar study, Dollimore and Tonge⁴⁸ discovered the best [Cu]:[Mn] ratios for CO oxidation were [12]:[69.8]. It is to be noted that Dollimore recorded significant quantities of Na^+ in the majority of his samples, which may explain their poor activity⁵⁴ and his differing conclusions.

Although the highest overall activity catalyst was produced at pH 9, the most active phase, pure CuMn_2O_4 was formed at pH 8.3. The temperature of 80°C was the highest practical value that could be used. Precipitation theory would predict a lower temperature would be more suited to forming high surface area nucleated crystals. This suggests that the increased temperature is promoting catalyst activity by another method. This could include improved solubility, and/or better mixing due to stronger convection currents.

Optimum aging time was reported as 12 h, although 0 min and 30 min aging times also produced active catalysts. Low aging time catalyst precursors are characterised as single phase copper hydroxynitrate and manganese carbonate. Mid aging time catalyst precursors are relatively inactive. Long-aging time catalyst precursor was characterised by XPS as only manganese carbonate, although this signal would block copper signals. The calcined catalyst from long aged precursor has enhanced manganese levels. Cole²² investigated zinc doped hopcalite and gold impregnated hopcalite. Using the data from his zinc experiment undoped reference batches, he discovered that that in terms of both activity and surface normalised activity, a 2 h catalyst aging is most effective. The reference sample from his gold doped experiment showed that activity for his 1 h, 6 h and 12 h aged batches was equivalent, while the 0.5h aged catalyst was less active.

Jones investigated the calcination time and temperature reported by Hutchings and discovered heating at 415°C for 2 h produced the most active catalyst. Jones⁷ has also reported that proper maintenance of the distribution of reaction temperature and pH are critical in producing reproducible catalysts. His work was used in developing the reaction apparatus described in Chapter 2.

These results can be compared to the investigations of Kanungo¹⁹. He electrostatically adsorbed Cu²⁺ ions in basic solution onto solid MnO₂, forming a surface compound with the formula CuMn₂O₄. He reported an increase in activity compared to undoped MnO₂. The high activity hopcalite precursor reported by Hutchings at 12 h aging would have been expected to contain small amounts of copper, as it remained dissolved during filtration. Kanungo's study indicates that it may have electrostatically adsorbed onto the manganese precipitate surface. This is supported by pH data – active catalyst is precipitated at pH 8.3-9.0. The iso-electric point (the point at which the surface shows zero charge) of manganese carbonate has been reported as between 7.75 and 9.47⁶⁰. This would also explain the absence of Cu from the XRD pattern, as this technique is bulk, rather than surface, sensitive. The calcined catalyst would also show low bulk copper ratios as the majority is on the catalyst surface or has been filtered off. However, Mirzaei *et al.*⁶¹ studied, via XPS, coprecipitated catalysts aged at different times and pH values. He reported that Cu²⁺ was the predominate surface copper species. He discovered little difference between the surface and bulk [Cu]:[Mn] ratios. This would rule out the theory that Cu is being removed during filtration or is preferentially segregating to the surface.

Recently, investigations have been made into modifying catalyst morphology with novel hopcalite preparation methods. Fortunato *et al.*⁶² reports hopcalite prepared by ultrasonic aerosol pyrolysis. They report pure CuMn₂O₄ spinel has been formed. The compound is described as 'metastable', and segregates at 300°C in air and 600°C in an inert atmosphere. The Cu^{I, II} ↔ Mn^{III,IV} redox system is confirmed by XPS. They also report the compound exists in a series of hollow spheres. The activity of this hopcalite was not compared against any standard hopcalite preparation.

Krämer *et al.*⁶³ reported hopcalite derived from a sol-gel process with ethylene glycol. They discovered a catalyst with a 20% Cu : 80% Mn reagent ratio to be most catalytically active. A change in the Cu content between 15% and 40% did not significantly affect activity. XPS characterisation displayed surface oxidation states of Cu²⁺ and Mn³⁺. In other regards, their findings were similar to reports of other researchers – max activity at 400°C calcination, spinel crystallisation above 400°C accompanying activity loss and low water tolerance. The catalyst was compared to commercial samples and was approximately as active.

Tang *et al.*⁶⁴ investigated hopcalite derived from supercritical acetate precipitation. They discovered a catalyst with a higher activity per unit of surface area than commercial hopcalite. The catalyst was also derived from acetate salts - a precursor less environmentally destructive than a nitrate. The catalyst precursor reports exceptional surface area of >300 m² g⁻¹. However, the reported surface area for the calcined catalyst was far lower than commercial hopcalite, leading to an overall lower activity. Zirong attributes this to the formation of crystalline spinel, the catalyst begins to crystallise at 250°C, lower than the 400°C reported by traditional co-precipitated hopcalite.

1.4.3 Activity of Copper-Manganese Oxides

Hopcalite is known to be catalytically active above the temperature of water loss. Upon loss of surface water, copper hydroxide dehydroxylates to Cu³⁺. Meanwhile Mn³⁺ in the form of MnOOH would deprotonate to MnOO⁻. Unstable Cu³⁺ would receive an electron transfer from Mn³⁺ forming Cu²⁺ and Mn⁴⁺. Mn³⁺/Mn⁴⁺ redox mechanism is known as the active centre for CO adsorption¹⁹. Schwab and Kanungo⁶⁵ made a major advance in 1977 when they linked the electronic transfer proposed by Sinha⁴⁵ (7) with the unusually high activity of CuMn₂O₄. They theorized the redox electron transfer system in hopcalite lattice was responsible for the simultaneous existence of two catalytically active ion pairs. Cocke and Veprek⁶⁶ confirmed this using XPS in 1986. CO oxidation over hopcalite catalysts was described as proceeding according to the redox formula mechanism in Figure 1. It can be explained in steps 1 to 6 (Equations 8 to 13), beginning and ending with the same active state:

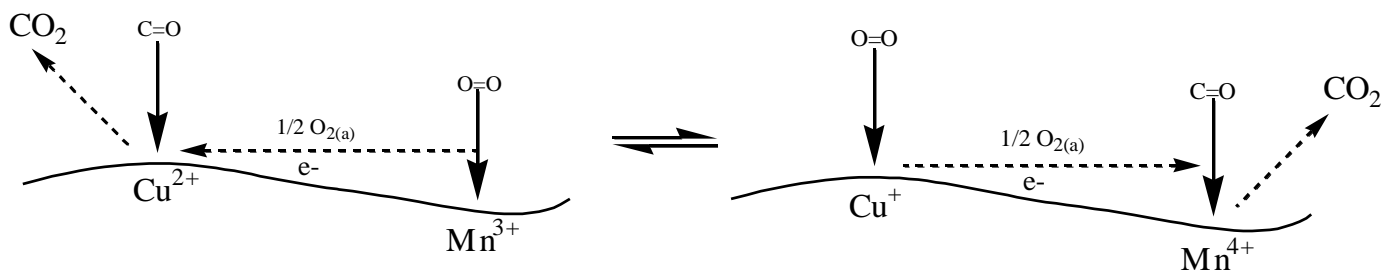


Figure 1 – Mechanism of CO oxidation on CuMn_2O_4

- | | | |
|--|---|------|
| 1) CO chemisorbs onto manganese(IV) ion | $\text{CO}_{(\text{g})} + \text{Mn}^{4+} \rightarrow \text{CO}^+_{(\text{ads})} + \text{Mn}^{3+}$ | (8) |
| 2) O_2 chemisorbs onto copper (I) ion | $\frac{1}{2}\text{O}_{2(\text{g})} + \text{Cu}^+ \rightarrow \text{O}^-_{(\text{ads})} + \text{Cu}^{2+}$ | (9) |
| 3) CO and O_2 react and CO_2 dissociates | $\text{CO}^+_{(\text{ads})}$ and $\text{O}^-_{(\text{ads})} \rightarrow \text{CO}_{2(\text{g})}$ | (10) |
| 4) O_2 chemisorbs onto manganese (III) ion | $\frac{1}{2}\text{O}_{2(\text{g})} + \text{Mn}^{3+} \rightarrow \text{O}^-_{(\text{ads})} + \text{Mn}^{4+}$ | (11) |
| 5) CO chemisorbs onto copper (II) ion | $\text{CO}_{(\text{g})} + \text{Cu}^{2+} \rightarrow \text{CO}^+_{(\text{ads})} + \text{Cu}^+$ | (12) |
| 6) CO and O_2 react and CO_2 dissociates | $\text{O}^-_{(\text{ads})}$ and $\text{CO}^+_{(\text{ads})} \rightarrow \text{CO}_{2(\text{g})}$ | (13) |

Previous investigations into catalyst bulk structure did not give an accurate picture of the composition of the catalyst surface. Veprek⁵⁵ used X-ray photoelectron spectroscopy to probe the catalyst surface. He established the existence of the copper-manganese redox couple in both the crystalline spinel and the amorphous counterpart. Confirming Vandenberghe⁵⁰, they also reported that the crystalline surface of CuMn_2O_4 shifts predominantly towards the more stable $\text{Cu}^{1+} \text{Mn}^{4+}$ couple. He postulated this effect was causing the decrease in activity in the crystalline spinel, although he also correlated increasing K^+ surface segregation. There is evidence for further synergetic activity for CO oxidation in hopcalite. Buciuman *et al.*²⁴ investigated hopcalite activity in comparison with that of single phase oxides and crystalline spinel CuMn_2O_4 . The hopcalite catalyst was as active as the mixed single oxides at low temperature, and far more active than the solitary oxides. Using TPR and kinetic theory, Buciuman proposed an oxygen spillover effect to explain the activity of hopcalite. This is shown in Figure 2. He postulated that oxidation reactions over CuO follow a redox mechanism using lattice oxygen. The mechanism over Mn_2O_3 is associative involving lattice oxygen. Oxygen spillover between the two systems drives high synergetic activity. This is supported by the individual CO oxidation behaviour of both copper and manganese detailed in Part 1.3.

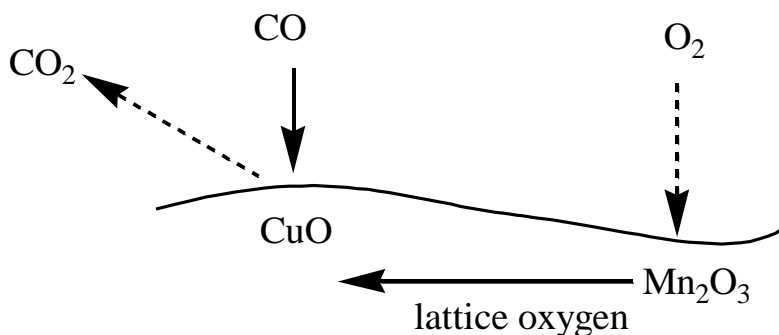


Figure 2 – Mechanism CO oxidation via oxygen spillover

1.4.4 Deactivation of Copper-Manganese Oxides

Catalysts can become mixed with impurities during synthesis, storage or use. If the activity, selectivity or rate of a catalyst is moved away from desired behaviour, these impurities are defined as a poison. Poisons are the opposite of promoters. Some materials may promote one component of a reaction, such as yield, while dropping reaction rate. These can be considered both poisons and promoters. Materials may poison the yield for one reaction product, effectively increasing the yield of other products without interacting in that respective catalytic reaction in any way. A poison with reversible effects is called an inhibitor.

Although originally chosen for its durability, hopcalite is susceptible to several poisons. Mirzaei *et al.*⁵⁴ has reported that Na⁺ surface adsorption during catalyst aging is correlated to poor activity. During hopcalite preparation, excess sodium carbonate is commonly used to drive the metal hydroxycarbonate precipitation. He demonstrates that catalyst aging can reduce the amount of Na⁺ adsorbed on the catalyst surface⁶¹. He reports that careful control to isoelectric point at pH 8.3 results in minimum Na⁺ coverage. He also reinforces the importance of catalyst washing to remove surface impurities.

Hopcalite, like copper and manganese oxides, is deactivated by water. Water tolerance is the main industrial weakness of hopcalite. The phenomena has been reported since its discovery¹³. The exact mechanism of hopcalite deactivation under moisture has not been investigated in the west, although several articles from the USSR have addressed the issue^{67, 68}. Recently, Kireev⁶⁹ reports to have developed water resistant hopcalite granules. In practical cases, hopcalite

catalysts and gas streams have to be dried thoroughly before and during use to prevent total failure. Studies have been made impregnating hopcalite with noble metals to improve performance under hydrated gas streams. Krämer⁶³ doped Pt onto hopcalite surface to improve activity under hydrated conditions, but was unsuccessful. Solsona⁷⁰ doped Au inside CuMn_2O_4 lattice. Cole²² impregnated gold onto hopcalite surface. Both reported an increase in catalyst activity and deactivation resistance. Morgan⁷¹ used TAP analysis on Cole's samples to determine that Au was promoting the Mars-van Krevelen redox mechanism while having no interaction with the Langmuir-Hinshelwood mechanism. Both these mechanisms are discussed in Part 1.3. Further studies on precious metal doped CuMn_2O_4 are reported in Part 1.5.

Cole²² investigated hopcalite under regular gas stream and gas stream where humidity had been reduced (but not to 0.00%) by molecular sieves or a cold trap. In all cases, including testing commercial hopcalite, the results were the same. In the dry tests, he observed decreased initial activity for ~40mins, followed by a highly active steady state. Under the regular gas stream catalysts displayed a characteristic early activity peak followed by steady deactivation. He postulated that surface hydroxyl ions were promoting the catalyst early in the reaction, until their rising frequency began physically blocking surface sites.

Veprek *et al.*⁵⁵ reported that as long as the redox mechanism of CuMn_2O_4 remained active, it is difficult to attribute catalyst deactivation to changes in oxidation state. Veprek reports that calcinations at 500°C for 2 h result in formation of crystalline spinel and complete activity loss, although he also correlates this phenomena with increased K^+ impurity surface coverage. He postulates that even ppm levels of alkali metals present in the structure can preferentially segregate to the catalyst surface. As such he was unable to connect catalyst deactivation absolutely to the formation of crystalline spinel. Yoon and Cocke⁵⁶ prepared model CuMn_2O_4 catalyst surface by oxidation of Cu-Mn alloys at 400-500°C in O_2 . Catalysts calcined at 400°C were reported to be dominated by Cu^{1+} in a tetrahedral environment and Mn^{4+} in an octahedral environment with limited Cu^{2+} and Mn^{3+} . In this respect it resembles deactivated crystalline spinel hopcalite. 300°C calcined catalyst consists of primarily Cu^{2+} and its XPS spectra is similar to amorphous active CuMn_2O_4 . This study supports the work of Veprek.

1.4.5 Promotion of Copper-Manganese Oxides

A promoter is defined as a material which although itself has little or no activity, when added to a catalyst can affect the activity, selectivity or lifetime of the catalyst⁷². If the activity or selectivity is moved closer to desired product yield at zero reaction time, it is defined as a promoter. Typically promoters are added to catalyst in relatively small amounts. They may be referred to as ‘dopants’, ‘impregnations’ or ‘deposits’ amongst other terms.

Promoters are normally introduced into the catalyst bulk before crystallisation. Promoters can affect catalyst structure, commonly surface area or surface morphology. Textural promoters raise the catalyst thermal stability, inhibiting the surface area change caused by sintering. Lattice defect promoters are introduced to be the centre of lattice defect structures on the catalyst surface. Many catalytic reactions are known to occur predominantly on catalyst defect sites^{73, 74}. Electronic promoters affect the vacant electron holes in catalytic molecules, allowing them effective bonding with adsorbent molecules.

Jones⁷ and Cole²² reported experiments doping CuMn_2O_4 with small amounts of other transition metals. Co, Ag, Ni and Fe nitrates (Jones) and Zn nitrates (Cole) were dissolved in the mixed copper manganese nitrate solution before precipitation. Between 1% and 25% of the reagent copper was replaced with an equal number of molecules of the dopant atom. Total reaction stoichiometry remained at $1[\text{Cu+dopant}]:2[\text{Mn}]$.

Cobalt doping, reported by Jones, was effective at increasing both catalyst stability against time and activity. CuCoMnO_4 catalysts were investigated by Wright *et al.*⁷⁵ and were discovered to be more active than CuMn_2O_4 or CoMn_2O_4 . Jones also postulates that Co is a cause of increased stability due to its participation in the Cu-Mn reoxidation mechanism. Co_3O_4 is also a good ambient temperature CO oxidation catalyst in its own right.

Silver doping was reported to increase catalyst stability, surface area and activity to a small degree. AgO is known as a low activity CO oxidation catalyst, which is promoted by calcium chloride¹³.

Nickel doping was reported to correlate with a small decrease in catalyst activity and an increase in catalyst stability. Nickel oxide is not a known low temperature CO oxidation catalyst. Jones theorises that nickel in the sample is bonding preferentially with atmospheric water, allowing the Cu \leftrightarrow Mn redox system to avoid deactivation until the nickel is saturated as Ni(OH)₂.

Iron doping experiments were conducted reporting that low levels of iron coincided with increased CO conversion rate, and a reduction of catalyst surface area. 20% Fe doped hopcalite displayed zero activity and an extremely low surface area.

Zinc doping was investigated on CuMn₂O₄ aged at different times by Cole. He reported that Zn doped catalyst displayed increasing reducibility measured with TPR. He also reports that catalyst aging in combination with the Zn dopant has a large effect on activity.

These five dopant molecules were selected based on the reported behaviour of analogous compounds. For example, cobalt is known to have catalytic properties when mixed with Copper⁷⁶ as CuCo₂O_x/TiO₂; Manganese⁷⁷ as Co and Mn nanoclusters in close proximity; and as an oxide catalyst of Co₃O₄. The ionic configuration of the dopant ions was also considered, including oxidation state, ionic radius (Table 1) and the availability of nitrate salts.

In this thesis, experiments will be reported on alternative dopant atoms. The first is **Vanadium**. Potentially, vanadium could be considered a good replacement for manganese in a spinel lattice. Vanadium in solution has a trend to hydrolyze towards higher oxidation states, V⁺⁴ and V⁺⁵, which makes it similar to manganese in a redox mechanism, which alternates between Mn³⁺ and Mn⁴⁺. The ionic radius (Table 1) of Vanadium^{+3/+4} is 64/58pm, which is closer to manganese^{+3/+4} (64.5/53pm) than copper^{+1/+2} (77/73pm)⁷⁸, so it would be a similar sized replacement in the spinel octahedral lattice. Vanadium is not commercially available as a nitrate salt, but multiple other salts exist – such as chlorides or sulfates. VOSO₄ forms VO²⁺ in aqueous solution. This V⁴⁺ ion configuration is theoretically the most promising V ion given its similarities to Mn⁴⁺. The electron potential of Mn⁴⁺/Mn³⁺, is E° = 0.95 V, compared to V⁴⁺/V³⁺

which is reported as $E^\circ = 0.34$ V. The elements Co, Ni, Fe and Ag, which have been reported as successful dopants, all display positive electron potentials for ionic state changes that could be found in redox reaction in a spinel lattice (Table 2). The ionization energy of Vanadium (IV) is 4507 kJ/mol, which is close when compared to manganese (IV) at 4940 kJ/mol. Ions such as Chromium, Iron, Cobalt and Nickel have been previously reported as successful dopants, and display ionization energies further removed from manganese (Table 3).

Copper-Vanadium catalysts have been reported as active for reactions involving VOC combustion at 300°C⁷⁹. Investigation on CO oxidation over V₂O₅ have reported that activity is affected by phase crystallinity and the mechanism is of the redox variety⁸⁰.

Cerium could potentially be a good replacement for Mn. Cerium primarily exists in two states, Ce³⁺ and Ce⁴⁺, which mimic the manganese redox resonance system active in CO oxidation. The ionic radius (Table 1) for Ce^{4+/3+} is 87/102pm, which is larger than either copper or manganese. It is not as large as Ag⁺ (115pm) which has been described as a successful dopant. The electron potential for Ce⁴⁺ + e⁻ ↔ Ce³⁺ resonance is $E^\circ = 1.44$ V. This is almost identical to the figures for Co^{4+/3+}, a successful hopcalite dopant.

The oxide of cerium is known for its ability to absorb and donate lattice oxygen at high temperature. This has been extensively studied for use in automotive emission control^{81, 82}. It has also been described as a CO oxidation promoter by both Serre *et al.*⁸³, Nunan *et al.*⁸⁴ and Yao *et al.*⁸⁵ in regard to Pt/Al₂O₃. Cerium oxide is widely available as an inexpensive nitrate salt.

Liu *et al.*^{86, 87} reported that CuCeO_x composite catalyst is highly active for carbon monoxide oxidation at 100°C. It also displayed resistance to water poisoning. Liu also discovered strong interactions between Cu and Ce ions by XPS and XRD. Luo *et al.*⁸⁸ reported that copper supported on cerium oxide exhibits high CO conversion activity at 70°C. He attributes this to well dispersed CuO particles, reporting the bulk of CuO as inactive. His TPR studies indicate that CuO/CeO₂ can adsorb CO, whereas singular CuO and CeO₂ cannot. These studies are supported by Zhu *et al.*⁸⁹, who reports mesoporous copper cerium bimetal oxides as active for CO oxidation at 350K.

Metal Ion	Ionic Radius (pm)
Cu ²⁺	73
Cu ⁺	77
Mn ³⁺	58 / 64.5
Mn ⁴⁺	53
Co ²⁺	65 / 74.5
Co ³⁺	54.5 / 61
Ag ⁺	115
Ni ²⁺	69
Fe ³⁺	55 / 64.5
V ³⁺	64
V ⁴⁺	58
V ⁵⁺	54
Ce ³⁺	102
Ce ⁴⁺	87
Si ⁴⁺	40
Pd ²⁺	100

Table 1 – Ionic Radius of Cations⁷⁸

Element	Standard Electron Potential	E°V
Copper	$\text{MnO}_2 + 4\text{H}^+ + \text{e}^- \leftrightarrow \text{Mn}^{3+} + 4\text{H}_2\text{O}$	0.159
Manganese	$\text{Cu}^{2+} + 1\text{e}^- \leftrightarrow \text{Cu}^+$	0.95
Cobalt	$\text{CoO}_2 + 4\text{H}^+ + \text{e}^- \leftrightarrow \text{Co}^{3+} + 2\text{H}_2\text{O}$	1.42
Nickel	$\text{Ni}^{4+} + 2\text{e}^- \leftrightarrow \text{Ni}^{2+}$	1.59
Iron	$\text{Fe}^{3+} \leftrightarrow \text{Fe}^{2+}$	0.77
Vanadium	$\text{VO}^{2+} + 2\text{H}^+ + \text{e}^- \leftrightarrow \text{V}^{3+} + \text{H}_2\text{O}$	0.34
Cerium	$\text{Ce}^{4+} + \text{e}^- \leftrightarrow \text{Ce}^{3+}$	1.44
Palladium	$\text{Pd}^{2+} + 2\text{e}^- \leftrightarrow \text{Pd}_{(s)}$	0.915
Silicon	$\text{SiO}_2 + 4\text{H}^+ + 4\text{e}^- \leftrightarrow \text{Si}_{(s)} + 2\text{H}_2\text{O}$	-0.91

Table 2 - Standard electron potentials of doping elements⁹⁰

Ionization Energies kJ mol ⁻¹	1st	2nd	3rd	4th	5th
Vanadium	650.9	1414	2830	4507	6298.7
Manganese	717.3	1509	3248	4940	6990
Iron	762.5	1561.9	2957	5290	7240
Cobalt	760.4	1648	3232	4950	7670
Nickel	737.1	1753	3395	5300	7339
Copper	745.5	1957.9	3555	5536	7700
Zinc	906.4	1733.3	3833	5731	7970
Cerium	534.4	1050	1949	3547	6325
Palladium	804.4	1870	3177	n/a	n/a
Silicon	786.5	1577.1	3231.6	4355.5	16091

Table 3 – Ionization energies of doping elements⁹¹

Imamura *et al.*⁹² investigated the behaviour between CeO₂ and MnO₂. They report that Ce donates oxygen to Mn at low temperatures but removes it at high temperatures. 5%Ce/MnO₂ was able to oxidise CO at 350°C, a lower temperature than MnO₂ or CeO₂. Arena *et al.*⁹³ also report strong Mn-Ce interactions in their novel MnCeO_x catalysts, which oxidise CO at 323-423K.

Supported **Palladium** metal and its oxide are both known as CO oxidation catalysts⁹⁴. The mechanism for CO oxidation over precious metals is described in section 1.11. Palladium doped hopcalite has not been previously reported by any literature. As a hopcalite dopant, the majority of Pd would not be accessible on the catalyst surface. Few studies have impregnated Pd onto hopcalite surface. Szyrkowska⁹⁵ reported Pd-impregnated hopcalite in regard to thiophene oxidation. Pd/CuMn₂O₄ was more active than Pt/CuMn₂O₄ or Au/Mn₂O₄. TPR data indicated that Pd lowered the temperature at which hopcalite was reduced significantly. Rogowski *et al.*⁹⁶ reported that hopcalite doped with Pd was more active for thiophene oxidation than Au or Pt doped samples. Krämer *et al.*⁶³ doped Pt into hopcalite in an attempt to improve water tolerance, but were unsuccessful.

Palladium oxide primarily exists in a single oxidation state as PdO. It is easily reduced to Pd metal and will decompose on extended contact with the atmosphere. It is commercially available as a nitrate salt Pd(NO₃)₂. Pd²⁺ has an ionic radius of 100pm, larger than either copper or manganese. The electrostatic potential of a Pd²⁺ ↔ Pd redox mechanism is E° = 0.915 V, which is positive like all other successful dopants. The ionisation energies for Pd are between the values for nickel and zinc, two successful hopcalite dopants.

Silicon oxide, SiO₂, would theoretically perform poorly as a dopant affecting the hopcalite redox mechanism. It has only one ionic state, (IV), and does not easily reduce. Its ion has a radius of 40pm, much smaller than either copper or manganese. Electron potential of SiO₂ + 4H⁺ + 4e⁻ ↔ Si_(s) + 2H₂O is E° = -0.91 V. However silicon dioxide, or silica, could be viewed as a successful hopcalite dopant due to its strong hydrophilic character⁹⁷. Jones⁷ has theorised that nickel doped into hopcalite was responsible for deactivation resistance. He attributed this to Nickel forming Ni(OH)₂ groups with atmospheric H₂O, allowing the Cu and Mn to avoid

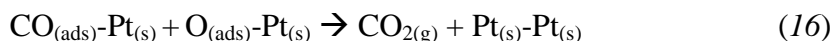
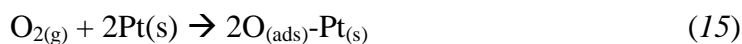
deactivation by water. Doping silica into hopcalite may have the same effect. Silicon salts do not easily dissolve in acids, but silicon tetraacetate was tested and found to dissolve in 2M Na_2CO_3 . It precipitates at $\text{pH}\sim 9$. Silicon can be added to a hopcalite co-precipitation by dissolving in the carbonate base. This is then added to the preparation, which under vigorous stirring would allow silicon particles to mix with the copper-manganese particles as they precipitate. The exact chemistry of this is unknown. The formation of a stable CuMnSiO_x compound is unlikely due to the difference in atomic size. The moment between reagent addition and mixing may also retard closely mixed precipitation. It is more likely that macroscopic SiO_2 particles will be present in the hopcalite powder. This is not important, as the proposed roles for silica is promotion by water absorbance, not by influence of redox catalysis.

The influence of silica on hopcalite has not been previously reported. Cu supported on SiO_2 was studied by Boccuzzi *et al.*⁹⁸, who investigated using FTIR spectroscopy. He discovered Cu on SiO_2 would reduce at 523K, and theorised that it would be an efficient CO oxidation catalyst at ambient temperature. The morphology of Mn on SiO_2 support has been investigated by Patcas and Buciman⁹⁹. They reported varied unloaded surfaces, transition zones, MnO_x "islands" and well crystallized manganese oxide spots consisting of Mn^{2+} and Mn^{3+} cations. Nohman¹⁰⁰ reported strong silica-manganese interactions in Mn/SiO_2 as well as detectable manganese silicates. He also reported that acetate deposition was more favorable for Mn-Si bonding than oxalate deposition.

1.5 CO Oxidation over Supported Precious Metals

Practical CO oxidation can also be performed by precious metals. Metallic copper, platinum, palladium, silver and gold are the most commonly used elements. Precious metals are chemically defined by their low reactivities. This makes them useful in catalysis, as they are reactive enough to bond with gaseous molecules without irreversible poisoning. Other strengths relative to metal oxides are high water tolerance and resistance to some common poisons such as sodium. Their main drawbacks are high cost, low durability and vulnerability to sulphur poisoning¹⁰¹. This is normally mitigated by dispersing the metal as nanoparticles across a cheap, durable high surface area support such as alumina, silica, carbon or titania. CO oxidation over

macroscopic metallic precious metals is accepted to take place via a Langmuir-Hinshelwood adsorption mechanism¹⁷. O₂ adsorbs onto two adjacent atoms on M_(surface) and then dissociates across both. CO adsorbs on a single M_(surface) site. Engel and Ertl¹⁰² proposed the following steps using Pt as an example:



This is a very simple model that does not take into account several factors. These include but are not limited to, firstly, the effects of CO self poisoning/asymmetric inhibition. As O₂ requires two adjacent atoms to adsorb onto M surface, and CO only one, CO in sufficient concentration will slow or block the adsorption of O₂. This results in the activation energy for the reaction closely correlating the heat of adsorption for CO onto a particular surface¹⁰³. Secondly, CO has been described¹⁰⁴ as more mobile on M surface than O₂, and must migrate to immobile O₂ atoms for the oxidation reaction. The surface diffusivity of CO varies over different M atoms which can affect activity. Modelling the behaviour of CO oxidation over precious metals has occupied entire departments for decades and is beyond the scope of this thesis. It is accepted that precious metals are far more active for CO oxidation than base metal oxides. Kummer¹⁰⁵ and Royer and Duprez¹⁷ reported the relative activities of these metals, displayed in Table 4.

Active Phase	Relative Activity	Active Phase	Relative Activity
Pd	500	CuO	45
Pt	100	Au	15
Co ₂ O ₃	80	MnO ₂	4.4

Table 4 – Relative Activities of Metals for CO oxidation at 300°C (1% CO in excess O₂)

CO oxidation over oxide supported nanoscale precious metals is much harder to study. The majority of the metal may be in catalyst pores. It could be too small to detect or have formed bimetallic complexes within the support. Studies on clean metal catalysts have provided some insight. The effect of the oxide support on the dispersed metal also cannot be underestimated. Supports are not chemically inactive, and metal-support interactions can promote or retard

catalytic processes. Depositing precious metals in nanoparticles increases their surface area exponentially, vastly increasing the available active sites. These particles can later agglomerate via sintering, which deactivates the surface.

Precious metals can be introduced onto a support in many ways. Incipient wetness (IW) techniques use minimum volume solution to dissolve metal salts, which are mixed with the support. Hydrolysis of metal oxides is exothermic, and the solution either adsorbs or evaporates leaving the metal salt on the surface. Salt groups are then removed via calcination or reduction. IW strengths include exactly 100% reagent/product yield and ease of procedure. Weaknesses include poor final metal dispersion.

Electrostatic Adsorption (EA), or ion exchange, is a wet impregnation technique. The support is immersed in excess water and pH adjusted. The surface is polarised by changing the pH relative to the support isoelectric point. Soluble metal salts with aqueous ions charged opposite that of the surface are added to the solution. This results in the metal ions bonding with the support surface. Finally, the filtrate is removed. The state of the metal can be adjusted by calcination or reduction. Strengths of EA include high dispersion. Weaknesses include lower than 100% yield, unknown side reactions during the experiment and poisoning by salt ions. It may also occur that metal salts, soluble in conditions that charge the support in the opposite direction, do not exist. This can be slightly mitigated by pH adjusting the support to its zero point charge. In this state it will be charge-neutral and more versatile.

Coprecipitation involves dissolving both the support and the active phase salts in the same solution, then precipitating them as carbonates or hydroxides via pH control. Effective mixing and temperature control is important. This poses a problem during industrial upscaling. In addition, active phase materials may be precipitated inside the support. For this reason this method is normally used for catalysts with a metal loading of 10% or higher.

Deposition Precipitation (DP) is similar, but involves precipitation of an active metal salt inside the pore of a solid support in aqueous solution. Careful mixing and slow pH control is needed to prevent large crystal agglomerates from blocking support pores.

After catalyst preparation, a reduction is often needed. Precious metals are also capable of reducing under atmospheric conditions to a certain degree. Reduction is normally performed by calcinations under H_2 . It can also be reached by addition of a reducing agent, such as sodium formate, to a wet catalyst preparation. This is normally followed by careful washing.

1.5.1 Catalyst Supports

A common catalyst support is **alumina**, Al_2O_3 . Alumina has a high surface area, is extremely durable, insoluble and inexpensive. Alumina can exist in many different phases, such as α , χ , η , δ , κ , θ , γ and ρ ¹⁰⁶. These are formed during the calcination of the precursor, aluminium hydroxide. Alumina is reported to possess Lewis acid sites¹⁰⁷. These have a major effect upon state and distribution of active components¹⁰⁸. Alumina also exhibits high thermal stability¹⁰⁹. Mo *et al.*¹¹⁰ have reported λ -alumina to possess cation vacancies which facilitate interactions between cations and the support. This is important as redox properties of precious metals can be influenced by their interactions with the support, as described by Otto *et al.*¹¹¹.

Supporting platinum on alumina is a common catalytic preparation. Ivanova *et al.*⁹⁴ investigates Pt/ Al_2O_3 catalysts prepared by incipient wetness and calcined at 450-600°C. He reports CO oxidation $T_{10\%}$ and $T_{50\%}$ conversion at >150°C, it can be assumed these catalysts are not active at ambient temperature. The gas feed used was 0.2% CO with 1.0% O_2 , which could result in CO self-poisoning due to the low oxygen content. Thus may explain the low activity. The effect of CO concentration on activity has been reported by Seo *et al.*¹¹². Using supported Pt/ TiO_2 catalysts he clearly demonstrates the loss in activity as CO concentration rises from 10.4 to 1032ppm in air. Room temperature activity was only exhibited by reduced catalysts. Reduction conditions involved H_2/N_2 gas stream at 600°C. Lieske *et al.*¹¹³ have discussed the effects of H_2 and O_2 treatment on Pt/ Al_2O_3 catalysts using TPR. They link platinum redispersion to the presence of Cl between 500 and 600°C.

The effects of water on Pt/ Al_2O_3 has been the subject of much interest. Muraki *et al.*¹¹⁴ investigated steam and H_2 effects on Pt/ Al_2O_3 below 200°C. They discovered that the catalysts were strongly promoted by steam and H_2 . They attributed this to the weakening of self

poisoning by CO. They also discovered no water-gas shift reaction occurring in this system. Pt was more strongly promoted than Pd or Rh. Ebbesen *et al.*¹¹⁵ investigated the effect of liquid water on Pt/Al₂O₃. He found strong interactions between H₂O, Pt and C≡O. This fundamentally changes the properties of CO adsorbed on Pt. CO affects the transition dipole of adsorbed CO, leading to increased back donation from the metal surface.

Investigations have been conducted into modifying the water tolerance of platinum catalysts, in an attempt to influence activity. The literature reports that CO oxidation over Pt/Al₂O₃ catalysts is promoted by humidity¹¹⁴. Accumulated macroscopic water could also act as a barrier to effective CO transfer on the catalyst surface. Graham's law of diffusion predicts that CO will be perfectly diffuse in the CO/O₂/N₂ gas stream. 5000ppm CO has a concentration of 2.2025×10^{-4} mol L⁻¹. Henry's law of diffusion shows that under a constant gas partial pressure, CO and O₂ will diffuse into a liquid surface to a constant concentration. Using 0.5% mole fraction and Henry's law CO constant, the concentration of CO in solution will be 4.75×10^{-5} mol L⁻¹. Consequently, CO in solution is 4.6 times less concentrated than found in the gas stream. It can be deduced the water/gas interface is a significant barrier to effective CO transfer.

Catalyst support hydrophobicity can be modified by doping with silyating reagents. SiO₂ is reported as hydrophilic. Si(CH₃)₂ methyl groups are known to be hydrophobic. Quintanilla *et al.*¹¹⁶ silyated Pd/SiO₂ towards the hydrogenation of aromatic ketones. Omota *et al.*¹¹⁷ studied silyated Pd/SiO₂ catalyst in regard to the hydrogenation of methyl acrylate. Both studies reported modification of hydrophilic silica behavior via organosilicon reagent impregnation. Alumina silyation has previously been reported by Slavov *et al.*¹¹⁸. Slavov silyated alumina with a N₂/silane feed gas at 220°C, and discovered Al-Si-OH groups forming without HCl products. In another experiment, Slavov *et al.*¹¹⁹ silyated alumina with hexamethyldisilazane (HMDS) in a N₂ feed gas between 150°C and 450°C. He discovered formation of -O-SiMe₃ moieties, which under increasing temperature react with hydroxyl groups to produce methane gas. A further experiment by Slavov *et al.*¹²⁰ confirmed that increasing the temperature of silyated alumina catalyst results in sequential removal of methyl groups from the Si molecule. Exactly 1 mol of methane is produced per 1 mole of reagent methyl group. Chloride remains bound to the alumina surface.

Palladium is also commonly supported on alumina. The mechanism of CO oxidation over Pd⁰ is reported to be a Langmuir-Hinshelwood model in a similar way to Pt. Kinetic studies by Szanyi and Goodman¹⁰³ have reported that CO self-poisoning is the most important factor in activity. The activation energy for the reaction was equivalent to the CO heat of adsorption. This results in a negative first order rate in regard to the concentration of CO. These factors are identical to those seen in Pt catalysis. Schwartz *et al.*¹²¹ reports Pd can be oxidised to PdO, which exhibits catalytic behaviour consistent with a metal-oxide semiconductor rather than a metal. Cordi and Falconer¹²² have described PdO as less active for CO oxidation than Pd⁰. Maillet *et al.*¹²³ has described PdO/Al₂O₃ as capable of reduction under CO to Pd⁰.

In the previously mentioned study Ivanova *et al.*⁹⁴ also reported metal support interactions between Pd and Al₂O₃. He discovered that Pd particles on Al₂O₃, exist in two phases, large agglomerated PdO phases of ~100 nm, and smaller dispersed Pd⁰ phases of ~1.5-3 nm. When calcined at 450-550°C, the smaller particles became covered by a thin layer of aluminate phase. This was confirmed by XPS, HRTEM and the inability to reduce Pd by H₂ between -15 and 450°C. This phase is destroyed by calcination between 450-1000°C, which agglomerates particles and reduces activity. The state of Pd is found to shift towards large PdO agglomerates at the expense of small Pd⁰ particles. Calcination at 1200°C resulted in reduction of large PdO particles to large Pd⁰ particles, which also exhibited low activity. The importance of chemical state of Pd was investigated by Maillet *et al.*¹²³. He tested pre-oxidised and pre-reduced Pd/ γ -Al₂O₃ for CO oxidation at 210°C. He discovered no difference in activities for CO oxidation under 0.8% CO/0.16% O₂/balance N₂. Using XRD data, he proved that PdO is reduced under CO before CO oxidation light off temperature was reached. This accounted for their identical activities. Otto *et al.*¹¹¹ also reported on Pd ionic state. Using XPS, he clearly distinguished between large PdO agglomerated particles and small dispersed Pd⁰ particles. He discovered that in weightings of more than 0.5%, PdO reduces under H₂ at ambient temperature. At lower weightings, PdO does not reduce at this temperature.

A catalyst support impregnated with two distinct metal elements is referred to as a bimetallic. Improvements in catalytic technology with Pt-Pd bimetallics have been reported by Castellazzi *et al.*¹²⁴ in regard to CH₄ combustion; Ito *et al.*¹²⁵ in regard naphthalene hydrogenation and Kim

*et al.*¹²⁶ in regard to oxidation of reactive dyes. Strobel *et al.*¹²⁷ investigated Pt-Pd bimetallics for methane combustion. He discovered that small Pt particles in Pd catalysts enhanced resistance to catalyst sintering. The majority of CO oxidation over Pt:Pd catalysts has been conducted towards the oxidation of CO under lean O₂ conditions. This is applicable to automotive exhaust catalysis. Ambient temperature oxidation under excess O₂ has seen less interest. Parinyaswan *et al.*¹²⁸ investigated Pt:Pd/CeO₂ alloys for Preferential Oxidation of CO in the presence of H₂. They discovered a 1:7 Pt:Pd ratio was most active. They also reported strong promotion effects by water, as well a strong poisoning effects by CO₂. Pt-Pd bimetallics have also been discussed in regard to sulphur resistance. Adding small amounts of Pd to Pt/SiO₂/Al₂O₃ catalyst, Jiang *et al.*¹⁰¹ reported a change in the adsorption properties of H₂ and H₂S on catalyst surface. Dissociative H₂ adsorption was made more competitive on the bimetallic surface compared to H₂S. He attributes this to the formation of electron deficient sites on the catalyst surface.

Park and Lee¹²⁹ have predicted that metal alloying occurs when mixing is exothermic. They estimated that heat of mixing of Pt and Pd is $-0.003 \text{ eV atom}^{-1}$. This supports slightly exothermic behaviour and it can be said that Pt and Pd could form weak alloys. Pd displays a lower melting temperature and heat of vaporization than Pt. As a result, it is expected to be lower co-ordinated than Pt and would segregate to the surface of bimetallic clusters¹³⁰.

Kaya and Üner¹³¹ investigated sequentially impregnated Pt/Pd/Al₂O₃ catalysts. They discovered that sequential impregnation did not result in the formation of alloyed particles. Monometallic Pt and Pd displayed higher activity than the bimetallic catalysts. Pd displayed a higher tolerance to CO self poisoning than Pt which was attributed to subsurface PdO layers. In a later study, Kaya *et al.*¹³², using Monte-Carlo simulations, reported that Pd segregated to the surface of Pt/Pd clusters. At low temperatures the bimetallic particles behaved identically to monometallic Pd. The surface mechanism of CO oxidation over Pd monolayer on Pt(111) was reported by Lucas *et al.*¹³³. This was achieved in aqueous environment under electrostatic potential control. He discovered that Pd was forming an inconsummate oxide structure during CO adsorption, which reverses upon dissociation. It should be noted that this is an electrostatic model system and Ebbesen *et al.*¹¹⁵ have reported that liquid water has a significant effect on the reaction.

The majority of supported Pd:Pt bimetallics have been synthesised by wet impregnation methods. Yashima *et al.*¹³⁴ prepared Pt and Pd particles by reaction in microemulsion. These were then deposited on Al₂O₃ and calcined at 600°C forming alloyed particles. They reported that a 20:80 Pt:Pd molar ratio was the most active catalyst. This was contrasted with their wet-impregnated catalyst which exhibited highest activity at 50:50 ratio. Viesz *et al.*¹³⁵ manufactured Pt:Pd powder catalysts using a colloid synthesis. They discovered preferential Pt surface segregation and also reported Pt:Pd alloying. They correlated this to inhibition of Pd oxidation to PdO by Pt.

Overall, there is much evidence of Pt:Pd interaction in bimetallic catalysts. Alloying is possible, and synergetic effects are not unprecedented.

Hopcalite has been described as an ambient temperature CO oxidation catalyst which is resistant to sulphur poisoning but deactivates under humidity. As discussed, Pt and Pd have been described as efficient CO oxidation catalysts which are vulnerable to poisoning by sulphur and promoted by water. Impregnating Pt and Pd onto hopcalite support could result in a versatile catalyst which exhibits resistance to both water and sulphur poisoning. This experiment has not been previously reported. However, Pt has been reported as impregnated onto singular copper and manganese oxides.

Gbric¹³⁶ investigated the effects of Mn on Pt in regard to the oxidation of CO and n-hexane. MnO_x was found to enhance the formation of Pt²⁺ ions which was correlated to poor CO oxidation activity. Activity for n-hexane oxidation rose significantly. He attributes this to the formation of Pt-Mn oxide like species which weaken the Pt-O bond.

Szynkowska *et al.*¹³⁷ investigated the effects of Cu and Mn on Pt in regard to the oxidation of thiophene. Pt/CuO support displayed a higher activity for thiophene oxidation than Pt/MnO₂ support. He also reported detectable metal-support interactions affecting the reducibility and activity of all species. Krämer⁶³ doped Pt onto hopcalite surface to improve activity under hydrated conditions, but was unsuccessful.

A study by Ferrandon *et al.*^{138, 139} investigated Pt on CuO/Al₂O₃ and MnO_x/Al₂O₃ in regard to oxidation of a feed gas comprised of carbon monoxide, naphthalene and methane. He reports Pt as capable of catalysing the reduction of MnO_x to Mn but not CuO to Cu. He also tested sulphur resistance and discovered Pt/MnO₂/Al₂O₃ had improved activity for CO oxidation after sulphur treatment. Ferrandon proposes that mixing a noble metal with a less electronegative cation leads to the formation of a noble metal oxide. Mn₂O₃-Pd interaction is reported to promote the formation of PdO. This may be out competed by the spontaneous reduction of PdO by CO at room temperature reported by Maillet¹²³. Ferrandon also reports that CuO-Pd interaction preferentially forms Pd⁰. He attributes this to the higher electronegativity of Cu atoms compared to Mn (displayed in Table 5). This is supported by Baylett *et al.*¹⁴⁰. He has described the impregnation of Pd onto Mn₂O₃ in regard to the oxidation of methane. He reports Mn₂O₃ favours the +2/+3 redox couple, which enhances methane oxidation. Mirzaei⁶¹ has reported the surface of active hopcalite to consist of Cu²⁺ and Mn^{3+/4+}. It could be theorised that Pd interaction would reduce Manganese surface oxidation state and negatively affect activity. As such, synthesis should attempt to minimise Pd-Mn interactions.

Element	Pauling Electronegativity
Mn	1.55
Al	1.61
Cu	1.9
Sn	1.96
Pt	2.28
Pd	2.2

Table 5 – Pauling Electronegativity of atoms¹⁴¹

Szynkowska *et al.*¹³⁷ has discussed the oxidation of thiophene over noble metal doped copper and manganese catalysts. Supported by the work of Rogowski *et al.*⁹⁶, he describes measurable support-metal interactions influencing the reducibility and activity of both systems.

The effects of bimetallic Pt and Pd have not been reported upon CuMn₂O₄. In addition, bimetallic Pt/Pd has also not been the study of extensive research when impregnated onto single phase Cu and Mn.

At ambient temperatures, **stannic oxide** is not catalytically active for CO oxidation. At the same temperature, CO oxidation over Pt is hindered by CO-self poisoning. Pt supported on stannic oxide exhibits synergy and is highly active at ambient temperature. The mechanism for this has been investigated by many researchers¹⁴²⁻¹⁴⁵. These competing explanations were followed up by a study by Grass and Lintz¹⁴⁶. Investigating the kinetics of CO oxidation of Al₂O₃ supported Pt/SnO₂ compounds, they report that CO chemisorption is restricted to Pt, whereas O₂ chemisorption can occur on both SnO₂ and Pt. They explain that the rate is zero order in regard to both CO and O₂ concentration. O₂ migration rate from SnO₂ surface to active sites is the determining step of the reaction. Oxygen spillover from SnO₂ to Pt cannot be excluded. In a supporting study, Matsui *et al.*¹⁴⁷ have reported that doping Pt electrodes with SnO_x increases the tolerance of Pt towards CO self poisoning.

Kamiuchi *et al.*¹⁴⁸ reported on the behaviour of Pt/SnO₂, in regard to catalyst sintering and redispersion. He reported that repeated calcination under reductive conditions followed by oxidative treatment at 400°C results in a reversible morphology change. Under reducing atmosphere, sintered Pt particles with increased size became predominant. Under further reoxidating conditions, smaller Pt particles were redispersed, displaying strong chemical interactions with the support. CO oxidation behaviour was strongly affected by this change. The oxidised catalyst displayed a light off temperature of 90°C. The catalysts reduced at 90°C under H₂ saw a reduction in light off temperature to 70°C. Catalysts reduced and reoxidised at 400°C showed a rise in light off temperature to 150 °C and 160°C respectively. This supports the theory that Pt⁰ is the more active Pt state for CO oxidation.

Palladium has a very similar behaviour when doped onto tin oxide as platinum, such that some researchers do not differentiate between the two elements¹⁴⁶. A concise study of CO oxidation at ambient temperature was conducted by Gadgil *et al.*¹⁴⁹. He reports that the reaction is driven by incorporation of lattice oxygen. The presence of Sn²⁺ in the support matrix is detected, indicating a redox mechanism at work. This supports the work of Fuller *et al.*³⁵ who first proposed a redox mechanism for CO oxidation over SnO₂.

Mirkelamoglu *et al.*¹⁵⁰ investigated the effect of sodium on Pd/SnO₂ catalysts. He postulates that sodium-promoted SnO₂ possesses increased oxygen affinity which leads to a reduction in CO self-poisoning on Pt.

The effects of bimetallic Pt and Pd have not been reported upon SnO₂.

1.6 Chapter 1 References

1. I. Blumenthal, *Journal of the Royal Society of Medicine*, 2001, **94**, 270-272.
2. M. Sowa, M. Murtz and P. Hering, *Journal of Breath Research*, 2010, **4**, 6.
3. S. T. Omaye, *Toxicology*, 2002, **180**, 139-150.
4. *EH40/2005 Workplace exposure limits*, <http://www.hse.gov.uk/cosHH/table1.pdf>.
5. M. Goldstein, *Journal of Emergency Nursing*, 2008, **34**, 538-542.
6. A. J. Lupinetti, S. Fau, G. Frenking and S. H. Strauss, *Journal of Physical Chemistry A*, 1997, **101**, 9551-9559.
7. C. D. Jones, Cardiff University, 2006.
8. *CO MSDS*, http://msds.chem.ox.ac.uk/CA/carbon_monoxide.html.
9. I. Langmuir, *Journal of the American Chemical Society*, 1918, **40**, 1361-1403.
10. U. Diebold, *Surface Science Reports*, 2003, **48**, 53-229.
11. C. H. Bartholomew, *Applied Catalysis a-General*, 2001, **212**, 17-60.
12. C. S. Song, *Catalysis Today*, 2002, **77**, 17-49.
13. A. B. Lamb, W. C. Bray and J. C. W. Frazer, *Journal of Industrial and Engineering Chemistry-Us*, 1920, **12**, 213-221.
14. G. Ertl and M. Neumann, *Zeitschrift Fur Physikalische Chemie-Frankfurt*, 1974, **90**, 127-134.
15. M. Haruta, S. Tsubota, T. Kobayashi, H. Kageyama, M. J. Genet and B. Delmon, *Journal of Catalysis*, 1993, **144**, 175-192.
16. J. Regalbuto, *Catalyst Preparation*, CRC Press, Taylor and Francis Group, 2007.
17. S. Royer and D. Duprez, *Chemcatchem*, 2011, **3**, 24-65.
18. J. Jansson, M. Skoglundh, E. Fridell and P. Thormahlen, *Topics in Catalysis*, 2001, **16**, 385-389.
19. S. B. Kanungo, *Journal of Catalysis*, 1979, **58**, 419-435.
20. X. W. Xie, Y. Li, Z. Q. Liu, M. Haruta and W. J. Shen, *Nature*, 2009, **458**, 746-749.
21. T. J. Huang and D. H. Tsai, *Catalysis Letters*, 2003, **87**, 173-178.
22. K. J. Cole, Cardiff University, 2008.
23. G. C. Bond, *Heterogeneous Catalysis, Principles and Applications*, Clarendon Press, 1974.
24. F. C. Buciuman, F. Patcas and T. Hahn, *Chemical Engineering and Processing*, 1999, **38**, 563-569.
25. M. Kang, M. W. Song and C. H. Lee, *Applied Catalysis a-General*, 2003, **251**, 143-156.
26. Y. Takita, T. Tashiro, Y. Saito and F. Hori, *Journal of Catalysis*, 1986, **97**, 25-35.
27. W. A. Whitesell and J. C. W. Frazer, *Journal of the American Chemical Society*, 1923, **45**, 2841-2851.
28. Kobayash.M, Matsumot.H and Kobayash.H, *Journal of Catalysis*, 1971, **21**, 48-&.
29. Kobayash.M and Kobayash.H, *Journal of Catalysis*, 1972, **27**, 100
30. Kobayash.M and Kobayash.H, *Journal of Catalysis*, 1972, **27**, 108
31. Kobayash.M and Kobayash.H, *Journal of Catalysis*, 1972, **27**, 114
32. J. A. Labinger and K. C. Ott, *Catalysis Letters*, 1990, **4**, 245-249.
33. G. G. Jernigan and G. A. Somorjai, *Journal of Catalysis*, 1994, **147**, 567-577.
34. J. W. Mellor, *A Comprehensive Treatise on Inorganic and Theoretical Chemistry*, Longmans, Green & Co., 1932.

35. M. J. Fuller and M. E. Warwick, *Journal of Catalysis*, 1973, **29**, 441-450.
36. A. Hagemeyer, Z. Hogan, M. Schlichter, B. Smaka, G. Streukens, H. Turner, A. Volpe, H. Weinberg and K. Yaccato, *Applied Catalysis a-General*, 2007, **317**, 139-148.
37. P. G. Harrison, C. Bailey and W. Azelee, *Journal of Catalysis*, 1999, **186**, 147-159.
38. K. Grass and H. G. Lintz, *Preparation of Catalysts Vi*, 1995, **91**, 1111-1119.
39. C. Corporation, *Carulite MSDS*,
<http://www.caruscorporation.com/resources/content/3/2/7/documents/CARULITE300GranularCatalyst.pdf>.
40. Puresphere, Editon edn., 2011.
41. G. J. Hutchings, A. A. Mirzaei, R. W. Joyner, M. R. H. Siddiqui and S. H. Taylor, *Applied Catalysis a-General*, 1998, **166**, 143-152.
42. C. E. Lanning, *Journal of the American Chemical Society*, 1930, **52**, 2411-2415.
43. M. Li, D. H. Wang, X. C. Shi, Z. T. Zhang and T. X. Dong, *Separation and Purification Technology*, 2007, **57**, 147-151.
44. L. E. Orgel and J. D. Dunitz, *Nature*, 1957, **179**, 462-465.
45. A. P. B. Sinha, N. R. Sanjana and A. B. Biswas, *Journal of Physical Chemistry*, 1958, **62**, 191-194.
46. A. Waskowska, L. Gerward, J. S. Olsen, S. Steenstrup and E. Talik, *Journal of Physics-Condensed Matter*, 2001, **13**, 2549-2562.
47. S. Miyahara, *Journal of the Physical Society of Japan*, 1962, **17**, 181
48. Dollimor.D and K. H. Tonge, *Journal of the Chemical Society a -Inorganic Physical Theoretical*, 1970, 1728-&.
49. R. Buhl, *Journal of Physics and Chemistry of Solids*, 1969, **30**, 805
50. R. E. Vandenberghe, *Physica Status Solidi a-Applied Research*, 1978, **50**, K85-K88.
51. B. Gillot, S. Buguet and E. Kester, *Journal of Materials Chemistry*, 1997, **7**, 2513-2517.
52. V. Koleva, D. Stoilova and D. Mehandjiev, *Journal of Solid State Chemistry*, 1997, **133**, 416-422.
53. D. G. Stoilova, R. N. Nickolov and K. T. Cheshkova, *Journal of Colloid and Interface Science*, 2000, **228**, 24-31.
54. A. A. Mirzaei, H. R. Shaterian, R. W. Joyner, M. Stockenhuber, S. H. Taylor and G. J. Hutchings, *Catalysis Communications*, 2003, **4**, 17-20.
55. S. Veprek, D. L. Cocke, S. Kehl and H. R. Oswald, *Journal of Catalysis*, 1986, **100**, 250-263.
56. C. H. Yoon and D. L. Cocke, *Journal of Catalysis*, 1988, **113**, 267-280.
57. P. Porta, G. Moretti, M. Musicanti and A. Nardella, *Solid State Ionics*, 1993, **63-5**, 257-267.
58. P. Porta, G. Moretti, M. Musicanti and A. Nardella, *Catalysis Today*, 1991, **9**, 211-218.
59. G. J. Hutchings, A. A. Mirzaei, R. W. Joyner, M. R. H. Siddiqui and S. H. Taylor, *Catalysis Letters*, 1996, **42**, 21-24.
60. M. Tsunekawa, *Memoirs of the Faculty of Engineering, Hokkaido University*, 1987, **17**, 133-144.
61. A. A. Mirzaei, H. R. Shaterian and M. Kaykhaii, *Applied Surface Science*, 2005, **239**, 246-254.
62. G. Fortunato, H. R. Oswald and A. Reller, *Journal of Materials Chemistry*, 2001, **11**, 905-911.

63. M. Kramer, T. Schmidt, K. Stowe and W. F. Maier, *Applied Catalysis a-General*, 2006, **302**, 257-263.
64. Z. R. Tang, C. D. Jones, J. K. W. Aldridge, T. E. Davies, J. K. Bartley, A. F. Carley, S. H. Taylor, M. Allix, C. Dickinson, M. J. Rosseinsky, J. B. Claridge, Z. L. Xu, M. J. Crudace and G. J. Hutchings, *Chemcatchem*, 2009, **1**, 247-251.
65. G. M. Schwab and S. B. Kanungo, *Zeitschrift Fur Physikalische Chemie-Frankfurt*, 1977, **107**, 109-120.
66. D. L. Cocke and S. Veprek, *Solid State Communications*, 1986, **57**, 745-748.
67. S. A. Solovev, G. M. Belokleitseva and V. M. Vlasenko, *Journal of Applied Chemistry of the Ussr*, 1992, **65**, 1555-1559.
68. B. Bruns, *Acta Physicochimica Urss*, 1937, **7**, 875-882.
69. A. S. Kireev, V. M. Mukhin, S. G. Kireev, V. N. Klushin and S. N. Tkachenko, *Russian Journal of Applied Chemistry*, 2009, **82**, 169-171.
70. B. Solsona, G. J. Hutchings, T. Garcia and S. H. Taylor, *New Journal of Chemistry*, 2004, **28**, 708-711.
71. K. Morgan, K. J. Cole, A. Goguet, C. Hardacre, G. J. Hutchings, N. Maguire, S. O. Shekhtman and S. H. Taylor, *Journal of Catalysis*, 2010, **276**, 38-48.
72. M. Bowker, *The Basis and Applications of Heterogeneous Catalysis*, Oxford University Press, United States, 1998.
73. D. Bom, R. Andrews, D. Jacques, J. Anthony, B. L. Chen, M. S. Meier and J. P. Selegue, *Nano Letters*, 2002, **2**, 615-619.
74. G. Pacchioni and T. Minerva, *Surface Science*, 1992, **275**, 450-458.
75. P. A. Wright, S. Natarajan, J. M. Thomas and P. L. Gaiboyes, *Chemistry of Materials*, 1992, **4**, 1053-1065.
76. X. Chen, J. F. Zhang, Y. Huang, Z. Q. Tong and M. Huang, *Journal of Environmental Sciences-China*, 2009, **21**, 1296-1301.
77. F. Jiao and H. Frei, *Energy & Environmental Science*, 2010, **3**, 1018-1027.
78. R. D. Shannon, *Acta Crystallographica Section A*, 1976, **32**, 751-767.
79. L. A. Palacio, J. M. Silva, F. R. Ribeiro and M. F. Ribeiro, *Catalysis Today*, 2008, **133**, 502-508.
80. F. Roozeboom, A. J. Vandillen, J. W. Geus and P. J. Gellings, *Industrial & Engineering Chemistry Product Research and Development*, 1981, **20**, 304-309.
81. J. C. Schlatter and P. J. Mitchell, *Industrial & Engineering Chemistry Product Research and Development*, 1980, **19**, 288-293.
82. G. Kim, *Industrial & Engineering Chemistry Product Research and Development*, 1982, **21**, 267-274.
83. C. Serre, F. Garin, G. Belot and G. Maire, *Journal of Catalysis*, 1993, **141**, 1-8.
84. J. G. Nunan, H. J. Robota, M. J. Cohn and S. A. Bradley, *Journal of Catalysis*, 1992, **133**, 309-324.
85. Y. F. Y. Yao, *Journal of Catalysis*, 1984, **87**, 152-162.
86. W. Liu and M. Flytzani-Stephanopoulos, *Journal of Catalysis*, 1995, **153**, 317-332.
87. W. Liu and M. Flytzani-Stephanopoulos, *Journal of Catalysis*, 1995, **153**, 304-316.
88. M. F. Luo, Y. J. Zhong, X. X. Yuan and X. M. Zheng, *Applied Catalysis a-General*, 1997, **162**, 121-131.
89. J. K. Zhu, Q. M. Gao and Z. Chen, *Applied Catalysis B-Environmental*, 2008, **81**, 236-243.

90. A. J. Bard, *Standard Potentials in Aqueous Solutions*, Marcel Dekker, New York, 1985.
91. D. Lide, *CRC Handbook of Chemistry and Physics*, 84th edn., CRC Press, Boca Raton, Florida, 2003.
92. S. Imamura, M. Shono, N. Okamoto, A. Hamada and S. Ishida, *Applied Catalysis a-General*, 1996, **142**, 279-288.
93. F. Arena, G. Trunfio, B. Fazio, J. Negro and L. Spadaro, *Journal of Physical Chemistry C*, 2009, **113**, 2822-2829.
94. A. S. Ivanova, E. M. Slavinskaya, R. V. Gulyaev, V. I. Zaikovskii, O. A. Stonkus, I. G. Danilova, L. M. Plyasova, I. A. Polukhina and A. I. Boronin, *Applied Catalysis B-Environmental*, 2010, **97**, 57-71.
95. M. I. Szykowska, A. Weglinska, L. Kowalczyk and T. Paryjczak, *Polish Journal of Chemistry*, 2009, **83**, 1163-1172.
96. J. Rogowski, M. I. Szykowska, A. Weglinska, E. Wojciechowska and T. Paryjczak, *Polish Journal of Chemistry*, 2008, **82**, 2359-2366.
97. Laskowsk.J and Kitchene.Ja, *Journal of Colloid and Interface Science*, 1969, **29**, 670-&.
98. F. Boccuzzi, S. Coluccia, G. Martra and N. Ravasio, *Journal of Catalysis*, 1999, **184**, 316-326.
99. F. Patcas and F. C. Buciuman, *Zeitschrift Fur Physikalische Chemie-International Journal of Research in Physical Chemistry & Chemical Physics*, 2001, **215**, 29-36.
100. A. K. H. Nohman, *Monatshefte Fur Chemie*, 2004, **135**, 269-278.
101. H. Jiang, H. Yang, R. Hawkins and Z. Ring, *Catalysis Today*, 2007, **125**, 282-290.
102. T. Engel and G. Ertl, *Chemical Physics Letters*, 1978, **54**, 95-98.
103. J. Szanyi, W. K. Kuhn and D. W. Goodman, *Journal of Physical Chemistry*, 1994, **98**, 2978-2981.
104. A. Vonoertzen, H. H. Rotermund and S. Nettesheim, *Surface Science*, 1994, **311**, 322-330.
105. J. T. Kummer, *Advances in Chemistry Series*, 1975, 178-192.
106. *Alumina - Different types of commercially available grades*, <http://www.azom.com/Details.asp?ArticleID=1389>.
107. M. Skotak, Z. Karpinski, W. Juszczyk, J. Pielaszek, L. Kepinski, D. V. Kazachkin, V. I. Kovalchuk and J. L. d'Itri, *Journal of Catalysis*, 2004, **227**, 11-25.
108. C. Morterra and G. Magnacca, *Catalysis Today*, 1996, **27**, 497-532.
109. C. B. Wang, H. G. Lee, T. F. Yeh, S. N. Hsu and K. S. Chu, *Thermochimica Acta*, 2003, **401**, 209-216.
110. S. D. Mo, Y. N. Xu and W. Y. Ching, *Journal of the American Ceramic Society*, 1997, **80**, 1193-1197.
111. K. Otto, L. P. Haack and J. E. Devries, *Applied Catalysis B-Environmental*, 1992, **1**, 1-12.
112. P. W. Seo, H. J. Choi, S. I. Hong and S. C. Hong, *Journal of Hazardous Materials*, 2010, **178**, 917-925.
113. H. Lieske, G. Lietz, H. Spindler and J. Volter, *Journal of Catalysis*, 1983, **81**, 8-16.
114. H. Muraki, S. Matunaga, H. Shinjoh, M. S. Wainwright and D. L. Trimm, *Journal of Chemical Technology and Biotechnology*, 1991, **52**, 415-424.
115. S. D. Ebbesen, B. L. Mojct and L. Lefferts, *Journal of Catalysis*, 2007, **246**, 66-73.
116. A. Quintanilla, J. J. W. Bakker, M. T. Kreutzer, J. A. Moulijn and F. Kapteijn, *Journal of Catalysis*, 2008, **257**, 55-63.

117. F. Omota, A. C. Dimian and A. Bliet, *Applied Catalysis a-General*, 2005, **294**, 121-130.
118. S. V. Slavov, K. T. Chuang and A. R. Sanger, *Journal of Physical Chemistry*, 1995, **99**, 17019-17027.
119. S. V. Slavov, A. R. Sanger and K. T. Chuang, *Journal of Physical Chemistry B*, 1998, **102**, 5475-5482.
120. S. V. Slavov, K. T. Chuang and A. R. Sanger, *Langmuir*, 1995, **11**, 3607-3609.
121. A. Schwartz, L. L. Holbrook and H. Wise, *Journal of Catalysis*, 1971, **21**, 199-&.
122. E. M. Cordi and J. L. Falconer, *Journal of Catalysis*, 1996, **162**, 104-117.
123. T. Maillet, C. Solleau, J. Barbier and D. Duprez, *Applied Catalysis B-Environmental*, 1997, **14**, 85-95.
124. P. Castellazzi, G. Groppi and P. Forzatti, *Applied Catalysis B-Environmental*, 2010, **95**, 303-311.
125. K. Ito, K. Satoh, T. Tomino, M. Miyake, M. Ohshima, H. Kurokawa, K. Sugiyama and H. Miura, *Journal of the Japan Petroleum Institute*, 2003, **46**, 315-321.
126. S. C. Kim, H. H. Park and D. K. Lee, *Catalysis Today*, 2003, **87**, 51-57.
127. R. Strobel, J. D. Grunwaldt, A. Camenzind, S. E. Pratsinis and A. Baiker, *Catalysis Letters*, 2005, **104**, 9-16.
128. A. Parinyaswan, S. Pongstabodee and A. Luengnaruemitchai, *International Journal of Hydrogen Energy*, 2006, **31**, 1942-1949.
129. B. Park and H. Lee, *Journal of Materials Research*, 1999, **14**, 281-285.
130. M. Harada, K. Asakura, Y. Ueki and N. Toshima, *Journal of Physical Chemistry*, 1992, **96**, 9730-9738.
131. S. Kaya and D. Uner, *Turkish Journal of Chemistry*, 2008, **32**, 645-652.
132. S. Kaya, E. Erunal, R. Shaltaf, S. Ellialtioglu and D. Uner, *Turkish Journal of Chemistry*, 2009, **33**, 11-21.
133. C. A. Lucas, N. M. Markovic, M. Ball, V. Stamenkovic, V. Climent and P. N. Ross, *Surface Science*, 2001, **479**, 241-246.
134. M. Yashima, L. K. L. Falk, A. E. C. Palmqvist and K. Holmberg, *Journal of Colloid and Interface Science*, 2003, **268**, 348-356.
135. B. Veisz, L. Toth, D. Teschner, Z. Paal, N. Gyorffy, U. Wild and R. Schlögl, *Journal of Molecular Catalysis a-Chemical*, 2005, **238**, 56-62.
136. B. Grbic, N. Radic, B. Markovic, P. Stefanov, D. Stoychev and T. Marinova, *Applied Catalysis B-Environmental*, 2006, **64**, 51-56.
137. M. I. Szykowska, A. Weglinska, E. Wojciechowska and T. Paryjczak, *Catalysis Letters*, 2009, **128**, 323-330.
138. M. Ferrandon, J. Carno, S. Jaras and E. Bjornbom, *Applied Catalysis a-General*, 1999, **180**, 141-151.
139. M. Ferrandon, J. Carno, S. Jaras and E. Bjornbom, *Applied Catalysis a-General*, 1999, **180**, 153-161.
140. A. Baylet, S. Royer, C. Labrugere, H. Valencia, P. Marecot, J. M. Tatibouet and D. Duprez, *Physical Chemistry Chemical Physics*, 2008, **10**, 5983-5992.
141. L. Pauling, *The Nature of the Chemical Bond*, 3rd Edition edn., Cornell University Press, Ithaca, New York, 1960.
142. N. D. Gangal, N. M. Gupta and R. M. Iyer, *Journal of Catalysis*, 1990, **126**, 13-25.
143. G. C. Bond, L. R. Molloy and M. J. Fuller, *Journal of the Chemical Society-Chemical Communications*, 1975, 796-797.

144. M. Sheintuch, J. Schmidt, Y. Lechthman and G. Yahav, *Applied Catalysis*, 1989, **49**, 55-65.
145. D. R. Schryer, B. T. Upchurch, B. D. Sidney, K. G. Brown, G. B. Hoflund and R. K. Herz, *Journal of Catalysis*, 1991, **130**, 314-317.
146. K. Grass and H. G. Lintz, *Journal of Catalysis*, 1997, **172**, 446-452.
147. T. Matsui, K. Fujiwara, T. Okanishi, R. Kikuchi, T. Takeguchi and K. Eguchi, *Journal of Power Sources*, 2006, **155**, 152-156.
148. N. Kamiuchi, K. Taguchi, T. Matsui, R. Kikuchi and K. Eguchi, *Applied Catalysis B-Environmental*, 2009, **89**, 65-72.
149. M. M. Gadgil, R. Sasikala and S. K. Kulshreshtha, *Journal of Molecular Catalysis*, 1994, **87**, 297-309.
150. B. Mirkelamoglu and G. Karakas, *Applied Catalysis a-General*, 2005, **281**, 275-284.

2

Experimental

The experimental procedures utilised in Chapters 3-6 are described in this chapter, along with a detailed discussion of the analytical techniques used to characterise synthesised catalysts.

2.1 Preparation of CuMn_2O_4 Hopcalite Catalyst

Copper/manganese mixed oxides produced by the co-precipitation method¹ have been reported to possess high surface areas and CO oxidation activities. This method has been the subject of extensive testing by previous researchers in this department (Jones *et al.*², Cole³, Mirzaei *et al.*⁴). These studies have described nine variables as having an effect on catalyst morphology, activity or both. For this thesis, coprecipitated hopcalite will be prepared using conditions supported by previously reported data. Table 6 details the reaction condition, the chosen method, and the supporting reference or hypothesis. Further details of these references can be found in Chapter 1.

Reaction Condition	Chosen Condition	Reference
Metal Salt	Nitrates	Koleva <i>et al.</i> ⁵
Cu:Mn ratio	1:2	Hutchings <i>et al.</i> ¹
Reaction pH	8.3 +/- 0.1	Mirzaei <i>et al.</i> ⁴
Reaction temperature	80°C	Hutchings <i>et al.</i> ¹
Pumping Speed	40.0 cm ³ min ⁻¹	Fastest realistic speed with accurate pH control ⁶
Precipitate aging time	2 h	Cole ³
Temperature and duration of calcination	415°C for 2 h	Jones ⁶
Solution Stirring	600 rpm	Vigorous stirring promotes crystal nucleation ⁶
Catalyst Washing	1 L chilled, 1 L boiling H ₂ O	Mirzaei <i>et al.</i> ⁴

Table 6 – Hopcalite Coprecipitation Reaction Conditions

Catalysts were prepared via a procedure known as co-precipitation, detailed in Figure 3. Copper nitrate, $\text{Cu}(\text{NO}_3)_2 \cdot 2\frac{1}{2}\text{H}_2\text{O}_{(\text{aq})}$ (Aldrich, 0.025 mol L^{-1}), was mixed with manganese nitrate, $\text{Mn}(\text{NO}_3)_2 \cdot 6\text{H}_2\text{O}$ (Aldrich, 0.025 mol L^{-1}), in a stoichiometric molar metal ratio of 1:2 Cu:Mn and diluted to 250.00 cm^3 . The solution was heated to 80°C . This mixed nitrate solution was pumped (at $40.0 \text{ cm}^3 \text{ min}^{-1}$) into a vessel containing $250.00 \text{ cm}^3 \text{ H}_2\text{O}$. This vessel was thermostatically maintained at 80°C and stirred at 600 rpm. $2 \text{ M Na}_2\text{CO}_{3(\text{aq})}$ (Aldrich) was added dropwise to this mixed nitrate solution via burette to maintain its pH at 8.3 ± 0.1 . The reaction precipitate was aged, at identical pH and temperature, for 2 h. The precipitate was then filtered and washed with 1 L cold distilled H_2O and 1 L boiling distilled H_2O . The filtrate was then tested to be pH neutral. The resulting residue was dried at 110°C in static air for 16 h and calcined at 415°C for 2 h.

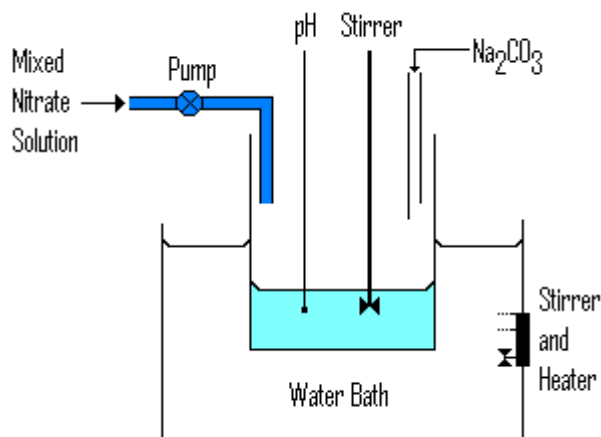


Figure 3 – Diagram of Coprecipitation Apparatus

2.1.1 Preparation of Doped Co-precipitate CuMn_2O_4 Catalyst

A modification to the above experiment has been discussed (Jones⁶, Cole³). Small proportions (1-10%) of Cu and Mn ions in the lattice are replaced with another metal ion. This is referred to exclusively as ‘doping’. This is achieved by reducing the quantities of reagent copper or manganese atoms, and replacing them with another ion from a soluble metal salt. An example of this is shown in Table 7.

Catalyst V Loading	Mass, Mols $\text{Cu}(\text{NO}_3)_2 \cdot 2\frac{1}{2}\text{H}_2\text{O}$	Mass, Mols $\text{Mn}(\text{NO}_3)_2 \cdot 6\text{H}_2\text{O}$	Mass, Mols $\text{VOSO}_4 \cdot 4\text{H}_2\text{O}$
0%	2.91 g, 0.0125 mols	7.18 g, 0.0250 mols	0 g, 0.00 mols
1%	2.88 g, 0.0124 mols	7.10 g, 0.0247 mols	0.0840 g, 0.000375 mols
2%	2.85 g, 0.0122 mols	7.03 g, 0.0245 mols	0.168 g, 0.000750 mols
5%	2.77 g, 0.0119 mols	6.80 g, 0.0237 mols	0.420 g, 0.00188 mols

Table 7 – Dual Copper and Manganese replacement by Vanadium, reagent weights

The total metal ratio in all experiments always equal 1:2 in terms of $[\text{Cu} (+ \text{X})]:[\text{Mn} (+ \text{X})]$. The reagent salts used are listed below:

Cerium and Palladium

In these cases, the dopant salts were the respective nitrates, $\text{Pd}(\text{NO}_3)_{2(\text{aq})}$ and $\text{Ce}(\text{NO}_3)_3 \cdot 6\text{H}_2\text{O}$.

Silicon

In the absence of a ‘silicon nitrate’, silicon tetraacetate was selected as a replacement. $\text{Si}(\text{Ac})_4$ dissolves in basic media, is insoluble in acid, and precipitates at below $\sim\text{pH}$ 10. To accommodate this, the dopant salt was dissolved in reagent 2 M Na_2CO_3 solution and added dropwise alongside the nitrate pumping. The solution pH of 8.3 ± 0.1 is sufficient to precipitate both the acidic nitrate solution and the basic carbonate/acetate solution.

Vanadium

Vanadium nitrate is not commercially available and as such a range of different metal salts were tested. Ammonium meta-vanadate, vanadium chloride, vanadium oxide and vanadium oxychloride were tested and found to be unsuitable. Vanadyl sulphate, VOSO_4 , was selected as the dopant salt. This is discussed in more detail in Chapter 1 and Chapter 3.

2.1.2 Incipient Wetness (IW) onto CuMn_2O_4 Catalyst Support

Standard coprecipitated CuMn_2O_4 was subjected to an IW procedure to synthesise Pd-impregnated CuMn_2O_4 . Incipient wetness (IW) is discussed in more detail in Chapter 1. 1.0 g $\text{CuMn}_2\text{O}_{4(s)}$ was mixed with 1.0 cm^3 $\text{Pd}(\text{NO}_3)_2(\text{aq})$. Pd concentration, and by extrapolation metal weightings, were calculated as a % of the weight of the support. The catalyst was dried at 110°C for 12 h and calcined for 3 h at 400°C. As a reference, 1.0g $\text{CuMn}_2\text{O}_{4(s)}$ was combined with 1.0 cm^3 0.188 M $\text{HNO}_3(\text{aq})$ and dried at 110°C for 12 h, then calcined for 3 h at 400°C. This catalyst is referred to as ‘reference hopcalite’. Hopcalite subjected to no additional conditions is referred to as ‘ancestor hopcalite’.

2.1.3 Deposition Precipitation (DP) onto CuMn_2O_4 Catalyst Support

Standard coprecipitated CuMn_2O_4 was subjected to a DP procedure to synthesise Pd and Pt-deposited CuMn_2O_4 . Deposition Precipitation (DP) is discussed in more detail in Chapter 1. 1.0 g CuMn_2O_4 was mixed with 10.0 cm^3 distilled H_2O . An additional 10.0 cm^3 H_2O was mixed with $\text{Na}_2\text{PdCl}_6(\text{aq})$ and $\text{PtCl}_4(\text{aq})$, then added to the hopcalite mixture under stirring. Pt and Pd metal weightings were calculated as a % of the weight of the support. $\text{NaOH}(\text{aq})$ (0.1 M) was added dropwise to adjust the pH to 9.0, and the mixture was aged for 1 h under further pH control. Upon completion, the mixture was dried at 110°C for 16 h, and then calcined at 400°C for 3 h. As a reference, 1.0g $\text{CuMn}_2\text{O}_{4(s)}$ was combined with 1.0 cm^3 2.46 M $\text{HCl}(\text{aq})$ and 19.0 cm^3 H_2O , then subjected to the same conditions as the catalysts above. This catalyst is referred to as ‘reference hopcalite’. Hopcalite subjected to no additional conditions is referred to as ‘ancestor hopcalite’.

2.1.4 Hopcalite Reduction

Unmodified hopcalite support was subjected to reductive conditions. This was a reference experiment to investigate the possibility of reducing deposited or impregnated surface precious metal particles on hopcalite. Reduction under aqueous $\text{NaCOOH}(\text{aq})$ was attempted. Active

hopcalite (1.0 g) was mixed with 0.10 g of $\text{NaCOOH}_{(\text{aq})}$ in $10.0 \text{ cm}^3 \text{ H}_2\text{O}$ for 16 h. The precipitate was then washed with 1 L cold and 1 L boiling H_2O , and dried at 110°C for 12 h.

In a reference experiment, reduction under $\text{H}_{2(\text{g})}$ was attempted. A series of hopcalite supports (1.0g) were reduced at either 80°C , 90°C , 100°C , 110°C , 120°C , 150°C and 500°C for 1 h under an atmosphere of 5% H_2/Ar . It was concluded by activity and TGA data that 100°C was the most reductive conditions that could be applied to the support. This is discussed in more detail in Chapter 4.

All deposited and impregnated noble metal catalysts were subjected to hydrogen reduction. Modified hopcalite support (1.0g) was reduced at 100°C for 1 h under an atmosphere of 5% H_2/Ar .

2.2 Preparation of Impregnated Alumina Sphere Catalysts

Pt and Pd metals supported on γ -alumina have been described as effective oxidation catalysts⁷⁻¹⁰. In this publication, an electrostatic adsorption (EA) technique was used to deposit metals on the support surface. This method is discussed in detail in Chapter 1. In an EA procedure, the support is charged by immersion in aqueous solution. The support surface can be considered to be positively charged if immersed in acidic media. Reagent salts are then added. Acidified PtCl_4 was selected. In aqueous acidic media, this compound forms PtCl_6^{2-} ions. Na_2PtCl_4 was also selected. In acidic solution, PtCl_4^{2-} ions are present. These anions will be attracted to the positively charged surface of the support. Investigations by Regalbuto¹¹ report metal dispersion during H_2PtCl_6 electrostatic adsorption is greatest at pH 3.15. During the synthesis, weak HCl is used to control solution pH. Several researchers^{12, 13} have reported that metallic Pt and Pd are far more active for CO oxidation at ambient conditions than the respective oxides.

γ -Alumina spheres (2-3 mm diameter, 20.0 g, Sasol) were hydrated for 1 h with 30.0 cm^3 distilled H_2O (Figure 4). PtCl_4 (0.86 g per 0.25% loading, Aldrich) acidified with 6 drops $\text{HCl}_{(\text{aq})}$ (3.33%) was mixed with Na_2PdCl_4 (0.420 cm^3 of 1.131 M per 0.25% loading, Aldrich) in 30.0 cm^3 distilled H_2O . The metal salt solution was mixed to the alumina solution and the pH was

measured. Dilute $\text{HCl}_{(\text{aq})}$ (3.70%) was added drop wise to adjust solution pH to 3.15 ± 0.25 . The solution was aged for 2 h, adjusting rising pH back to 3.15 ± 0.25 every 15 min. The yellow-brown solution colour was observed to disappear and a similar colour appeared on the surface of the alumina spheres. After aging, 0.30 g of Na_2COOH was added, the vessel sealed and aged for 16 h. After this treatment, the catalyst spheres were filtered and washed with 1 L boiling H_2O , followed by 1 L chilled H_2O . The catalysts were then split into 1 g batches and desiccated for 48 h.

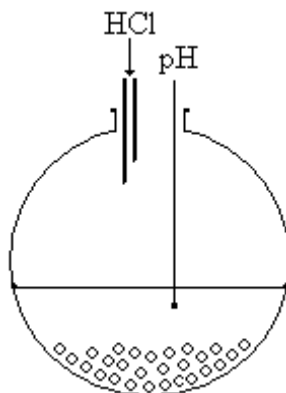


Figure 4 – Diagram of EA Apparatus

2.2.1 Silicon Deposition onto Alumina Spheres

It has been established^{14, 15} that Pt and Pd are sensitive to water on the catalyst surface. Modification of alumina surface with hydrophobic species is of interest for fine tuning catalyst water tolerance. This is discussed in more detail in Chapter 1. Quintanilla *et al.*¹⁶ reports that toluene can be used a Dichlorodimethyl silane (DDMS) solvent. Silylation was carried out in advance of Pt/Pd adsorption to avoid chlorine leeching by DDMS ligands.

γ -Alumina spheres (2-3 mm, 12.0 g, Sasol) were pre-treated with 30.0 cm^3 of distilled water, dried and desiccated for 48 h. These spheres were added to toluene (100 cm^3) under vigorous stirring and N_2 atmosphere. DDMS (0.52 mL per 1% loading, Aldrich) was added drop wise to the mixture under stirring and N_2 . After mixing for 30 min, 50.0 cm^3 of H_2O was slowly introduced. After a further 30 min, the spheres were filtered off and washed in succession with 1

1 L ethanol, 1 L boiling distilled H₂O and 1 L chilled distilled H₂O. The spheres were desiccated for 48 h and impregnated with Pt and Pd using the EA procedure detailed in Part 2.2.

2.2.2 Tin Oxide Impregnated Alumina Spheres

Synergy between SnO₂ and Pt has been reported by several researchers¹⁷⁻²⁰. Tin Oxide/Pt catalysts are widely used, and are commonly synthesised by impregnation of stannic oxide powder. In an attempt to reduce the high cost of tin, commercial catalysts are occasionally synthesised by impregnation of alumina with tin salts such as Na₂SnO₃. These synthesis methods produce hazardous waste products which must be rendered harmless. In an attempt to devise an atom efficient process for the production of tin oxide catalysts, a novel method using tin oxalate will be investigated in this chapter. This synthesis will be compared with two existing tin oxide synthesis methods, firstly using unmodified stannic oxide, and secondly using sodium stannate. All three methods will attempt to impregnate an egg shell coating of tin onto 2-3mm γ -alumina spheres, to reduce cost and improve durability. These spheres will be subsequently impregnated with Pt and Pd using an EA procedure.

Acid Tin Oxide - Alumina spheres (2-3 mm, 20 g, Sasol) were combined with a slurry comprised of acid tin oxide (0.51 g per 2.0% loading) and 26.6 mL H₂O. An exothermic reaction was observed. After thorough mixing, the spheres were desiccated for 48 h. Batches were then impregnated with Pt/Pd using the EA procedure detailed in 2.2.

Tin Oxalate - Alumina spheres (2-3mm, 20 g, Sasol) were combined with an adhesive slurry comprised of Sn(C₂O₄) (0.7 g per 2.0% tin loading) in 26.6 mL H₂O_{2(aq)} (conc 0.92% per 2.0% loading). After thorough mixing, the spheres were desiccated for 48 h. Spheres were subsequently calcined at 350°C for 1 h. Batches were then impregnated with Pt/Pd using the EA procedure detailed in Part 2.2

Sodium Stannate - Alumina spheres (2-3 mm, 20 g, Sasol) were combined with a solution of Na₂SnO₃.3H₂O (0.9 g per 2.0% tin loading) in 26.6 mL H₂O. Mixing was performed for 20 min at room temperature; followed by 30 min at 70°C, followed by cooling for 30 min. After

thorough mixing, the spheres were desiccated for 48 h. Batches were subsequently impregnated with Pt/Pd using the EA procedure detailed in Part 2.2

2.3 Catalyst CO Activity Testing

Both hopcalite-supported and alumina-supported catalysts were tested for CO oxidation activity at ambient temperature. Carbon monoxide (~5000 ppm) in 21% O₂ and balance N₂ was fed into the apparatus using a MKS mass flow controller. Due to the differences in size and composition of supports, distinct microreactors were designed for each procedure.

For hopcalite based catalysts, the gas stream was first passed over a cold trap containing isopropanol/N₂(l) with an approximate temperature of -196°C. The gas was subsequently passed through a microreactor, which was placed in an isothermally maintained water bath at 25°C. 100 mg of 24 h desiccated catalyst was placed in a cylindrical fixed bed laboratory microreactor with a diameter of 4.65 mm and a bed length of 0.5 cm. Gas flow of 21.4 mL min⁻¹ was passed through the reactor, resulting in a gas hourly space velocity of 12'000 h⁻¹ and a contact time of 0.3 sec.

For alumina sphere catalysts, the gas stream was first passed through a humidifier containing distilled water. The gas was subsequently passed through a microreactor, which was placed in an isothermally maintained water bath at 25°C. 1 g of 24 h desiccated alumina supported catalyst was placed in a cylindrical fixed bed laboratory microreactor with a diameter of ~7 mm. Gas was fed into the reactor at 25 mL min⁻¹ (for all catalysts in Chapter 5) or 50 mL min⁻¹ (for all catalysts in Chapter 6, due to incomparable activities of 100% at 25 mL min⁻¹) using a MKS mass flow controller. This change was due to the majority of the catalysts in Chapter 6 exhibiting 100% activity at 25 mL min⁻¹, which made comparison between them difficult. The spherical shape of the catalyst made calculating the bed area difficult. The density of the catalyst was assumed to be ~1.0 g cm⁻³. This equated to a gas hourly space velocity of 1'500 and 3'000 h⁻¹ and a contact time of 1.2 and 2.4 sec respectively.

The gas stream then passed through to the injection port, and was vented into a fume cupboard. Gas samples were analysed by the Varian CP-3800 gas chromatograph using a 1.5 m packed carbosieve column. The chromatograph was programmed to sample the gas stream at 4.5 min intervals for a set period of hours depending on experiment. Gas samples were mixed with carrier gas and heated to 165°C in the injection port. The gas was then carried into the column and separated into distinct batches, which eluted from the column over a thermal conductivity detector. The retention times of CO, O₂ and N₂ were ~30 sec, while CO₂ eluted at ~1.5 min. Water in the system, not always present, eluted at ~3 min. The apparatus is detailed in Figure 5.

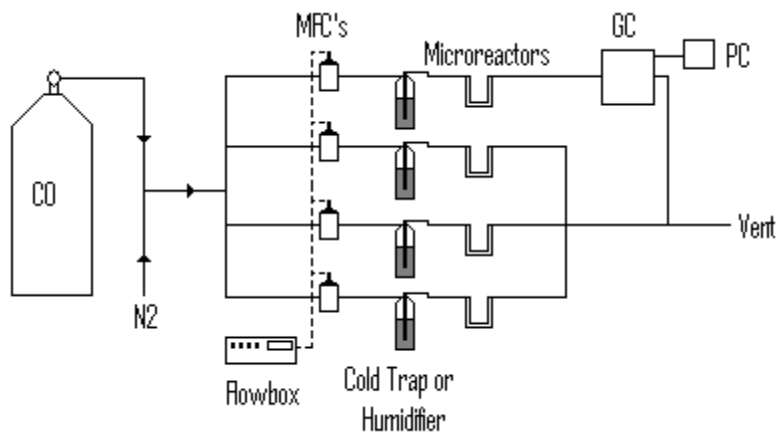


Figure 5 – Schematic of Catalyst testing system

The GC was calibrated with known concentrations of CO₂ in order that 100% activity (5000 ppm CO₂) could be attributed. This is referred to as ‘Total CO₂ counts’. The CO₂ conversion data was compared with this value using equation (17) in order to calculate % CO conversion for each gas sample.

$$\text{CO Conversion (\%)} = \left(\frac{\text{CO}_2 \text{ Counts}}{\text{Total CO}_2 \text{ Counts}} \right) * 100 \quad (17)$$

Experimental error for this system was calculated by running four CuMn₂O₄ samples simultaneously. These four samples were taken from the same synthesis batch and accurately weighed to 100.0mg. The activity data for the four batches was used to calculate an experimental error of ± ~3% for this apparatus.

2.3.1 Calculation of Surface Area Normalised Activities (SANA)

Conversion percentages combined with data on the surface area of a catalyst can be used to determine the rate of CO conversion per second per square meter. This can be used to determine comparisons between the activities of different catalysts after removal of the variable of surface area.

$$\text{SANA Conversion Rate} = 7.9563 * 10^{-8} * \left(\frac{\frac{\text{Con \%}}{100}}{\frac{1}{10} * SA} \right) \quad (18)$$

In equation (18), the value 7.9563×10^{-8} was determined from the carrier gas flow rate ($21.4 \text{ cm}^3 \text{ min}^{-1}$), and is the moles of CO passed through the catalyst bed in one second. $21.4 \text{ cm}^3 \text{ min}^{-1}$ of 0.5% CO equates to $0.107 \text{ cm}^3 \text{ min}^{-1}$ pure CO passing over the active sites. The ideal gas law assumes that one mole of gas occupies 22414 cm^3 of volume, so this equates to 4.7738×10^{-6} mols min^{-1} or 7.9563×10^{-8} mols sec^{-1} . 'SA' is the surface area of the catalyst in $\text{m}^2 \text{ g}^{-1}$ determined by BET analysis, and the (1/10) factor is due to the 100 mg samples used in the GC and BET apparatus compared to the one gram units described in the BET surface area data. SANA rates are displayed in units of 'Mols CO oxidised $\text{m}^{-2} \text{ s}^{-1}$ '. The experimental error for this technique is ~8%, equal to the combined errors of the BET technique added to the error of the activity measurement.

2.4 Activity Measurement by Gas Chromatography

Gas chromatography is a characterization method for measuring both qualitative and quantitative composition data of gaseous mixtures. The five core components of a gas chromatograph (GC) are described in more detail below and in Figure 6:

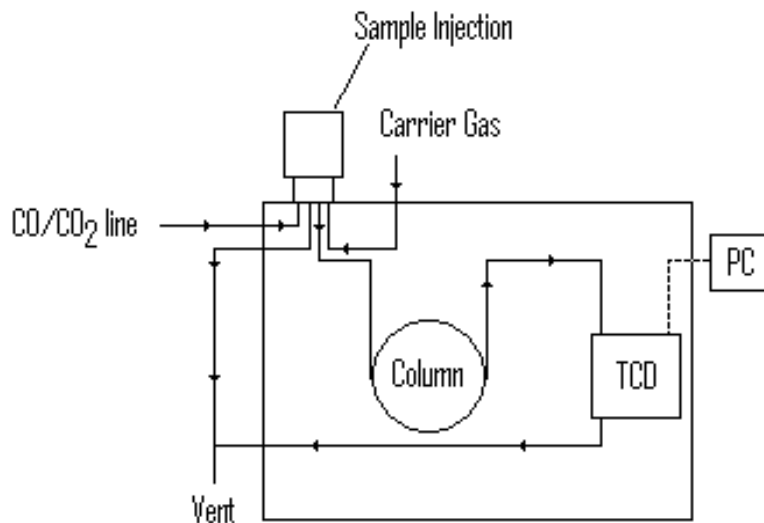


Figure 6 – Gas Chromatography System Diagram

Inert Gas Supply

A mobile phase, a carrier gas, is used to elute an analyte gas mixture through an inert solid stationary phase, a capillary column. The flow allows the elution of analytes from the sample. To avoid detection, the carrier gas must be chemically inert. One of most common detectors (thermal conductivity detector or TCD) is more accurate with a gas that has a high thermal conductivity. A gas with a small molar mass typically has a higher thermal conductivity. Hydrogen would be the ideal candidate ($0.1805 \text{ W}/(\text{m}\cdot\text{K})$)²¹. As H₂ is flammable, helium ($0.1513 \text{ W}/(\text{m}\cdot\text{K})$), is the most commonly used carrier phase.

Sample Injection Port

The injection port is the device which introduces the analytes into the chromatograph. Analytes are vaporised by the high temperature in the port, and are then swept into the column by the carrier phase. A rotary sampling valve is commonly used to introduce accurate quantities of sample gas into the column without disrupting flow. Figure 7 displays a schematic of the Valco 6-port switching valve in use for these experiments.

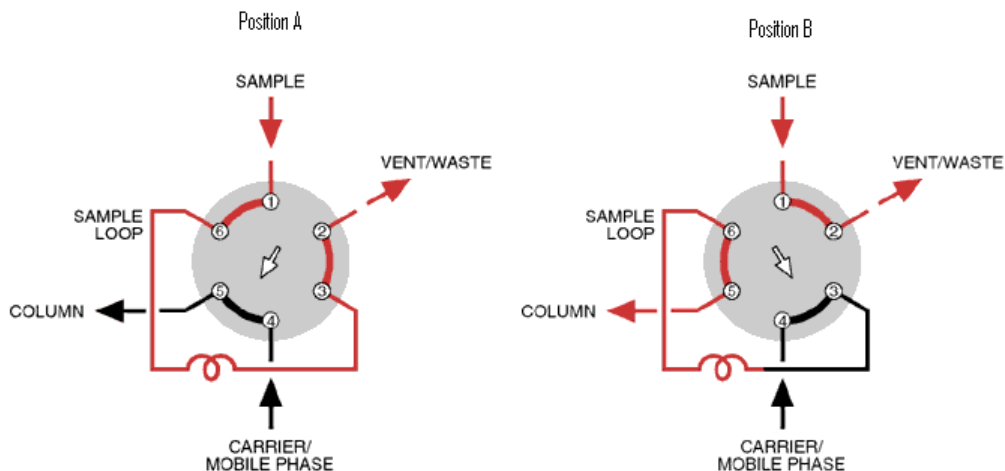


Figure 7 – Schematic of Valco 6-port valve

In position A, the carrier gas is carried into the column. The sample gas is carried through the external sample loop to the vent line. The valve then rotates to position B, and the gas currently occupying the sample loop flows into the carrier gas stream and into the column. The valve later rotates in reverse both injecting a second sample and resetting the system.

Column

Gas chromatography columns are typically tubular and packed with stationary material such as silica or carbosieve. Analytes passed into the top of the column with the carrier gas pass through the solid phase at different rates according to their molecular properties. This delay is referred to as the ‘retention time’. This retention time can then be used to determine the identity of the analyte. The columns used for all experiments in this thesis were 1.5 m packed carbosieve columns.

Detector

Molecules that elute from the column are passed over a thermal conductivity detector (TCD) for identification. A TCD comprises of four tungsten-rhenium filaments in a Wheatstone bridge configuration. Electrical current passing along the filaments causes them to heat. The carrier gas, helium, is passed over the detector removing heat at a set rate, in concordance with its thermal

conductivity. Other molecules passing over the detector remove heat at different specific rates. A TCD is commonly used to detect CO, N₂, O₂, CO₂, NO, NO₂ and H₂S.

Data Acquisition

A PC workstation equipped with Varian Star was used to collect the raw data from the chromatograph. Results were saved and manipulated in variable scales.

2.5 BET Surface Area Analysis

Surface area measurement of a solid sample can be accurately determined by physisorption of nitrogen. At extremely low temperatures, physisorption of nitrogen onto a surface is identical regardless of the material. Given the known area of the N₂ molecule, 0.16 nm², a change in the pressure of nitrogen gas in a system can be attributed to specific surface area adsorption. This approach was pioneered by Brunauer, Emmett and Teller²², who formulated the BET equation (19) and the BET constant (20)

$$\frac{p}{n^a(p_o - p)} = \left(\frac{1}{n_m^a C} \right) \frac{p}{p_o} \quad (19)$$

In the BET equation (19), several assumptions are made. Firstly, a new monolayer can start before the previous is completely filled. Secondly, the energy of adsorption does not differ between layers. The BET constant, C (20), is the difference in heat of adsorption between the first and second monolayer. The larger the value of C, the stronger the adsorption. The range of a BET plot is restricted with known experimental isotherms, specifically type II and type IV isotherms. These are the only isotherms at which V_m can be determined. If C < 2, the isotherm changes from type II to type III or IV. Typical C values for metal oxides are between 70 and 120. C values of below 50 were rejected and re-run for up to three repetitions.

n^a = volume of adsorbed gas

p_o = saturated vapour pressure of liquid adsorbate at experimental temperature

p = Pressure of the gas

n_m^a = Monolayer capacity

C = BET constant

$$C = \exp\left(\frac{E_1 - E_L}{RT}\right) \quad (20)$$

During the procedure for BET analysis, a known volume of powdered sample (~50 mg) is weighed and degassed at 120°C for 45 min under flowing N₂ in a standard sample tube, to remove physisorbed material. The weight loss is recorded, and the sample tube and an empty reference tube were loaded into a Micromeritics Gemini 2360 analyzer. The sample and reference tubes were evacuated and then immersed in a liquid N₂ dewar. The analysis gas was pumped into both tubes. A differential pressure transducer then recorded the difference in the pressures of both tubes, caused by adsorption of the analysis gas onto the sample. The pressure inside the sample tube was raised to the level of the reference to compensate for the adsorption. The sample was measured at 5 known pressures, P, ranging from 0.05 to 0.30. Data was recorded on a PC. To attain experimental error, a single hopcalite sample was tested 10 times in succession. The data was used to calculate an experimental error for the BET measurement of ± ~9.0%.

R = 8.314 J mol⁻¹

T = Temperature in Kelvin

E₁ = the heat of adsorption for the first layer

E_L = heat of adsorption for higher layers, also heat of liquefaction

C = BET constant

2.6 Powder X-Ray Diffraction (XRD)

X-Ray Diffraction is a non-destructive technique used to characterize the bulk structure of crystalline material. The technique projects an X-ray beam onto a powdered sample of crystallites. This is under continuous 360° rotation to ensure a random dispersal of crystals. Interactions between X-rays and the interplanar spacings in the crystalline powder produce diffracted X-ray beams in characteristic directions. In concordance with constructive/destructive interactions of X-rays, the diffracted radiation can only escape the sample where the angle between incident and diffracted beams is 2θ . The angle of detected X-rays is defined by Bragg's law (21).

$$n\lambda = 2d \sin \theta \quad (21)$$

The theory behind the Bragg equation is explained in Figure 8. A X-ray beam is directed onto a powdered sample at a glancing angle. A detector measures the diffracted X-rays at all angles. At Bragg angle or angles, θ , high frequencies of diffracted X-rays are collected which are referred to as 'peaks'. A collection of peaks is referred to as an XRD pattern, which is compared to a database of known samples. If Bragg angles are known, lattice spacing, d , can also be calculated. XRD patterns are compared against a literature database to assign crystalline morphology. This leads to the identification of the sample. A limitation of XRD is that long range order is required for the generation of diffraction signals. Amorphous samples, such as hopcalite, do not register any diffraction peaks. As discussed in Chapter 1, highly active hopcalite typically displays amorphous character.

n = an integer

λ = radiation wavelength

d = inter planar lattice spacing

θ = Bragg angle

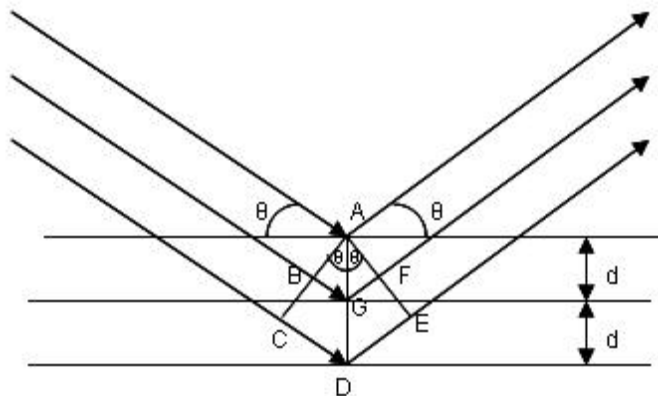


Figure 8 – Diagram of Bragg's Law

XRD patterns were collected using an X'Pert PRO X-ray diffraction system. This comprised of an Analytical X-Pert Pro X-Ray generator, with a $\text{Cu K}\alpha$ source. X-rays were detected between 20° and 80° , and the system was operated at 40mA and 40kV. The sample was spun through 360° to ensure a random arrangement of crystallites. The sample was run for 20 min and the collected diffraction patterns were compared to the known patterns on the JCPDS database.

2.7 Thermogravimetric Analysis (TGA)

Thermogravimetric analysis is a technique whereby samples are accurately weighed and subjected to increasing temperature in a known atmosphere. Material undergoing thermal treatment can exhibit several phenomena, such as decomposition, oxidation or reduction. Changes in the mass of the sample are then correlated to the experimental temperature. Changes in weight are as a result of the breaking or formation of chemical bonds and the removal or addition of the subsequent products. Measurement is carried out under inert atmosphere, such as N_2 , reductive atmosphere such as 5% H_2/Ar , or oxidative atmosphere such as air.

A sample is placed into an alumina TGA crucible on a tared microbalance. The crucible, together with an empty reference, is placed in a cold furnace. The sample weight is taken, and the weight of the sample is continuously tracked over the course of the experiment. The furnace is programmed to raise the temperature over a period of time at a set rate. Data is collected and sample weight is presented as a function of furnace temperature. The mass losses exhibited by

the sample is then calculated as a % of initial mass, and known possible chemical processes are correlated to the observed phenomena.

Samples were analysed on a Setaram Labsys TG-DTA/DSC 1600 device. Each test used a 20-40 mg sample.

2.8 Scanning Electron Microscopy (SEM)

High resolution images of microscopic particles can be achieved using a scanning electron microscope. Under high vacuum, a beam of electrons with an energy of 1-50 keV is focussed onto a surface. The interaction caused by the beam produces the emission of secondary electrons from the top 10 nm of the surface which are detected to produce an image. Particles displayed in the image can be measured for size and morphology, or backscattered electrons can be used to measure approximate atomic mass.

In this thesis SEM has been used to measure the average particle size of powdered samples. Twenty random, spherical particles were selected and their diameter in microns was averaged to give a result. A SEM image of the sample will be displayed with a particle equivalent to the average measured to give a reference. The accuracy of this technique was measured by measuring the same sample 10 times (for a total of 200 measurements). The near limitless number of particles ensured no duplication would occur. Calculating the standard deviation resulted in an accuracy of $\pm 2.94\%$.

Backscatter SEM images are used to illustrate the contrast between low and high atomic mass particles on catalyst surface. As backscatter technique produces no numerical data, this method is of limited use.

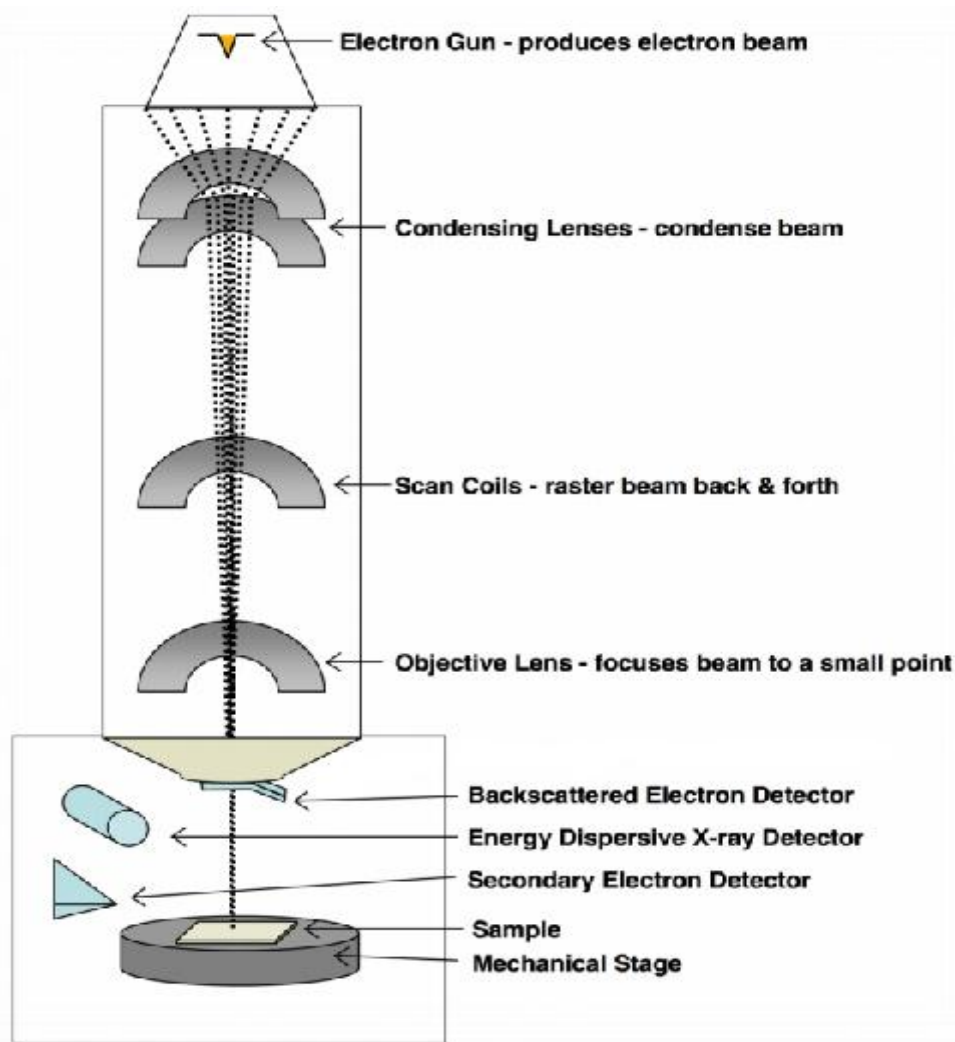


Figure 9 – Schematic of SEM²³

A Ziess Evo-40 Series scanning electron microscope was used to obtain images with a size of 110x80 μm . The apparatus is displayed in Figure 9.

2.9 Energy Dispersive X-ray Spectroscopy (EDX)

A scanning electron microscope can perform a microanalysis technique known as energy dispersive x-ray spectroscopy. A beam of electrons is aimed into a sample. This beam is capable of exciting low energy electrons from the inner shell of an atom. These electrons are ejected from their shell forming an electron hole. An electron from a higher energy shell fills this

vacancy, and the resulting difference in energy is released as an X-ray photon. These photons are collected by an EDX detector. Each element has a characteristic X-ray energy pattern which is compared to the emitted radiation. This enables identification of both elements and their concentration. This is detailed in Figure 10.

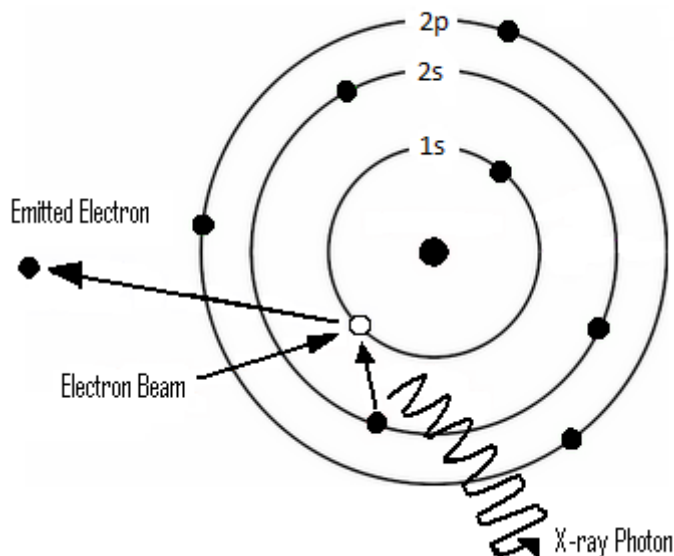


Figure 10 – EDX Interaction

The SEM electron beam must be at least 16-20 keV. EDX is a bulk technique as X-ray photons have little difficulty passing through solid matter. EDX analysis is capable of giving data on the % composition of the catalyst bulk under the scanned area. As catalyst composition can vary across different samples taken from the same batch, multiple scans were taken. 110x80 μm scans were taken of 8 catalyst samples and the results averaged to give EDX data presented in this thesis. The instrument used in this thesis is a Zeiss Evo-40 series SEM in conjunction with an INCA x-sight EDX detector.

2.10 X-Ray Photoelectron Spectroscopy (XPS)

XPS is a surface sensitive, non-destructive, qualitative analysis technique. It is used to determine the elemental composition, empirical formula, chemical state and electronic state of the top 1-10nm of a surface. Under vacuum, X-ray photons are directed onto a catalyst. This achieves excitation of electrons in the atoms on the catalyst surface. These electrons are emitted and collected. Kinetic energy and frequency are measured, and the electron binding energy of emitted electrons can be calculated (22).

$$E_{binding} = E_{photon} - (E_{kinetic} + \phi) \quad (22)$$

Plotting electron binding energy intensity values against the detected number of counts gives a plot with peaks corresponding to the electron configuration of emitted electrons. These can be compared to a reference database and identified. Chemical and electronic states can be inferred from this data. As electrons cannot pass through more than 1-10 nm of solid matter, XPS can be considered surface sensitive.

XPS studies were achieved using a Kratos Axis Ultra-DLD XPS. Also well received was the assistance of Dr. Dave Morgan and Dr. Albert Carley.

$E_{binding}$ = The binding energy of the electron.

E_{photon} = The energy of the X-ray photons being used.

$E_{kinetic}$ = The kinetic energy of the electron as measured by the instrument.

ϕ = The work function of the spectrometer.

2.11 Ultraviolet Visible Spectroscopy (UV Vis)

UV-Vis spectroscopy refers to absorption spectroscopy in the visible and near UV ranges. In this region of the electromagnetic spectrum, valence electrons undergo electronic transitions which give matter its characteristic colours. Determination is normally carried out in solution (Figure 11). An incident light beam is directed into a solution of known pathlength. The beam is measured after transmittance through the fluid and compared to an identical beam transmitted through a reference solvent. Application of the Beer Lambert Law (23) allows for absorbance, A , to be calculated. This absorbance is compared to a calibration plot using solutions of known concentration. Absorbance is directly related to concentration if the path length remains constant.

$$A = \log_{10} \left(\frac{I_0}{I} \right) = e \cdot c \cdot L \quad (23)$$

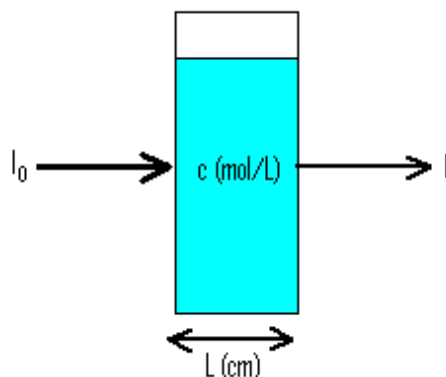


Figure 11 – Schematic of UV Vis. Spectrometer

A = Measured absorbance

I_0 = Intensity of incident light at given wavelength

I = Transmitted intensity

L = Pathlength of sample

c = Concentration of the absorbing species

e = Extinction coefficient

2.12 Chapter 2 References

1. G. J. Hutchings, A. A. Mirzaei, R. W. Joyner, M. R. H. Siddiqui and S. H. Taylor, *Applied Catalysis a-General*, 1998, **166**, 143-152.
2. C. Jones, K. J. Cole, S. H. Taylor, M. J. Crudace and G. J. Hutchings, *Journal of Molecular Catalysis a-Chemical*, 2009, **305**, 121-124.
3. K. J. Cole, Cardiff University, 2008.
4. A. A. Mirzaei, H. R. Shaterian, R. W. Joyner, M. Stockenhuber, S. H. Taylor and G. J. Hutchings, *Catalysis Communications*, 2003, **4**, 17-20.
5. V. Koleva, D. Stoilova and D. Mehandjiev, *Journal of Solid State Chemistry*, 1997, **133**, 416-422.
6. C. D. Jones, Cardiff University, 2006.
7. P. Castellazzi, G. Groppi and P. Forzatti, *Applied Catalysis B-Environmental*, 2010, **95**, 303-311.
8. K. Ito, K. Satoh, T. Tomino, M. Miyake, M. Ohshima, H. Kurokawa, K. Sugiyama and H. Miura, *Journal of the Japan Petroleum Institute*, 2003, **46**, 315-321.
9. S. C. Kim, H. H. Park and D. K. Lee, *Catalysis Today*, 2003, **87**, 51-57.
10. R. Strobel, J. D. Grunwaldt, A. Camenzind, S. E. Pratsinis and A. Baiker, *Catalysis Letters*, 2005, **104**, 9-16.
11. J. Regalbuto, *Catalyst Preparation*, CRC Press, Taylor and Francis Group, 2007.
12. E. M. Cordi and J. L. Falconer, *Journal of Catalysis*, 1996, **162**, 104-117.
13. T. Maillot, C. Solleau, J. Barbier and D. Duprez, *Applied Catalysis B-Environmental*, 1997, **14**, 85-95.
14. H. Muraki, S. Matunaga, H. Shinjoh, M. S. Wainwright and D. L. Trimm, *Journal of Chemical Technology and Biotechnology*, 1991, **52**, 415-424.
15. S. D. Ebbesen, B. L. Mojet and L. Lefferts, *Journal of Catalysis*, 2007, **246**, 66-73.
16. A. Quintanilla, J. J. W. Bakker, M. T. Kreutzer, J. A. Moulijn and F. Kapteijn, *Journal of Catalysis*, 2008, **257**, 55-63.
17. N. D. Gangal, N. M. Gupta and R. M. Iyer, *Journal of Catalysis*, 1990, **126**, 13-25.
18. G. C. Bond, L. R. Molloy and M. J. Fuller, *Journal of the Chemical Society-Chemical Communications*, 1975, 796-797.
19. M. Sheintuch, J. Schmidt, Y. Lechthman and G. Yahav, *Applied Catalysis*, 1989, **49**, 55-65.
20. D. R. Schryer, B. T. Upchurch, B. D. Sidney, K. G. Brown, G. B. Hoflund and R. K. Herz, *Journal of Catalysis*, 1991, **130**, 314-317.
21. D. Lide, *CRC Handbook of Chemistry and Physics*, 84th edn., CRC Press, 2003.
22. S. Brunauer, P. H. Emmett and E. Teller, *Journal of the American Chemical Society*, 1938, **60**, 309-319.
23. C. Geology, *SEM/EDX Schematic*,
<http://departments.colgate.edu/geology/instruments/sem.htm#pic>.

3

Transition Metal Doped Hopcalite

In this chapter investigations are made into modification of hopcalite, designated CuMn_2O_4 , toward CO oxidation at ambient temperature. Hopcalite spinel lattice is modified through the introduction of dopant ions. Hutchings *et al.*¹ and Mirzaei *et al.*² have reported that modification of hopcalite co-precipitation preparation conditions have effects upon catalyst morphology and activity. The most important variable in regards to ambient temperature CO oxidation activity has been described as aging time, which has been discussed in detail by Cole³ and Jones⁴. Both have also discussed the effect of water upon catalyst activity, as well as catalyst calcination times. Based on previous work, the optimum preparation conditions of hopcalite are described in Part 2.1.

Jones *et al.*⁴ and Cole *et al.*³ have reported that modifying, or ‘doping’, a CuMn_2O_4 hopcalite catalyst with quantities of metal cations (Co^{3+} , Ni^{2+} , Fe^{3+} , Ag^+ , and Zn^{2+}) can improve activity toward CO oxidation. Compared to undoped Hopcalite, 2.0% Co/ CuMn_2O_4 with 6 h aging is reported by Jones as being unusually active. Coles reports 25.0% Zn/ CuMn_2O_4 with 0.5 h aging as more than twice as active as the undoped sample. These findings have been discussed in more detail in Chapter 1.

Several alternative dopant ions have not been previously investigated. Vanadium, cerium, palladium and silicon were selected as candidates for hopcalite promotion. Selection criteria is discussed in Chapter 1, based on ion size, oxidation states, ionization energy, and the availability of salt precursors. As a noble metal, palladium is discussed in more detail in Chapter 4.

3.1 V-doped CuMn_2O_4 - Mn Replacement

Vanadium was selected as a doping agent for introduction into a CuMn_2O_4 spinel lattice. As vanadium nitrate is not available, the salt VOSO_4 was selected under criteria discussed in Chapter 1. Despite tests showing a low yield in vanadium recovery (value 15.9%) it was the most promising reagent compared to the others tested.

A series of V-doped CuMn_2O_4 catalysts were prepared using the co-precipitation method. Vanadium in weightings of 1.0%, 2.0%, 5.0% and 10.0% were added to the lattice replacing a corresponding reduction in molecules of reagent manganese. In all cases the total reactant stoichiometry ratio remained at $[\text{Cu}]$ 1:2 $[\text{Mn} + \text{V}]$. The stoichiometric formula is referred to as $\text{CuMn}_{2-x}\text{V}_x\text{O}_4$.

3.1.1. CO Oxidation Activity

The activities of the undoped and vanadium doped CuMn_2O_4 catalysts are shown in Figure 12. It displays that replacement of manganese by vanadium has a detrimental effect on catalyst activity. All four V/ CuMn_2O_4 samples display no initial activity peak, in comparison to the peak present in the reference sample. The activity of the four V/ CuMn_2O_4 batches slowly rise, reaching steady state at ~ 60 min. Catalyst steady state activity is far lower for the V-doped samples than the reference sample. A correlation between rising catalyst V-loading and reduction in activity is observed for the 1, 2 and 10% loading catalysts. The 5% doped catalyst defies this trend and is more active than the 1% doped sample, though it is still far less active than the undoped sample.

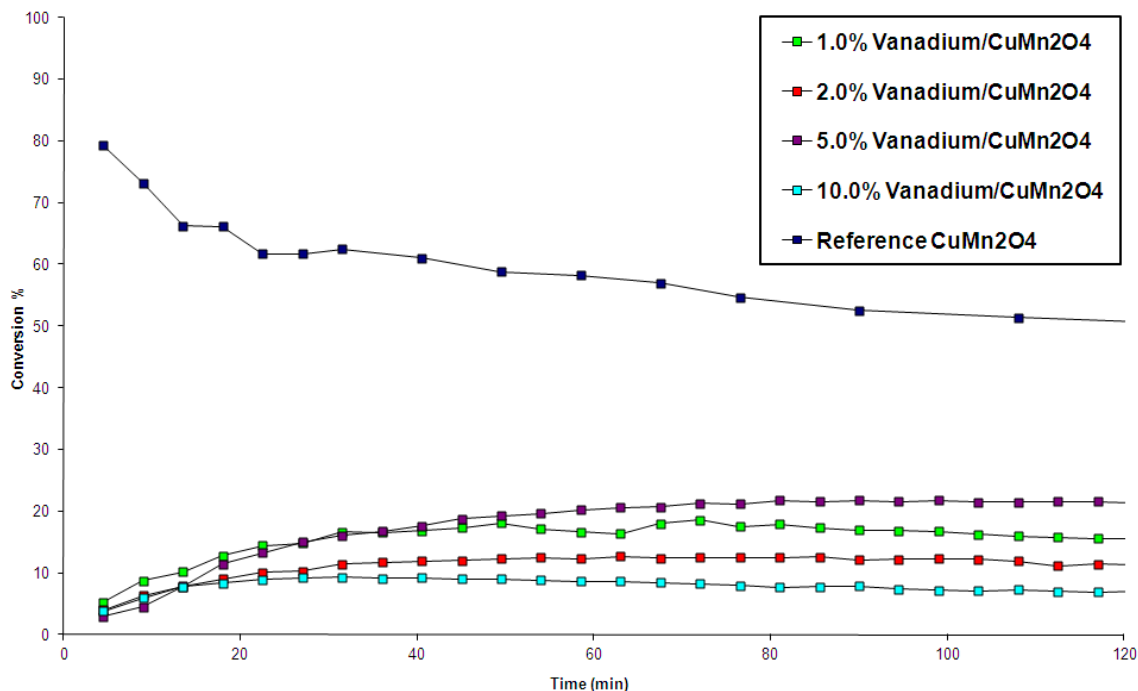


Figure 12 – CO Oxidation – V Doped $\text{CuMn}_{2-x}\text{V}_x\text{O}_4$ Catalyst

3.1.2 BET Surface Area, SANA and EDX Molar Ratio

The surface areas of the vanadium doped and reference catalysts were measured by BET analysis. The data is displayed in Table 8. Also displayed is the vanadium content of the samples, analyzed by EDX spectroscopy.

Sample	Surface Area (m^2g^{-1})	C value	EDX V loading
1.0%V/CuMn ₂ O ₄	71	88	0.10 %
2.0%V/CuMn ₂ O ₄	76	92	0.42 %
5.0%V/CuMn ₂ O ₄	34	76	1.24 %
10.0%V/CuMn ₂ O ₄	47	102	2.14 %
CuMn ₂ O ₄	56	87	0.00%

Table 8 – BET surface areas and EDX molar percentages of $\text{CuMn}_{2-x}\text{V}_x\text{O}_4$

Analyzing the BET data, 1.0% and 2.0% loadings of vanadium show an increase in catalyst surface area from the reference. The 5.0% and 10.0% doped samples show a decreased surface area from the reference. The activities of the five catalysts were normalized to take into account the differences in surface areas. This is displayed in

Figure 13. The 1.0, 2.0 and 10.0% loaded samples are much less active than the reference sample in regard to surface normalized activity. The 5.0% doped sample is approximately four times as active as the other vanadium samples, but it is still underperforming compared to the reference batch. It can be concluded that the change in catalyst activity is not correlated to the change in catalyst surface area.

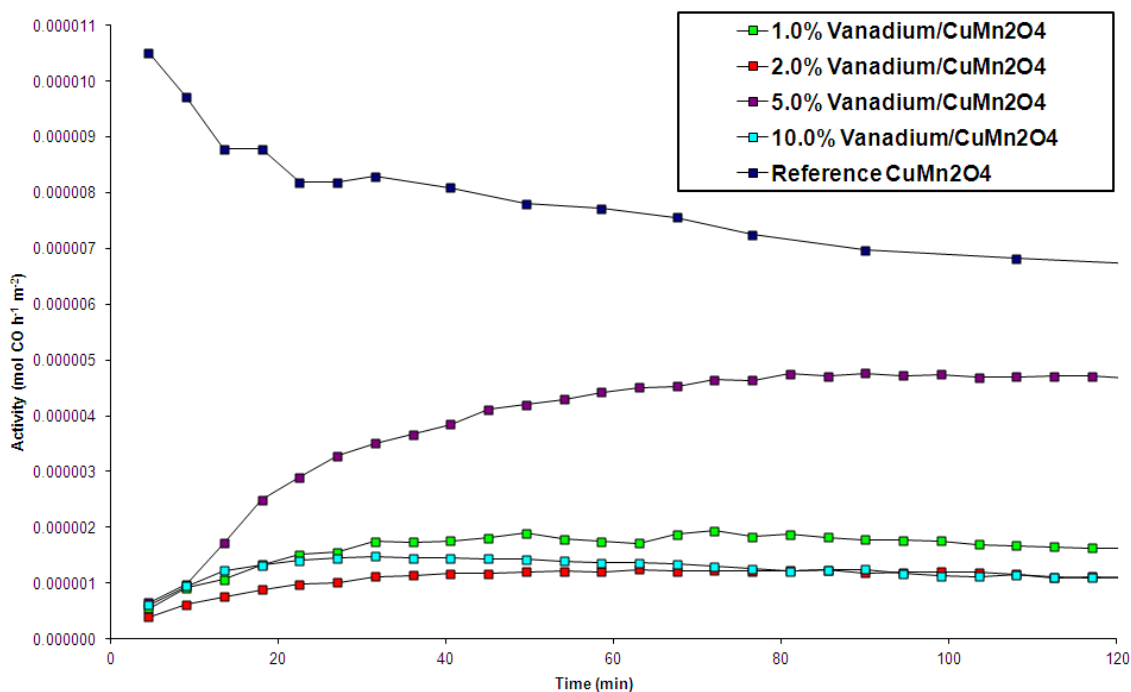


Figure 13 – Surface area normalized activity – Vanadium-doped $\text{CuMn}_{2-x}\text{V}_x\text{O}_4$

EDX data shown in Table 8 displays that as reagent vanadium volumes rise, increasing amounts of vanadium are present in the catalyst. However, final catalyst stoichiometry does not follow the initial reagent ratio. Approximately 10-20% of the reagent vanadium appears to have incorporated into the catalyst. This follows the trend discussed in Chapter 1 regarding the precipitation of VOSO_4 , which does not precipitate in the same manner as nitrate solutions.

3.1.3 Powder X-Ray Diffraction

The powder XRD data of undoped and V doped catalysts (Figure 14) display a slight trend toward a more crystalline structure. This is evidenced by the peaks forming at 2θ ca. 31.7° , 41.7° and 52.3° . In all cases, predominately amorphous structure and broad peaks makes phase identification difficult.

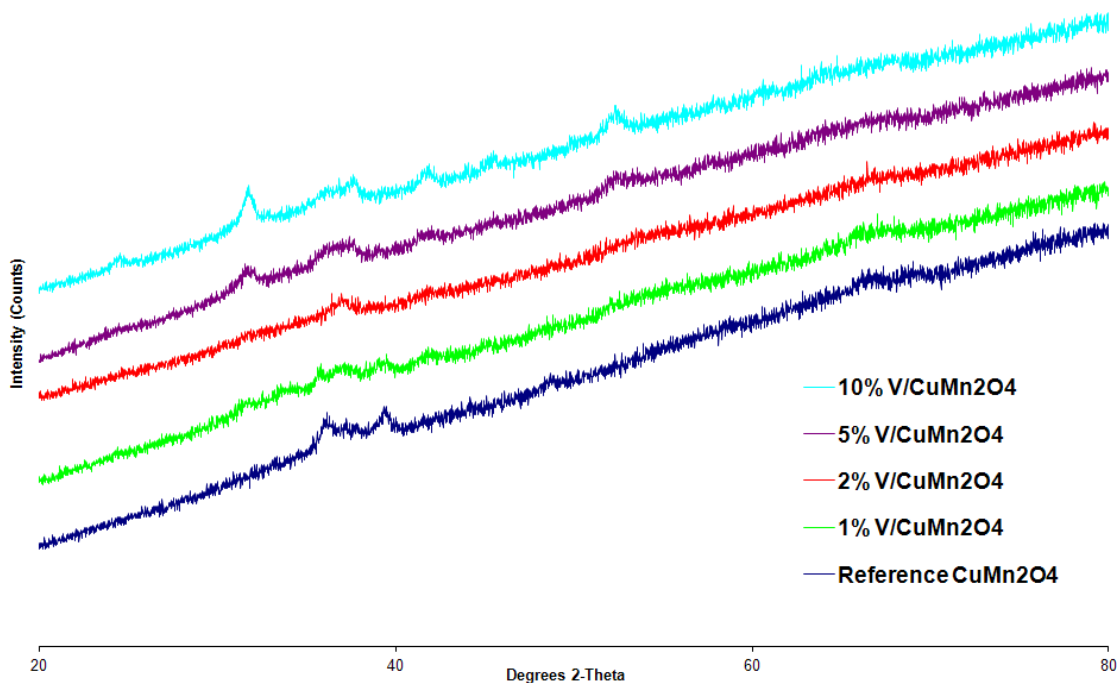


Figure 14 - Powder XRD – V doped $\text{CuMn}_{2-x}\text{V}_x\text{O}_4$ catalysts

Evidence of slightly increasing crystalline structure runs in correlation with introduction of greater amounts of vanadium into the crystal lattice. This also correlates with the reduction in catalyst activity displayed by catalysts with higher vanadium loadings. Hopcalite activity has been postulated to be due to its amorphous structure⁵. No Vanadium compounds were detected from these diffraction patterns, though this is not evidence of their absence.

3.1.4 SEM Analysis

SEM microstructure analysis of V-Doped $\text{CuMn}_{2-x}\text{V}_x\text{O}_4$ is described in Table 9. The average particle size displayed is in all cases smaller than the undoped sample. This could be attributed to the increase in surface area, though there is no direct correlation between change in surface area and change in particle size. Figures 15-18 display the SEM images of the V-doped samples.

Sample	Average Particle Diameter (μm)
CuMn_2O_4	7.55
1% Vanadium Doped CuMn_2O_4	5.06
2% Vanadium Doped CuMn_2O_4	4.33
5% Vanadium Doped CuMn_2O_4	4.23
10% Vanadium Doped CuMn_2O_4	5.51

Table 9 – Particle sizes of V-Doped $\text{CuMn}_{2-x}\text{V}_x\text{O}_4$ analyzed by SEM

Displayed in Figure 19 is the SEM microstructure analysis of undoped CuMn_2O_4 . Powder particles with a spherical morphology are displayed, with an approximate average particle diameter of 7.5 microns.

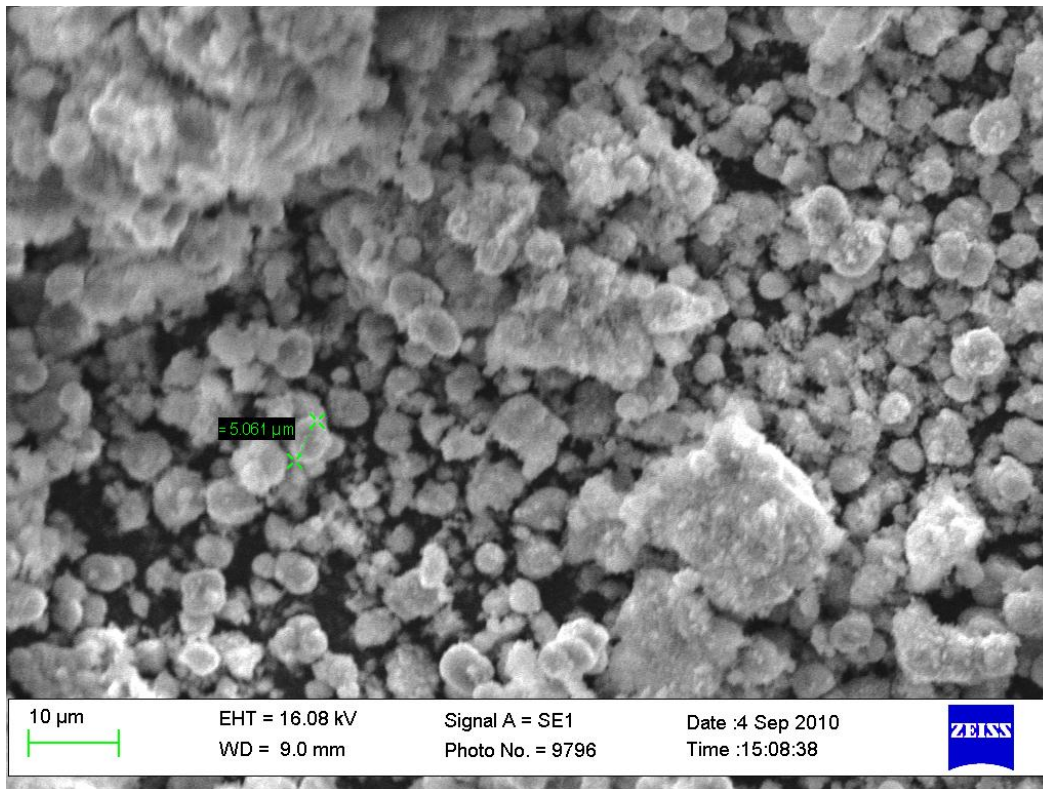


Figure 15 - SEM image of 1% V-doped $\text{CuMn}_{2-x}\text{V}_x\text{O}_4$, displaying average particle size

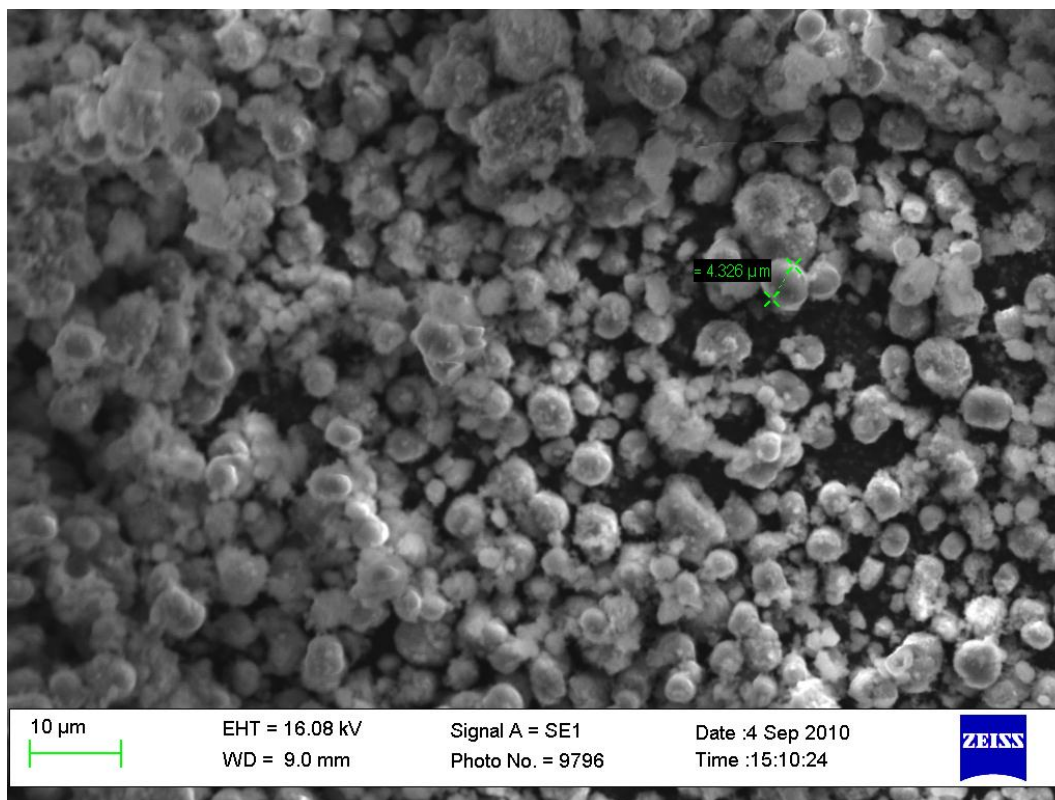


Figure 16 - SEM image of 2% V-doped $\text{CuMn}_{2-x}\text{V}_x\text{O}_4$, displaying average particle size

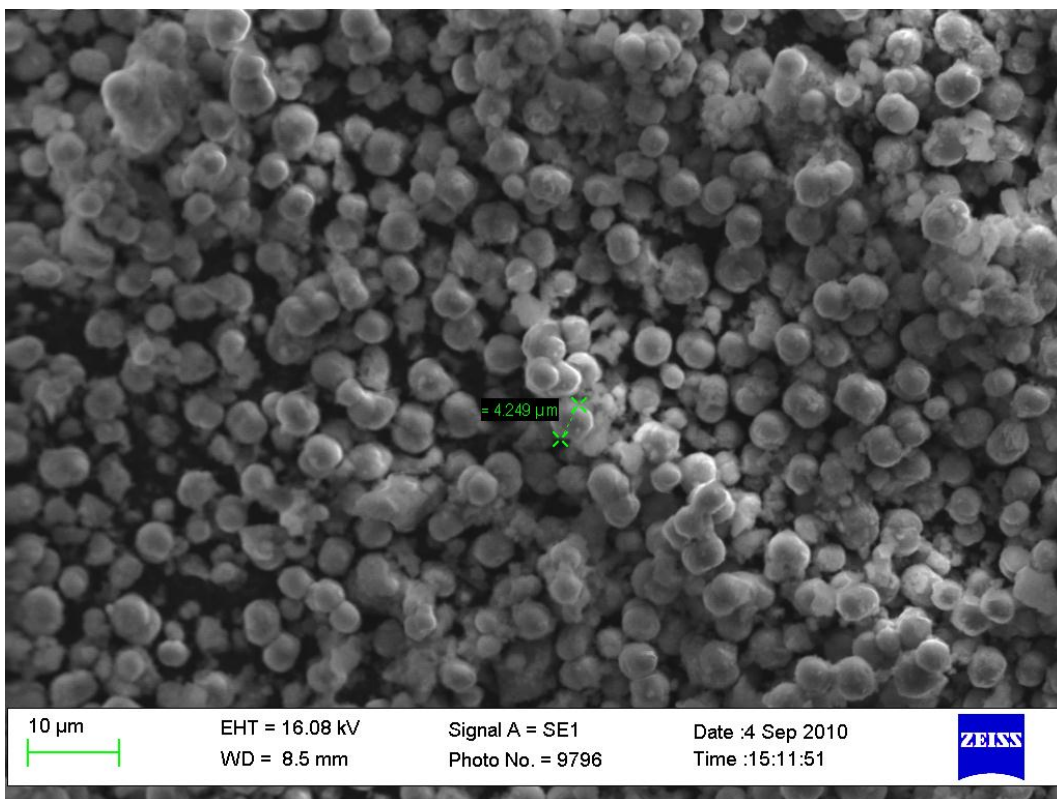


Figure 17 - SEM image of 5% V-doped $\text{CuMn}_{2-x}\text{V}_x\text{O}_4$, displaying average particle size

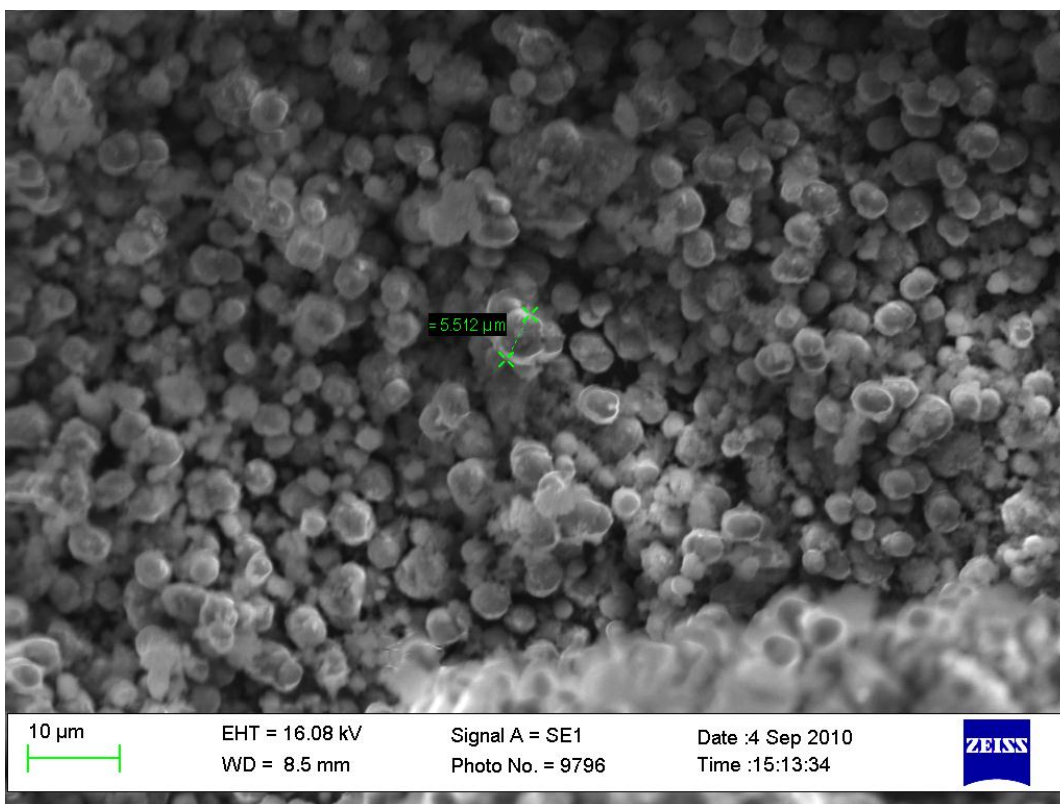


Figure 18 - SEM image of 10% V-doped $\text{CuMn}_{2-x}\text{V}_x\text{O}_4$, displaying average particle size

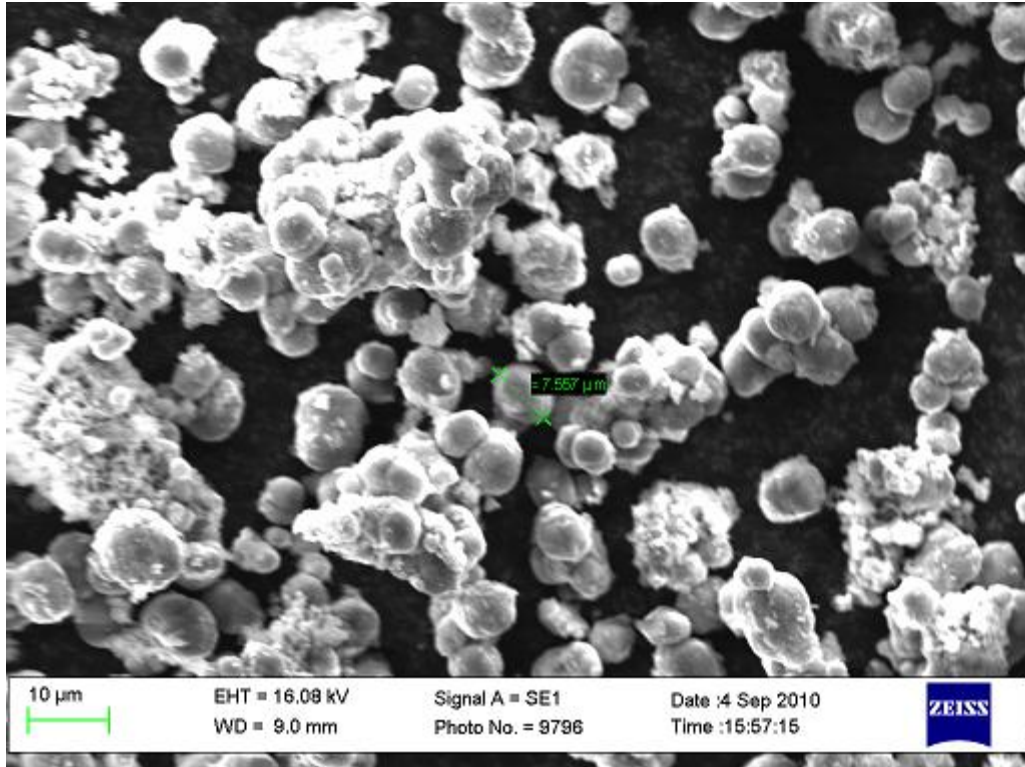


Figure 19 - SEM image of unmodified reference CuMn_2O_4

3.2 V-doped CuMn_2O_4 - Copper Replacement

A series of V-doped CuMn_2O_4 catalysts were prepared using the co-precipitation method. Vanadium in levels of 1.0%, 2.0%, 5.0% and 10.0% were added to the lattice replacing a corresponding reduction in reagent molecules of copper. In all cases the total reactant stoichiometry ratio remained at $[\text{Cu} + \text{V}] 1:2 [\text{Mn}]$. The stoichiometric formula is referred to as $\text{Cu}_{1-x}\text{Mn}_2\text{V}_x\text{O}_4$.

3.2.1 CO Oxidation Activity

The activities of the undoped and vanadium doped CuMn_2O_4 catalysts are shown in Figure 20.

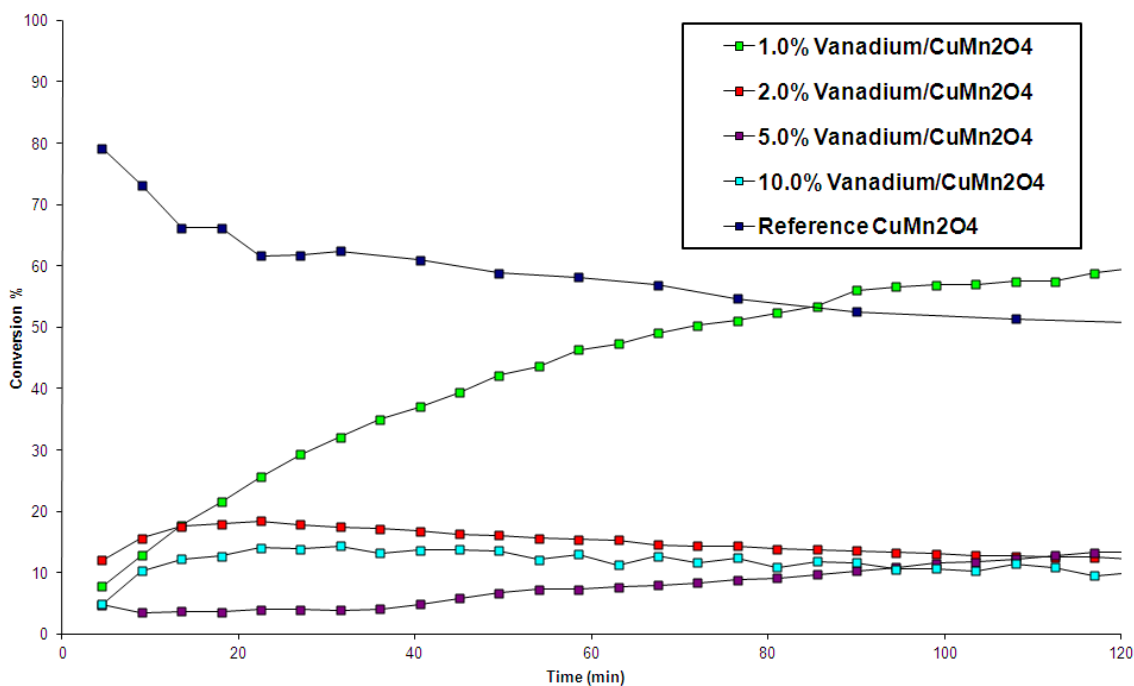


Figure 20 – CO Oxidation – V Doped $\text{Cu}_{1-x}\text{Mn}_2\text{V}_x\text{O}_4$ Catalysts

Figure 17 displays evidence that replacement of copper by vanadium has an overall detrimental effect on catalyst activity, with the exception of the 1.0% doped catalyst. In the case of the 2.0%, 5.0% and 10.0% doped catalysts, activities have decreased

significantly from the undoped reference. The activity of the 2.0% and 10.0% samples peak at ~25 min and gradually deactivate. The 5.0% doped catalyst does not peak by the end of the experiment, although activity levels are still very low. The 1.0% doped catalyst displays a low initial activity which slowly rises, surpassing the undoped reference at ~85 min and continuing to rise to ~ 65%.

3.2.2 BET Surface Area, SANA and EDX molar ratio

The surface areas of the undoped and vanadium doped catalysts were analyzed by BET and are displayed in Table 10. Also displayed is the vanadium content of the samples, analyzed by EDX spectroscopy.

Sample	Surface Area (m ² g ⁻¹)	C value	EDX V loading
1.0%V/CuMn ₂ O ₄	109	57	0.10%
2.0%V/CuMn ₂ O ₄	66	112	0.15%
5.0%V/CuMn ₂ O ₄	71	64	0.50%
10.0%V/CuMn ₂ O ₄	60	67	1.19%
CuMn ₂ O ₄	56	87	0.00%

Table 10 – BET surface areas and EDX molar percentages of Cu_{1-x}Mn₂V_xO₄

Replacement of copper by vanadium into CuMn₂O₄ correlates to an increase in catalyst surface area. 2.0%, 5.0% and 10.0% doped catalysts possess increased surface areas. 1.0% V/CuMn₂O₄ possesses approximately double the catalyst surface area of the undoped sample. The activities of the five catalysts were normalized to take into account the differences in surface areas. This is displayed in Figure 21.

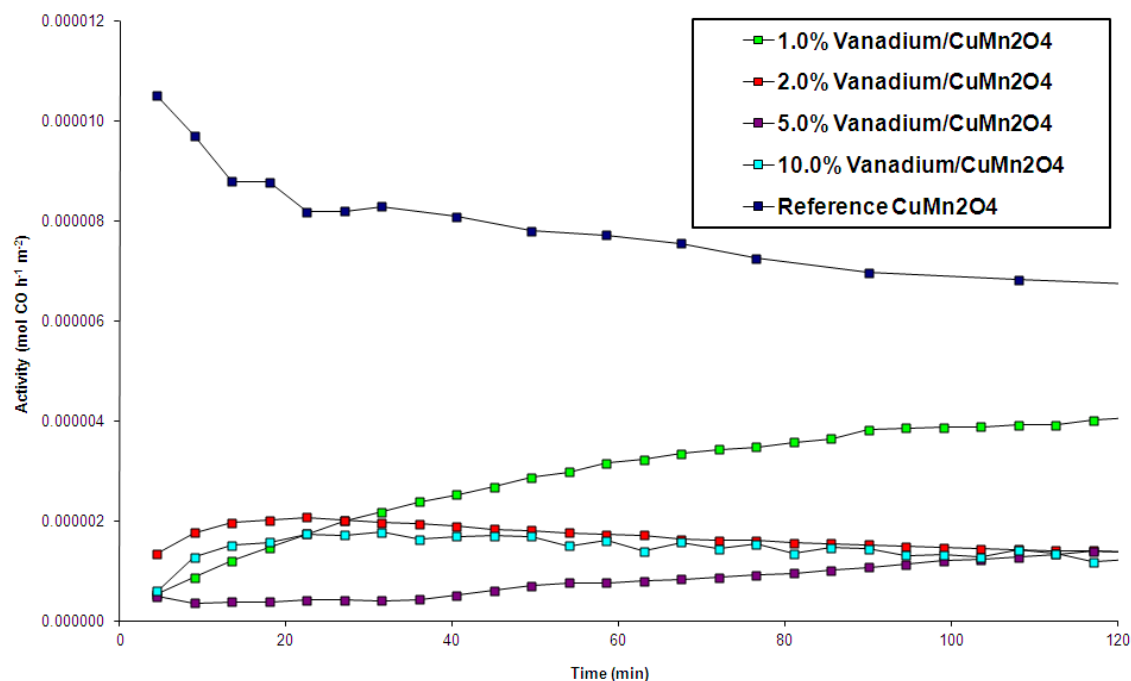


Figure 21 – Surface area normalized activity – Vanadium-doped $Cu_{1-x}Mn_2V_xO_4$

When the surface area of the catalysts is taken into account, the activities of the 2.0%, 5.0% and 10.0% doped catalysts are further removed from the reference sample. The 1.0% doped catalyst has an approximately doubled surface area compared to the undoped sample. When normalized this shows that the 1.0% sample is less catalytically active than the undoped sample in terms of oxidized moles $CO\ h^{-1}\ m^{-2}$.

The displayed EDX molar vanadium loadings are in correlation, but with much lower than the reagent loadings. Roughly 10.0% of the reagent vanadium appears to be present in the catalyst.

3.2.3 Powder X-Ray Diffraction

The XRD data of undoped and V doped catalysts is displayed in Figure 22. There is evidence of increasing crystalline character in the samples. This is most evidenced by the peaks developing at 2θ ca. 31.5° , 35.9° , 37.3° , 41.6° , 45.2° , 52° . In all cases, predominately amorphous structure and broad peaks makes phase identification difficult.

Across the five samples, this is in correlation with introduction of increasing amounts of vanadium into the crystal lattice. This also correlates with the reduction in activity displayed by catalysts with higher vanadium loadings. No vanadium compounds were detected from these diffraction patterns, though this is not evidence of their absence.

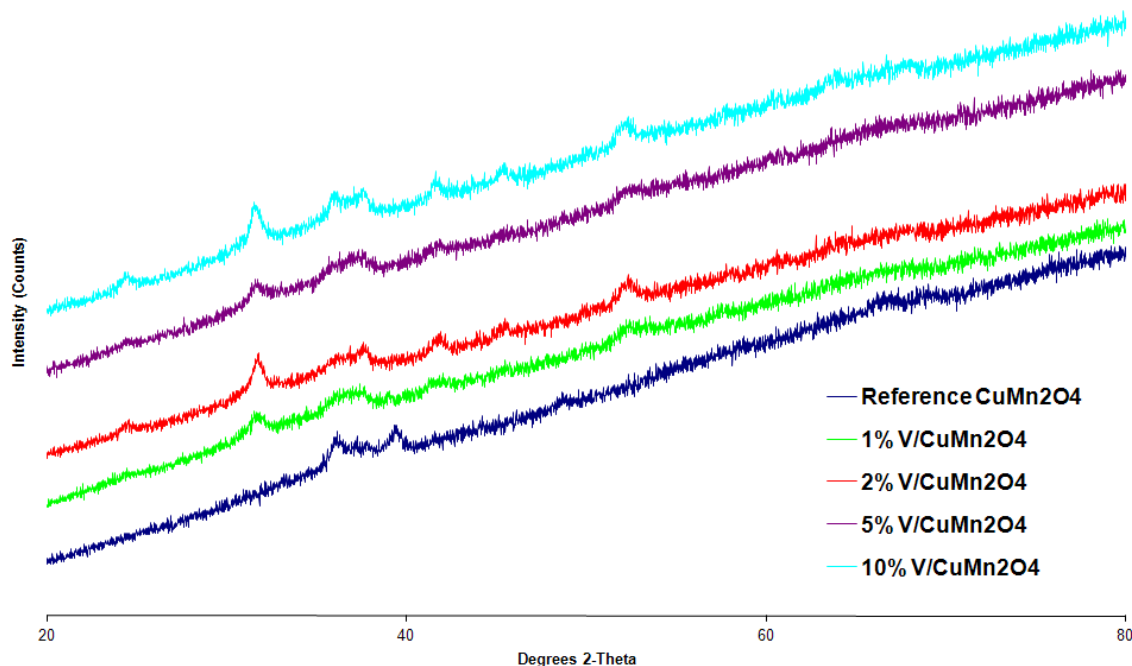


Figure 22 - Powder XRD – V doped $Cu_{1-x}Mn_2V_xO_4$ catalyst

3.2.4 SEM Analysis

SEM microstructure analysis of V-Doped $Cu_{1-x}Mn_2V_xO_4$ is described in Table 11. The average particle size displayed is in all cases smaller than the undoped sample. This cannot be attributed to their increase in surface area, as there is no correlation between change in surface area and change in particle size. Figures 23-26 display the SEM image of the four V-doped samples.

Sample	Average Particle Diameter (μm)
$CuMn_2O_4$	7.55
1% Vanadium Doped $CuMn_2O_4$	5.38
2% Vanadium Doped $CuMn_2O_4$	4.53
5% Vanadium Doped $CuMn_2O_4$	4.35
10% Vanadium Doped $CuMn_2O_4$	3.98

Table 11 – Particle sizes of V-Doped $Cu_{1-x}Mn_2V_xO_4$ analyzed by SEM

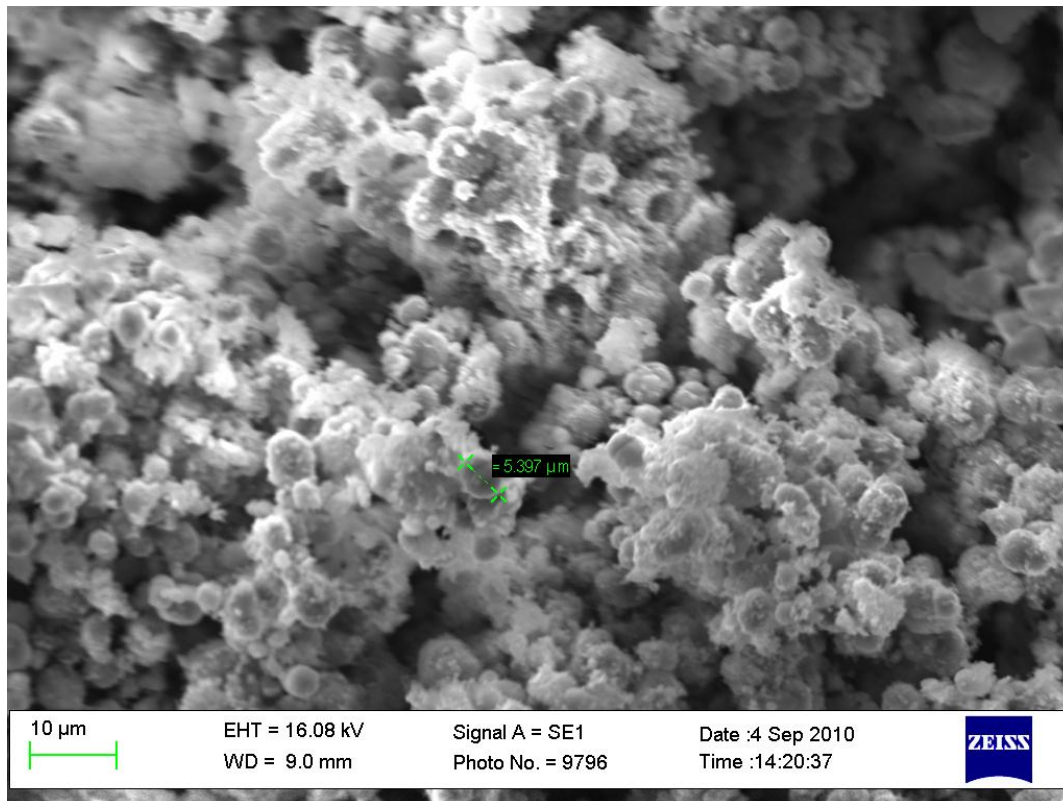


Figure 23 - SEM image of 1% V-doped $\text{Cu}_{1-x}\text{Mn}_2\text{V}_x\text{O}_4$

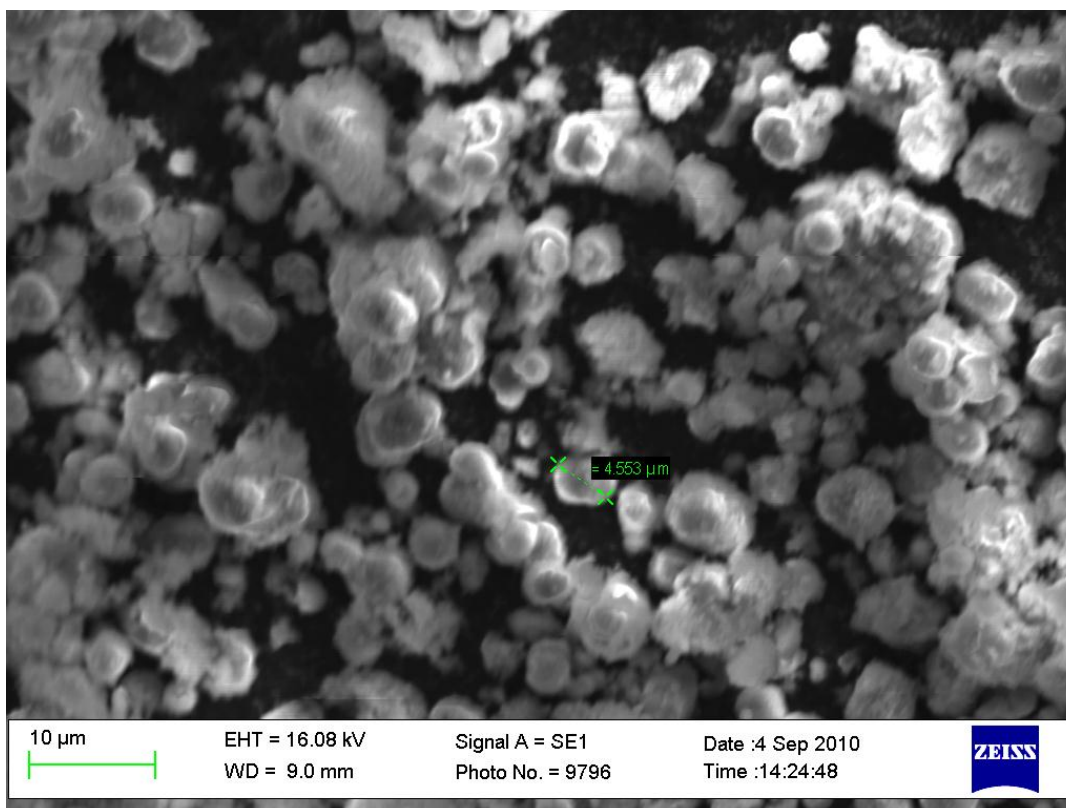


Figure 24 - SEM image of 2% V-doped $\text{Cu}_{1-x}\text{Mn}_2\text{V}_x\text{O}_4$

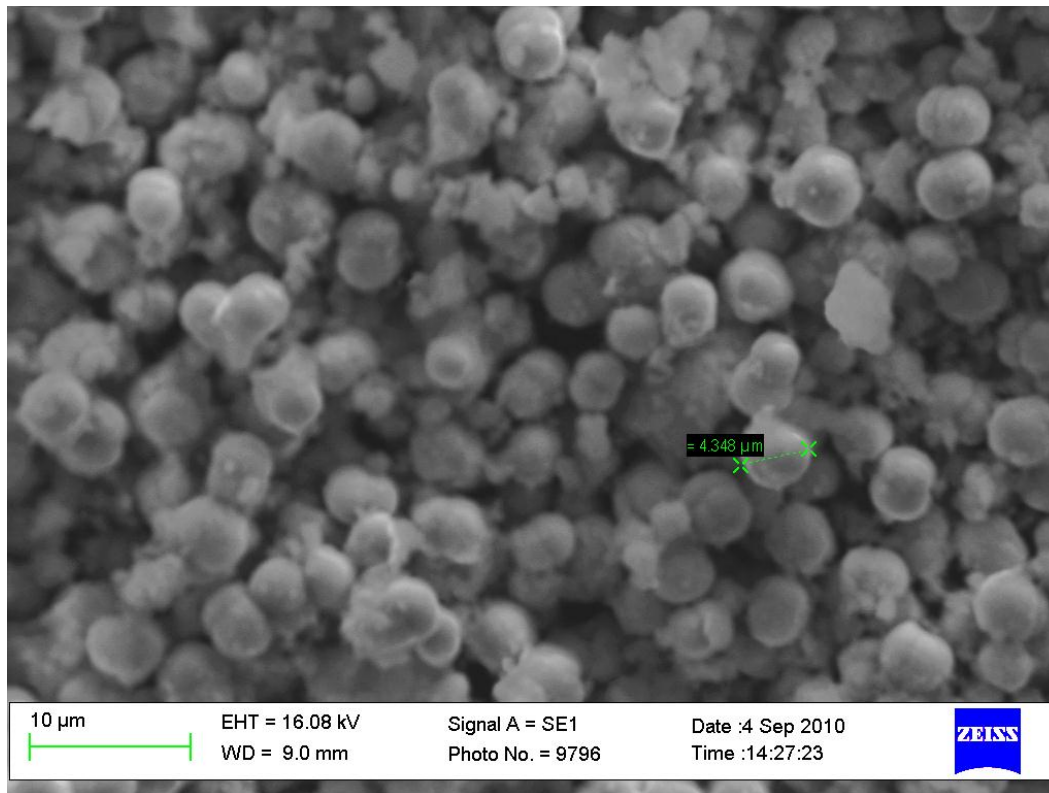


Figure 25 - SEM image of 5% V-doped $Cu_{1-x}Mn_2V_xO_4$

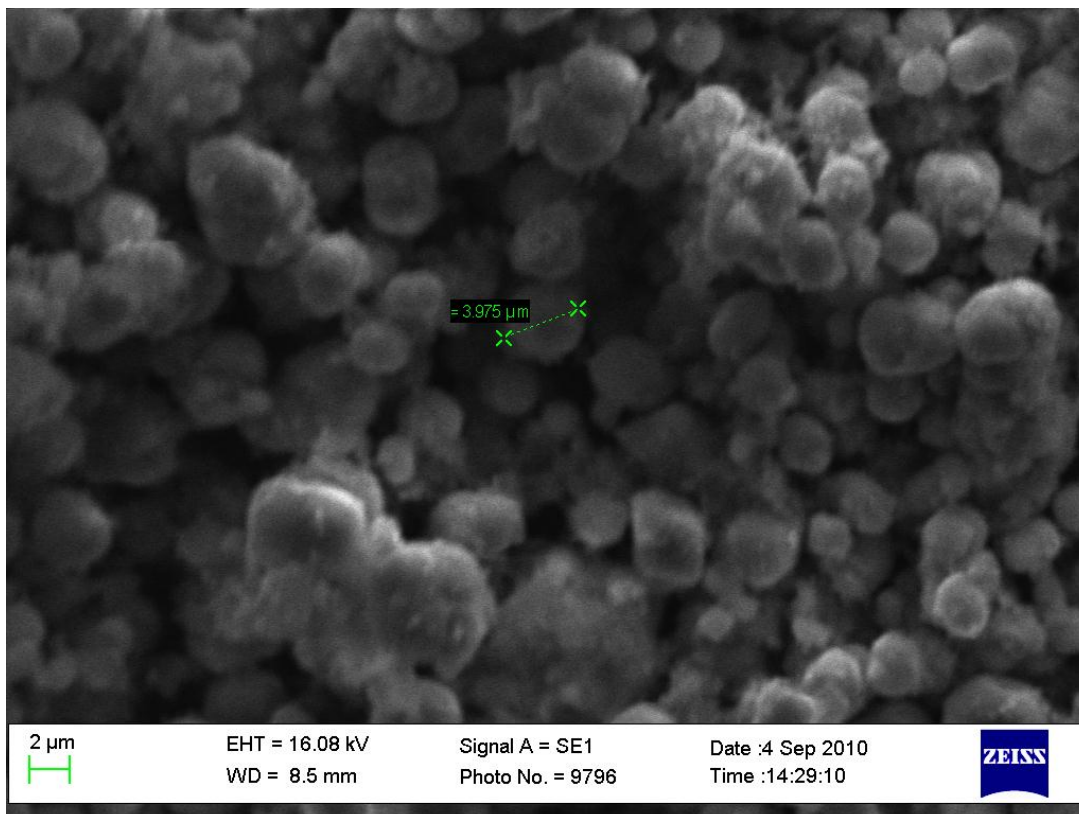


Figure 26 - SEM image of 10% (bottom right) V-doped $Cu_{1-x}Mn_2V_xO_4$

3.3 V-doped CuMn_2O_4 – Dual Cu & Mn Replacement

A series of V-doped CuMn_2O_4 catalysts were prepared using the co-precipitation method. Vanadium in levels of 1.0%, 2.0%, 5.0% and 10.0% were added to the CuMn_2O_4 lattice. This replaced an equivalent reduction in molecules of copper and manganese. In all cases the total reactant stoichiometry ratio remained at $[\text{Cu} + \frac{1}{2}\text{V}]$ 1:2 $[\text{Mn} + \frac{1}{2}\text{V}]$. The stoichiometric formula is referred to as $\text{Cu}_{1-\frac{1}{2}X}\text{Mn}_{2-\frac{1}{2}X}\text{V}_X\text{O}_4$.

3.3.1 CO Oxidation Activity

The activities of the undoped and vanadium doped CuMn_2O_4 catalysts are shown below in Figure 27.

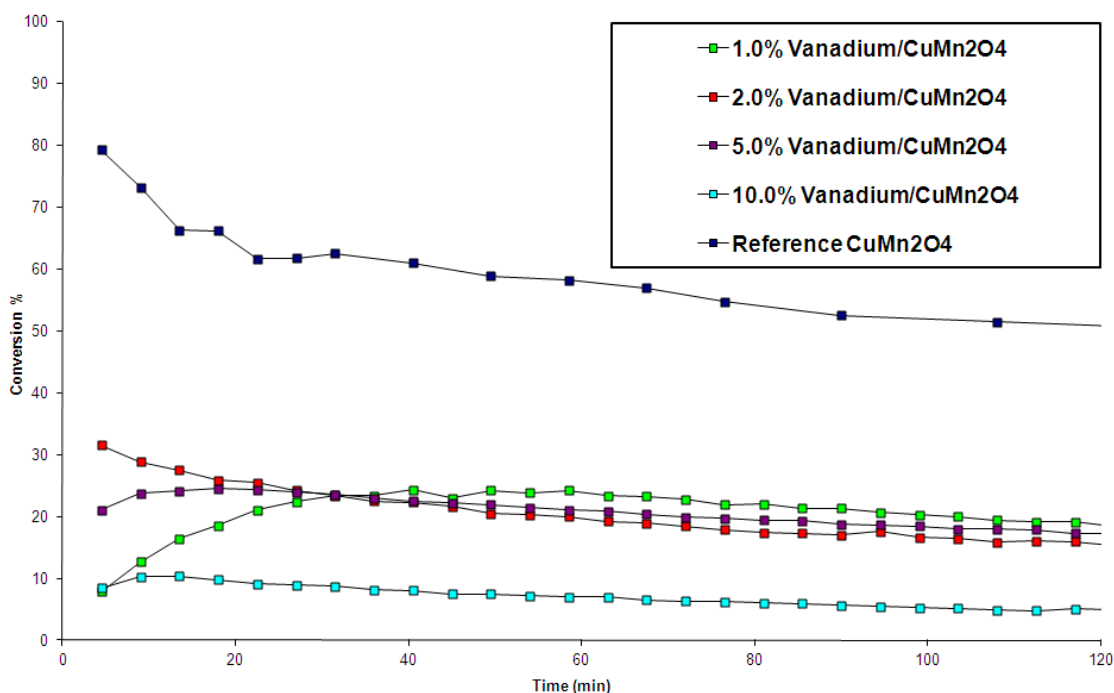


Figure 27 – CO Oxidation – V Doped $\text{Cu}_{1-\frac{1}{2}X}\text{Mn}_{2-\frac{1}{2}X}\text{V}_X\text{O}_4$ Catalysts

Figure 21 shows that replacement of the copper and manganese by vanadium has a detrimental effect on catalyst activity. In the case of the 1.0%, 2.0% and 5.0% doped catalysts, activities have decreased significantly from the undoped reference. All three display different initial activity peaks, but show similar steady state activity of ~2.0%. The 10.0% doped sample displays very low activity levels of below 10.0% and nearing zero after two hours.

3.3.2 BET Surface Area, SANA and EDX molar ratio

The surface areas of the undoped and vanadium doped catalysts were measured by BET analysis and are displayed in Table 12. Also displayed is the vanadium content of the samples, analyzed by EDX spectroscopy.

Sample	Surface Area (m^2g^{-1})	C value	EDX V loading
1.0%V/CuMn ₂ O ₄	62	51	0.20%
2.0%V/CuMn ₂ O ₄	70	88	0.65%
5.0%V/CuMn ₂ O ₄	99	76	1.70%
10.0%V/CuMn ₂ O ₄	55	156	2.20%
CuMn ₂ O ₄	56	87	0.00%

Table 12 – BET surface areas and EDX molar percentages of $\text{Cu}_{1-1/2x}\text{Mn}_{2-1/2x}\text{V}_x\text{O}_4$

For the dual-replaced catalyst, the 1.0%, 2.0% and 5.0% doped catalysts show a steady increase in surface area. The 10.0% doped catalyst displays an equivalent surface area to the undoped sample.

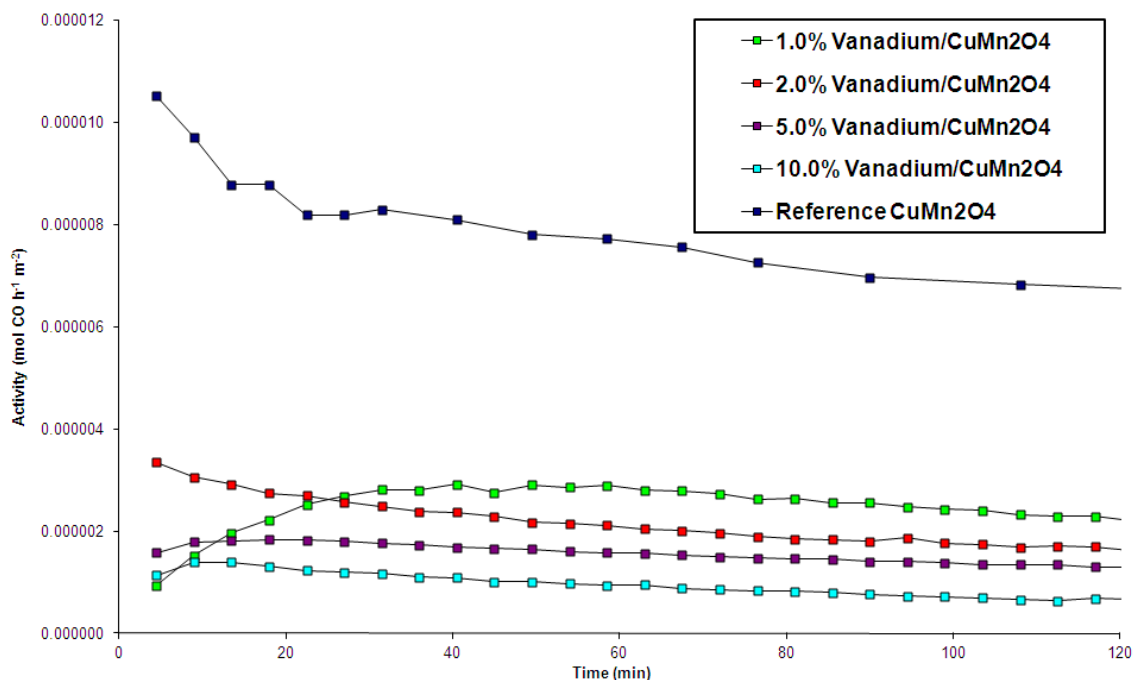


Figure 28 – Surface area normalized activity – Vanadium-doped $\text{Cu}_{1-1/2x}\text{Mn}_{2-1/2x}\text{V}_x\text{O}_4$

When normalized for the effects of surface area (displayed in Figure 28), the activities of the four doped batches are still far less than those of unmodified hopcalite. There is a clear correlation between reduction in activity and rising vanadium loading.

The displayed EDX molar Vanadium loadings are in correlation, but much lower than the reagent loadings. Roughly 20% of the reagent vanadium appears to be present in the catalyst.

3.3.3 Powder X-Ray Diffraction

The powder XRD data of unmodified and V doped catalysts are displayed in Figure 29. They display a slight trend toward a less amorphous structure, evidenced particularly by the peak developing at 36° . Predominately amorphous structure and broad peaks makes phase identification difficult. The peaks developing at 2θ ca. 30.5° , 57.6° , 63.4° are characteristic of crystalline spinel $\text{Cu}_{1.5}\text{Mn}_{1.5}\text{O}_4$. Across the five samples, this development is in correlation with introduction of increasing amounts of vanadium into the crystal lattice. This also correlates with the reduction in activity displayed by catalysts with higher vanadium loadings. No vanadium compounds were detected from these diffraction patterns, though this is not evidence of their absence.

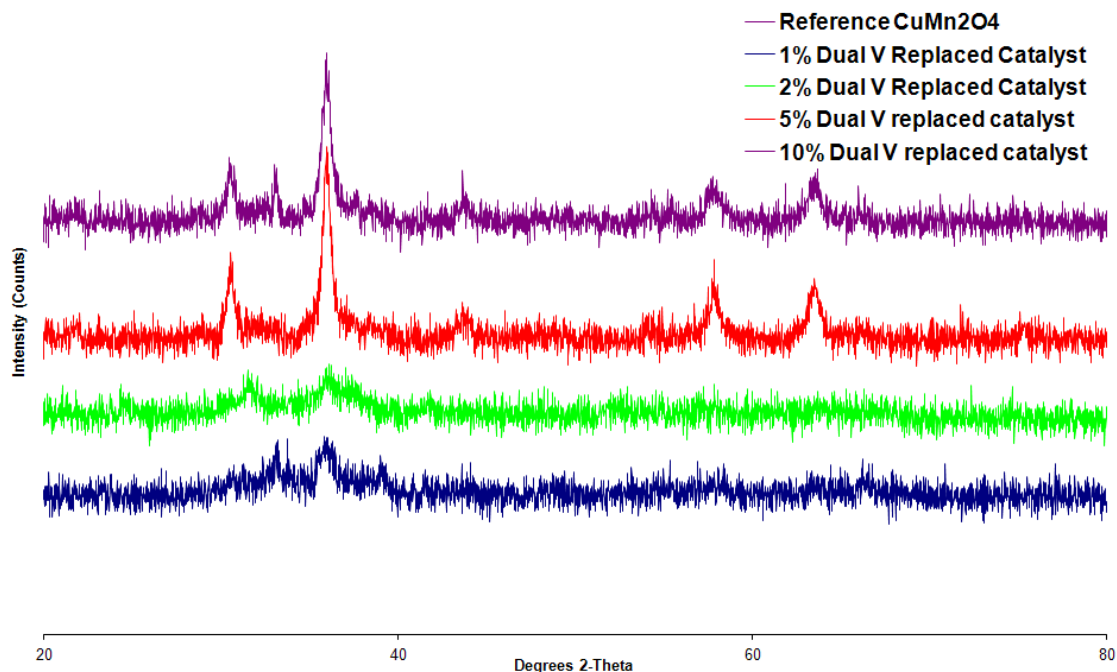


Figure 29 - Powder XRD – V doped $Cu_{1-1/2x}Mn_{2-1/2x}V_xO_4$ catalyst

3.3.4 SEM Analysis

SEM microstructure analysis of V-Doped $Cu_{1-1/2x}Mn_{2-1/2x}V_xO_4$ is described in Table 13. The average particle size displayed is in all cases smaller than the undoped sample. This could be attributed to their increase in surface area, though there is a slight correlation between change in surface area and change in particle size. Figures 30-33 displays the SEM image of the four doped samples.

Sample	Average Particle Diameter (μm)
$CuMn_2O_4$	7.55
1% Vanadium Doped $CuMn_2O_4$	5.54
2% Vanadium Doped $CuMn_2O_4$	5.28
5% Vanadium Doped $CuMn_2O_4$	5.28
10% Vanadium Doped $CuMn_2O_4$	6.08

Table 13 – Particle sizes of V-Doped $Cu_{1-1/2x}Mn_{2-1/2x}V_xO_4$ analyzed by SEM

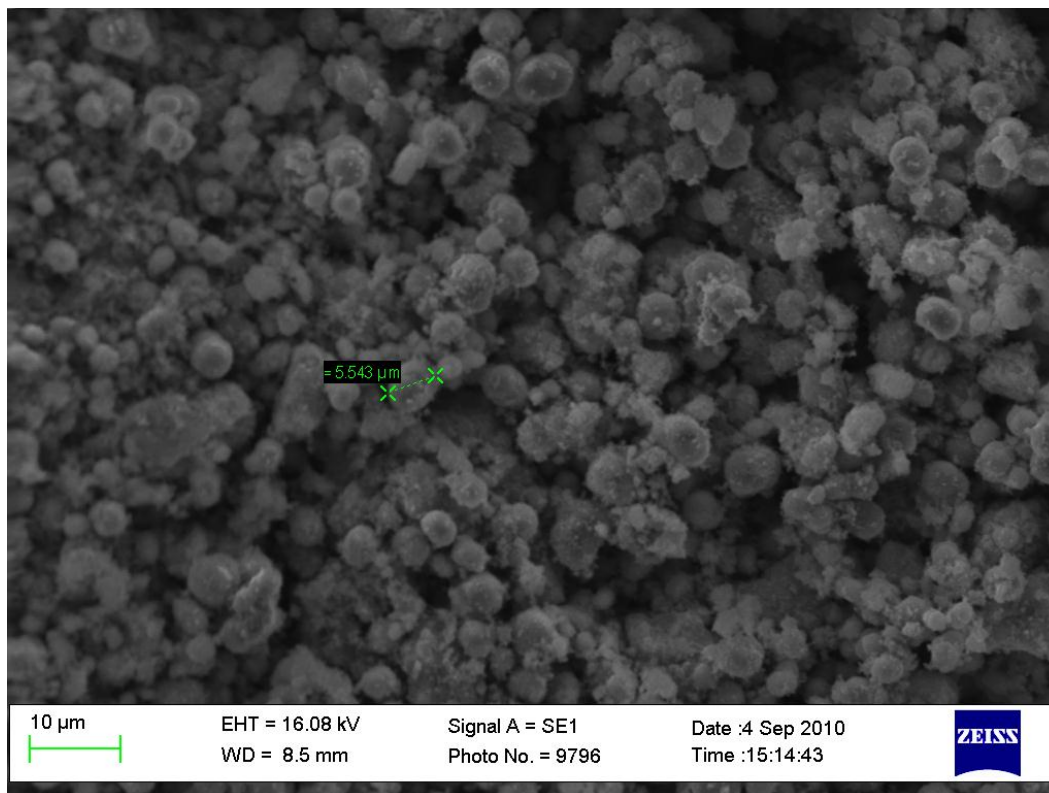


Figure 30 - SEM image of 1% V-doped $Cu_{1-1/2x}Mn_{2-1/2x}V_xO_4$

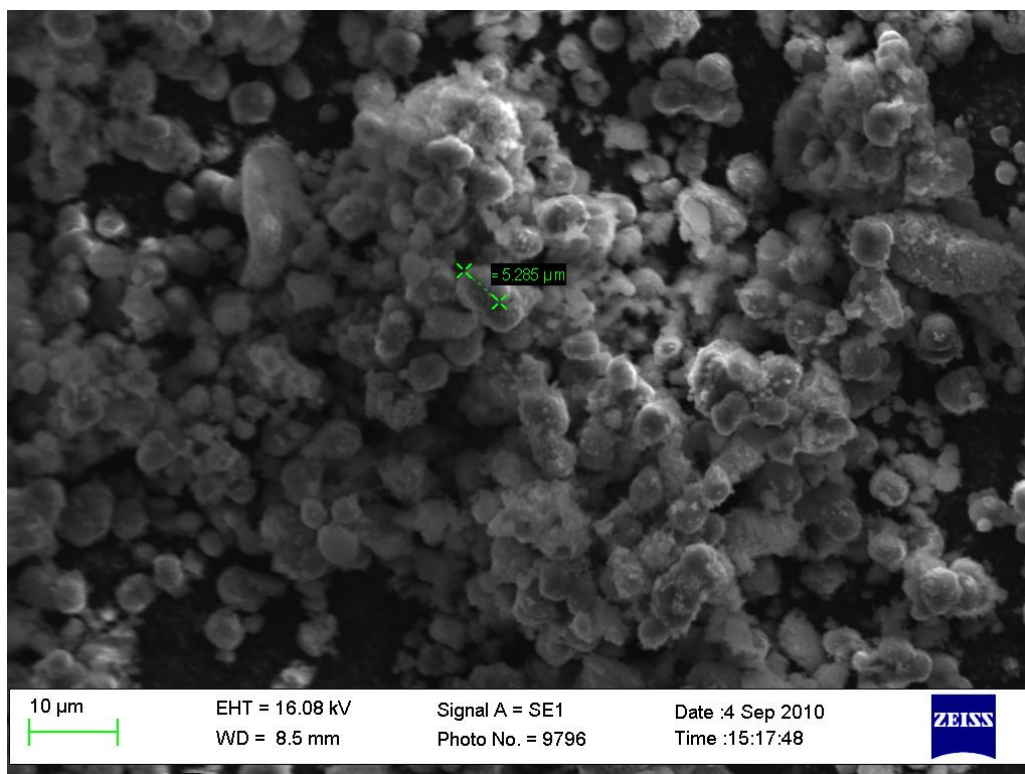


Figure 31 - SEM image of 2% V-doped $Cu_{1-1/2x}Mn_{2-1/2x}V_xO_4$

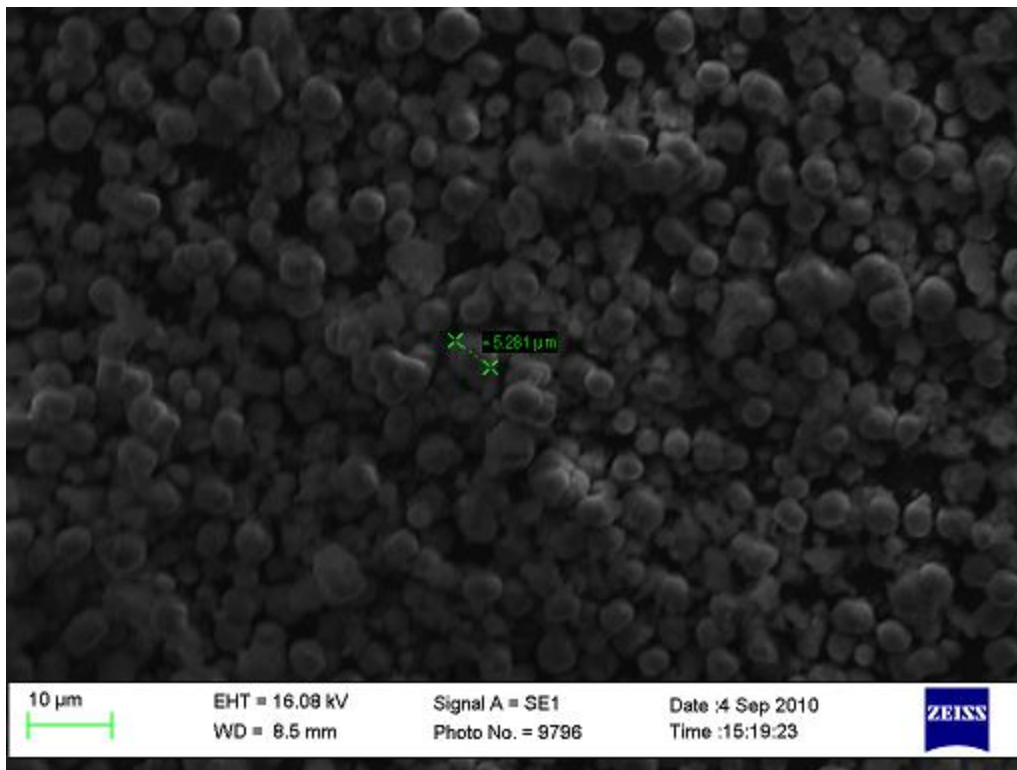


Figure 32 - SEM image of 5% V-doped $Cu_{1-1/2x}Mn_{2-1/2x}V_xO_4$

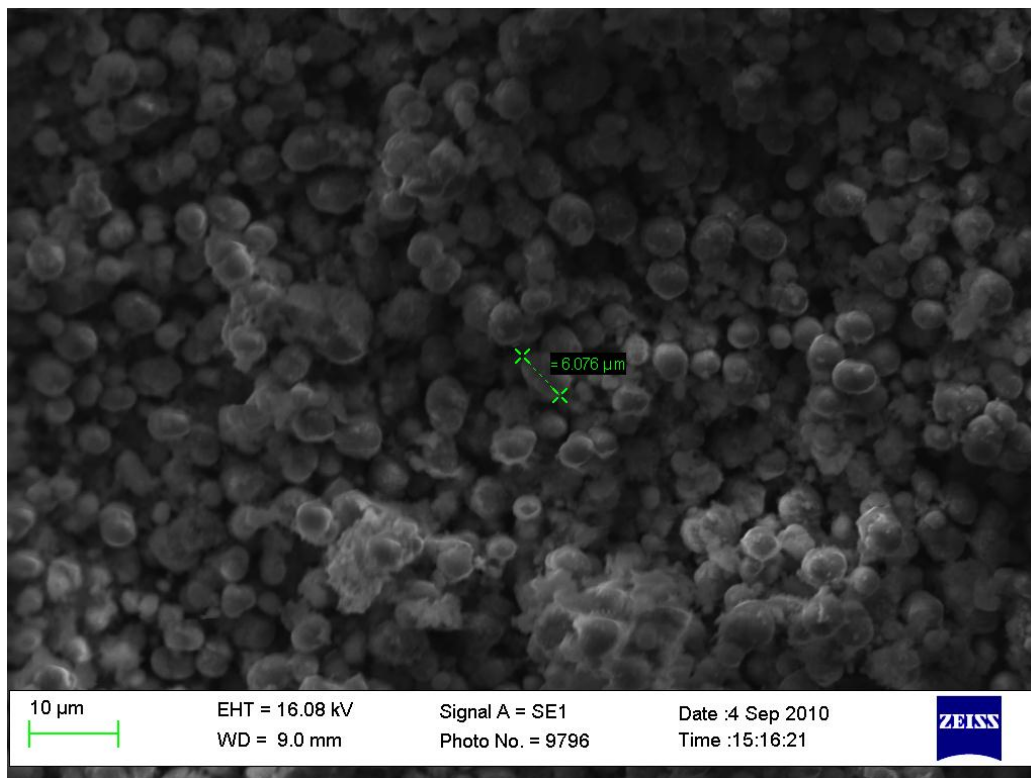


Figure 33 - SEM image of 10% V-doped $Cu_{1-1/2x}Mn_{2-1/2x}V_xO_4$

3.4 Cerium Doping

Cerium was selected as a doping agent for introduction into a CuMn_2O_4 spinel lattice. A series of cerium doped catalysts were prepared using standard co-precipitation methods detailed in Chapter 2. The salt $\text{Ce}(\text{NO}_3)_3 \cdot 6\text{H}_2\text{O}$ was selected under criteria discussed in Chapter 1. Cerium in weightings of 1.0%, 2.0%, 5.0% and 10.0% were added to the lattice replacing a reduction of copper and manganese molecules in a 1:2 ratio. In all cases the total molar ratio remained at $[\text{Cu} + 0.5\text{Ce}]$ 1:2 $[\text{Mn} + 0.5\text{Ce}]$.

3.4.1 CO Oxidation Activity

The activities of the undoped and cerium doped CuMn_2O_4 catalysts are shown in Figure 34.

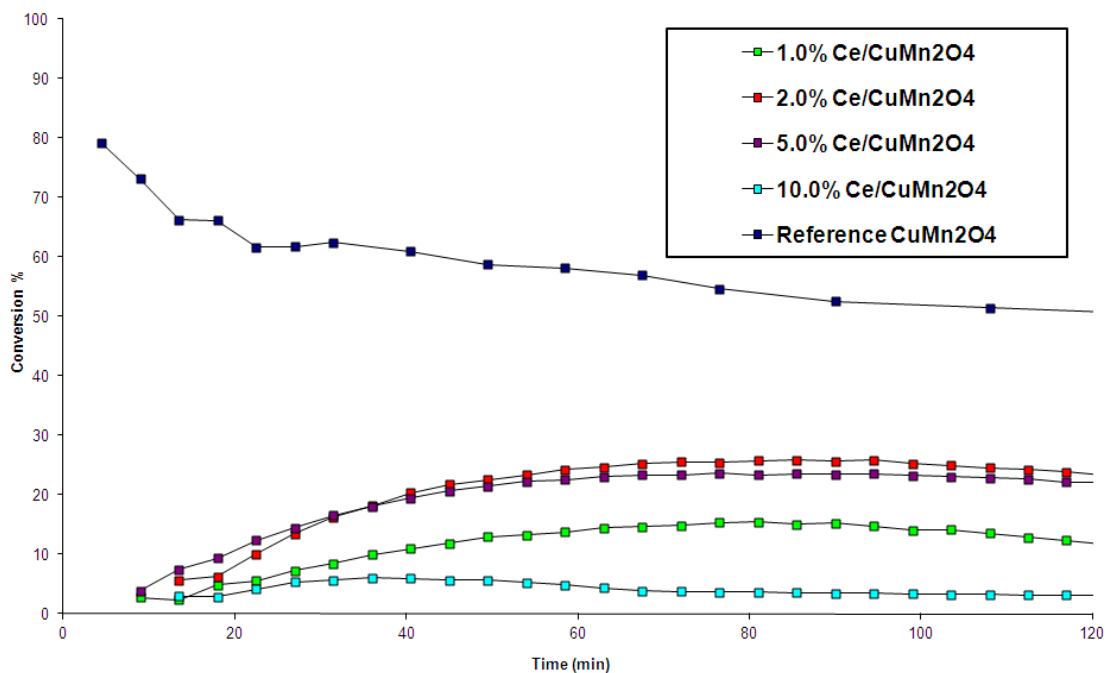


Figure 34 – CO Oxidation – Ce Doped CuMn_2O_4 Catalysts

Displayed is the evidence that replacement of the manganese by cerium has a detrimental effect on catalyst activity. The 1.0% doped catalyst display inferior activity to the

undoped reference, ~ 11.0% at steady state. The 2.0% and 5.0% doped catalysts are more active, ~ 23.0% conversion, but still far inferior to the undoped sample. The 10.0% doped catalyst displays very low activity of ~ 4.0% conversion. All doped catalysts display no initial activity spike, and reach steady state at ~ 60 min.

3.4.2 BET Surface Area, SANA and EDX molar ratio

The surface areas of the undoped and cerium doped catalysts were measured by BET and are displayed in Table 14. In addition, also displayed is the molar cerium content of the samples, analyzed by EDX spectroscopy.

Sample	Surface Area (m ² g ⁻¹)	C value	EDX Cerium Loading
1.0%Ce/CuMn ₂ O ₄	56.5	55	0.27%
2.0%Ce/CuMn ₂ O ₄	86.5	91	0.68%
5.0%Ce/CuMn ₂ O ₄	96	120	1.97%
10.0%Ce/CuMn ₂ O ₄	93.5	51	1.80%
CuMn ₂ O ₄	56	87	0.00%

Table 14 - BET surface areas and EDX molar percentages of Ce-doped CuMnO₄

The data displayed here suggests that cerium has a positive effect on catalyst surface area. 1.0% doped Ce/CuMn₂O₄ displays no relative change in surface area, which suggests cerium is null as a structural promoter in this regard. 2.0%, 5.0% and 10.0% doped catalysts display an increase in surface area. The surface normalized activities of the five catalysts are displayed in Figure 35.

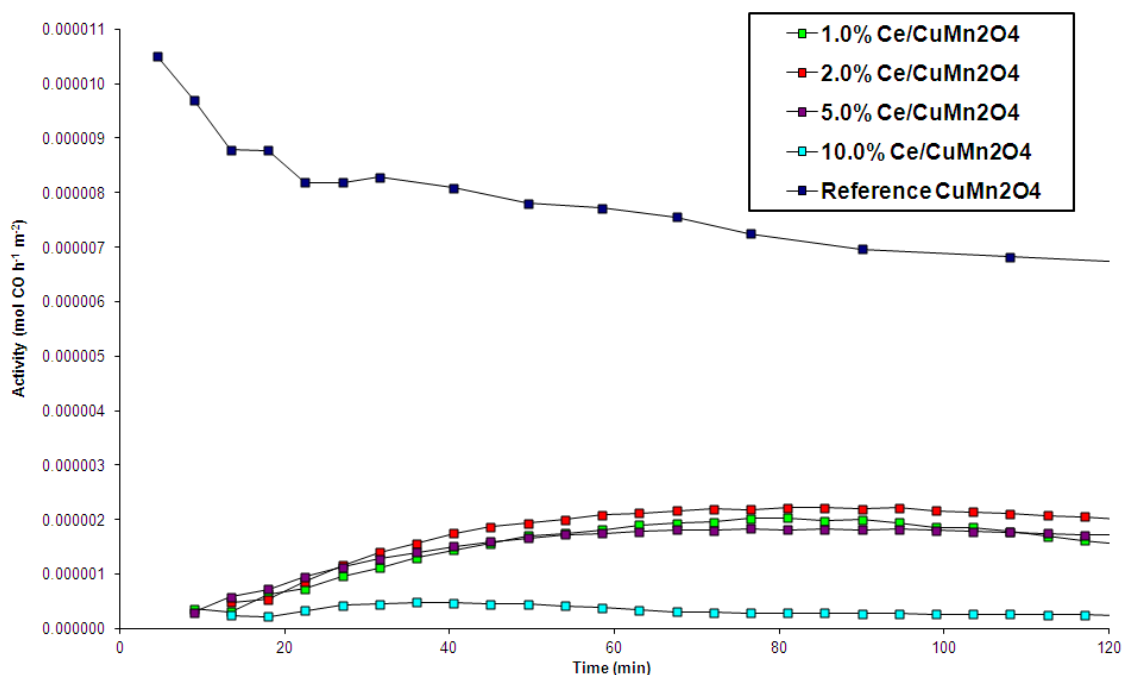


Figure 35 – Surface area normalized activity – Cerium-doped CuMn_2VO_4

When normalized for the effects of surface area, increasing cerium loading is strongly correlated to reduction in activity. This suggests a chemical or structural poisoning effect.

EDX measurement of Cerium loadings in the catalyst indicate that in the case of the 1.0%, 2.0% and 5.0% loaded catalysts, approximately 33% of the reagent loading has been incorporated into the bulk product. As the cerium reagent was cerium nitrate a 100% incorporation was expected. The 10.0% doped catalyst displays similar catalyst loading (within experimental error) to the 5.0% doped catalyst. Comparing the surface area for the 5.0% and 10.0% catalysts, the similar surfaces areas are in correlation with the similar cerium loadings.

3.4.3 Powder X-Ray Diffraction

The powder XRD data of undoped and Ce-doped catalysts (Figure 36) display a slight trend toward a more crystalline structure.

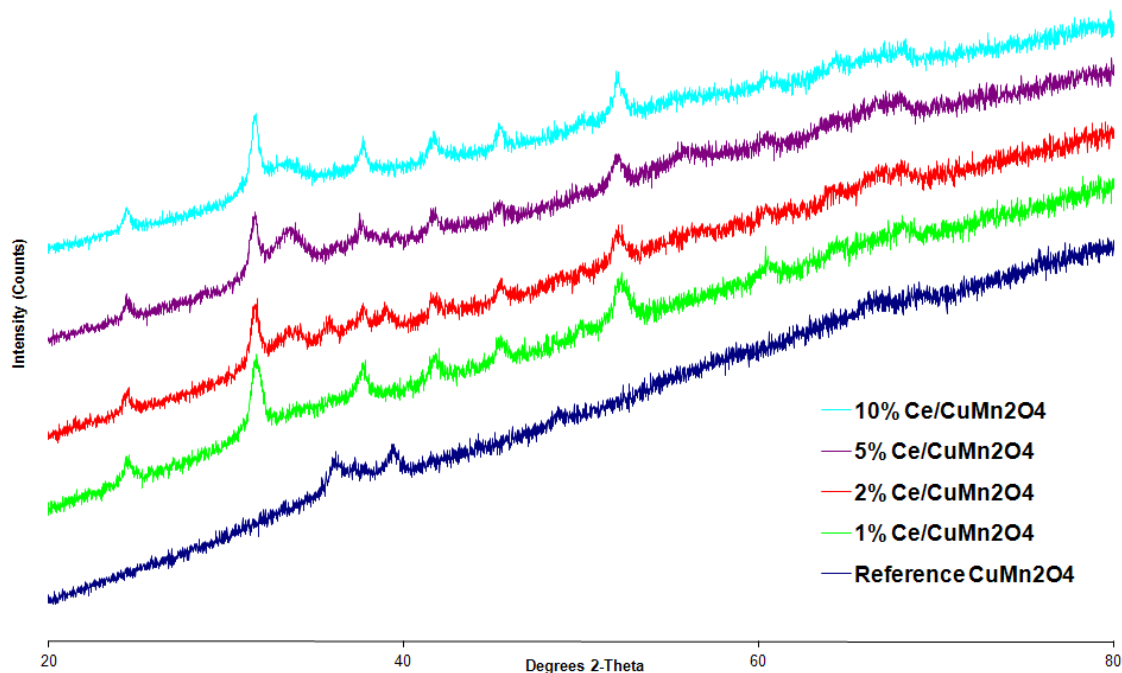


Figure 36 - Powder XRD – Ce doped CuMn_2O_4 catalyst

Cerium doped hopcalite displays broad, poorly defined peaks, which makes phase identification difficult. However, the development of peaks at 2θ ca. 31° , 38° , 42° , 46° and 52° is characteristic of MnCO_3 , which was predicted to be completely oxidized during calcination. The typical double peak characteristic of CuO at 2θ ca. 35.5° and 39° is missing in all but the undoped reference. No evidence of cerium oxide was detected.

3.4.4 SEM Analysis

SEM analysis of 1.0% Cerium-doped CuMn_2O_4 , displayed in Figure 28, shows that particle size has dropped to 4.4 microns, however the powder grains have agglomerated into large clusters, which could explain the drop in surface area.

SEM analysis of 2.0%, 5.0% and 10.0% doped catalysts (Figure 37-40) display rising particle sizes, together with increasing particle agglomeration. Surfaces can be observed with a fractured, highly dispersed coating which could be responsible for the rise in surface area.

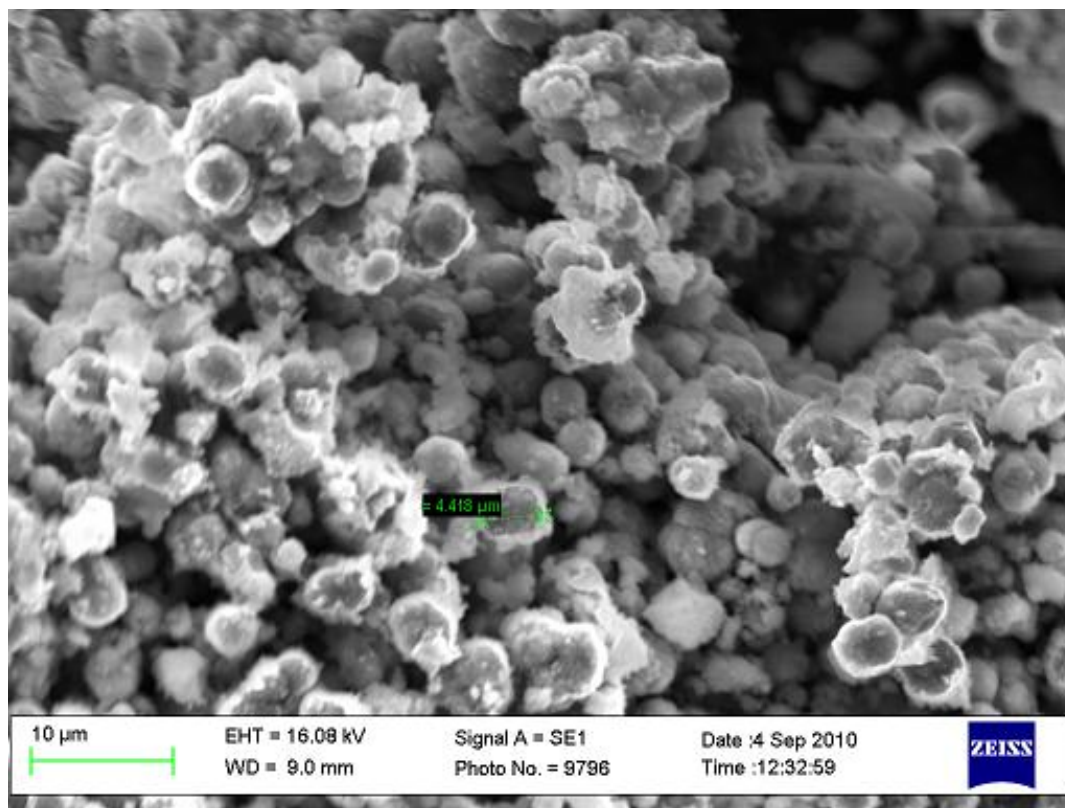


Figure 37 - SEM image of 1% Ce-doped $\text{Cu}_{1-1/2x}\text{Mn}_{2-1/2x}\text{Ce}_x\text{O}_4$

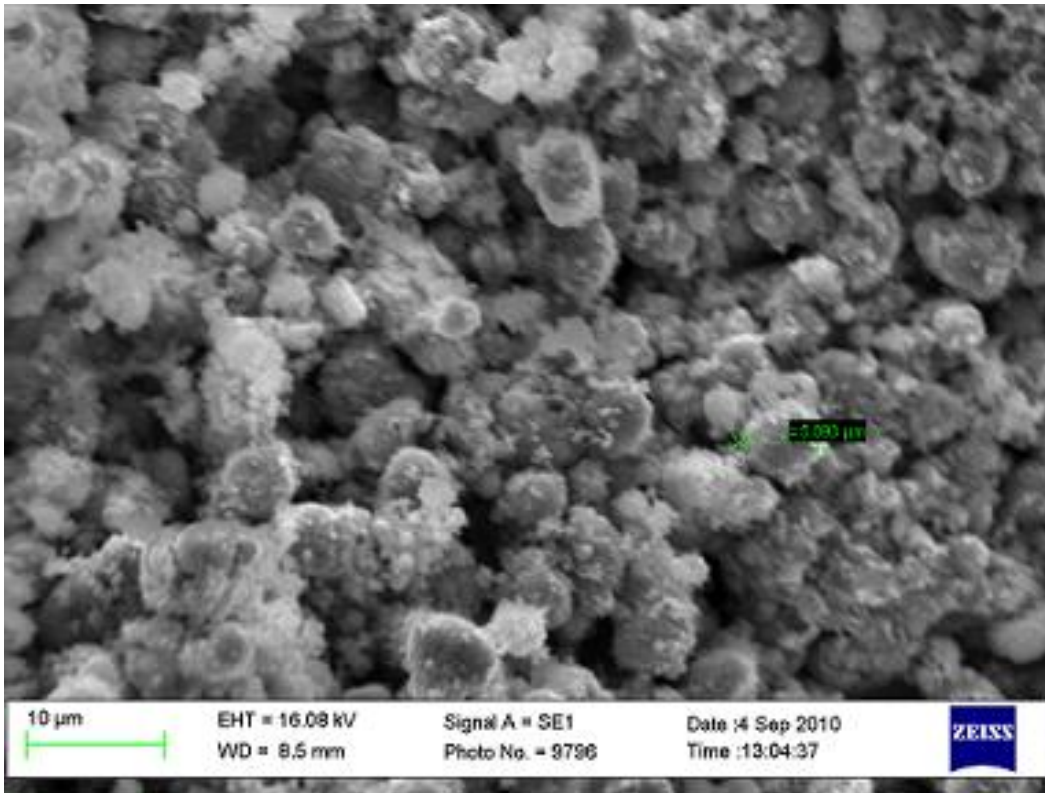


Figure 38 - SEM image of 2% (top right) Ce-doped $\text{Cu}_{1-1/2x}\text{Mn}_{2-1/2x}\text{Ce}_x\text{O}_4$

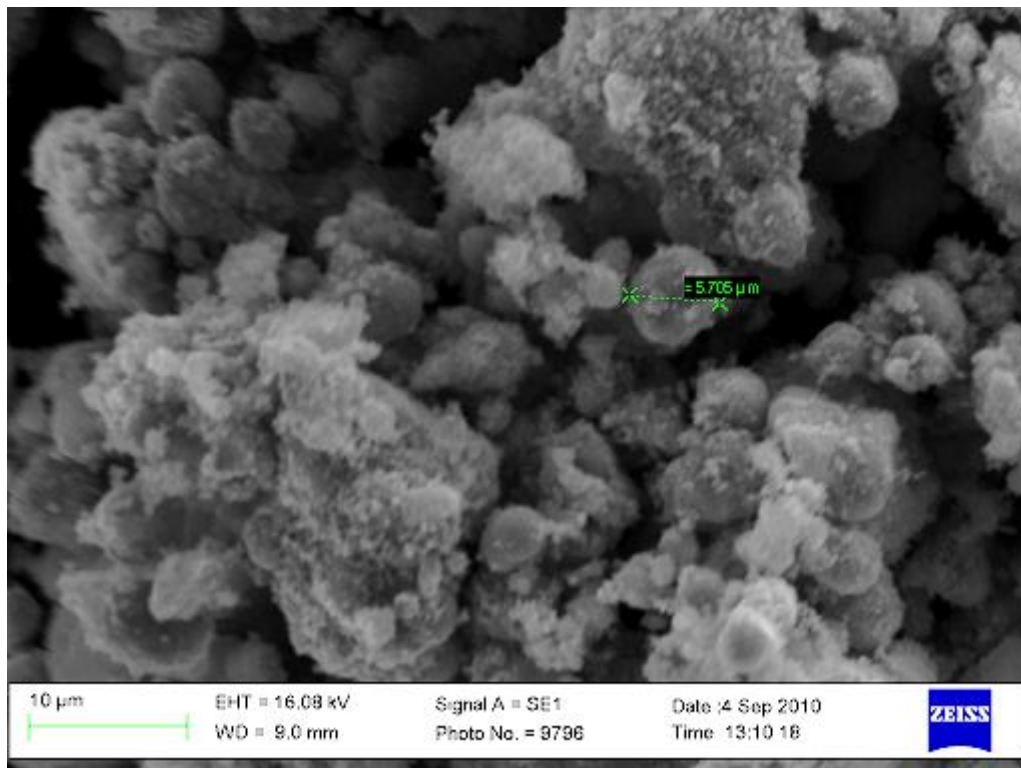


Figure 39 - SEM image of 5% Ce-doped $\text{Cu}_{1-1/2x}\text{Mn}_{2-1/2x}\text{Ce}_x\text{O}_4$

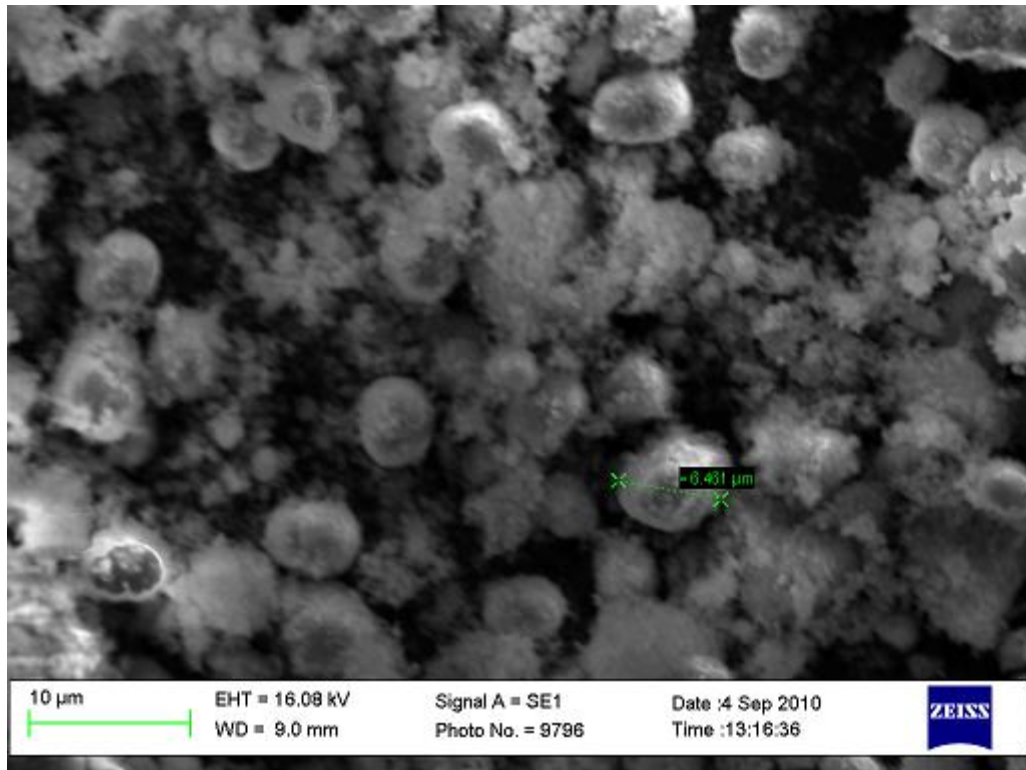


Figure 40 - SEM image of 10% Ce-doped $Cu_{1-1/2x}Mn_{2-1/2x}Ce_xO_4$

3.5 Silicon Doping

Silicon was selected as a doping agent for introduction into a CuMn_2O_4 spinel lattice. The salt $\text{Si}(\text{OCOCH}_3)_4$ was selected under criteria discussed in Chapter 1.

A series of silicon doped catalysts were prepared using co-precipitation methods detailed in Chapter 2. Metals in molar weightings of 1.0%, 2.0% and 5.0% were added to the lattice replacing a molar reduction of copper and manganese in a 1:2 ratio, with the aim of promoting the ambient temperature CO oxidation activity of the catalyst. In all cases the total molar ratio remained at $[\text{Cu} + \text{Si}]$ 1:2 $[\text{Mn} + \text{Si}]$.

3.5.1 CO Oxidation Activity

The activities of the undoped and silicon doped CuMn_2O_4 catalysts are shown in Figure 41.

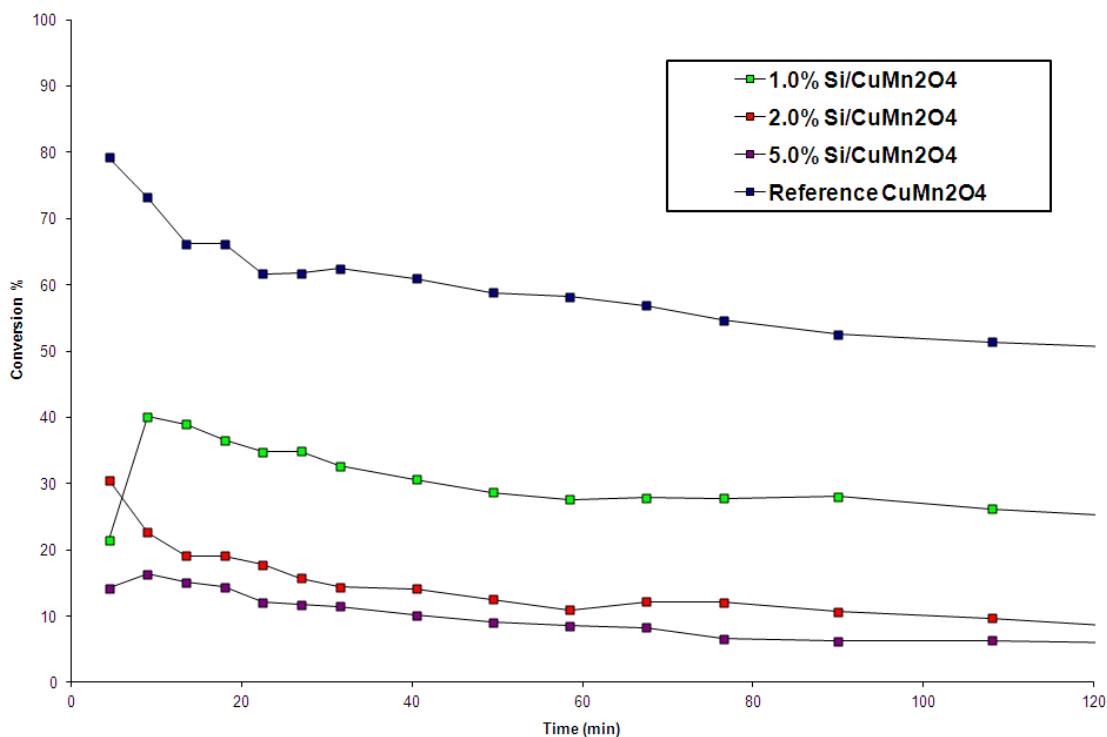


Figure 41 – CO Oxidation – Si Doped CuMn_2O_4 Catalysts

Displayed in Figure 29 is evidence that replacement of copper and manganese by silicon has a negative effect on catalyst activity. Increasing levels of silicon are in correlation with decreasing activity. The 1.0% doped catalyst shows a ~ 50% drop in catalyst activity compared to the unmodified reference. The 2.0% and 5.0% doped catalysts show negligible steady state activity of ~ 8% and ~ 6%.

In terms of catalyst water tolerance, the Si-doped catalysts performed no better under a hydrated gas stream than reference hopcalite. All batches display 0.00% conversion under ~ 4% humidity after 4 minutes. This was the fastest sampling time possible.

3.5.2 EDX Molar Ratio and BET Surface Area

The surface areas of the undoped and silicon-doped catalysts were analyzed by EDX spectroscopy (Table 15).

Sample	EDX Si loading
CuMn_2O_4	0.00%
1%Si/ CuMn_2O_4	0.28%
2%Si/ CuMn_2O_4	2.08%
5%Si/ CuMn_2O_4	4.87%

Table 15 - EDX molar percentages of Si -doped CuMnO_4

Due to EDX limitations, silicon will be expected to register in lower than accurate quantities when analyzed alongside heavier elements such as Cu and Mn. BET surface analysis repeatedly failed due to lack of stable vacuum, no surface area data could be recorded.

3.5.3 Powder X-Ray Diffraction

The powder XRD data of undoped and Si doped catalysts (Figure 42) display a slight trend toward a more crystalline structure.

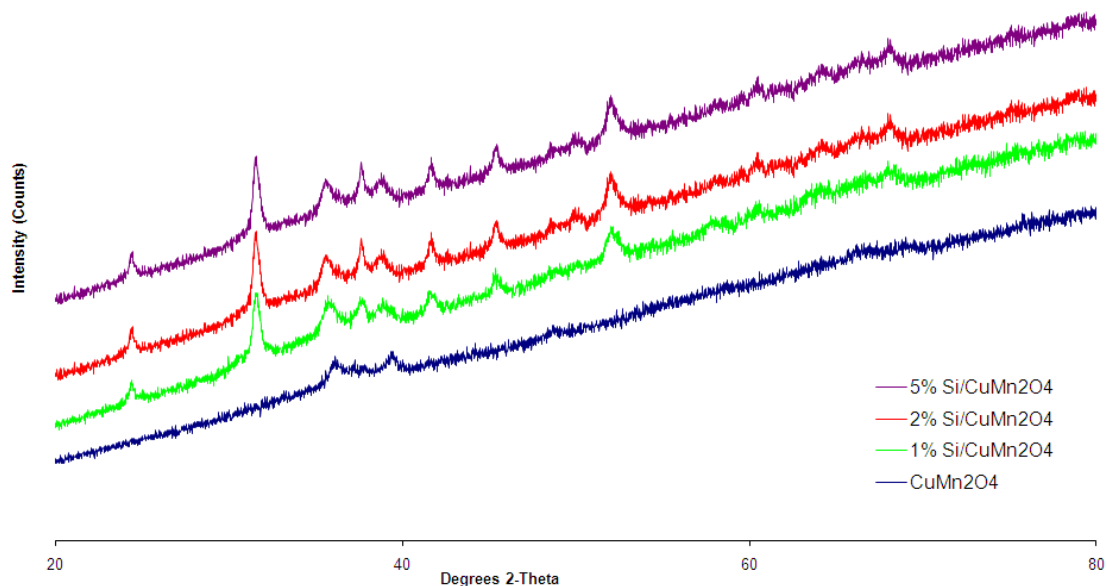


Figure 42 - Powder XRD – Si-doped CuMn_2O_4 catalyst

Silicon doped hopcalite displays broad, low definition peaks, which makes phase identification difficult. However, the development of peaks at 2θ ca. 31° , 38° , 42° , 46° and 52° is characteristic of MnCO_3 , which was predicted to be completely oxidized during calcination. The typical double peak characteristic of CuO at 2θ ca. 35.5° and 39° is present in all samples. Peaks indicating crystalline spinel hopcalite formation at 2θ ca. 30° and 58° are absent. No evidence of silicon oxide or hydroxide compounds was detected.

3.6 Discussion

3.6.1 Vanadium Doping

A series of hopcalite catalysts were prepared with varying amounts of vanadium reagent. Doping metal cations into a hopcalite lattice has been described^{3,4} as capable of catalyst promotion or poisoning depending upon element, weighting, and preparation method. Based on the evidence in this chapter, Vanadium can be described as a catalytic poison when introduced into a hopcalite precipitation. A decrease in hopcalite activity is in correlation with increasing vanadium loading across all three experiments. In addition, no doped catalysts displayed an initial activity peak, which is characteristic of undoped reference hopcalite. This poisoning effect could be attributed to either morphological changes in the hopcalite lattice, or electronic interference in the Cu ↔ Mn redox mechanism.

Considering changes in catalyst morphology, V/CuMn₂O₄ samples display a change in surface area when doped with vanadium. Analysis of pre-synthesis molar Vanadium reagent weightings (Figure 43), and post calcination EDX determined Vanadium molar weightings (Figure 44) is displayed. Although it is difficult to draw any quantitative conclusions from this data the trend is the same in both cases – low levels (1% reagent, or 0.1% EDX) of vanadium promote the surface area of the catalyst. Higher levels (2.0%, 5.0% and 10.0%) gradually reduce this figure.

This effect could be attributed to structural modification of the hopcalite lattice by vanadium. XRD and SEM analysis indicates some structural modification has taken place. XRD data displays increasing vanadium loading correlating with increasing crystalline character. Hopcalite activity has been repeatedly linked to the amorphous spinel and the crystalline spinel character is known to be less active for CO oxidation⁶. SEM microstructure analysis indicated that vanadium doped hopcalite displays a lower particle size than the undoped variety, which could attribute to the higher surface area displayed in the catalyst.

It is also possible that there has been deposition of a separate vanadium complex mixed with the hopcalite. XRD data detected no vanadium compounds, although this technique is unlikely to detect low levels of V compounds. EDX analysis showed the presence of vanadium. It is possible that vanadium based compounds could be blocking active sites upon the hopcalite surface. A separate vanadium species could also register as an increase on the surface area data.

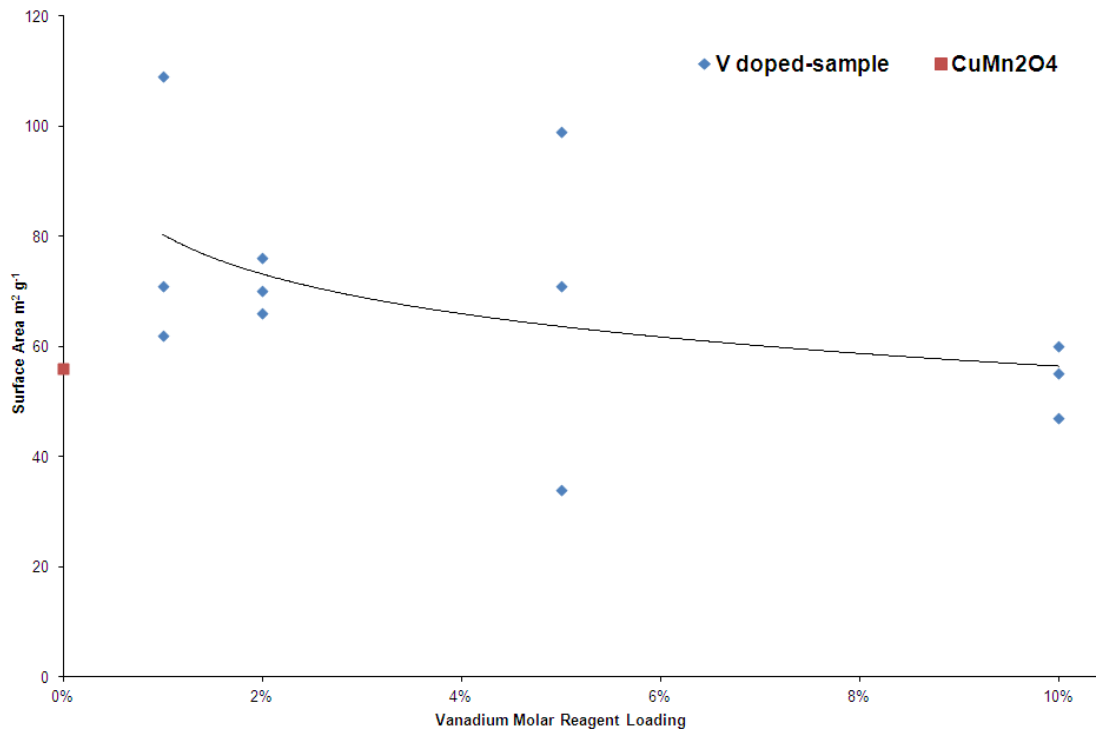


Figure 43 – Reagent Molar Vanadium loadings vs. BET Surface Area trend

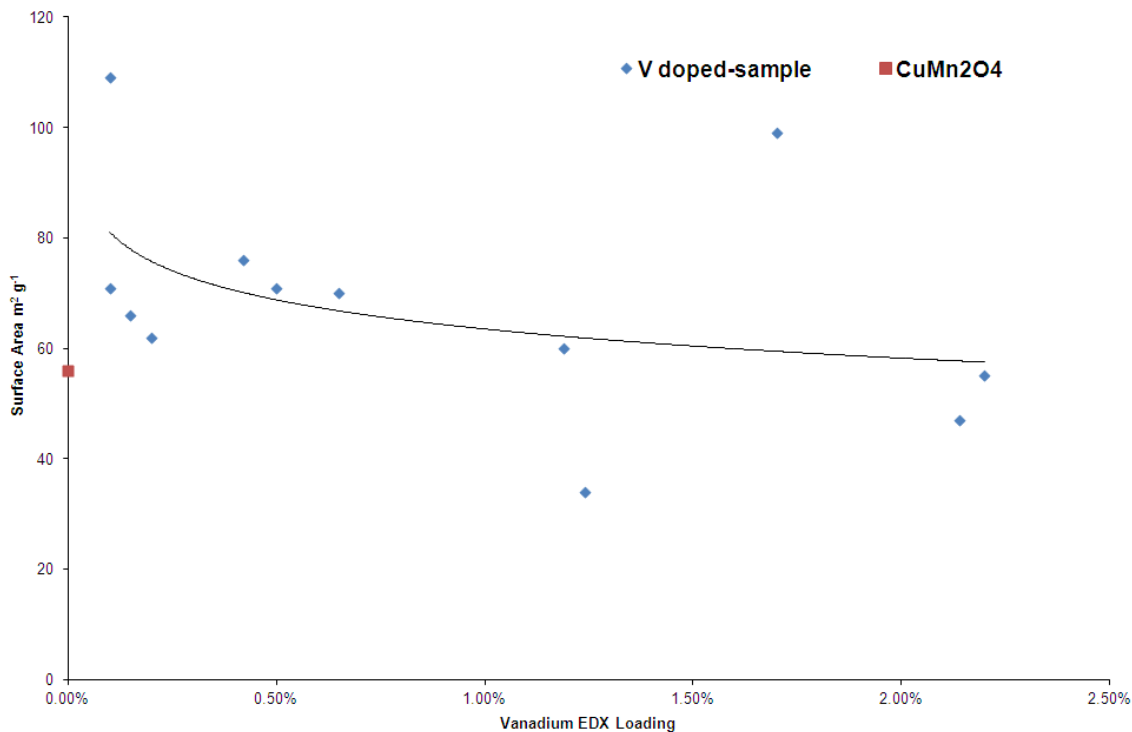


Figure 44 – EDX Molar Vanadium loadings vs. BET Surface Area trend

Any structural promotion of surface area by vanadium is significantly outweighed by the poisoning effect displayed by activity data. Activity drops in correlation with reagent and EDX loading. The drop is more pronounced when the increased surface area of the catalyst is taken into account by SANA analysis. Only the 1% V loaded catalyst, replacing copper, displayed a higher steady-state activity than the undoped hopcalite. In addition, the modified hopcalite displayed no initial activity peak, but does rise slowly in activity whereas the reference hopcalite activity drops with time. It has always been assumed that this drop in reference activity was due to humidity poisoning, as catalysts can be reactivated by drying. The same levels of humidity do not deactivate the modified catalysts. The modified catalyst activity is stable or rising, which could be as the result of surface restructuring (TPR, XPS) or removal of the V-poisoning effect by CO. Whatever the exact poisoning mechanism of vanadium on hoplite, when then humidity levels of the catalyst are low enough to cause an spike in activity, the vanadium poisoning effect is most pronounced. Thus the modified catalysts display no initial activity spike.

Investigations using recalcined V-CuMn₂O₄, TPR or XPS could investigate the surface composition and test this hypothesis.

This was also inferior when relative surface areas were taken into account. The effect of vanadium on a copper manganese redox mechanisms has not been described before. Some investigations into Cu-V and Cu-Mn systems have been studied. Cousin *et al.*⁷ described a positive synergetic effect between copper and vanadium on ceria regarding carbon black oxidation. Palacio *et al.*⁸ has described toluene oxidation over novel copper-vanadium catalysts. He reports that the mixed oxide catalysts display significantly different TRP behavior from the single mixed oxides. Cu reduction temperature was raised, while vanadium was lowered. This indicates that vanadium may be interacting with the Cu ↔ Mn redox mechanism in hopcalite. Kim *et al.*⁹ reported on vanadium-impregnated manganese oxides for NH₃ oxidation. He discovered that at low temperatures, vanadium blocks lewis acid sites on the manganese surface reducing activity. This effect could explain the reduction in hopcalite activity.

In addition, vanadium was introduced into the lattice via reagent VOSO₄. This adds another variable to the experiment - the presence of sulfur in the reaction vessel, which was not present in previous nitrate-doped synthesis. Hopcalite has previously been described as sulfur intolerant¹⁰. However, sulfur does not register in EDX analysis of the final catalyst – it could have been reduced to undetectable levels by washing.

Negative effects of transition metal doping are not unprecedented. Fierro *et al.*¹¹ has described negative effects upon transition metal doped zinc manganese spinels, who reports differing effects on lattice structure depending upon the nature of the element. Reduction was inhibited by iron in some extent, almost unchanged by cobalt and markedly enhanced by copper.

3.6.2 Cerium Doping

A series of hopcalite catalysts were prepared with varying amounts of cerium present. The CO oxidation activity data displays a clear correlation between increasing cerium loadings and loss in activity. The Ce-doped catalysts also display no initial activity spike. This is similar to the data for the V-doped catalysts discussed in 3.6.1.

Surface area data, recorded by BET, illustrates an increase in catalyst surface area with increasing cerium loading. This suggests cerium to be a structural promoter; however, SEM microstructure analysis reveals that increasing cerium loading correlates to the catalyst particles becoming increasingly agglomerated. This would significantly lower the surface area of the catalyst. SEM also notes the formation of a fractured, highly dispersed coating on the particles. There are two candidates for the identity of this compound. The first of these is a cerium compound such as oxide, carbonate or hydroxide, introduced into the lattice as a reagent. No evidence of any isolated cerium-based compound was detected with XRD, although EDX analysis did display the presence of cerium. The compound state of the element, however, was unknown. The second candidate is manganese carbonate. XRD analysis reveals that increasing cerium loadings correlates to the appearance of a series of bands identified as MnCO_3 . This compound is known as the catalyst precursor following the work of Porta¹², which according to experimental theory and research¹³ would have been completely oxidized by the calcination process at 410°C. It could be postulated that cerium loadings have had the effect of changing the calcination behavior of the catalyst. Manganese carbonate will decompose to MnO at 200°C. This study indicates that this process could have been retarded by the presence of Ce. Imamura *et al*¹⁴. described an investigation into the effect of cerium on manganese oxide at a range of temperatures. He reports that at temperatures below 700K, cerium provides oxygen to manganese. This spillover is reversed at higher temperatures. It could be possible that cerium is causing the formation of manganese oxides to be energetically unfavorable at the optimum hopcalite calcination conditions. In another scenario, cerium carbonates or hydroxides, on the surface of Cu-Mn clusters, are causing a lack of atmospheric oxygen flow to manganese carbonate inhibiting calcinations.

Using EDX data to confirm the presence of carbon (and thus MnCO_3) in the catalyst is not possible. It is possible that the rise in surface area is predominately due to this unidentified species. Given this unresolved identity of the fractured coating observed by SEM, BET surface area data cannot be used to infer the active surface area of CuMn_2O_4 .

The XRD data indicates that increasing Ce loadings do not correlate to increasing crystalline character. If peaks corresponding to MnCO_3 are ignored, the XRD pattern for Ce loaded sample is largely amorphous. The activity decrease cannot be linked to increasing crystalline character of the catalyst.

Manganese-Cerium catalysts were prepared by Arena *et al.*¹⁵. He described Mn-Ce catalysts as exhibiting redox characteristics for CO oxidation between 323-423 K. Imamura *et al.*¹⁴ described an investigation into the effect of cerium on manganese oxide at a range of temperatures. He reports that at low temperatures (< 700K) cerium provides oxygen to manganese. Luo *et al.*¹⁶ reported that copper supported on cerium oxide exhibits high CO conversion activity at 70°C. His TPR studies indicate that CuO/CeO_2 can adsorb CO, whereas singular CuO and CeO_2 cannot. These three studies suggest it is possible that Ce is capable of participating in the $\text{Cu} \leftrightarrow \text{Mn}$ redox reaction.

Despite the unresolved issue surrounding the precise effects of cerium on a CuMn_2O_4 lattice, unambiguous ambient temperature activity data has shown the overall effect of introducing the Ce ion into the co-precipitation procedure to be negative. Although the literature suggests that Ce promotes the activity of single phase copper and manganese oxides, Ce appears to be a poison in regard to CuMn_2O_4 .

3.6.3 Silicon Doping

A series of hopcalite catalysts were prepared with varying amounts of silicon present. Doping metal cations into a hopcalite lattice has been described^{3,4} as capable of catalyst promotion or poisoning depending upon element, weighting, and preparation method.

The results indicate that silicon can be described as a catalytic poison for ambient temperature CO oxidation. A correlation between Si doping levels and a reduction in catalyst activity is evident. XRD diffraction patterns indicate that catalyst precursors (MnCO_3 and CuO) remain in the calcined catalyst bulk. As they are inactive for this reaction, this could contribute to this activity loss.

BET surface area data could not be obtained, and as such normalization of activity cannot be calculated. Similar studies have been attempted. Zheng¹⁷ *et al.* have described copper-manganese-silicon catalysts, with the silicon levels affecting BET surface area, acidity and copper dispersion. The addition of manganese as the third component to the Cu–Si co-precipitated catalyst can increase the catalytic performance for synthesis of cyclohexanone and 2-methylfuran. Zheng found that increasing silicon loading corresponded to rising surface area.

EDX analysis displays the presence of silicon in the catalyst, although in low loadings. No silicon compounds were detected by XRD analysis. SEM microstructure analysis shows that the average particle diameter of Si doped hopcalite is approximately half that of undoped hopcalite. These particles have agglomerated into a single mass and display a fractured, highly dispersed coating not present in the undoped sample. This could be a remnant of the catalyst precursor. Similar phenomena have been displayed in cerium doped catalysts. This is in concordance with the XRD pattern, which shows separate phase MnCO_3 and CuO .

In regard to catalyst water tolerance, the silicon doped hopcalite displayed no increase in water resistance when compared to the undoped sample. It had been postulated that SiO_2 in the catalyst would act as a sacrificial agent, preferentially adsorbing water in the feed gas and protecting CuMn_2O_4 active sites from water poisoning. Such a phenomenon has been reported by Jones⁴ in regard to Ni doped CuMn_2O_4 . This effect was not observed for Si-doped CuMn_2O_4 . The Si could be having a small effect on catalyst water resistance;

however the minimum test conditions (4% humidity for 4 min) were humid enough to reduce the activity of both catalysts to zero.

3.7 Conclusions

Vanadium could be considered a structural promoter of CuMn_2O_4 at low loadings ($< 1\%$), causing increasing surface area and reduced particle size. However, any gains in catalyst activity are outweighed by an electronic poisoning effect on the CuMn_2O_4 lattice which is present in all tested samples.

Cerium is in all regards a catalyst poison when doped into CuMn_2O_4 . In an unknown mechanism, Ce interferes with the calcinations of hopcalite precursor, resulting in the presence of manganese carbonate in the final catalyst. It is also likely that Ce interferes with the Cu-Mn redox system, reducing activity.

Silicon is a catalytic poison in regards to ambient temperature CO oxidation by hopcalite. In an unknown mechanism, Si interferes with the calcinations of hopcalite precursor, resulting in the presence on manganese carbonate and copper oxide in the final catalyst. Si did not affect the water tolerance of the catalyst in a measureable manner.

3.8 Chapter 3 References

1. G. J. Hutchings, A. A. Mirzaei, R. W. Joyner, M. R. H. Siddiqui and S. H. Taylor, *Applied Catalysis a-General*, 1998, **166**, 143-152.
2. A. A. Mirzaei, H. R. Shaterian, M. Habibi, G. J. Hutchings and S. H. Taylor, *Applied Catalysis a-General*, 2003, **253**, 499-508.
3. K. J. Cole, Cardiff University, 2008.
4. C. D. Jones, Cardiff University, 2006.
5. D. L. Cocke and S. Veprek, *Solid State Communications*, 1986, **57**, 745-748.
6. S. Veprek, D. L. Cocke, S. Kehl and H. R. Oswald, *Journal of Catalysis*, 1986, **100**, 250-263.
7. R. Cousin, S. Capelle, E. Abi-Aad, D. Courcot and A. Aboukais, *Applied Catalysis B-Environmental*, 2007, **70**, 247-253.
8. L. A. Palacio, J. M. Silva, F. R. Ribeiro and M. F. Ribeiro, *Catalysis Today*, 2008, **133**, 502-508.
9. S. S. Kim, S. M. Lee, K. H. Park, D. W. Kwon and S. C. Hong, *Journal of the Air & Waste Management Association*, 2011, **61**, 552-558.
10. C. H. Bartholomew, P. K. Agrawal and J. R. Katzer, *Advances in Catalysis*, 1982, **31**, 135-242.
11. G. Fierro, G. Ferraris, R. Dragone, M. Lo Jacono and M. Faticanti, *Catalysis Today*, 2006, **116**, 38-49.
12. P. Porta, G. Moretti, M. Musicanti and A. Nardella, *Solid State Ionics*, 1993, **63-5**, 257-267.
13. J. W. Mellor, *A Comprehensive Treatise on Inorganic and Theoretical Chemistry*, Longmans, Green & Co., 1932.
14. S. Imamura, M. Shono, N. Okamoto, A. Hamada and S. Ishida, *Applied Catalysis a-General*, 1996, **142**, 279-288.
15. F. Arena, G. Trunfio, B. Fazio, J. Negro and L. Spadaro, *Journal of Physical Chemistry C*, 2009, **113**, 2822-2829.
16. M. F. Luo, Y. J. Zhong, X. X. Yuan and X. M. Zheng, *Applied Catalysis a-General*, 1997, **162**, 121-131.
17. H. Y. Zheng, Y. L. Zhu, L. Huang, Z. Y. Zeng, H. J. Wan and Y. W. Li, *Catalysis Communications*, 2008, **9**, 342-348.

4

Noble Metal Modified Hopcalite

In this chapter investigations are made into modification of hopcalite with noble metals. Hopcalite spinel lattice is modified through doping, impregnation and deposition with precious metal ions.

Jones *et al.*¹ and Cole *et al.*² have reported that modifying, or ‘doping’, a CuMn_2O_4 hopcalite catalyst with quantities of metal cations (Co^{3+} , Ni^{2+} , Fe^{3+} , Ag^+ , and Zn^{2+}) can improve activity toward CO oxidation. Using the selection criteria discussed in Chapter 1; based on ion size, oxidation states, ionization energy, and the availability of salt precursors; palladium was selected as a candidate for hopcalite promotion. As non-noble metals, vanadium, cerium and silicon are discussed in more detail in Chapter 3.

The effect of Pt and Pd particles on CuMn_2O_4 support has not been previously reported. Ferrandon *et al.*^{3, 4} have reported that Pt and Pd doped onto single phase CuO and Mn_2O_3 oxides are of interest for ambient temperature CO oxidation. In this chapter, CuMn_2O_4 is used as a catalytic support. Firstly, palladium nitrate is impregnated onto calcined CuMn_2O_4 support via incipient wetness synthesis. Secondly, platinum and palladium chlorides are added to calcined CuMn_2O_4 via pH controlled deposition precipitation.

4.1 Palladium Doping

Palladium was selected as a doping agent for introduction into a CuMn_2O_4 spinel lattice. The salt $\text{Pd}(\text{NO}_3)_2$ was selected under criteria discussed in Chapter 1. A series of palladium doped catalysts were prepared using standard co-precipitation methods detailed in Chapter 2. Metals in molar weightings of 1.0%, 2.0% and 5.0% were added to the lattice replacing a molar reduction of copper and manganese in a 1:2 ratio, with the aim of promoting the ambient temperature CO oxidation activity of the catalyst. In all cases the total molar ratio remained at $[\text{Cu} + \text{Pd}] 1:2 [\text{Mn} + \text{Pd}]$.

4.1.1 CO Oxidation Activity

The activities of the undoped and palladium doped CuMn_2O_4 catalysts are shown in Figure 45. Displayed is the evidence that replacement of the copper and manganese by palladium has a positive effect on catalyst activity.

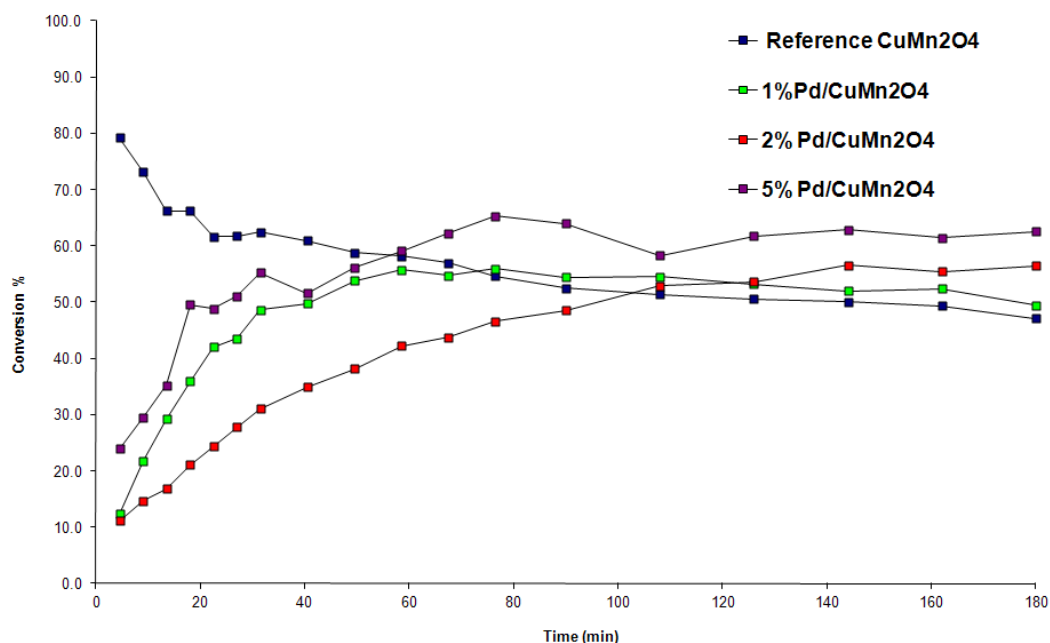


Figure 45 – CO Oxidation – Pd Doped CuMn_2O_4 Catalysts

The undoped reference, displaying a steady state conversion of $\sim 47\%$, shows equivalent steady state activity to the 1.0% doped catalyst, at $\sim 49\%$. The undoped reference displays an initial activity spike for the first 90 min of testing. The 2.0% and 5.00% doped catalysts show higher final activity than the undoped reference, at \sim

56% and ~ 63% respectively. Both are also rising at the end of the experiment. In a similar fashion to the 1.0% doped catalyst, they display no initial activity spike.

4.1.2 BET Surface Area, SANA and EDX Molar Ratio

The surface areas of the undoped and palladium doped catalysts were analyzed by BET method and are displayed in Table 16. In addition, also displayed is the molar palladium content of the samples, analyzed by EDX spectroscopy.

Sample	Surface Area ($\text{m}^2 \text{g}^{-1}$)	C value	EDX Cu:Mn ratio	EDX Pd loading
CuMn_2O_4	56	108	1 : 1.48	0%
1.0%Pd/ CuMn_2O_4	99	16	1 : 1.70	0.91%
2.0%Pd/ CuMn_2O_4	97	49	1 : 1.69	1.90%
5.0%Pd/ CuMn_2O_4	113	96	1 : 1.78	4.45%

Table 16 - BET surface areas and EDX molar percentages of Pd doped CuMnO_4

The BET data displayed suggests that palladium has a promotional effect upon catalyst surface area. The 1.0% and 2.0% doped catalysts display an ~ 71% increase in catalyst surface area, whilst the 5.0% doped catalyst is further increased with a surface area ~200% of the value of the undoped reference.

Using catalyst surface area, normalized activity data is displayed in Figure 46. It is demonstrated that all three Pd-doped catalysts display equivalent normalised activity levels regardless of catalyst loading. The undoped reference displays an activity of ~52% higher per m^2 than the doped samples.

The Pd loadings of the catalyst were analyzed by EDX spectroscopy. Approximately 90% of the Pd reagent was detected in all three samples. It can be assumed that the majority of the Pd reagent has been incorporated into the catalyst.

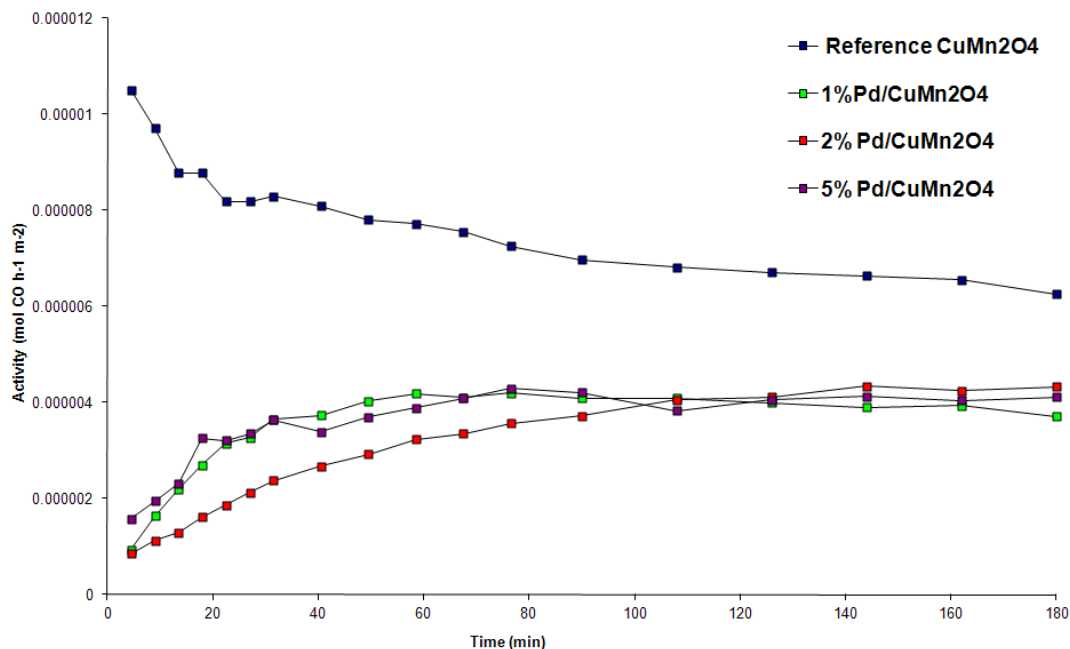


Figure 46 – Surface area normalized activity – Palladium-doped CuMn_2O_4

4.1.3 Powder X-Ray Diffraction

The XRD diffraction patterns for $\text{Pd/CuMn}_2\text{O}_4$ are displayed in Figure 47. Undoped hopcalite displays some residual XRD patterns. These can be attributed to the formation of crystalline CuMn_2O_4 spinel at 2θ ca. 30.5° , 37.5° , 41.5° and 52° , and/or segregated copper oxide within the lattice (2θ ca. 35.5° , 39°). These peaks can be clearly distinguished in a largely amorphous CuMn_2O_4 diffraction pattern.

In correlation with increased Pd doping, all XRD bands across the spectrum are reduced. Two diffraction peaks remain. The peak at 2θ ca. 35° is extremely broad and may be a combination of two or more signals, likely candidates being CuO at 2θ 35.5° and 39° , and/or PdO at 33.5° . The peak at 2θ ca. 44.5° is present in all samples, and does not reduce with increasing Pd loading. This peak remains unassigned. Overall, the catalyst gains a more amorphous configuration with increasing Pd doping levels.

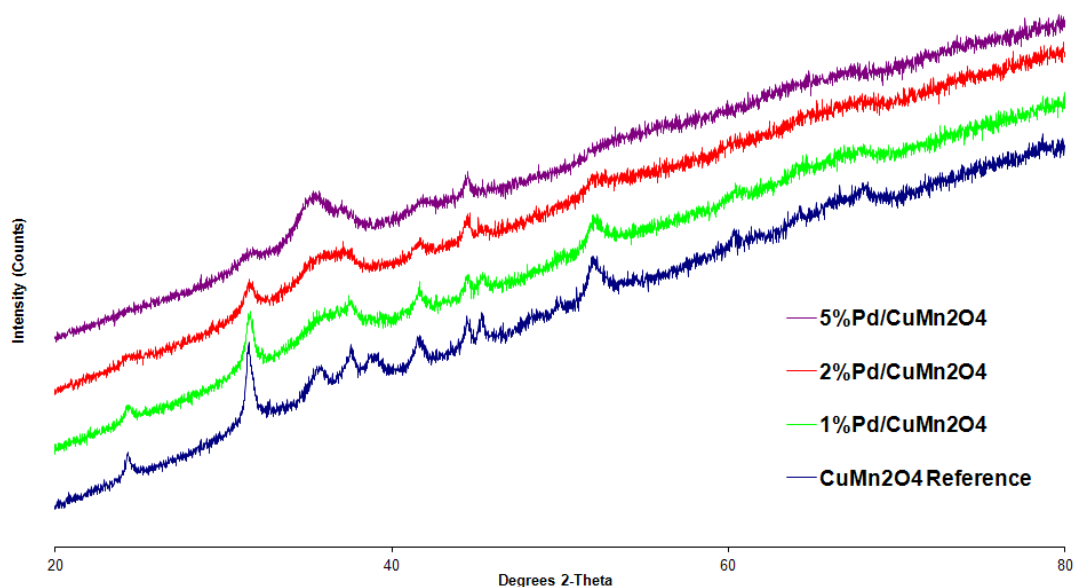


Figure 47 - Powder XRD – Pd doped CuMn_2O_4 catalyst

4.1.4 SEM Analysis

The SEM analysis of undoped CuMn_2O_4 has been described previously. Powder particles with a spherical morphology, with an approximate average particle diameter of 7.52 microns, were characterized.

The SEM analysis of Pd-doped CuMn_2O_4 is displayed in Figures 48, 49 and 50, and summarised in Table 17. Pd doped CuMn_2O_4 displays a reduction in average particle size correlating with increase in Pd loading. This could be postulated as an origin of the rising surface area in the catalyst.

Catalyst Pd Loading	Average Particle Size(μm)
0%	7.52
1%	4.62
2%	4.47
5%	3.50

Table 17 - Average particle size of Pd-doped CuMn_2O_4

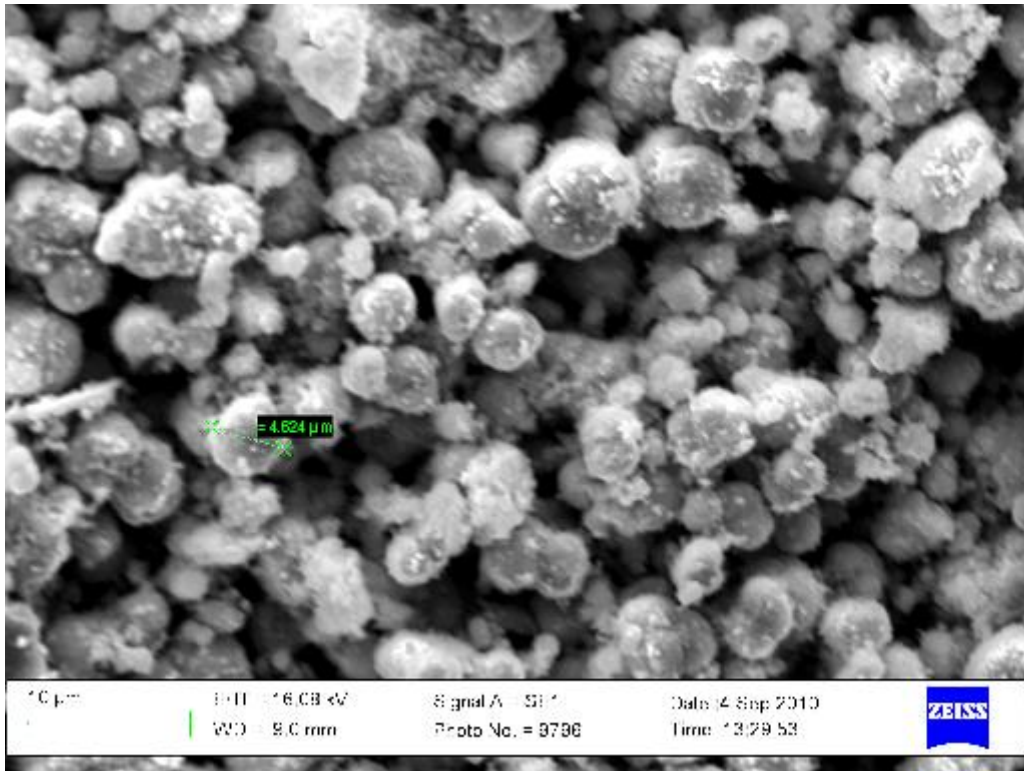


Figure 48 - SEM image of 1% Pd doped CuMn_2O_4

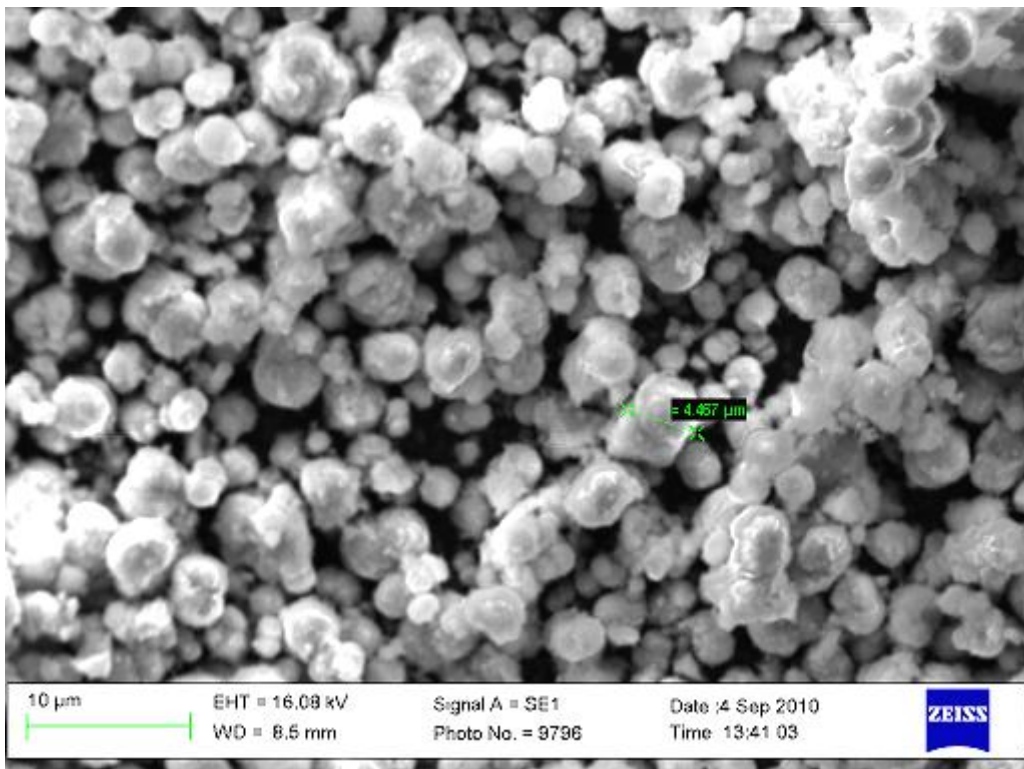


Figure 49 - SEM image of 2% Pd-doped CuMn_2O_4

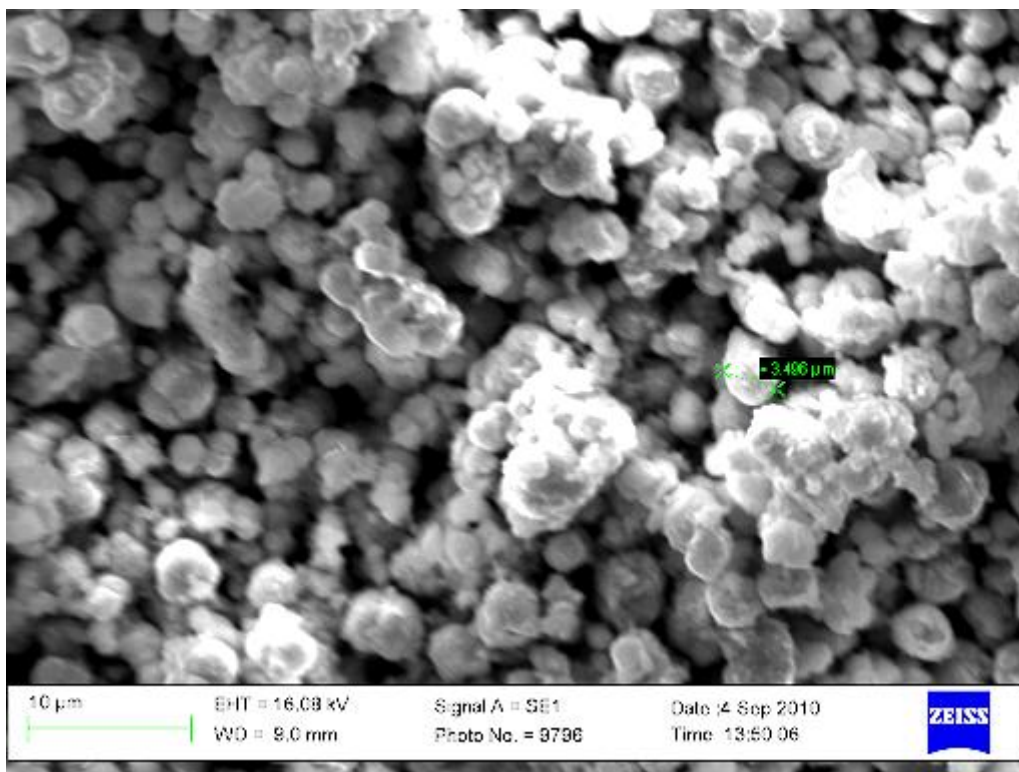


Figure 50 - SEM image of 5% Pd - doped CuMn₂O₄

4.2 Palladium Impregnation

Palladium impregnated onto the surface of a CuMn_2O_4 spinel lattice was selected as of potential interest for ambient temperature CO oxidation. The salt $\text{Pd}(\text{NO}_3)_{2(\text{aq})}$ was selected as a reagent under criteria discussed in Chapter 2. Palladium in relative mass weightings of 0.25%, 0.5% and 1.0% were added to batches of CuMn_2O_4 powder via a wet impregnation method. The preparation method is discussed in more detail in Chapter 2. These catalysts were characterized and tested for CO oxidation activity.

In this experiment, a single batch of coprecipitated hopcalite was split into five 1.0g samples. The unmodified hopcalite support is referred to as ‘ancestor hopcalite support’. Hopcalite which has been subjected to wet impregnation conditions without the addition of Pd nitrate (HNO_3 was substituted in the same concentration as the 1.0% PdNO_3 IW procedure) is referred to as ‘reference hopcalite support’.

4.2.1 Catalyst Reduction

Unmodified hopcalite support was subjected to reductive conditions. This was a reference experiment to investigate the possibility of reducing impregnated surface precious metal particles on hopcalite. Reduction under aqueous $\text{NaCOOH}_{(\text{aq})}$ was attempted. The experiment is detailed in Chapter 2. The resulting hopcalite was completely deactivated. This is in concordance with the work of Mirazei⁵, who described sodium as a catalytic poison for CuMn_2O_4 .

In another experiment, reduction under $\text{H}_{2(\text{g})}$ was attempted. The method is detailed in more detail in Chapter 2. At 100°C, the hopcalite support exhibited no mass loss and no deactivation. Calcination at higher temperatures (120°C, 150°C and 500°C) resulted in loss of support mass (measured by TGA) and loss in activity. It was concluded that 100°C was the most reductive conditions that could be applied to the support. All impregnated catalysts (0.25%, 0.5% and 1.0% Pd) were subjected to reduction at 100°C for 1 hour under 5% H_2 in Ar. In all cases the Pd-impregnated catalysts did not change in activity or morphology measured by any technique. Beyond the variation expected by experimental error; activity, BET surface area,

EDX molar percentages, XRD and SEM were identical to that of the unreduced samples. To avoid unnecessary repetition, these results are not reported. It could be postulated that the catalysts were pre-reduced by atmospheric conditions, or the reduction was not powerful enough to reduce the noble metals.

4.2.2 CO Oxidation Activity

The activities of the ancestor, reference and palladium-impregnated CuMn_2O_4 catalysts are shown in Figure 51. The evidence is displayed that Pd impregnation has a positive effect on catalyst activity.

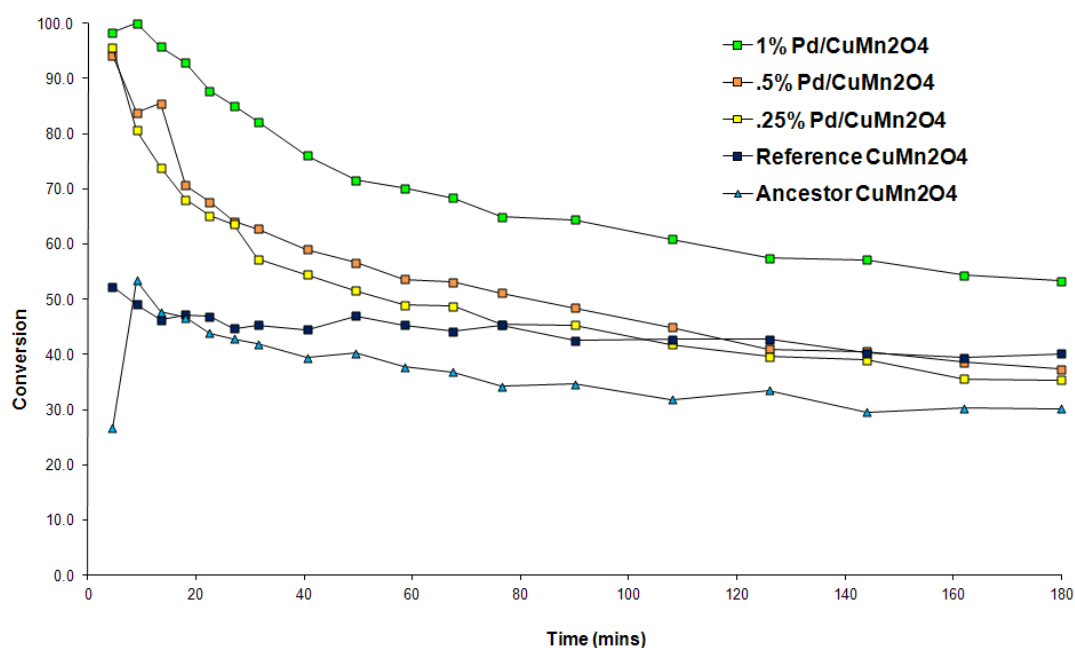


Figure 51 – CO Oxidation – Pd-impregnated CuMn_2O_4

The reference catalyst support displays no initial activity spike and a steady state activity of ~40%. Ancestor hopcalite is less active than the reference sample, displaying equivalent initial activity, a more pronounced deactivation and a steady state activity of ~30%. The three Pd catalysts all display an initial activity approaching 100%. The 0.25% and 0.5% weight impregnated catalysts then deactivate until they are equivalent in activity to the reference catalyst at steady state. The 1.0% doped catalyst also displays a 100% initial activity and displays a higher steady state activity of ~53%. The catalysts were tested against gas stream containing

4% humidity, and displayed 0% conversion at 4 min, the shortest testing time possible (no data to display).

4.2.3 BET Surface Area, SANA and EDX Molar Ratio

The surface areas of the non-impregnated and palladium-impregnated catalysts were analyzed by BET technique and are displayed in Table 18. In addition, displayed is the relative mass loading palladium content of the samples, analyzed by EDX spectroscopy.

Sample	Surface Area (m ² g ⁻¹)	C value	EDX Pd Loadings
1.0%Pd/CuMn ₂ O ₄	58	44	0.95%
0.5%Pd/CuMn ₂ O ₄	63	118	0.48%
0.25%Pd/CuMn ₂ O ₄	61	32	0.22%
CuMn ₂ O ₄ (Reference)	61	58	0.00%
CuMn ₂ O ₄ (Ancestor)	50	67	0.00%

Table 18 - BET surface areas and EDX molar percentages of Pd-impregnated CuMn₂O₄

The three catalysts subjected to the IW procedure display a surface area ~20% higher than the ancestor sample. The reference catalyst also shows a ~20% rise in surface area. This would suggest that the rise is not a result of interaction with the Pd ion.

The surface normalised activities of the catalysts batches is displayed in Figure 52. When ± 8% experimental error is applied, the 0.25%, 0.5%, reference and ancestor samples all show equivalent normalized activity at steady state. The ancestor hopcalite shows slightly higher initial activity for the first 50 min. The 0.25% and 0.5% doped samples show much improved initial activity for 80 min. The 1.0% doped catalyst shows the highest initial and steady state normalized activity, outperforming all others by 60% at steady state.

The Pd loadings of the catalyst were analyzed by EDX spectroscopy. Approximately 91-95% of the Pd reagent was detected in all three samples. It can be assumed that the majority of the Pd atoms have been incorporated into the catalyst.

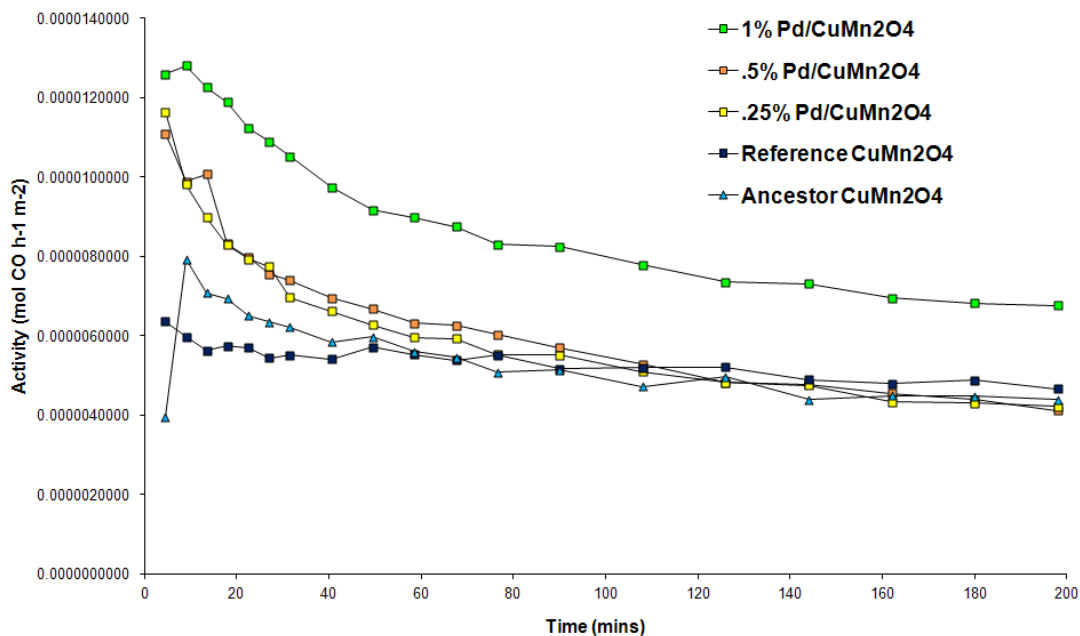


Figure 52 – Surface area normalized activity – Pd-impregnated CuMn₂O₄

4.2.4 Powder X-Ray Diffraction

The XRD diffraction patterns for Pd impregnated onto CuMn₂O₄ are displayed in Figure 53. The reference, ancestor and impregnated samples display extremely similar XRD patterns – amorphous, with wide, ill-defined peaks. These correspond to single phase CuO (characteristic double peak at 2θ ca. 35°, 39°), Mn₂O₃ (2θ ca. 32°, 56° and 66°) and crystalline spinel Cu_{1.5}Mn_{1.5}O₄ (2θ ca. 30°, 58°, 63°). No pattern corresponding to palladium oxide or metallic palladium is displayed, though this is anticipated given the low loadings. The lack of change across the XRD patterns of the samples indicate that the bulk structure of the CuMn₂O₄ has not been affected by the IW procedure.

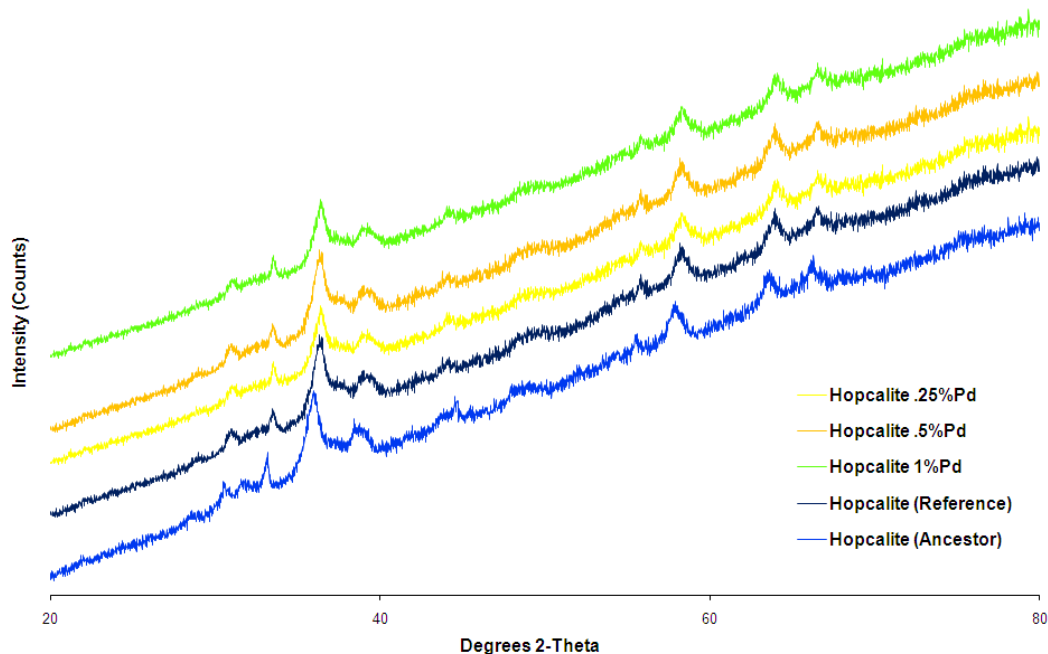


Figure 53 - Powder XRD – Pd-impregnated CuMn_2O_4

4.2.5 SEM analysis

The microstructure SEM analysis of the catalyst batches is displayed in Figures 54 to 57. In all cases, the average particle size measured for each Pd-treated batch is equivalent to the average of the undoped reference (displayed in Table 19). The ancestor sample displays a slightly higher average particle size. Backscatter analysis of the samples did not display the evidence of any atoms with disproportionately high relative atomic mass atoms on the visible surface.

Catalyst Pd Loading	Average Particle Size(μm)
0% (Ancestor)	7.50
0% (Reference)	6.74
0.25%	6.33
0.50%	6.59
1%	6.48

Table 19 – Average particle size of Pd-impregnated CuMn_2O_4

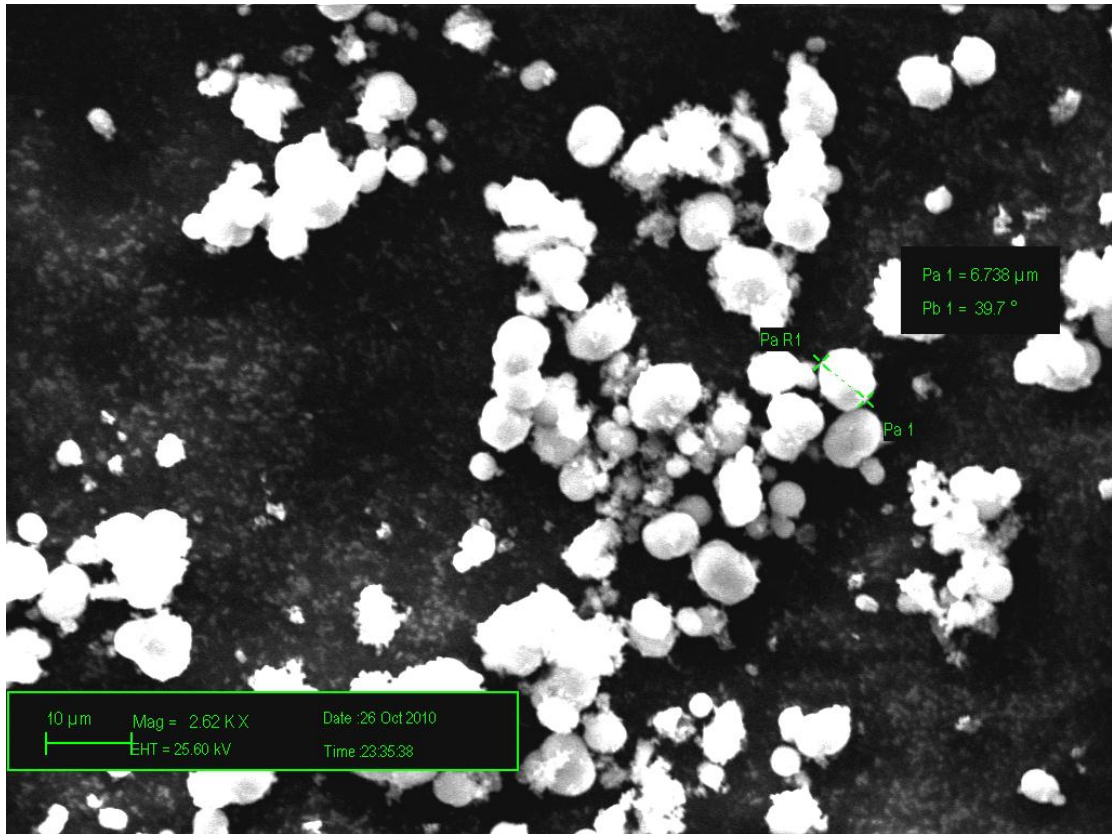


Figure 54 - SEM image of Pd impregnated on CuMn_2O_4 : undoped reference

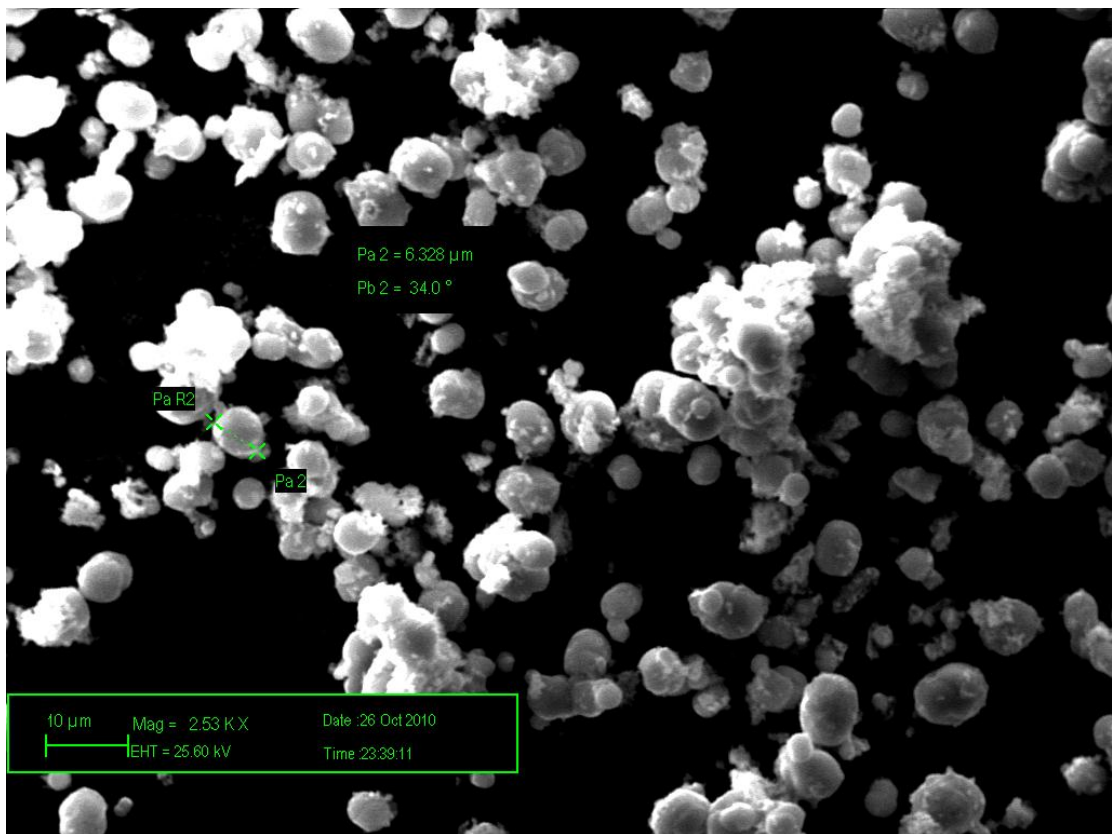


Figure 55 - SEM image of Pd impregnated on CuMn_2O_4 : .25% Pd

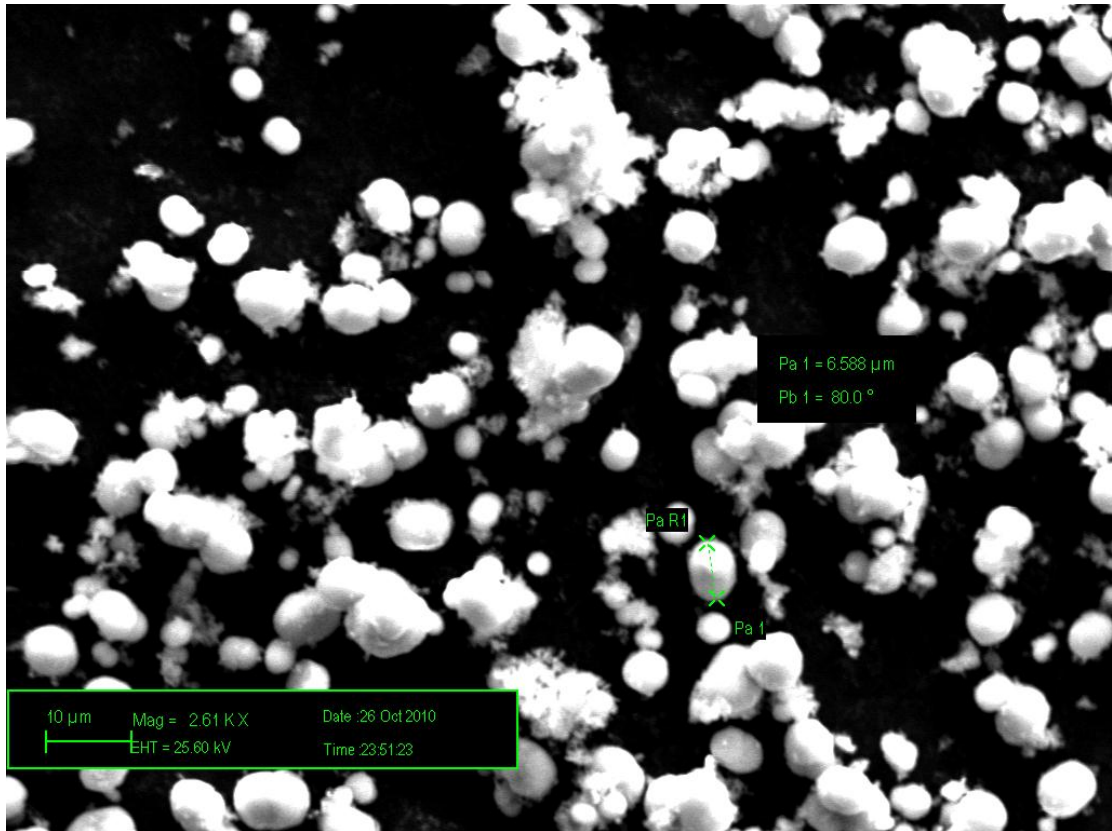


Figure 56 - SEM image of Pd impregnated on CuMn_2O_4 : .5%Pd

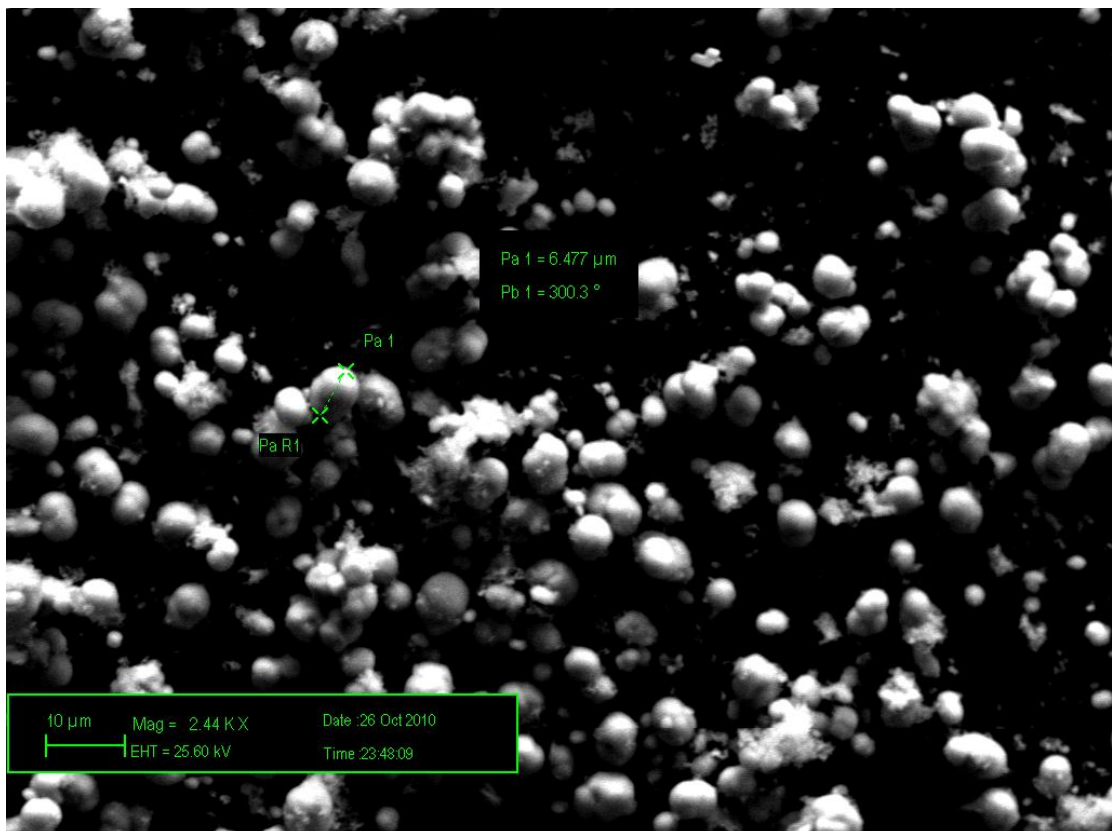


Figure 57 - SEM image of Pd impregnated on CuMn_2O_4 : 1% Pd

4.3 Deposition Precipitation of Noble Metals

Platinum and palladium deposited onto a CuMn_2O_4 spinel lattice is of potential interest for ambient temperature CO oxidation. The chloride salts of platinum and palladium were selected as reagents under criteria discussed in Chapter 1. Platinum in relative mass weightings of 1.0%, and palladium in relative mass weightings of 4.0% were added to CuMn_2O_4 lattice via a pH controlled, deposition precipitation method. The catalysts were dried, recalcined and characterized. The activity of these catalysts was then tested. These catalysts were characterized and tested for CO oxidation activity.

In this experiment, a single batch of coprecipitated hopcalite was split into five 1g samples. Unmodified hopcalite support is referred to as ‘ancestor hopcalite support’. Hopcalite which has been subjected to deposition precipitation conditions without the addition of Pt or Pd chlorides (HCl is substituted in the same concentration as the 1.0% PtCl_4 , 4.0% Na_2PdCl_6 deposition) is referred to as ‘reference hopcalite support’.

4.3.1 Catalyst Reduction

Unmodified hopcalite support was subjected to reductive conditions. This was a reference experiment to investigate the possibility of reducing impregnated surface noble metal particles on hopcalite. Reduction under aqueous $\text{NaCOOH}_{(\text{aq})}$ was attempted. The experiment is detailed in Chapter 2. The resulting hopcalite was completely deactivated. This is in concordance with the work of Mirazei⁵, who described sodium as a catalytic poison.

In another experiment, reduction under $\text{H}_{2(\text{g})}$ was attempted. The method is detailed in more detail in Chapter 2. At 100°C, the hopcalite support exhibited no mass loss and no deactivation. Calcination at higher temperatures (120°C, 150°C and 500°C) resulted in loss of support mass (measured by TGA) and loss in activity. It was concluded that 100°C was the most reductive conditions that could be applied to the support. All impregnated catalysts (4.0% Pd-1.0% Pt, 4.0% Pd and 1.0%Pt) were subjected to reduction at 100°C for 1 h under 5% H_2 in Ar. In all cases the Pt/Pd-

deposited catalysts did not change in activity or morphology measured by any technique. Beyond the variation expected by experimental error; activity, BET surface area, EDX molar percentages, XRD and SEM were identical to that of the unreduced samples. To avoid unnecessary repetition, these results are not reported. It could be postulated that the noble metals were pre-reduced by atmospheric conditions, or the reduction was not powerful enough to change the catalyst surface.

4.3.2 CO Oxidation Activity

The activities of the reference, ancestor and precious metal deposited CuMn_2O_4 catalysts are shown in Figure 58. The evidence is displayed that Pd and Pt deposition has a slight negative effect on catalyst activity.

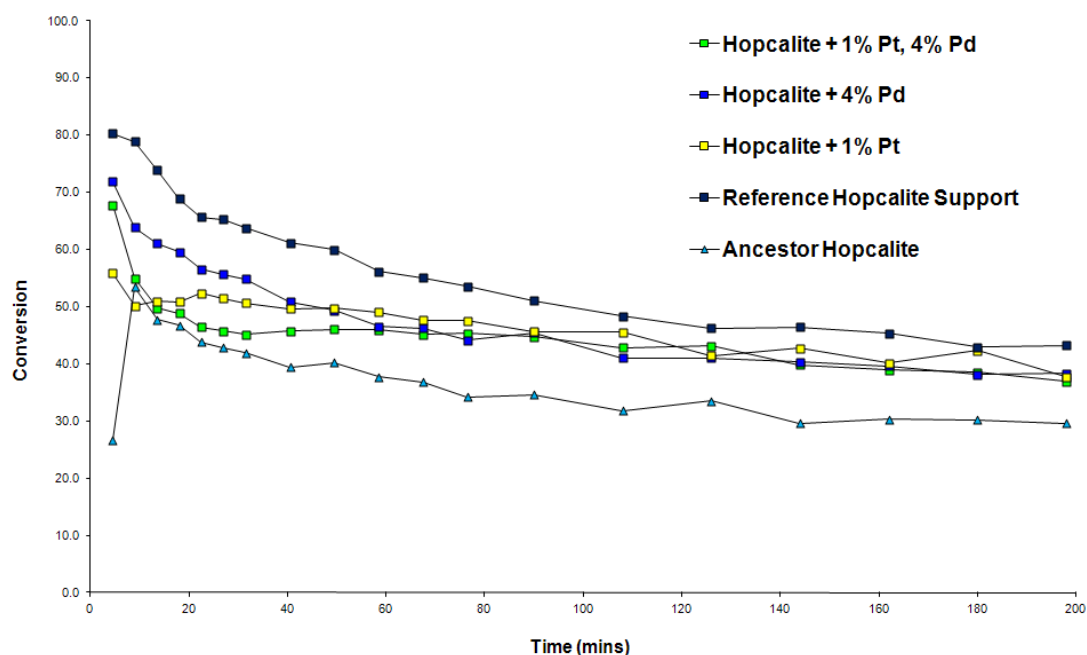


Figure 58 – CO Oxidation – Deposited Pt and Pd on CuMn_2O_4

Ancestor hopcalite support is less active than any of the four treated catalysts. It displays a less active initial activity, and steady state activity of ~ 30%. The three precious metal deposited catalysts show a small activity improvement, an equivalent steady state of ~ 38%. 4.0% Pd deposited hopcalite displays an improved initial activity for the first 40 min. This is also displayed in the 1.0% Pt, 4.0% Pd deposited catalyst, however only for the first 15 min. The reference hopcalite displays the highest activity, with a high initial activity of ~ 80%, followed by a smooth

deactivation and a steady state activity of ~ 43%. The catalysts were tested against gas stream containing 4% humidity, and displayed 0% conversion at 4 min, the shortest testing time possible (no data to display).

4.3.3 BET Surface Area, SANA and EDX Molar Ratio

The surface areas of the untreated and precious metal deposited catalysts were analyzed by BET technique and are displayed in Table 20. In addition, displayed is the relative mass loading palladium content of the samples, analyzed by EDX spectroscopy.

Sample	Surface Area (m ² g ⁻¹)	C value	EDX Pd Loadings	EDX Pt Loadings
Hopcalite Ancestor	70	58	n/a	n/a
Hopcalite Reference	78	45	n/a	n/a
1.0% Pt	81	60	n/a	0.00%
4.0% Pd	82	58	4.73%	n/a
1.0% Pt + 4.0% Pd	85	81	5.39%	0.00%

Table 20 - BET surface areas & EDX molar percentages of deposited Pd and Pt on CuMnO₄

The precursor hopcalite support displays the lowest surface area, at 70 m² g⁻¹. The three deposited catalysts display equivalent surface areas, with an average of ~82 m² g⁻¹. The reference hopcalite shows a surface area of 78 m² g⁻¹. The experimental error of 8% shows that the four treated catalysts have equivalent surface area. The reference catalyst shows the same surface area increase, indicating that this phenomenon is not due to interaction with Pd or Pt ions.

When normalized for surface area (Figure 59) at steady state, it can be observed that the reference hopcalite outperforms the ancestor sample by 31%. The 1.0%, 4.0% Pt/Pd shows activity equivalent to the reference sample, while both monometallic catalysts outperform the ancestor sample by 10%.

Palladium loadings detected by EDX are in correlation with reagent loadings of Pd. Platinum is not detected in the EDX data. A 1.0% Pt loading would be expected to be detected; the reason for this is unclear.

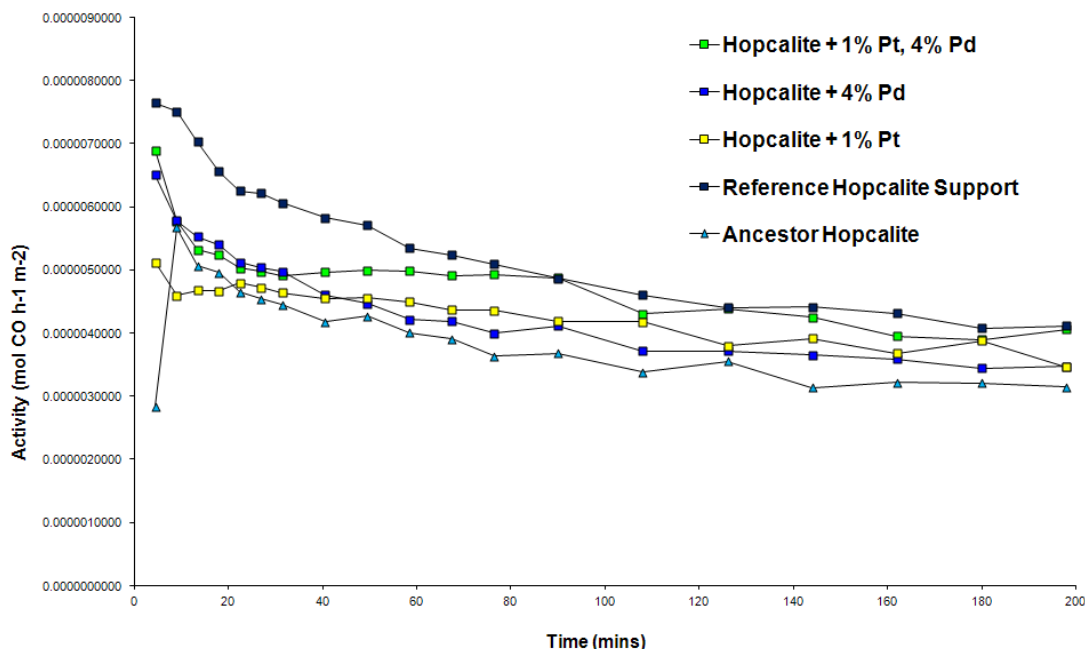


Figure 59 – Surface area normalized activity – Deposited Pd and Pt on CuMnO_4

4.3.4 Powder X-Ray Diffraction

The XRD diffraction patterns for Pd and Pt deposited onto CuMn_2O_4 are displayed in Figure 60. The ancestor and impregnated samples display extremely similar XRD patterns – amorphous, with wide, ill-defined peaks. These correspond to single phase CuO (characteristic double peak at 2θ ca. 35° , 39°) and Mn_2O_3 (2θ ca. 32° and 56°). Reference hopcalite displays similar CuO peaks but shows reduced Mn_2O_3 peaks. Patterns corresponding to Pd, PdO, Pt, PtO and PtO_2 are not present. The patterns of the three impregnated samples are virtually identical to the ancestor. As no evidence of Pt or Pd was observed, it can be concluded that precious metal particles cannot be detected by this technique. The reference catalyst displays a pattern with a reduced Mn_2O_3 signal, but an identical CuO pattern.

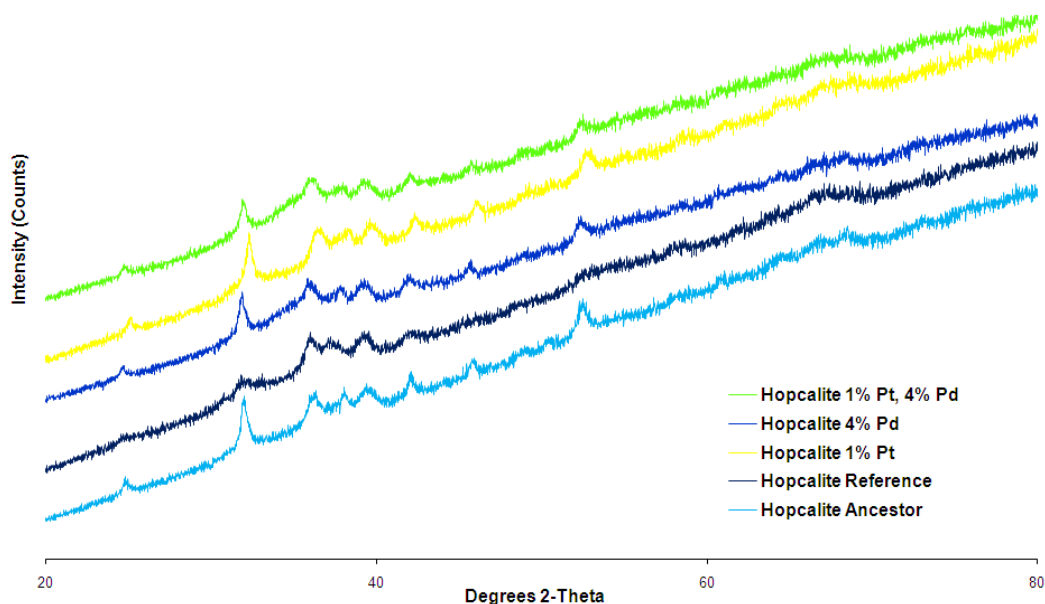


Figure 60 - Powder XRD – Pd doped CuMn_2O_4 catalyst

4.3.5 SEM Analysis

The microstructure SEM analysis of the catalyst batches is displayed in Figures 61-65 and the mean average particle size is displayed in Table 21. Due to the error of $\pm 2.94\%$, it can be considered that there is significant change in the particle size of the ancestor, reference and deposited catalysts. Backscatter SEM analysis of the deposited catalysts displays particles containing atoms of significantly higher atomic mass dispersed on the larger CuMn_2O_4 particles. The particles defy accurate measurement due to their fractured nature, but it can be postulated that these are particles of high atomic mass elements such as Pt, PtO, PtO_2 , Pd or PdO.

Catalyst Pd Loading	Average Particle Size(μm)
0% (Ancestor)	6.57
0% (Reference)	7.43
1% Pt	7.33
4% Pd	8.87
1%Pt, 4% Pd	7.25

Table 21 – Average particle size of Pt and Pd deposited on CuMn_2O_4

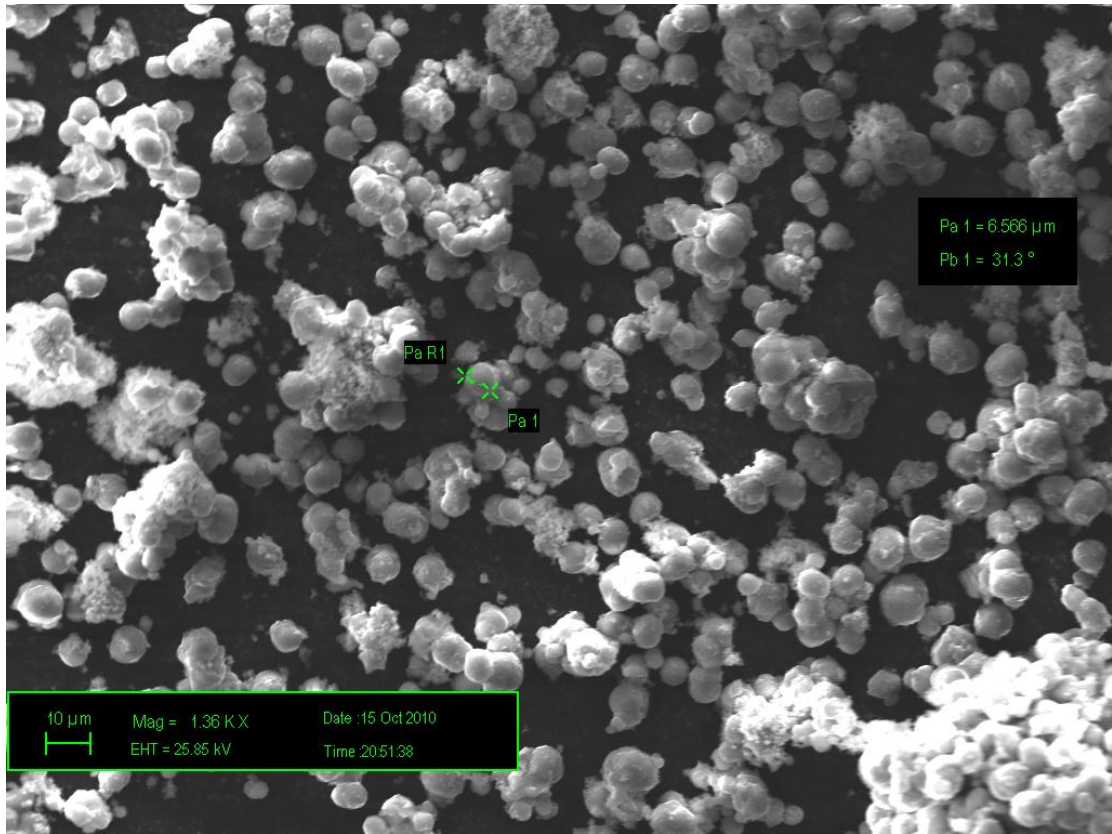


Figure 61 - SEM image of undoped CuMn_2O_4 ancestor sample

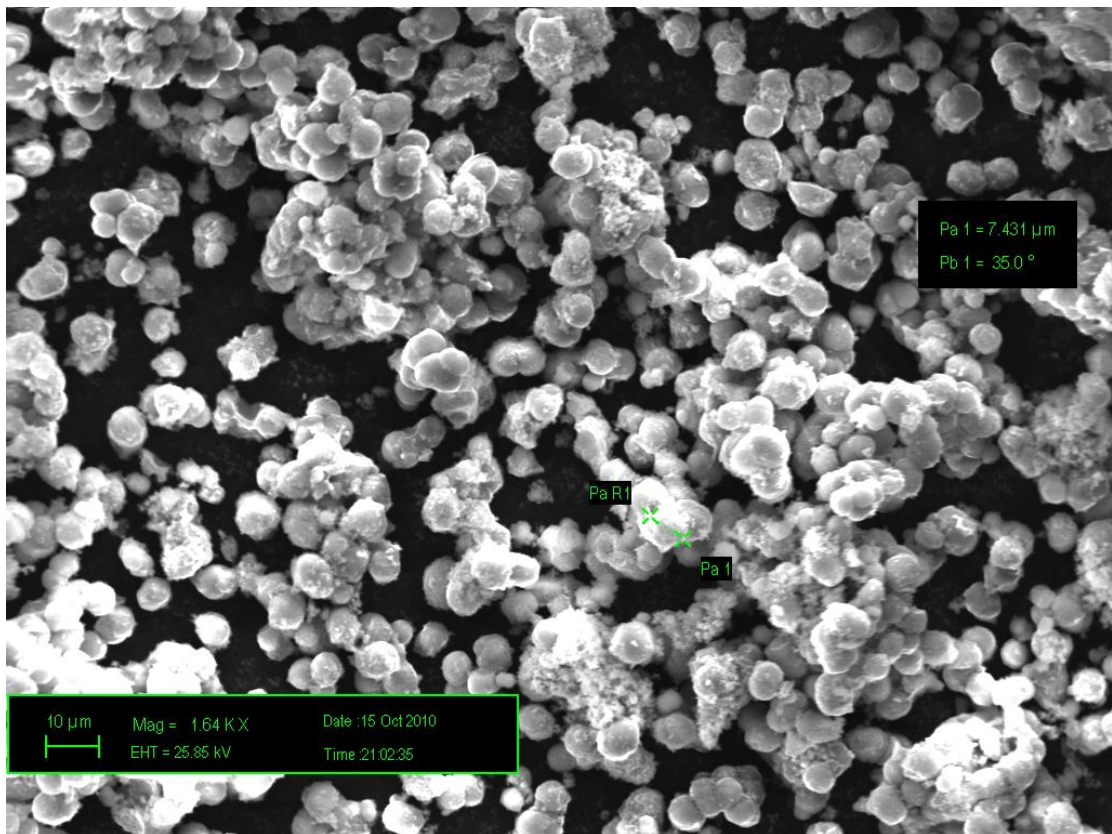


Figure 62 - SEM image of undoped CuMn_2O_4 reference sample

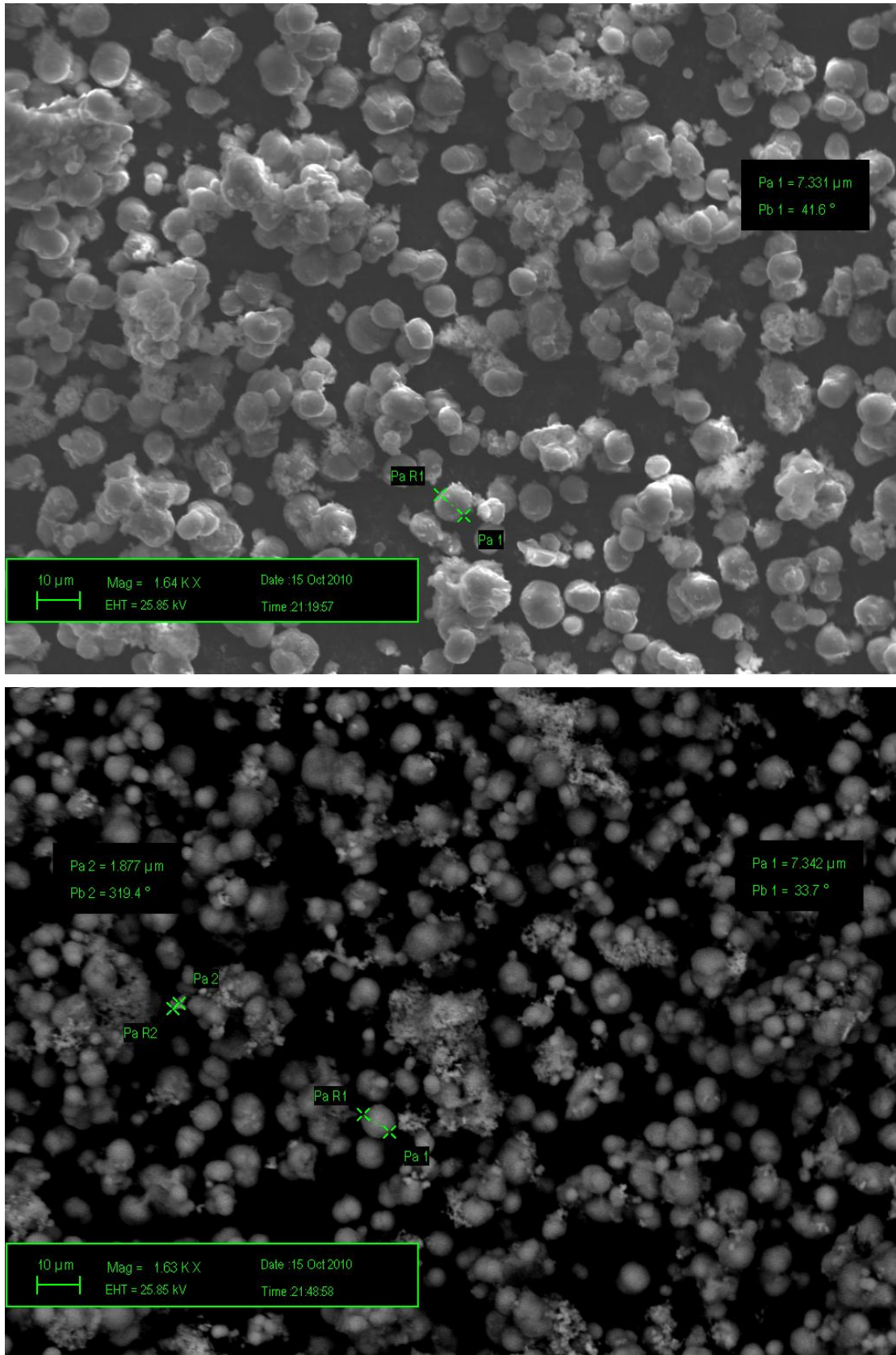


Figure 63 - SEM image of Pt and Pd deposited on CuMn₂O₄: 1% Pt (top), 1%Pt backscatter (bottom)

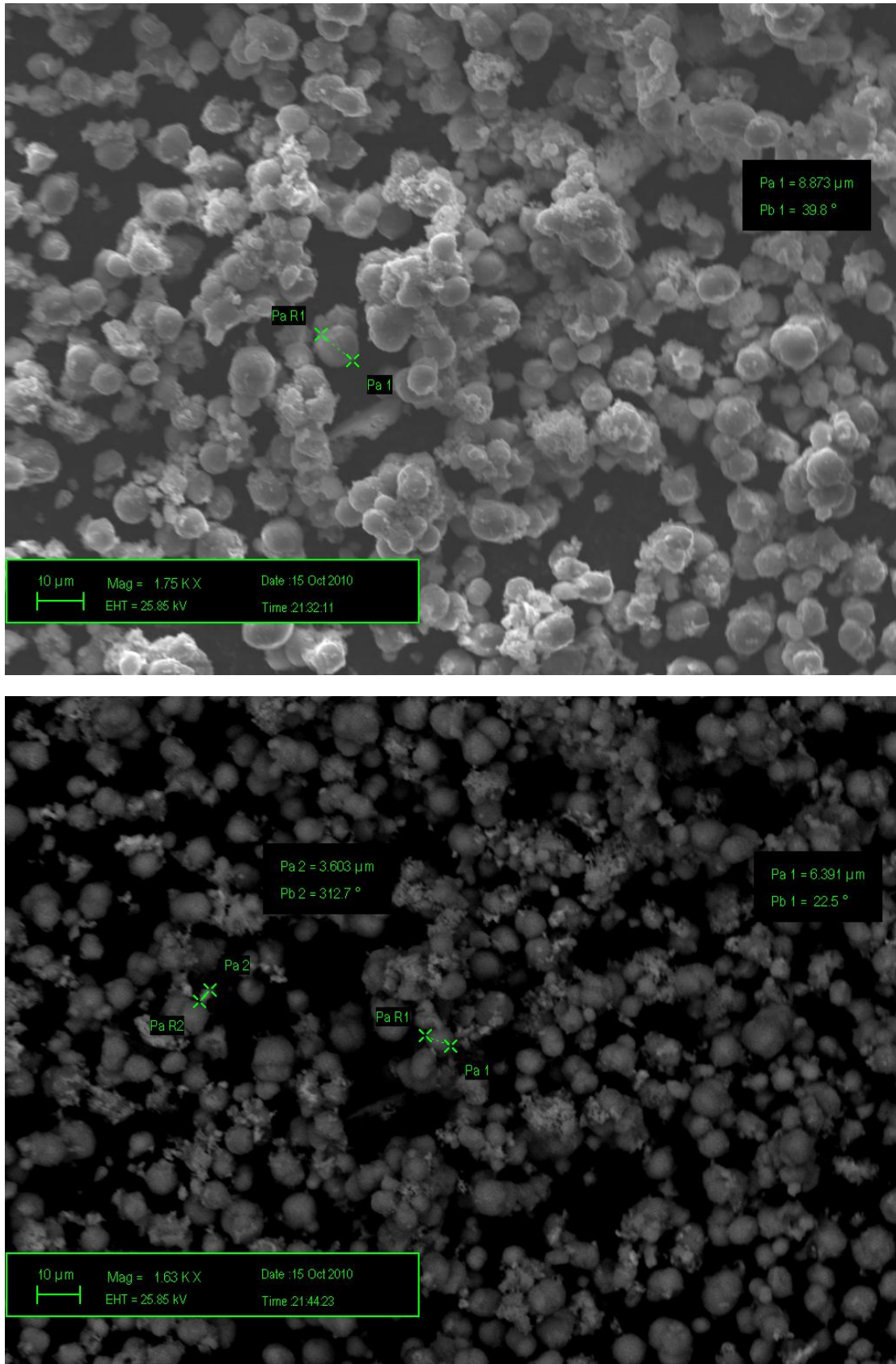


Figure 64 - SEM image of Pt and Pd deposited on CuMn₂O₄: 4% Pd (top), 4% Pd Backscatter (bottom)

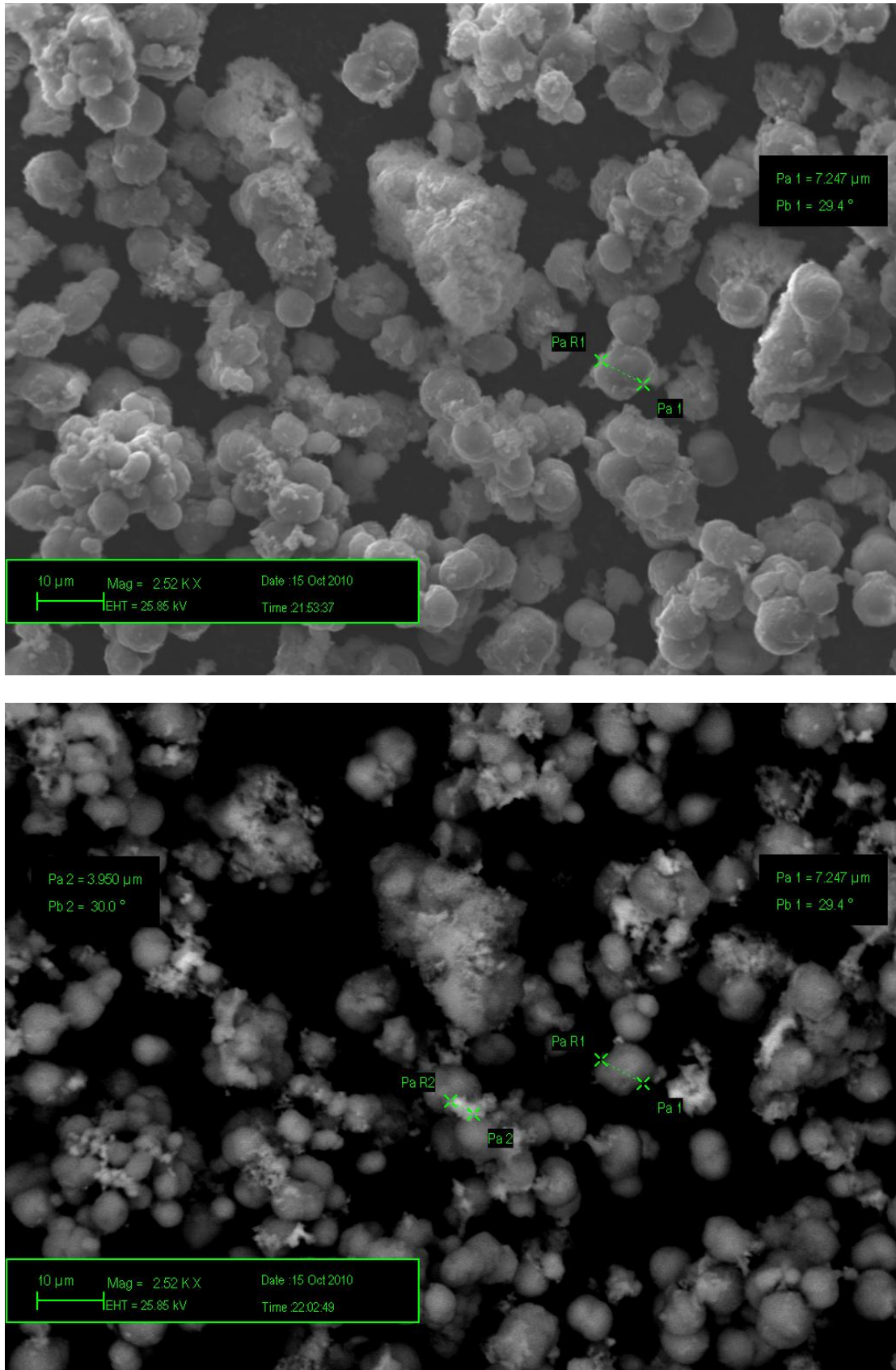


Figure 65 - SEM image of Pt and Pd deposited on CuMn₂O₄: 1%Pt, 4%Pd (top) 1%Pt, 4% Pd Backscatter (bottom).

4.4 Discussion

4.4.1 Effects of Pd doping on CuMn_2O_4

Coprecipitated CuMn_2O_4 was doped with small quantities of $\text{Pd}(\text{NO}_3)_2$. A correlation between rising Pd loading and steady state activity increase is discovered. The initial activity peak normally seen in hopcalite catalysts is not present. This phenomenon is also witnessed in V and Ce doped catalysts in Chapter 3. The hypothesis postulated in these discussions can also be applied to Pd-doped CuMn_2O_4 . The explanation is that the activity spike in unmodified hopcalite is due to low humidity levels at the beginning of the reaction. The doped catalyst suffers increased poisoning at the start of a reaction which is gradually reduced by surface restructuring. This poisoning is sufficient to overcome the effects of the low humidity. Testing recalcined catalysts for activity, under TPR and XPS would test this hypothesis.

PdO and $\text{Pt}_{(s)}$ have been described⁶⁻⁸ as oxidation catalysts in their own right, which could explain the increase steady state activity. Pd has been doped into the hopcalite lattice, and according to the nature of the synthesis procedure (co-precipitation) the majority of the metal would not be accessible unless significant surface segregation had occurred. Veprek *et al.*⁹ has described surface segregation of K^+ ions to the surface of CuMn_2O_4 . He describes this in a crystallized catalyst (calcined at 550°C), and finds that ions smaller than K^+ (138pm), specifically Ca^{2+} (100pm), do not segregate to the surface of CuMn_2O_4 . Pd^{2+} , with an ionic radius of 86pm¹⁰, would not be a likely candidate for segregation. This makes it unlikely that activity rises are to be solely a result of Pd or PdO acting as an independent catalyst, due to lack of accessibility. Analysis with surface sensitive XPS and/or investigation into relative surface energies of Cu-Mn-Pd-O compounds could resolve this question, but that is beyond the scope of this thesis and has not been previously studied. The conclusion that Pd is inaccessible on the surface is supported by the surface normalized activity data, which shows no rise or fall in activity in line with Pd loadings. The difference in activities can be correlated exactly to change in surface area, which would be predominately CuMn_2O_4 .

As Pd has been ruled out as an independent CO oxidation catalyst, activity rises can be attributed to improvement in the activity of the hopcalite spinel, either by structural promotion or catalytic promotion. The loss of initial activity must also be accounted for by structural or catalytic poisoning.

Evidence to suggest that Pd is a structural promoter of CuMn_2O_4 was observed. XRD data correlates increasing Pd weighting with a decrease in the crystalline nature of the catalyst. This occurs in both single phase CuO and Mn_2O_3 , as well as crystalline $\text{Cu}_{1.5}\text{Mn}_{1.5}\text{O}_4$. The single phase oxides have been tested at Cardiff as inactive at ambient temperature. The ambient temperature CO oxidation activity of hopcalite has been repeatedly linked to the redox mechanism formed by amorphous spinel CuMn_2O_4 , rather than crystalline copper manganese oxides^{9, 11-13}. This shift towards amorphous character could account for a rise in the activity of the catalyst. This is not unprecedented – studies in the Chapter 3 of V and Ce doped catalysts correlate increasing transition metal loading with increasing crystalline character. The work of Cole² on Fe, Ni, Si and Co doped catalysts have correlated increased ion doping with both increasing and decreasing crystalline character. However, the effects he observed were small and unpredictable, with no clear correlation between loading and change in character. Pd-doped hopcalite is an example of increasing ion doping correlating to decreasing crystalline character.

The mechanism whereby dopant ions affect catalyst crystalline structure is currently unknown. Synthesis of hopcalite to promote amorphous character has been studied extensively by Jones¹, Hutchings¹⁴ and others – it could be deduced that even slight deviation from reaction conditions (such as the introduction of a new reagent) could influence the catalyst morphology. Three changes in the reaction conditions were made by the introduction of $\text{Pd}(\text{NO}_3)_2$. Firstly, a slight reduction (1-5%) in concentration of Cu and Mn ions (although still in the 2:1 ratio). This is unlikely to have any effect on catalyst morphology. Due to evaporation and use of measuring cylinders, the total aqueous solution (and thus concentration) present in the reaction vessel was not tightly controlled across experiments. Reproducible results have been achieved regardless.

Secondly, a slight reduction in nitrate ion concentration (Mn has three nitrate ligands, compared to two on the replacement Pd), which would result in a slightly higher pH and thus slightly less Na_2CO_3 needed to maintain pH control. This could improve activity as Na^+ ions have been described as a catalyst poison by Mirzaei⁵. He found that sodium ions adsorbed from the reaction mixture onto the hopcalite surface were correlated with decreasing hopcalite activity. The total reduction of Na^+ ions can be estimated at between and 0.22% (for 1.0% Pd) and 1.11% (for 5.0% Pd). Mirzaei postulated the rate limiting step of Na^+ ion adsorption to be surface isoelectric point rather than Na^+ concentration, so it is safe to assume this effect is negligible if even existent. In addition, Na^+ ion concentration has never been linked to catalyst morphology, only activity.

Thirdly, Pd^{2+} and precipitated Pd hydroxides/oxides present in the reaction mixture. The effect of dopant ions present during synthesis on hopcalite morphology has been investigated at Cardiff. A predictive theory regarding effects has never been made however – a comparison of ionic radius, electronegativity and ionisation energies across Ni, Co, Fe, Ag, V, Si, Ce, Au and Pd has shown no clear pattern regarding ion character and catalyst morphology. It is right to conclude that the effect of reagent Pd is correct, as the evidence suggests the first two are unlikely.

SEM analysis displays a trend towards reduction in average particle size with increasing Pd loadings. BET surface area data reports that catalyst surface area rises significantly in line with increased Pd loadings. This data supports the hypothesis that Pd is a structural promoter. Reduction in average particle size has been witnessed in Chapter 3 in respect to vanadium, and Jones¹ has reported improvements in catalyst surface area in 1%Ni/CuMn₂O₄ and 1%Ag/CuMn₂O₄.

When normalized for surface area, it can be deduced that the activity of Pd-doped CuMn₂O₄ can be correlated exactly to its change in surface area. It can also be seen that Pd doped CuMn₂O₄ is less active in terms of 'mol CO oxidized h⁻¹ m⁻²', than the undoped catalyst, in terms of both steady state activity and initial activity. It could be postulated that Pd is a structural promoter of hopcalite, but is catalytically poisonous in regard to activity levels.

This decrease in initial activity and steady state activity is not easily explained. The decrease is identical across the three doped catalysts - if the palladium were a typical poison, the effect would be in correlation with metal loadings. During the experiment, the catalysts undergo a change and become less active than the undoped reference. Defining palladium as a catalytic poison is difficult. As noted on pg. 117, significant surface segregation of Pd is considered unlikely. This would also limit the effect of Pd to physically block active Cu or Mn sites on the surface of the catalyst in a poisoning role. As Pd doping is correlated to increasing amorphous character in the catalyst, this rules out segregation to crystalline oxides as a mechanism for deactivation. A possibility is that Pd is acting as a chemical poison. Interactions between Pd and CuO/Mn₂O₃ have been studied by Ferrandon *et al.*⁴ and Baylet *et al.*¹⁵. Ferrandon proposes that mixing a noble metal with a less electronegative cation (such as Manganese, 1.55 Pauling) leads to the formation of the noble metal oxide. Palladium's interaction with copper would favour Pd_(s) over PdO due to the higher electronegativity of Cu (1.90 Pauling). Mixed phase CuMn₂O₄, comprised of predominately manganese, would have overall electronegativity closer to manganese than copper. Pd in the presence of would predominately form PdO. Cordi and Falconer¹⁶ have described PdO as less active for CO oxidation than Pd_(s).

It has already been postulated that Pd has no direct role in this reaction, PdO/Pd⁰ or otherwise, due to accessibility. However, it must be established that if Mn can oxidize Pd to PdO, Pd can reduce manganese to a lower oxidation state (in this case, +4, to +3 and perhaps +2). The redox mechanism proposed by Cocks *et al.*¹²; widely accepted as the reason for the high activity of hopcalite, is dependent on free redox state changes between Cu^{1+/2+} and Mn^{+3/+4}. It could be postulated that Pd/PdO is interfering with this system, reducing Mn oxidation state. This is supported by the work of Baylet¹⁵, who described Pd impregnation on Mn₂O₃ as favouring the +3/+2 redox couple, which he found is favourable in the oxidation of methane. If this were the case, however, it would be expected to find an increase in catalyst poisoning in line with increasing Pd loading. This is not observed, as all three doped catalysts display the same level of poisoning, regardless of Pd loading. The reason for this is unclear and has not been previously investigated.

4.4.2 Effects of Pd impregnation on CuMn₂O₄

CuMn₂O₄ spinel was impregnated with small amounts of Pd(NO₃)₂, dried and recalcined. A reference sample was prepared substituting Pd nitrate with nitric acid. Reference hopcalite displays identical initial activity but higher steady state activity for CO oxidation than ancestor hopcalite. Reference hopcalite was exposed to low concentration HNO₃ in an incipient wetness impregnation, dried at room temperature, and recalcined at for 3 h at 400°C to remove nitrate ions. As no additional transition metals have been incorporated into the lattice by this procedure, it is certain that a change in hopcalite morphology is responsible for this effect. Comparing XRD patterns of both materials displays no differences between the two samples, so a change in catalyst morphology towards the amorphous state is unlikely. BET surface area displays a 20% increase in surface area of the reference catalyst compared to ancestor. This exactly correlates to the increase in activity witnessed. This data is reinforced by the decrease in mean average particle size witnessed by SEM. It can be concluded that an increase in catalyst surface area is responsible for the activity rise.

This observation could be attributed to one or two effects. Firstly, as CuMn₂O₄ is known to dissolve in acidic media¹⁷, the acid HNO₃ in solution may partially dissolve the surface of CuMn₂O₄, leading to smaller particle sizes and a change in surface morphology. Similar studies carried out by Cole² involving H₂AuCl_{4(aq)} deposition on CuMn₂O₄ did not record a change in particle size or catalyst surface area. It should be noted that the hopcalite synthesised in the Cole experiment did not follow the same preparation procedures used in this thesis, as catalysts were aged for lengths of time between 30 min and 6 h. This could explain the differences in observation, as Hutchings¹⁴ and Mirzaei¹⁸ have noted that catalyst aging is directly correlated to final catalyst morphology and surface structure.

Alternatively, the secondary calcination could affect catalyst particle size and surface area. Jones *et al.*¹⁹, Hutchings *et al.*¹⁴ and Veprek *et al.*⁹ have described catalyst calcinations to be important in regards to defining final hopcalite morphology and surface area. Cole subjected hopcalite to secondary calcinations (400°C for 3 h) after Au deposition, and did not witness an increase in surface area. As has been discussed, Cole did prepare his catalyst in a slightly different manner. Regardless of mechanism,

there is an exact correlation between surface area and activity. The reference catalyst lacks other possible promoters. This leads to the conclusion that the activity increase is attributable to the rise in surface area.

The 0.25% and 0.5% Pd- impregnated CuMn_2O_4 display equivalent activity – improved initial activity over reference CuMn_2O_4 , and identical steady state activity. As Pd^0 is known as a CO oxidation catalyst in its own right⁶⁻⁸, it is likely that this initial activity increase is due to oxidation of CO by surface $\text{Pd}_{(s)}$ atoms.

Pd^0 is described as an effective CO oxidation catalyst by Maillet *et al.*⁷, who describes $\text{PdO}/\text{Al}_2\text{O}_3$ as capable of reduction at room temperature under CO to Pd^0 . PdO is described as relatively inactive for CO oxidation reaction at ambient temperature. This finding correlates with the observations made in Chapter 5, in which reduced $\text{Pt}/\text{Pd}/\text{Al}_2\text{O}_3$ is ~20 times as active as the unreduced variety. Ferrandon *et al.*⁴ finds that Pd impregnated onto Mn_2O_3 is preferentially oxidised to PdO . The time delayed deactivation witnessed in the activity graph could be explained by Pd^0 oxidising to PdO under the increasing temperature of the active sites and the influence of Mn. Fernando also describes Pd impregnated on CuO , which is preferentially reduced to Pd^0 . He concludes that the higher electronegativity of Cu leads to a metal-support interaction favouring Pd^0 over PdO . The surface of CuMn_2O_4 has been described by Mirzaei¹⁸ as comprised of Cu^{2+} and $\text{Mn}^{3+/4+}$. The exact morphology of CuMn_2O_4 surface has never been deduced, but it would be wise to accept the characteristics of more frequent ion, Mn, which would explain the loss of activity of Pd in these catalysts.

In the discussion in section 4.4.1, a negative effect of Pd^0/PdO on the Cu/Mn manganese spinel was proposed. In this case it is not witnessed. Incipient wetness impregnation of metal salts onto support normally results in macroscopic agglomerated particles²⁰ of precious metal and thus limited $\text{Pd} \leftrightarrow \text{Cu/Mn}$ interactions. The relatively lower loadings of Pd in this experiment compared to the doped catalysts could also be an explanation.

The 1% impregnated $\text{Pd}/\text{CuMn}_2\text{O}_4$ catalyst displays a similar initial activity spike to the 0.25% and 0.5% catalysts, but has a shallower deactivation curve and a higher

steady state activity. The EDX data displays higher Pd loading in the catalyst. Ruling out a synergetic effect between PdO/Pd(s) and CuMn₂O₄ (as discussed, literature suggests the opposite) the activity increase can only be attributed to increased CO oxidation by Pd⁰. This indicates that a portion of the Pd has escaped the influence of Mn - perhaps on the surface of larger agglomerated clusters of PdO caused by the rise in Pd loading.

4.4.3 Effects of Pt and Pd deposition on CuMn₂O₄

Small amounts of PtCl₄ and Na₂PtCl₆ were deposited upon CuMn₂O₄ spinel, which was then dried and recalcined. A reference sample was prepared substituting hydrochloric acid with the relevant metal salts. In a similar observation to Pd-impregnated CuMn₂O₄ in Part 4.4.2, reference hopcalite is significantly more active than the ancestor sample. Reference hopcalite was exposed to identical concentrations of HCl, adjusted to pH 9 with NaOH for 1 h, washed and dried at 120°C, then recalcined at 400°C for 3 h. Reference hopcalite displays a more amorphous character than the ancestor sample (particularly in the reduction of Mn₂O₃ peaks). Catalyst particle sizes have risen by ~13% in the reference sample, and hopcalite surface area has risen ~11%. Surface normalised activities indicate that hopcalite activity has increased more than the change in surface area would account for. This additional promotion cannot be explained by promotion by dopant ions. Exposure to Na⁺ ions is unlikely to promote catalyst activity – Mirzaei *et al.*⁵ have described increasing sodium levels on the surface of the catalyst as detrimental to hopcalite activity. Exposure to Cl⁻ ions is also unlikely to promote catalyst activity. Vu *et al.*²¹ described catalyst deactivation due to Cl when combusting chlorinated VOC's over hopcalite at 350°C. It may be that the additional treatment of CuMn₂O₄ has removed poisons present in the initial sample. As additional Na⁺ treatment has not resulted in an activity loss, it could be postulated that a wet deposition at controlled pH 9 has resulted in removal of Na⁺ ions on the surface of CuMn₂O₄ which were as result of the coprecipitation synthesis. Mirzaei⁵ has reported that as the pH of a synthesis rises, Na⁺ concentrations on the surface of the catalyst precursor drop and activity rises. In this case however, Mirzaei was describing Na⁺ adsorption onto the catalyst precursor

(Copper oxide, and manganese carbonates) rather than the calcined CuMn_2O_4 as this study has described, so relative zero point charges (ZPC's) may differ.

The exact isoelectric point and ZPC of hopcalite has not been measured. As discussed in Chapter 1.4, although hopcalite is given the structure ' CuMn_2O_4 ' for ease of reference, the exact morphology of the catalyst surface cannot be reduced to simply $\text{CuO} + \text{Mn}_2\text{O}_3$. Mirzaei¹⁸ discovers that the surface manganese oxidation state is between Mn^{3+} and Mn^{4+} , while copper is predominately Cu^{2+} . Park²² has described the isoelectric point of $\text{Cu}^{(\text{II})}\text{O}$ as 9.5 ± 0.4 . Morimoto²³ calculates the isoelectric point of $\text{Mn}_2^{(\text{III})}\text{O}_3$ at 7.6-9.0. $\text{Mn}^{(\text{IV})}\text{O}_2$ is calculated as <5.1 . Jarra²⁴ has described the isoelectric point of a mixed oxide as intermediate to that of the corresponding pure oxides. Mirzaei¹⁸ has described the surface composition of CuMn_2O_4 as identical to the bulk structure, so it could be theorised that the isoelectric point of bulk CuMn_2O_4 to be approximately between 8.23 and 9.16. As discussed, this figure is an estimate at best, as it does not account for $\text{Mn}^{(\text{IV})}\text{O}_2$. The figures indicate that a wet impregnation at pH 9 could be interfering with Na^+ ion adsorption as the isoelectric point of hopcalite is approximately in this area.

EDX analysis of the three Pt/Pd deposited samples displays the presence of Pd on samples, Pt was not detected. The relatively low loadings of Pt may make its detection difficult. Backscatter SEM clearly shows the presence of clusters of high mass particles on the monometallic Pt doped samples. There is no direct evidence that Pt is present in the catalyst. Due to the similarities between Pd and Pt chemistry, and the differing activities of Pt treated catalysts, Pt would be expected to deposit onto the catalyst. The high mass particle on the monometallic 1.0% Pt catalyst can be safely assumed to be Pt. All samples show virtually identical XRD patterns to the reference sample, with the exception of a Mn_2O_3 peak which is equivalent to the peaks displayed in the ancestor sample. BET surface areas are equivalent to the reference sample. Given the % error in the BET analysis, the three doped catalysts have equivalent activities when normalised for surface area. The precious metal doped catalysts display equivalent activities compared to the reference hopcalite, regardless of metal loading.

Given the described effect on Mn_2O_3 on Pd, which has already been discussed in this chapter (the work of Ferrandon⁴), the lack of activity of Pd in the experiment is not unexpected. Deposition precipitation synthesis normally produces smaller particles on the surface of a support²⁰, which may explain why 1.0% impregnated Pd/CuMn₂O₄ from the incipient wetness experiment is more active than the 4.0% deposited catalysts in this experiment. Given the smaller particle sizes in this experiment, a larger amount of Pd would be susceptible to oxidation by Mn. Boronin²⁵ describes Pd on CeO₂; boundary atoms of the palladium islands undergo a strong polarizing effect from oxygen of the support, leading to the formation of Pd¹⁺.

The effect of Cu and Mn oxides on Pt has been described by Grbic²⁶. MnO_x was found to affect the state of Pt sites, generating Pt²⁺ from Pt⁰. This is a very similar mechanism to that already described for the effect of Mn on Pd. PtO has been described as inactive for CO oxidation at room temperature by Seo²⁷, while Pt⁰ is highly active.

The effect of residual Cl ions on Pt and Pd must be considered. Gelin *et al.*⁶ and Oran *et al.*²⁸ have described the effects, both promotional and poisonous, of Cl adsorption on the surface of a precious metal for oxidation reactions. In this case however, both Pd and Pt display 0% activity at ambient temperature, and no study has suggested that low level Cl poisoning can reduce activity to 0%.

4.4.4 Effects of Reduction of Pt and Pd on CuMn₂O₄

The discussion in Part 4.4.2 & 3 suggest that Pt and Pd on the surface of hopcalite is oxidised by Mn to the less active oxide form. All samples from this chapter were subjected to reducing conditions. These conditions were calculated by experimenting on ancestor and reference hopcalite, and were designed to be the most reductive possible without deteriorating the hopcalite spinel activity. Wet reduction by Na₂COOH was tested and discounted due to 90% loss in hopcalite activity. This can be correlated to the findings of Mirzaei⁵, who found that Na⁺ ions electrostatically adsorbed onto a hopcalite surface are directly correlated to the reduction in catalyst activity for CO oxidation at ambient temperature.

H₂ reduction was attempted. TGA analysis displayed that hopcalite underwent thermal mass loss at temperatures over 120°C, which coincided with a loss of activity. As a result, all samples (Pd impregnated, and Pt/Pd deposited) were subjected to 100°C calcinations for 1 h under 5% H₂ in Ar. This temperature did not affect the activity or morphology of reference hopcalite, the goal being to reduce Pt and Pd on the surface of the support.

However, in all cases, this H₂ reduction had no effect on catalyst morphology or activity. This indicates that nothing has happened – a reduction from PdO to Pd⁰ or PtO to Pt⁰, would likely be accompanied by an increase in activity, as reported in the work of Seo *et al.*²⁷ and Grbic *et al.*²⁶. PdO will reduce at room temperature under H₂ when supported on Al₂O₃²⁹ or CeO₂²⁵ provided the particles are large enough to avoid significant metal-support interactions. Similar observations have been made³⁰ on Pt dispersed on Al₂O₃. The findings of Ferrandon⁴ would suggest that the reductive effect of Mn₂O₃ on Pt and Pd is sufficient to reoxidise catalysts between the reduction and testing stages, or to prevent their reduction entirely at 100°C.

In conclusion, reductive conditions applied to the catalysts are not sufficient to reduce PtO/PdO and increase activity.

4.5 Conclusions

The improved activity of Pd doped CuMn_2O_4 can be attributed to improvements in surface area of the CuMn_2O_4 . Pd does not participate as an independent catalyst. There is also an improvement in amorphous character, and a reduction in initial and steady state activity. All changes can be attributed to Pd ions in the synthesis solution. The exact chemistry whereby Pd influences synthesis chemistry is unclear; however our results are in concordance with other research institutions.

Pd impregnated onto CuMn_2O_4 displays improved activity at only 1% loading. This is possibly due to Pd:Mn metal support interactions oxidising the Pd to PdO. Recalcined reference hopcalite has better activity due to increasing surface area. The mechanism for this change is unknown.

Pd and Pt deposited onto CuMn_2O_4 does not display any activity changes. This is most likely due to metal support interactions between the metals and Mn. Recalcined hopcalite has better activity due to either increasing surface area, removal of Na^+ ions in the deposition preparation synthesis, or both.

Attempts to reduce precious metals on the surface of CuMn_2O_4 resulted in no change. It can be postulated that Mn is inhibiting this mechanism, and more reductive conditions would harm the activity of the CuMn_2O_4 lattice.

4.6 References

1. C. D. Jones, Cardiff University, 2006.
2. K. J. Cole, Cardiff University, 2008.
3. M. Ferrandon, J. Carno, S. Jaras and E. Bjornbom, *Applied Catalysis a-General*, 1999, **180**, 141-151.
4. M. Ferrandon, J. Carno, S. Jaras and E. Bjornbom, *Applied Catalysis a-General*, 1999, **180**, 153-161.
5. A. A. Mirzaei, H. R. Shaterian, R. W. Joyner, M. Stockenhuber, S. H. Taylor and G. J. Hutchings, *Catalysis Communications*, 2003, **4**, 17-20.
6. P. Gelin and M. Primet, *Applied Catalysis B-Environmental*, 2002, **39**, 1-37.
7. T. Maillot, C. Solleau, J. Barbier and D. Duprez, *Applied Catalysis B-Environmental*, 1997, **14**, 85-95.
8. F. Marino, C. Descorme and D. Duprez, *Applied Catalysis B-Environmental*, 2004, **54**, 59-66.
9. S. Veprek, D. L. Cocke, S. Kehl and H. R. Oswald, *Journal of Catalysis*, 1986, **100**, 250-263.
10. R. D. Shannon, *Acta Crystallographica Section A*, 1976, **32**, 751-767.
11. I. Spassova, M. Khristova, D. Panayotov and D. Mehandjiev, *Journal of Catalysis*, 1999, **185**, 43-57.
12. D. L. Cocke and S. Veprek, *Solid State Communications*, 1986, **57**, 745-748.
13. C. Yoon and D. L. Cocke, *Journal of Non-Crystalline Solids*, 1986, **79**, 217-245.
14. G. J. Hutchings, A. A. Mirzaei, R. W. Joyner, M. R. H. Siddiqui and S. H. Taylor, *Applied Catalysis a-General*, 1998, **166**, 143-152.
15. A. Baylet, S. Royer, C. Labrugere, H. Valencia, P. Marecot, J. M. Tatibouet and D. Duprez, *Physical Chemistry Chemical Physics*, 2008, **10**, 5983-5992.
16. E. M. Cordi and J. L. Falconer, *Journal of Catalysis*, 1996, **162**, 104-117.
17. A. Rathje and D. Marcero, *American Industrial Hygiene Association Journal*, Editon edn., 1976, vol. 37, pp. 311-314.
18. A. A. Mirzaei, H. R. Shaterian and M. Kaykhahi, *Applied Surface Science*, 2005, **239**, 246-254.
19. C. Jones, K. J. Cole, S. H. Taylor, M. J. Crudace and G. J. Hutchings, *Journal of Molecular Catalysis a-Chemical*, 2009, **305**, 121-124.
20. J. Regalbuto, *Catalyst Preparation*, CRC Press, Taylor and Francis Group, 2007.
21. V. H. Vu, J. Belkouch, A. Ould-Dris and B. Taouk, *Journal of Hazardous Materials*, 2009, **169**, 758-765.
22. G. A. Parks and P. L. D. Bruyn, *Journal of Physical Chemistry*, 1962, **66**, 967
23. T. Morimoto and S. Kittaka, *Bulletin of the Chemical Society of Japan*, 1974, **47**, 1586-1588.
24. A. A. Jara, S. Goldberg and M. L. Mora, *Journal of Colloid and Interface Science*, 2005, **292**, 160-170.
25. A. I. Boronin, E. M. Slavinskaya, I. G. Danilova, R. V. Gulyaev, Y. I. Amosov, P. A. Kumetsov, I. A. Polukhina, S. V. Koscheev, V. I. Zaikovskii and A. S. Noskov, *Catalysis Today*, 2009, **144**, 201-211.
26. B. Grbic, N. Radic, B. Markovic, P. Stefanov, D. Stoychev and T. Marinova, *Applied Catalysis B-Environmental*, 2006, **64**, 51-56.

27. P. W. Seo, H. J. Choi, S. I. Hong and S. C. Hong, *Journal of Hazardous Materials*, 2010, **178**, 917-925.
28. U. Oran and D. Uner, *Applied Catalysis B-Environmental*, 2004, **54**, 183-191.
29. K. Otto, L. P. Haack and J. E. Devries, *Applied Catalysis B-Environmental*, 1992, **1**, 1-12.
30. H. Lieske, G. Lietz, H. Spindler and J. Volter, *Journal of Catalysis*, 1983, **81**, 8-16.

5

Bimetallic Pt-Pd Impregnated γ -Alumina

Monometallic, alumina supported, platinum and palladium metals are well known CO oxidation catalysts at ambient temperature¹. The reaction is known to be a Langmuir-Hinshelwood adsorption mechanism². The reaction is sensitive to CO/O₂ ratio concentration due to the effects of CO self-poisoning. It is promoted by atmospheric water and vulnerable to sulphur poisoning. Previous work on the reaction is discussed in more detail in Chapter 1.

Bimetallic Pt and Pd catalysts have also been reported as effective catalysts³. Synergetic effects between Pt and Pd have been observed by Ito *et al.*⁴ for naphthalene hydrogenation. This effect was attributed to molecular geometry rather than electronic interference between the two metals. Rousset *et al.*⁵ studied bimetallic catalysts for toluene hydrogenation and did not describe any synergetic effect, though an absence of electronic interference between Pt and Pd atoms was observed. The effects of synergy between Pt and Pd for CO oxidation was investigated by Babu *et al.*⁶ Babu theorised, in regard to formic acid oxidation, interaction of Pt with Pd reduces the strength of CO adsorption.

The exact synergy relationship between Pt and Pd on γ -Al₂O₃ for low temp, low concentration CO oxidation has not been previously reported. For this reaction, the optimum Pt:Pd ratio for bimetallics is not known. This chapter investigates these effects.

5.1 Investigation into Pt/Pd/ Al_2O_3 synergy

The effect of synergy between Pt and Pd on catalyst activity can be measured. This can be achieved by comparing bimetallic catalyst activities with ‘theoretical’ activities obtained from single metal catalysts. This is described in more detail on Figure 55.

Platinum and palladium were electrostatically adsorbed onto 2-3 mm γ - Al_2O_3 spheres. Platinum tetrachloride and sodium palladium tetrachloride were selected as the most promising cationic reagents, as described in Chapter 2. A series of catalysts were impregnated with Pt and Pd, as both monometallics and bimetallics. The exact synthesis method is described in Chapter 2. Precious metals in mass weightings of between 0.25% and 4.00% were deposited onto the sphere surface in an effort to find the most efficient CO oxidation catalysts. The alumina support, Al_2O_3 , has been tested and has no independent activity for this reaction.

5.1.1 CO Oxidation Activity

The activities of monometallic Pd or Pt impregnated catalysts are shown respectively in Figures 66 and 67. Displayed is evidence that singular Pt and Pd metals supported on Al_2O_3 are active for CO oxidation at ambient temperature. Figure 66 displays that Pd impregnated catalysts are active for CO oxidation. All catalysts display a low initial activity peak and a smooth deactivation period. The 0.25% and 0.50% impregnated catalysts display equivalent activities of ~12% conversion. The 0.75% loaded catalyst displays ~18% conversion at steady state. The 1.00% loaded catalyst displays ~23% conversion at steady state. Although the 0.50%, 0.75% and 1.00% loaded catalysts display activity in correlation with their increasing palladium loading, the 0.25% catalyst is equivalent to 0.50% loaded catalyst.

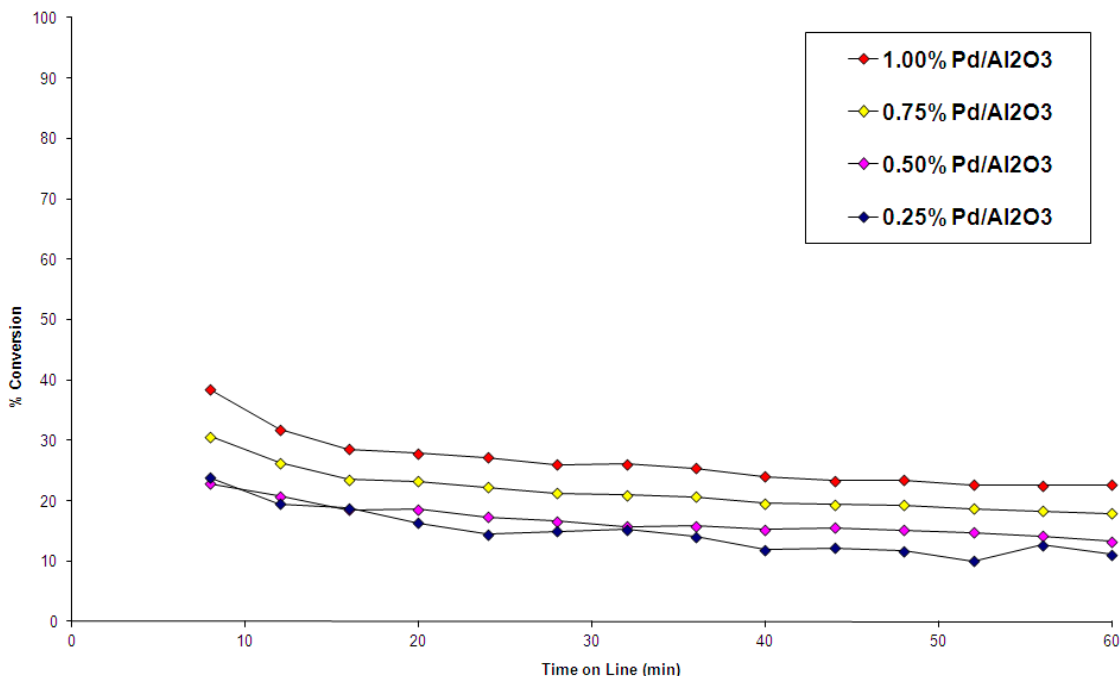


Figure 66 – CO Conversion % - variable Pd-doped Al₂O₃ spheres

Figure 67 shows the activity of Pt/Al₂O₃ for CO oxidation. The 0.25% loaded catalyst displays a steady ~22% activity, and the 0.50% loaded catalyst shows a steady ~31.5% activity. Neither sample displays an initial activity peak. The 0.75% catalyst shows a steadily rising activity, equivalent to the 0.50% doped sample until ~40 min, rising to ~39% conversion at 60 min. The activity does not peak before the end of the experiment.

Figure 68 displays the activity of bimetallic Pt and Pd impregnated on the same Al₂O₃ support. The catalysts show differing initial activities, 0.25% metal loading begins at ~16%, 0.50% loading begins at ~44% and 0.75% loading begins at ~61%. All three catalysts show rising activity through the course of the experiment. The lower the catalyst metal loading, the steeper its activation curve. The 0.25% and 0.50% samples end the experiment on an equivalent activity of ~61%. The 0.75% sample displays a higher final activity of 78%.

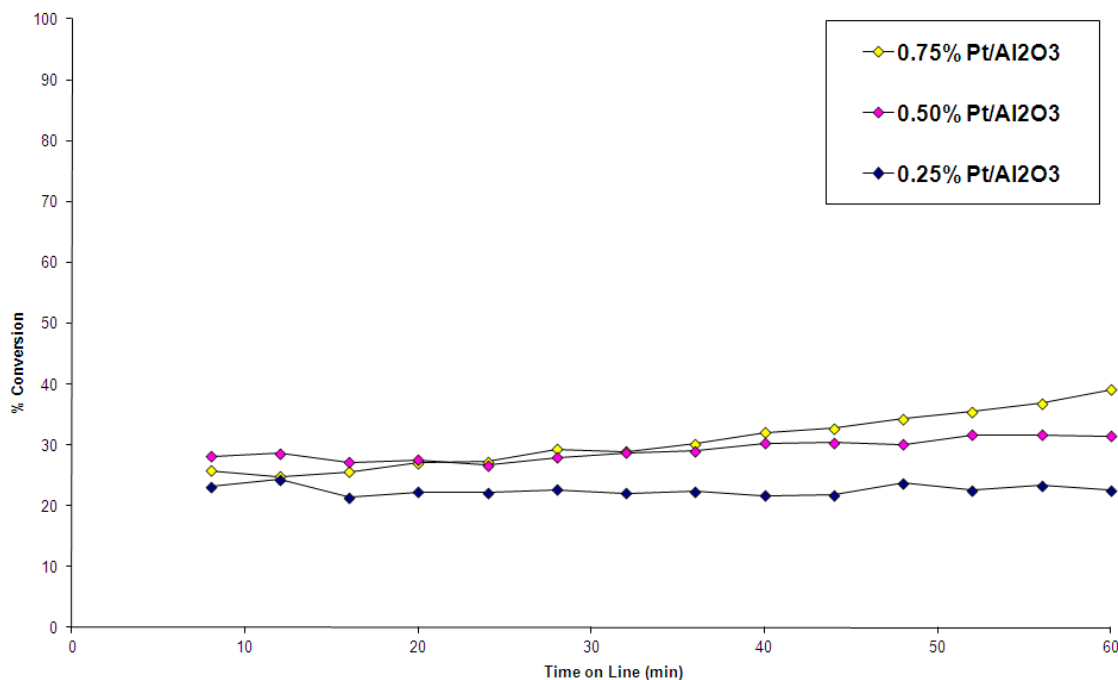


Figure 67 – CO Conversion % - variable Pt-doped Al₂O₃ spheres

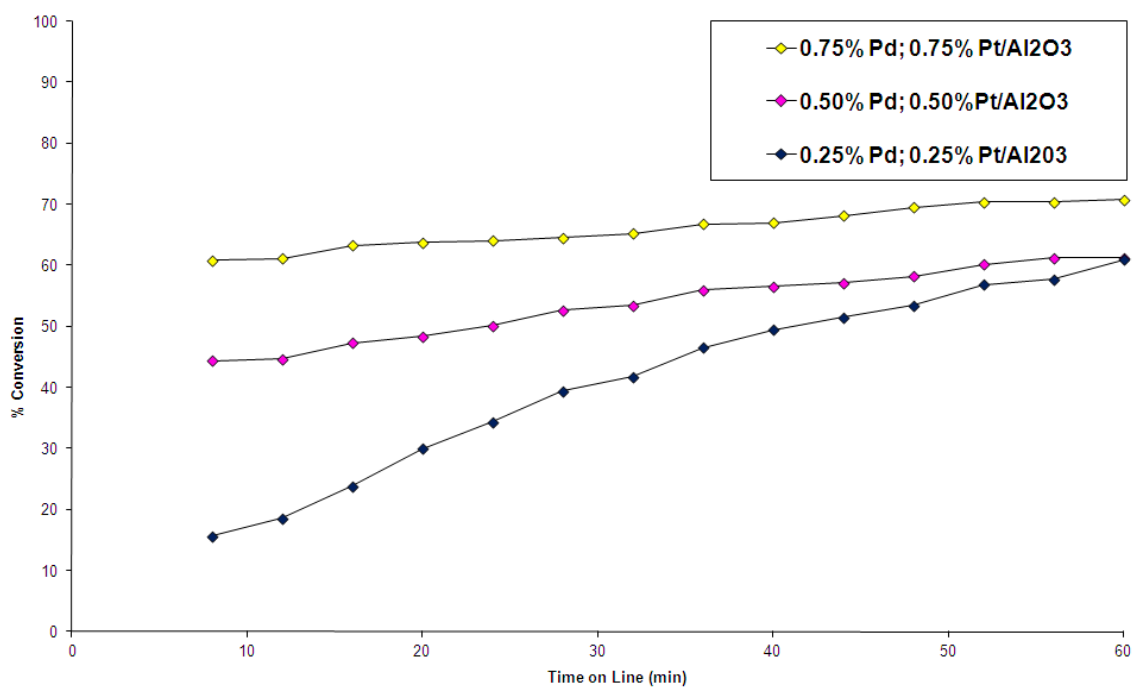


Figure 68 – CO Conversion % - variable bimetallic Pt/Pd-doped Al₂O₃ spheres

An investigation into Pt/Pd catalyst synergy was conducted using the data displayed in Figures 66-68. In Figure 69 the activities of a bimetallic Pt and Pd catalysts (Batch 3), are compared to the activities of the single metal counterparts (Batches 1 and 2). Batch 3

consists of 1 g of bimetallic 0.75% Pt, 0.75% Pd impregnated spheres. This will exhibit the combined activities of Pt, Pd and any synergy between the two. Comparing Batch 3 activity to a batch which contains the activity of monometallic Pd and Pt, without direct Pt \leftrightarrow Pd interactions, will show the synergy between the two metals. This comparison batch could not be experimentally synthesised. A perfect catalyst comparison would have identical support volume and metal weighting, without the distinct metal atoms in direct contact. This requires the metal salts to be impregnated onto separate Al_2O_3 beads. Given the divergent activities displayed in Figures 66, 67 & 68, doubling the metal loading (to 1.50%) on half the volume of support would result in a changed catalyst surface with non-comparable results. Doubling the support volume, and thus the bed length, would result in a change in gas contact time. As a result, the comparison batch activity was necessarily calculated theoretically from data collected with comparable batches.

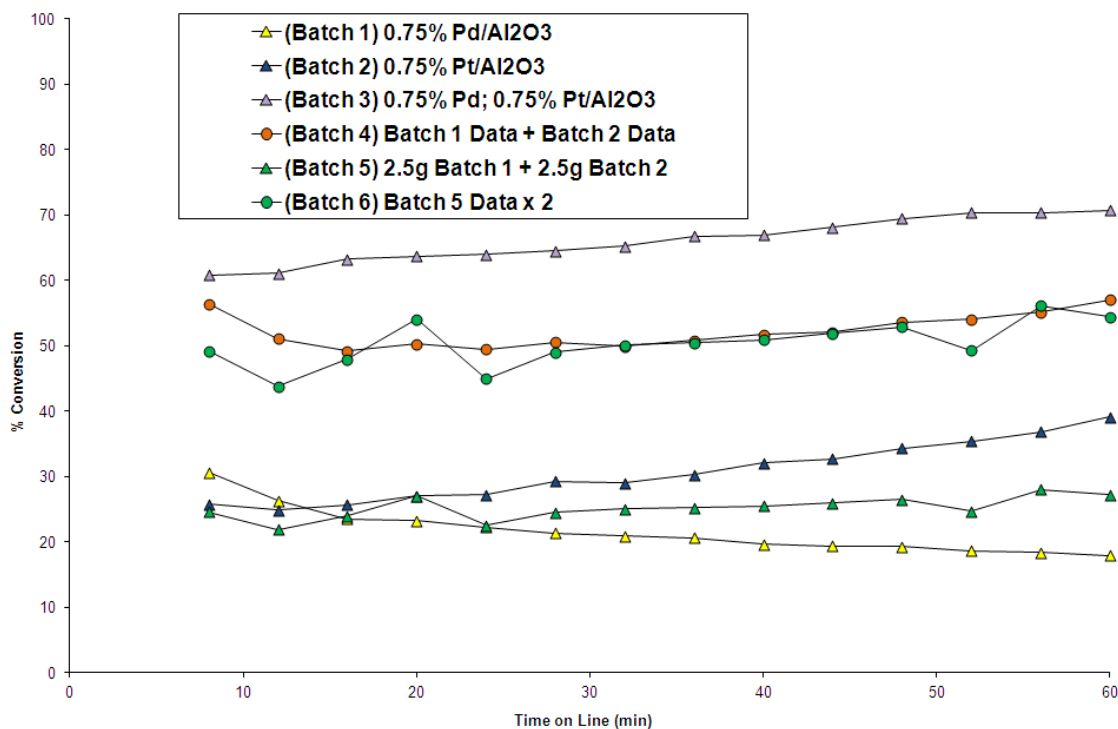


Figure 69 – 0.75% Pt, 0.75% Pd Synergy Activity Graph

Batch 4 is a theoretical activity, the activities of batches 1 and 2 added together. This data can only be called an approximation, as a ‘true’ catalyst batch would witness slightly

lower activity. This is because CO oxidised by one of the metals would not be available for oxidation by the other. For this reason, a second testing procedure was used. Batch 5 is comprised of 0.50g Al_2O_3 support impregnated with 0.75% Pt, as well as 0.5g Al_2O_3 support impregnated with 0.75% Pd. The bed dynamics and testing procedures for this batch are identical to the other 1g batches. The total metal loadings are half that of Batch 3. For this reason, Batch 5 activity is doubled and reported as 'theoretical' Batch 6. This testing method is also an approximation. A 'true' catalyst batch would have double the total metal loading to interact with H_2O in the gas stream, which necessarily remains a constant. CO oxidation over Pt has been described as promoted by water⁷. Doubling the activity could also lead to a theoretical activity of over 100%.

Figure 69 displays that the activity of the two 'theoretical' batches (4 and 6) are equivalent, showing steady state activity ~57%. This is evidence that the theoretical methods of measuring them are sound. The chance of the unique weaknesses in each approach resulting in an equivalent activity supports this. Batch 3, the bimetallic catalyst, displays activity higher than is predicted by batches 4 and 6, with a steady state of ~70%. This additional activity could be attributed to a synergy between Pt and Pd metals. However, the modifications to the catalyst bed have allowed other variables to change in this experiment. The 'half sized' catalyst beds will display changed mass transfer effect as well as variations in the bed exotherm. The 25°C water bath will not be effective in reducing the temperature at active sites. As the CO oxidation reaction is both exothermic and temperature dependant, this data cannot be simply 'doubled' akin to the metal loadings. This experimental weakness means Pt-Pd synergy is probable, and would need further confirmation.

Displayed in Figures 70 and 71 is data detailing equivalent experiments with 0.50% Pt, 0.50% Pd and 0.25% Pt, 0.25% Pd catalysts. Equivalent activity is observed for all paired theoretical batches. A deactivation from 47% to 35% occurs in the 0.25%/0.25% catalyst batch. The experimental activity shows that synergetic effects between Pt and Pd are more complicated than have been previously observed. 0.25%/0.25% and 0.50%/0.50% bimetallic catalysts display a lower initial activity (~16% and ~43% respectively,

compared to ~61% for the 0.75%, 0.75% catalyst) than the theoretical values. This conversion rises with time, and all batches exceed the activity of the theoretical data before the conclusion of the experiment. The 0.25%, 0.25% catalyst displays lower initial activity than either of the single metal catalysts. This data could indicate that Pt/Pd synergetic effects are responsible for raising the long term activity of a catalyst, and poisoning the short term activity. Alternatively, the possible exotherm or mass transfer effects described earlier maybe affecting the result. Activity loss attributable to a lower temperature would be correlated to lower active site concentrations and thus lower reagent Pt and Pd loadings.

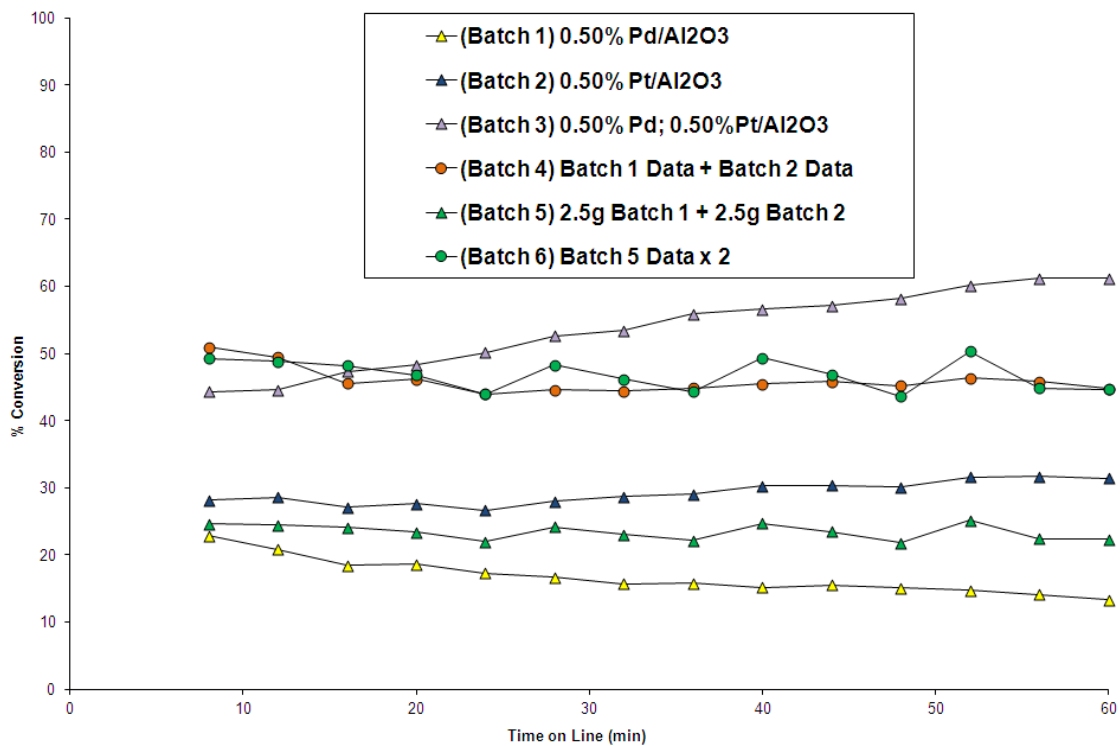


Figure 70 – 0.50% Pt, 0.50% Pd Synergy Activity Graph

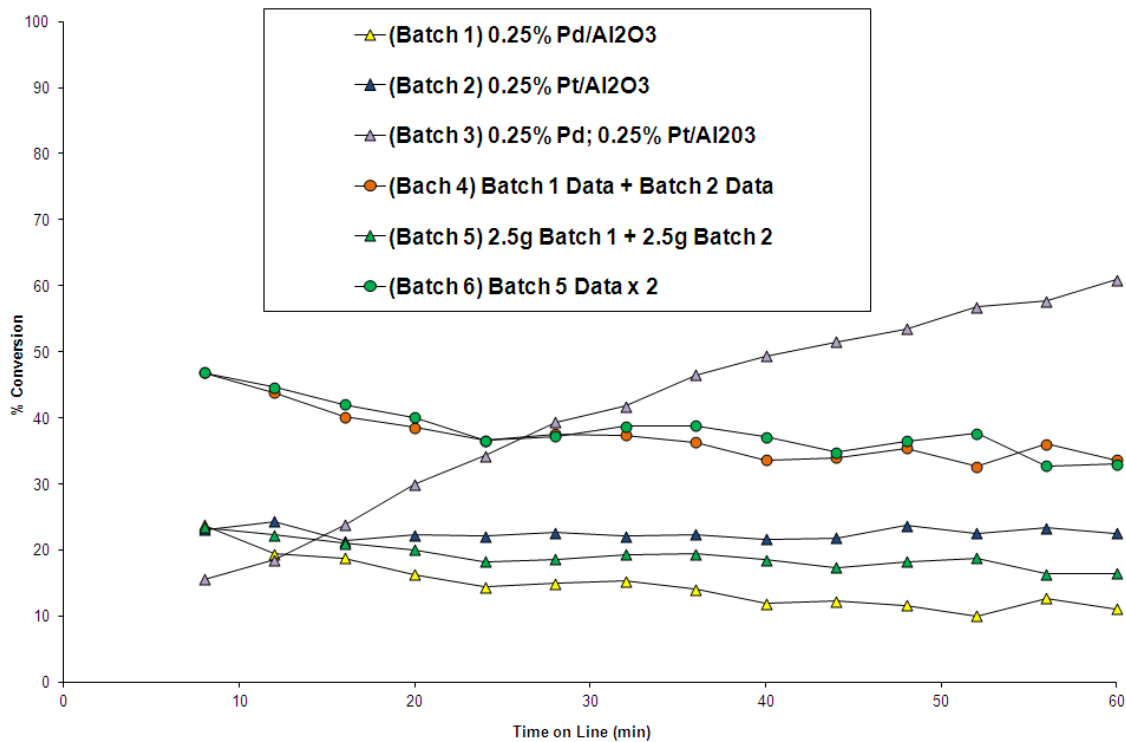


Figure 71 – 0.25% Pt, 0.25% Pd Synergy Activity Graph

5.1.2 Ultraviolet Visible Spectra

The filtrate solution of each experiment was tested using a UV visible spectrometer. Band maximum ' λ^{\max} ' and absorbance 'A' in respect to time is listed in Tables 22 & 23. The catalysts were tested according to the experimental procedure detailed in Chapter 2. The 0 h solution describes the metal salt solution directly after dilution to experimental volume. The 'reference experiment' details a preparation identical to the experimental method described in Chapter 2, without the introduction of alumina support.

		Experiment							
		0 h		0.5 h		24 h		48 h	
Pt%	Pd%	λ^{\max}	A	λ^{\max}	A	λ^{\max}	A	λ^{\max}	A
0.00	0.00	no abs	no abs	no abs	no abs	no abs	no abs	no abs	no abs
0.00	0.25	293nm	0.37	291nm	0.11	291nm	0.02	no abs	no abs
0.00	0.50	300nm	0.72	298nm	0.13	295nm	0.01	no abs	no abs
0.00	0.75	298nm	1.11	300nm	0.13	298nm	0.03	no abs	no abs
0.00	1.00	299nm	1.44	295nm	0.14	300nm	0.03	no abs	no abs
0.25	0.00	306nm	0.76	297nm	0.10	295nm	no abs	no abs	no abs
0.50	0.00	297nm	1.55	300nm	0.10	302nm	0.02	292nm	0.02
0.75	0.00	302nm	2.23	301nm	0.11	297nm	0.03	293nm	0.02
0.25	0.25	305nm	1.40	292nm	0.13	293nm	0.03	295nm	0.03
0.50	0.50	297nm	2.76	294nm	0.13	298nm	0.10	294nm	0.03
0.75	0.75	298nm	3.97	296nm	0.14	304nm	0.12	295nm	0.03

Table 22 – UV visible spectra data of filtrate solutions for each experiment

λ^{\max} = Band Maximum, A = Absorption

The data displays that during the experiment, adsorption, and thus by extrapolation⁸ concentration, drops over time. Adsorption reduces by more than 95% at 24 h regardless of initial concentration. This would indicate that the ion responsible for the λ^{\max} band is no longer present in an aqueous state. This could mean that aqueous ions are now present as solid particles in a colloid, or have been adsorbed on the alumina surface. The experimental observations were of the yellow/brown coloration present in solution disappearing and a similar colour appearing on the surface of the alumina pellets in an

eggshell⁹ coating. The colours of the Pt and Pd salt solutions were, respectively, yellow and brown.

		Reference Experiment							
		0 h		0.5 h		24 h		48 h	
Pt%	Pd%	λ^{\max}	A	λ^{\max}	A	λ^{\max}	A	λ^{\max}	A
0.00	0.00	no abs	no abs	no abs	no abs	no abs	no abs	no abs	no abs
0.00	0.25	293nm	0.37	291nm	0.35	292nm	0.32	300nm	0.30
0.00	0.50	300nm	0.72	295nm	0.69	295nm	0.64	298nm	0.60
0.00	0.75	298nm	1.11	299nm	1.05	300nm	0.97	297nm	0.91
0.00	1.00	299nm	1.44	302nm	1.22	301nm	1.15	301nm	1.10
0.25	0.00	306nm	0.76	306nm	0.82	294nm	0.82	305nm	0.80
0.5	0.00	297nm	1.55	297nm	1.35	297nm	1.28	304nm	1.25
0.75	0.00	302nm	2.23	295nm	1.89	306nm	1.74	307nm	1.71
0.25	0.25	305nm	1.40	300nm	1.21	301nm	1.15	302nm	1.13
0.50	0.50	297nm	2.76	305nm	2.54	298nm	2.41	296nm	2.36
0.75	0.75	298nm	3.97	307nm	3.61	300nm	3.52	299nm	3.45

Table 23 – UV visible spectra data of filtrate solution each reference experiment

λ^{\max} = Band Maximum, A = Absorption

Evidence for ion adsorption is supported by the reference experiment, which displays a smaller reduction in concentration over the same time period with all other variables accounted for. The decrease observed in the reference experiment can be accounted for by ligand exchange to $\text{Pd}(\text{Cl})_x(\text{OH}_x)^{2-}$. This is due to interaction with the introduced NaOH, as described in Tait *et al.*¹⁰.

Identifying the adsorption bands observed is problematic. Literature values of UV visible spectra are varied. Duyckaerts¹¹ compiles several studies and places Pd^{2+} λ^{\max} at 505, 305, 383, 380, 408, 500, 500 and 376 nm. PtCl_6^{2-} λ^{\max} is reported located at 403, 263, 500 and 500 nm. Harada *et al.*¹² displays the adsorption band for Na_2PdCl_4 at ~208 nm. He also discusses a reduction in the absorbance correlating to introduction of NaOH. He theorises that ligand exchange from Cl^- to OH^- accounts for this observation. His theory would account for the reduction in absorbance observed in the reference experiments displayed in Table 23. Reference experiments were supplemented with NaOH to

compensate for pH rise from 3.15. Harada¹² also describes Pd(OH)_x compounds as superior for forming small Pd deposits on carbon supports. This suggests that the NaOH introduced into solution may be responsible for factors other than pH control. Tait *et al.*¹⁰ described PdCl₄²⁻ UV band λ^{\max} occurring at 474 nm. He also described a reduction in absorbance correlating with introduction of OH⁻ ligands to the chloride complex.

Given the lack of literature consensus, the exact location of bands attributable to Pd and Pt salts in solution cannot be inferred from this data. It is known from the work of Tait, Duyckearts and Harada that Pt and Pd ions register as clear adsorption bands on UV spectra. The large observed bands are greatly reduced in the 24 h and 48 h stages of the experiments. It can be deduced that at least ~75% of Pt and Pd ions are no longer present in solution after 24 h of electrostatic adsorption onto gamma alumina pellets. They may be present as ions with hydroxide ligands, or adsorbed onto the alumina support.

5.1.3 EDX Molar Ratio

The Pt and Pd weight % content of each sample defined by EDX spectroscopy is displayed in Tables 24. The EDX method is described in more detail in Chapter 2. This data shows that Pt and Pd are present in the sample, in approximately the same loadings as the reagent quantities.

Sample	0.00%Pt, 0.00%Pd		0.25%Pt, 0.00%Pd		0.50%Pt, 0.00%Pd		0.75%Pt, 0.00%Pd	
	Pt %	Pd %	Pt %	Pd %	Pt %	Pd %	Pt %	Pd %
1	0.00	0.00	0.23	0.00	0.42	0.00	1.04	0.00
2	0.00	0.00	0.27	0.00	0.68	0.00	0.76	0.00
3	0.00	0.00	0.34	0.00	0.24	0.00	0.72	0.00
4	0.00	0.00	0.11	0.00	0.64	0.00	0.58	0.00
5	0.00	0.00	0.23	0.00	0.5	0.00	0.75	0.00
6	0.00	0.00	0.25	0.00	0.48	0.00	0.82	0.00
7	0.00	0.00	0.29	0.00	0.38	0.00	0.65	0.00
8	0.00	0.00	0.20	0.00	0.50	0.00	0.98	0.00
Mean	0.00	0.00	0.24	0.00	0.48	0.00	0.79	0.00

Sample	0.00%Pt, 0.25%Pd		0.00%Pt, 0.50%Pd		0.00%Pt, 0.75%Pd		0.00%Pt, 1.00%Pd	
	Pt %	Pd %	Pt %	Pd %	Pt %	Pd %	Pt %	Pd %
1	0.00	0.23	0.00	0.51	0.00	0.97	0.00	1.00
2	0.00	0.43	0.00	0.54	0.00	0.97	0.00	0.78
3	0.00	0.21	0.00	0.62	0.00	0.67	0.00	0.56
4	0.00	0.34	0.00	0.34	0.00	0.64	0.00	0.67
5	0.00	0.25	0.00	0.49	0.00	0.45	0.00	1.45
6	0.00	0.19	0.00	0.43	0.00	0.79	0.00	1.32
7	0.00	0.23	0.00	0.56	0.00	0.78	0.00	1.12
8	0.00	0.15	0.00	0.65	0.00	0.58	0.00	1.01
Mean	0.00	0.25	0.00	0.52	0.00	0.73	0.00	0.99

Sample	0.25%Pt, 0.25%Pd		0.50%Pt, 0.50%Pd		0.75%Pt, 0.75%Pd	
	Pt %	Pd %	Pt %	Pd %	Pt %	Pd %
1	0.24	0.26	0.50	0.56	0.65	0.76
2	0.31	0.32	0.54	0.39	0.69	0.43
3	0.23	0.21	0.42	0.54	0.79	0.79
4	0.29	0.34	0.69	0.10	0.75	1.01
5	0.19	0.27	0.50	0.25	0.65	0.45
6	0.23	0.20	0.32	0.36	0.59	0.73
7	0.25	0.24	0.45	0.44	0.81	0.68
8	0.21	0.31	0.47	0.59	0.78	0.69
Mean	0.24	0.27	0.49	0.40	0.71	0.69

Table 24 – EDX Spectroscopy, mean average Pt & Pd weightings

5.2 Investigation into optimum Pt/Pd ratio

Platinum and palladium deposited on Al_2O_3 have been described as exhibiting synergetic activity increases in regard to ambient temperature CO oxidation in Section 5.1. This phenomenon was observed with Pt and Pd loadings in a 1:1 ratio. This section investigates the most effective Pt:Pd loading ratio. Ratios reported in this chapter will always be in the form of (Pt):(Pd). Economically, the commercial price of Pt (ranging from \$1400 to \$1780/oz during 2010) is roughly three times as expensive as Pd (\$350 to \$775/oz in 2010)¹³. Pd will therefore be the major component of a mixed Pt/Pd catalyst.

Persson *et al.*¹⁴ studied bimetallic Pt/Pd catalysts for methane combustion and reported 50:50 and 67:33 ratios most active and stable compared to four others tested. Castellazzi *et al.*¹⁵ reported an inhibiting effect correlating with rising Pt weight on a PdO catalyst in regard to CH_4 oxidation. Kaya *et al.*¹⁶ investigated Pt:Pd bimetallics on alumina for CO oxidation. Rising Pd content was correlated with an increase in particle size. Kaya did not observe any Pt:Pd synergy below 423K. The catalysts prepared by Kaya were from incipient wetness techniques and were not reduced by sodium formate. This could explain the differences seen between her experiments and those in Section 5.1.

A series of Pt & Pd impregnated catalysts were prepared. Individual metal Pt and Pd catalysts were prepared as reference standards. The exact synthesis method is described in Chapter 2. Pd weightings of between 0.10% and 0.70%, and Pt weightings of 0.04% to 0.16%, were deposited onto 1 g batches of Al_2O_3 spheres in an effort to find the most efficient CO oxidation catalyst. The alumina support, Al_2O_3 , is known to have no independent activity for this reaction.

Palladium and platinum were electrostatically adsorbed onto 2-3mm γ - Al_2O_3 spheres. Platinum tetrachloride and sodium palladium tetrachloride were selected as the most applicable cationic reagents, as described in Chapter 1.

5.2.1 CO Oxidation Activity

The activity of catalyst batches containing a 0.10% loading of platinum and a variable loading of palladium between 0.10% to 0.70% weight is displayed in Figure 72.

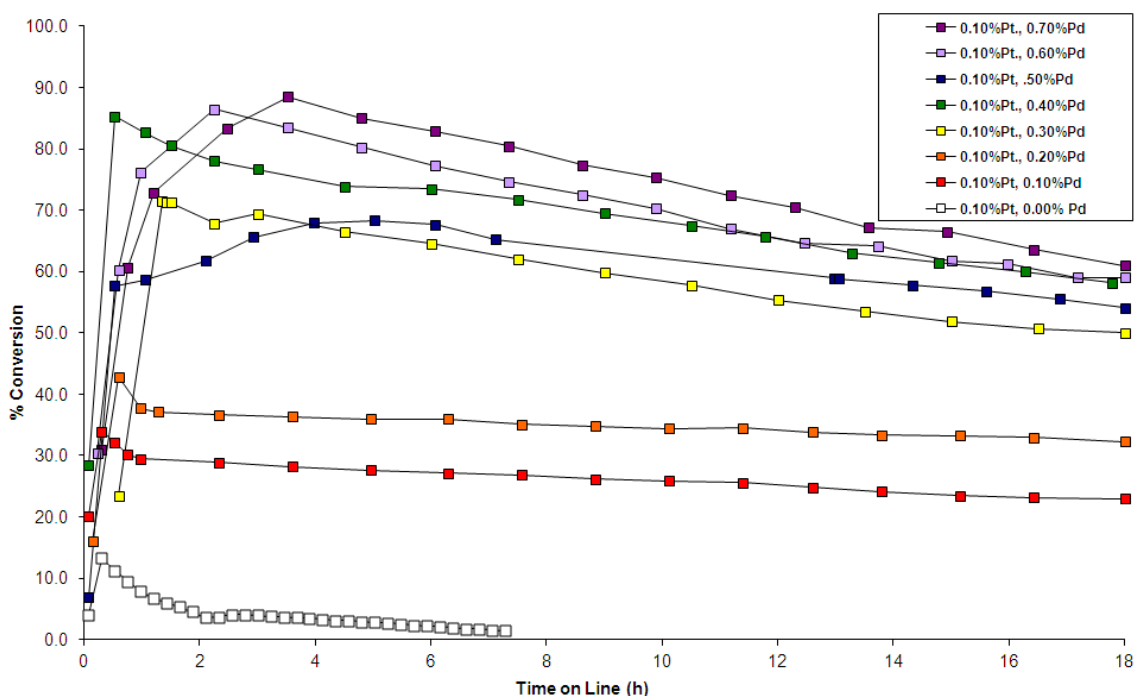


Figure 72 – CO Oxidation Activity, 0.10% Pt, variable % Pd/ Al_2O_3

All catalyst batches display a similar initial activity peak, followed by a smooth line out period. Steady state activity of the 0.10, 0.20 and 0.30% Pd doped catalysts increase significantly in line with the palladium loadings. The 0.40%, 0.60% and 0.70% doped catalysts display improved duration of initial activity peaks in line with palladium loadings. The 0.50% catalyst does not follow this trend, displaying an inferior initial activity peak to even the 0.30% doped catalyst. In regard to overall activity, the 0.40 to 0.70% Pd loaded catalysts do not display increasing activity in line to the trend established with the 0.10 to 0.30% Pd loadings. All data points are equivalent at the conclusion of the data set approximating ~59% activity. The 0.40 to 0.70% catalysts do not display a steady state activity at this conclusion, and are continuing to slowly fall in activity. This data suggests that increasing the Pd loading beyond 0.40% has a much

smaller effect on activity than the increase seen between 0.10% and 0.40% loading. All mixed metal catalysts are far more active than the single Pt catalyst, which peaks at ~15% conversion and becomes inactive at ~8 h. An experimental observation was made, at around 4 h, droplets of water began to form on the inside of the micro reactor and also lay on the surface of the alumina pellets. The rate of deactivation for the catalysts did not change at the 4 h mark.

The activity of catalyst batches containing a variable loading of platinum and a 0.40% loading of palladium is displayed in Figure 73.

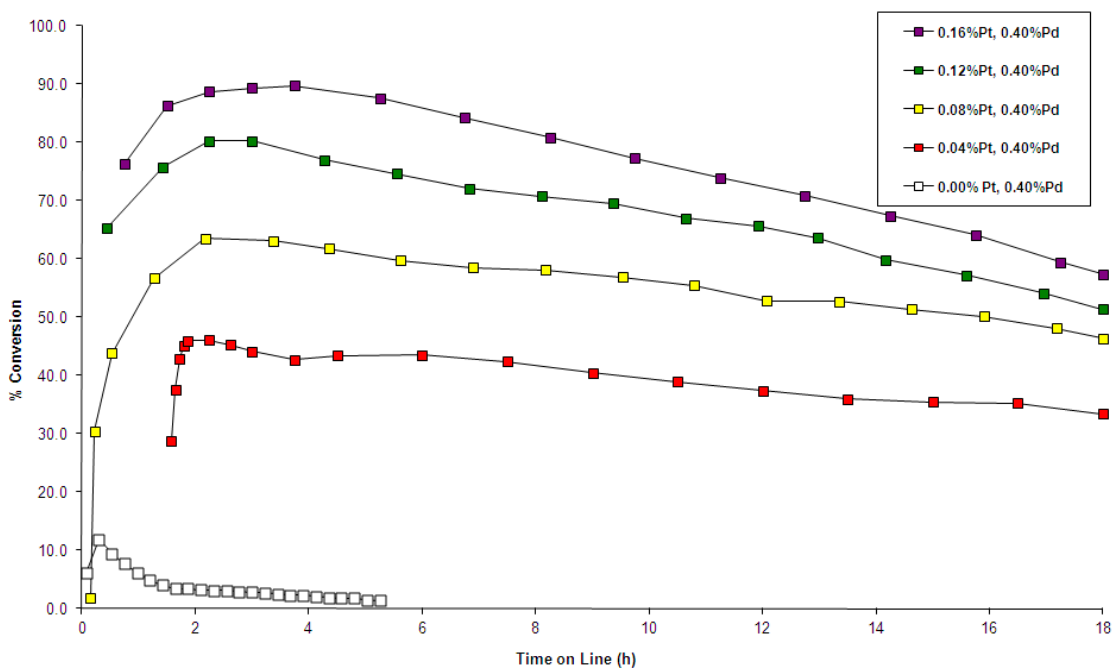


Figure 73 – CO Oxidation Activity, variable % Pt, 0.40% Pd/ Al_2O_3

All catalyst batches display an initial activity peak, and a gradually decreasing deactivation period concluding without reaching steady state activity. Catalyst activity rises with increased Pt loading, although the rise in activity is not directly correlated to the exact Pt loading. Sequential 0.04% increases in weight of Pt result in progressively smaller activity rises. All mixed metal catalysts are far more active than the single Pd catalyst, which peaks at ~11% conversion and becomes inactive at ~6 h.

5.2.2 Ultraviolet Visible Spectra

The filtrate solution of each experiment was tested using a UV visible spectrometer. Band maximum, λ^{\max} , and absorbance, A, in respect to time is listed in Tables 25 to 28. The filtrates were testing according to the experimental procedure detailed in Chapter 2. The 0h describes metal salt solution directly after dilution to experimental volume. The reference experiment details a preparation identical to the experimental method described in Chapter 2, without the addition of alumina pellets. The issues with deducing chemical identification with this technique are discussed in Section 5.1.

		Reference Experiment							
		0 h		0.5 h		24 h		48 h	
Pt%	Pd%	λ^{\max}	A	λ^{\max}	A	λ^{\max}	A	λ^{\max}	A
0.00	0.00	no abs	no abs	no abs	no abs	no abs	no abs	no abs	no abs
0.10	0.00	294nm	0.31	294nm	0.28	295nm	0.27	302nm	0.26
0.10	0.10	306nm	0.36	299nm	0.44	295nm	0.43	300nm	0.42
0.10	0.20	302nm	0.67	300nm	0.70	298nm	0.68	297nm	0.50
0.10	0.30	297nm	0.97	296nm	0.75	300nm	0.74	296nm	0.70
0.10	0.40	299nm	1.21	298nm	0.96	294nm	0.94	294nm	0.94
0.10	0.50	298nm	1.31	300nm	1.05	297nm	1.01	290nm	0.86
0.10	0.60	300nm	1.54	296nm	1.19	300nm	1.14	305nm	1.10
0.10	0.70	299nm	1.65	298nm	1.45	302nm	1.36	302nm	1.26

		Variable Pd Experiment							
		0 h		0.5 h		24 h		48 h	
Pt%	Pd%	λ^{\max}	A	λ^{\max}	A	λ^{\max}	A	λ^{\max}	A
0.00	0.00	no abs	no abs	no abs	no abs	no abs	no abs	no abs	no abs
0.10	0.00	294nm	0.31	292nm	0.10	292nm	0.03	no abs	no abs
0.10	0.10	306nm	0.36	294nm	0.10	290nm	0.03	no abs	no abs
0.10	0.20	302nm	0.67	288nm	0.11	289nm	0.03	no abs	no abs
0.10	0.30	297nm	0.97	290nm	0.11	293nm	0.04	no abs	no abs
0.10	0.40	299nm	1.21	292nm	0.13	289nm	0.05	no abs	no abs
0.10	0.50	298nm	1.31	291nm	0.13	290nm	0.05	no abs	no abs
0.10	0.60	300nm	1.54	290nm	0.13	287nm	0.06	290nm	0.02
0.10	0.70	299nm	1.65	291nm	0.15	290nm	0.08	292nm	0.07

Tables 25 & 26 – UV visible spectra data of filtrate solutions, variable Pd experiment

λ^{\max} = Band Maximum, A = Absorption

It can be observed that during the experiments, the metal chloride band reduces by ~90-95% during the first 24 h of the deposition procedure. By comparison, the reference experiment shows an approximate reduction between 5% and 40%. It can be deduced that the chloride solution concentration has dropped, according the Beer-Lambert law⁸. Assuming this is being adsorbed onto the alumina support, gives the catalyst a total metal weighing of ~95% the reagent weighting. Extension of the deposition time increases this total to ~95-100% yield at 48 h. It can be inferred that ~55-95% Pt and Pd ions are no longer present in solution after 24 h of EA conditions with γ -alumina pellets.

		Reference Experiment							
		0 h		0.5 h		24 h		48 h	
Pt%	Pd%	λ^{\max}	A	λ^{\max}	A	λ^{\max}	A	λ^{\max}	A
0.00	0.00	no abs	no abs	no abs	no abs	no abs	no abs	no abs	no abs
0.00	0.40	299nm	0.60	301nm	0.65	302nm	0.71	306nm	0.61
0.04	0.40	296nm	0.73	297nm	0.74	296nm	0.72	296nm	0.72
0.08	0.40	297nm	0.82	298nm	0.87	297nm	0.89	297nm	0.74
0.12	0.40	296nm	0.97	297nm	1.01	300nm	1.00	295nm	0.94
0.16	0.40	296nm	1.15	297nm	1.06	298nm	1.00	300nm	0.99

		Variable Pt Experiment							
		0 h		.5 h		24 h		48 h	
Pt%	Pd%	λ^{\max}	A	λ^{\max}	A	λ^{\max}	A	λ^{\max}	A
0.00	0.00	no abs	no abs	no abs	no abs	no abs	no abs	no abs	no abs
0.00	0.40	299nm	0.60	292nm	0.14	292nm	0.13	292nm	0.12
0.04	0.40	296nm	0.73	294nm	0.12	290nm	0.11	291nm	0.11
0.08	0.40	297nm	0.82	293nm	0.14	291nm	0.11	292nm	0.10
0.12	0.40	296nm	0.97	289nm	0.13	290nm	0.12	290nm	0.11
0.16	0.40	296nm	1.15	291nm	0.15	293nm	0.14	289nm	0.12

Table 27 & 28 – UV visible spectra data of filtrate solutions, variable Pt experiment

λ^{\max} = Band Maximum, A = Absorption

5.2.3 EDX Molar Ratio

The Pt and Pd content of each sample defined by EDX spectroscopy is displayed in Tables 29 and 30. The EDX method is described in more detail in Chapter 2. Data shows that Pt and Pd are present in the sample, within approximate loadings of the reagent quantities.

Sample	0.00%Pt, 0.00%Pd		0.00%Pt, 0.40%Pd		0.04%Pt, 0.40%Pd	
	Pt %	Pd %	Pt %	Pd %	Pd %	Pt %
1	0.00	0.00	0.00	0.37	0.02	0.41
2	0.00	0.00	0.00	0.45	0.01	0.42
3	0.00	0.00	0.00	0.40	0	0.49
4	0.00	0.00	0.00	0.41	0.05	0.43
5	0.00	0.00	0.00	0.34	0.04	0.34
6	0.00	0.00	0.00	0.42	0.04	0.32
7	0.00	0.00	0.00	0.57	0.03	0.40
8	0.00	0.00	0.00	0.35	0.04	0.43
Mean	0.00	0.00	0.00	0.41	0.03	0.41

Sample	0.08%Pt, 0.40%Pd		0.12%Pt, 0.40%Pd		0.16%Pt, 0.40%Pd	
	Pd %	Pt %	Pd %	Pt %	Pd %	Pt %
1	0.04	0.41	0.13	0.43	0.17	0.27
2	0.01	0.62	0.14	0.31	0.15	0.34
3	0.10	0.40	0.11	0.42	0.12	0.41
4	0.09	0.40	0.12	0.43	0.16	0.42
5	0.13	0.36	0.11	0.67	0.15	0.45
6	0.08	0.43	0.14	0.40	0.20	0.78
7	0.07	0.40	0.13	0.45	0.10	0.47
8	0.08	0.41	0.12	0.43	0.16	0.31
Mean	0.08	0.43	0.13	0.44	0.15	0.43

Table 29 – EDX Spectroscopy, mean average Pt & Pd weightings

Sample	0.00%Pt, 0.00%Pd		0.10%Pt, 0.00%Pd		0.10%Pt, 0.10%Pd	
	Pt %	Pd %	Pt %	Pd %	Pt %	Pd %
1	0.00	0.00	0.09	0.00	0.04	0.05
2	0.00	0.00	0.07	0.00	0.05	0.24
3	0.00	0.00	0.09	0.00	0.18	0.09
4	0.00	0.00	0.04	0.00	0.24	0.07
5	0.00	0.00	0.09	0.00	0.01	0.04
6	0.00	0.00	0.16	0.00	0.04	0.10
7	0.00	0.00	0.10	0.00	0.05	0.15
8	0.00	0.00	0.11	0.00	0.07	0.13
Mean	0.00	0.00	0.09	0.00	0.09	0.11

Sample	0.10%Pt, 0.20%Pd		0.10%Pt, 0.30%Pd		0.10%Pt, 0.40%Pd	
	Pt %	Pd %	Pt %	Pd %	Pt %	Pd %
1	0.08	0.12	0.04	0.30	0.02	0.45
2	0.03	0.15	0.05	0.38	0.13	0.42
3	0.12	0.45	0.15	0.39	0.08	0.87
4	0.18	0.08	0.07	0.23	0.01	0.32
5	0.23	0.23	0.10	0.25	0.23	0.34
6	0.21	0.27	0.24	0.13	0.21	0.35
7	0.10	0.27	0.12	0.46	0.10	0.42
8	0.02	0.21	0.09	0.30	0.12	0.40
Mean	0.12	0.22	0.11	0.31	0.11	0.45

Sample	0.10%Pt, 0.50%Pd		0.10%Pt, 0.60%Pd		0.10%Pt, 0.70%Pd	
	Pt %	Pd %	Pt %	Pd %	Pt %	Pd %
1	0.09	0.45	0.01	0.61	0.10	0.76
2	0.04	0.98	0.10	0.62	0.13	0.75
3	0.10	0.23	0.11	0.78	0.17	0.68
4	0.12	0.43	0.12	0.41	0.14	0.63
5	0.21	0.34	0.20	0.65	0.10	0.67
6	0.23	0.51	0.08	0.43	0.24	0.62
7	0.10	0.45	0.02	0.70	0.03	0.61
8	0.05	0.60	0.10	0.64	0.05	0.73
Mean	0.12	0.50	0.09	0.61	0.12	0.68

Table 30 – EDX Spectroscopy, mean average Pt & Pd weightings

5.2.4 X-Ray Photoelectron Spectroscopy

XPS spectra of monometallic catalysts are displayed in Figure 74. Al 2s peak (not shown) at 119eV shows surface Al appears to be present as Al_2O_3 – this is not unexpected.

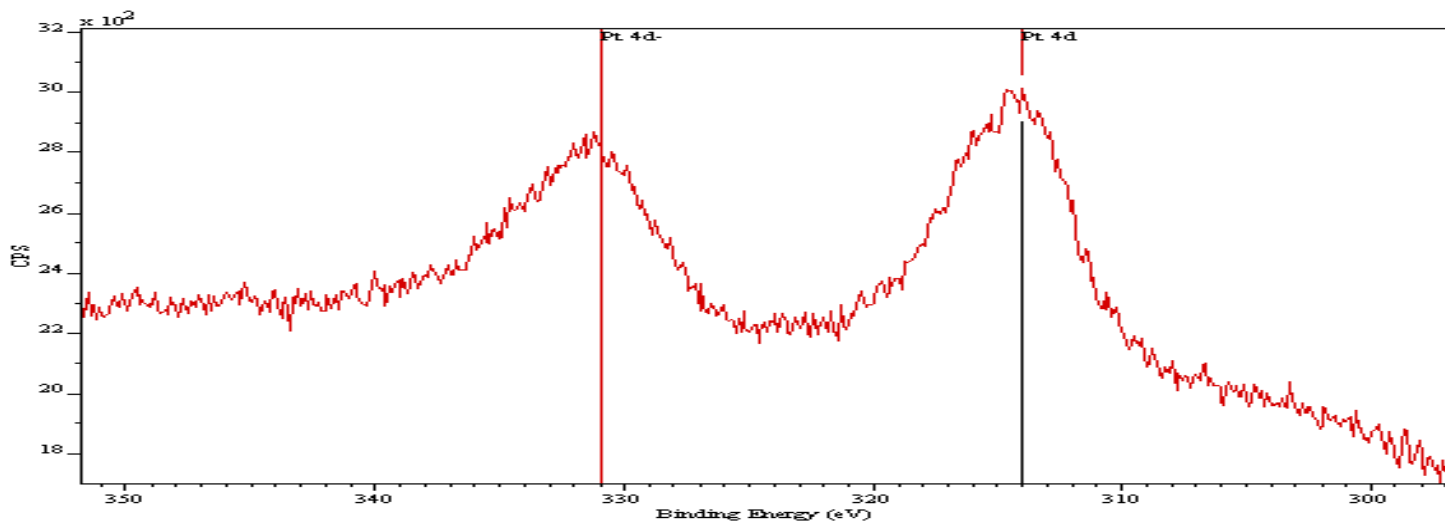
0.10% Pt/ Al_2O_3 (top and centre graphs) displays characteristic Pt 4d doublets at 331, 314 eV and Pt 4f at 74, 71 eV. Other peaks are obscured by the support Al_2O_3 signals. Neither peak displays the characteristic upward eV signal shift emitted by Pt^{2+} . The Pt 4f peak displays a small downward shift. This could be as a result of surface charging, or Pt alloying.

0.40% Pd/ Al_2O_3 (bottom) displays a Pd 3d doublet at 340, 335 eV. This peak shows no upward shift and corresponds to surface Pd^0 . There is a smaller doublet peak emerging at 336, 341. This peak splitting normally indicates the presence of a Pd oxide species.

XPS spectra of Pt/Pd/ Al_2O_3 bimetallics were also measured (not displayed to avoid repetition). In the first batch, Pt levels are fixed at 0.10% while Pd levels rise from 0.10% to 0.70%. In the second batch, Pd levels are fixed at 0.40% while Pt levels rise from .04% to 0.12%. The Pt and Pd signals across all ten samples display peaks at identical binding energies to the monometallic samples in Figure 60. This infers that surface Pt and Pd are present as Pt^0 and Pd^0 with some PdO. In addition, across both batches, as the variable loading of the second metal increases, the XPS signal of the fixed metal is not suppressed. This indicates that neither Pt nor Pd is preferentially segregating to the surface of bimetallic clusters. With this technique, measuring peak area is normally used to infer abundance. Difficulties due to the nature of the spherical support rendered the area data non-comparable across separate spheres. Thus relative abundance cannot be inferred from this technique, only presence.

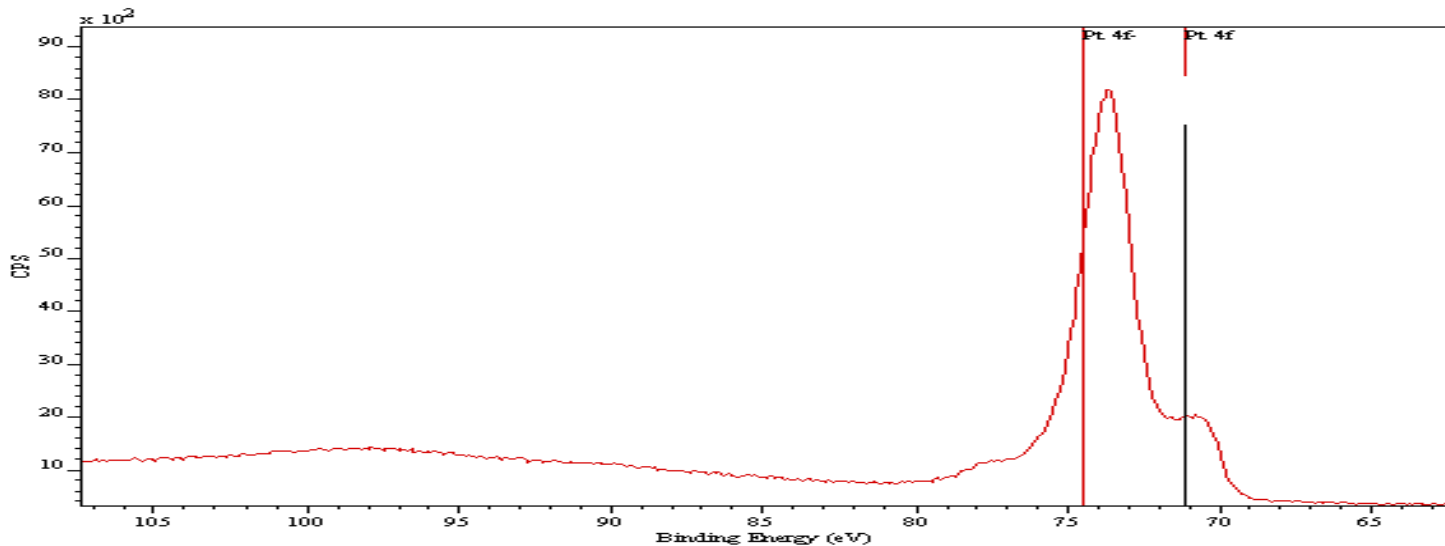
Chapter 5 - Bimetallic Pt-Pd Impregnated γ -Alumina

Pd 3d Pt 4d



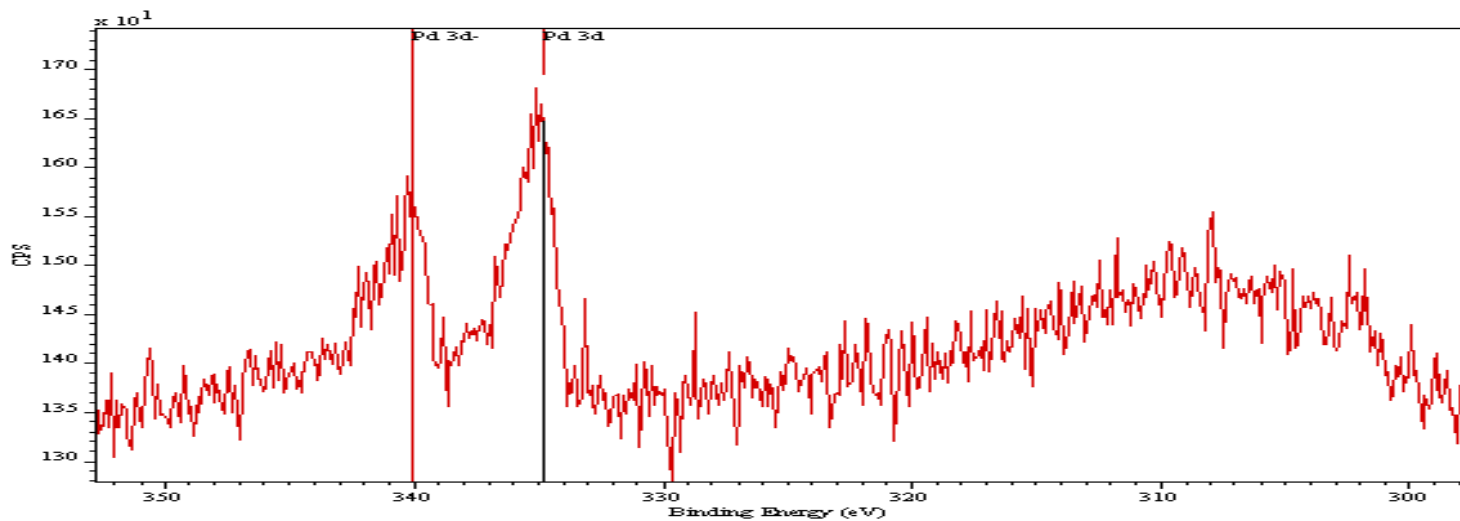
Cardiff Catalysis Institute, Cardiff, UK

Pd4s Al2p Pt4f



Cardiff Catalysis Institute, Cardiff, UK

Pd 3d Pt 4d



Cardiff Catalysis Institute, Cardiff, UK

Figure 74 – XPS Spectra of 0.10% Pt/Al₂O₃ (top & centre) and 0.40% Pd/Al₂O₃ (bottom)

5.3 Deposition of Pt/Pd upon Si /Al₂O₃

The literature reports that CO oxidation over Pt/Al₂O₃ catalysts is promoted by humidity⁷. An observation was made during the 18 h experiments detailed in 5.2. Water droplets were forming on the walls of the catalyst bed, commencing at ~4 h. These droplets also lay upon the surface of the alumina pellets. As discussed in Chapter 1.5.1, macroscopic water could act as a barrier to effective CO transfer. Modifying the water tolerance of the catalyst could allow compensation for this effect. Catalyst support hydrophobicity can be modified by doping with silyating reagents. Gas phase silylation of alumina has been reported by researchers such as Quintanilla *et al.*¹⁷, Omota *et al.*¹⁸ and Slavov *et al.*¹⁹⁻²¹. It has been established that SiO₂ displays hydrophilic properties, and Si(CH₃)₂ groups display hydrophobic properties. These studies are discussed in more detail in Chapter 1. Liquid phase silylation of alumina has not been previously reported. Adsorption of dichlorodimethylsilane (DDMS) onto alumina in toluene is likely to result in silylation of the alumina surface. This may change the hydrophobicity of the alumina surface.

Silicon was hydrothermally impregnated onto 2-3mm Al₂O₃ spheres. Spheres were later impregnated with Pt and Pd via electrostatic adsorption. Dichlorodimethylsilicon under toluene, platinum tetrachloride and sodium palladium tetrachloride was selected as reagents. A series of 2.0%, 5.0% and 10.0% Si impregnated catalysts were prepared. The exact synthesis method is described in Chapter 2. Precious metals in mass weightings of 0.10% Pt and 0.40% Pd were deposited onto the Si/Al₂O₃ sphere surface in an effort to find the most efficient CO oxidation catalysts.

5.3.1 CO Oxidation Activity

The activity of catalyst batches containing a 0.10% loading of Pt and a 0.40% loading of Pd weight is displayed in Figure 75.

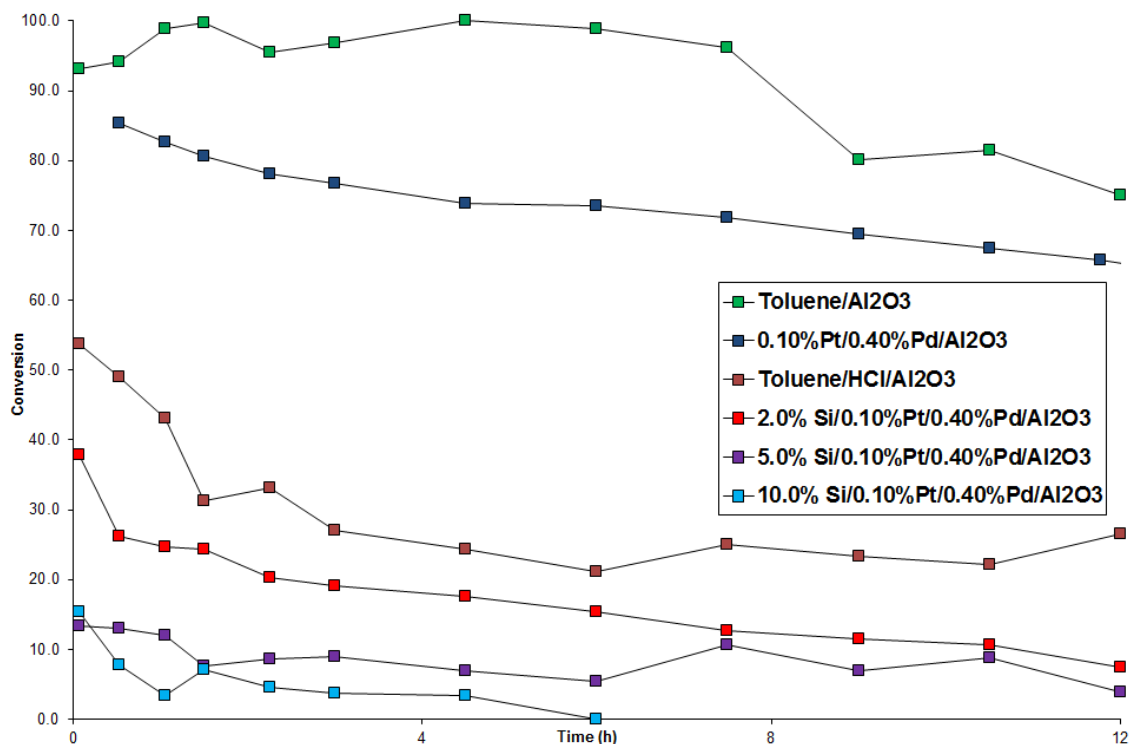


Figure 75 – CO Oxidation, variable Si/0.1%Pt/0.4%Pd doped Al₂O₃

The data displayed here is unambiguous. Increasing silicon loading on the support surface correlates to increasingly large reductions in catalyst activity. The untreated reference catalyst displays an initial activity of ~85%, displaying a smooth deactivation curve and a steady state of ~66%. The three silicon doped batches; 2.0%, 5.0% and 10.0%, display much lower initial activities of ~39%, ~15% and ~16% respectively. All three batches show smooth deactivation curves. The 2.0% and 5.0% Si batches show final activities of less than 10%, while the 10.0% Si doped catalyst becomes inactive at 6 h. The other two reference catalysts show unusual behaviour. The ‘solvent & ion’ reference was treated with toluene and HCl and shows deactivation similar to the Si doped batches. Activity begins at ~53% and drops to a steady state of ~28%. This indicates that a portion of catalyst activity loss is due to factors not influenced by Si. The solvent reference, treated with toluene only, is more active than the unmodified reference. This is not unexpected, as oxidised toluene will vaporise as CO₂. The activity displayed above cannot be attributed solely to oxidised CO.

5.3.2 BET Surface Area and XPS

Although useful in previous characterisation, neither of these techniques was successful in producing data. Both rely on high vacuum conditions which were unobtainable. This is most likely due to resilient methyl groups or catalysed CO₂ from toluene effervescing and disrupting analysis.

5.3.3 EDX Molar Ratio

The Pt, Pd, Si and Cl content of two samples of each batch analysed by EDX spectroscopy is displayed in Table 31. The EDX method is described in more detail in Chapter 2. This data shows that Si, Pt and Pd are present in the sample. Significant quantities of chlorine were also detected. Carbon would not be detected with this technique. Unmodified alumina displayed only aluminium and oxygen signals.

		Pellet No.	EDX Weight Percentage %					
			O	Al	Cl	Si	Pd	Pt
2.0% Si		1	55.24	42.62	1.98	0.16		
		2	55.94	41.88	2.02	0.17		
2.0% Si	.1, .4; Pt, Pd	1	54.15	44.46	0.29	0.08	0.83	0.19
		2	56.00	41.80	0.25	0.24	1.34	0.28
5.0% Si		1	55.10	41.73	2.63	0.54		
		2	53.24	43.43	2.67	0.70		
5.0% Si	.1, .4; Pt, Pd	1	53.20	43.78	1.22	0.80	0.64	0.38
		2	54.27	42.76	1.24	0.61	0.80	0.32
10.0% Si		1	51.87	44.68	2.53	0.92		
		2	53.25	43.36	2.46	0.93		
10.0% Si	.1, .4; Pt, Pd	1	55.93	42.14	0.84	0.43	0.37	0.30
		2	52.98	44.46	0.80	0.63	0.74	0.38

Table 31 – EDX data for Si, Pt and Pd doped Al₂O₃ spheres

5.3.4 Thermogravimetric Analysis

The TGA of single silylated alumina spheres was tested in a furnace from 25 to 400°C. All samples were silylated and desiccated before testing (see Chapter 2). This procedure was attempted to investigate the relative strength of H₂O adsorption on the sphere surface, as well as the stability of residual methyl groups from DDMS. The acquired data is displayed in Figure 75.

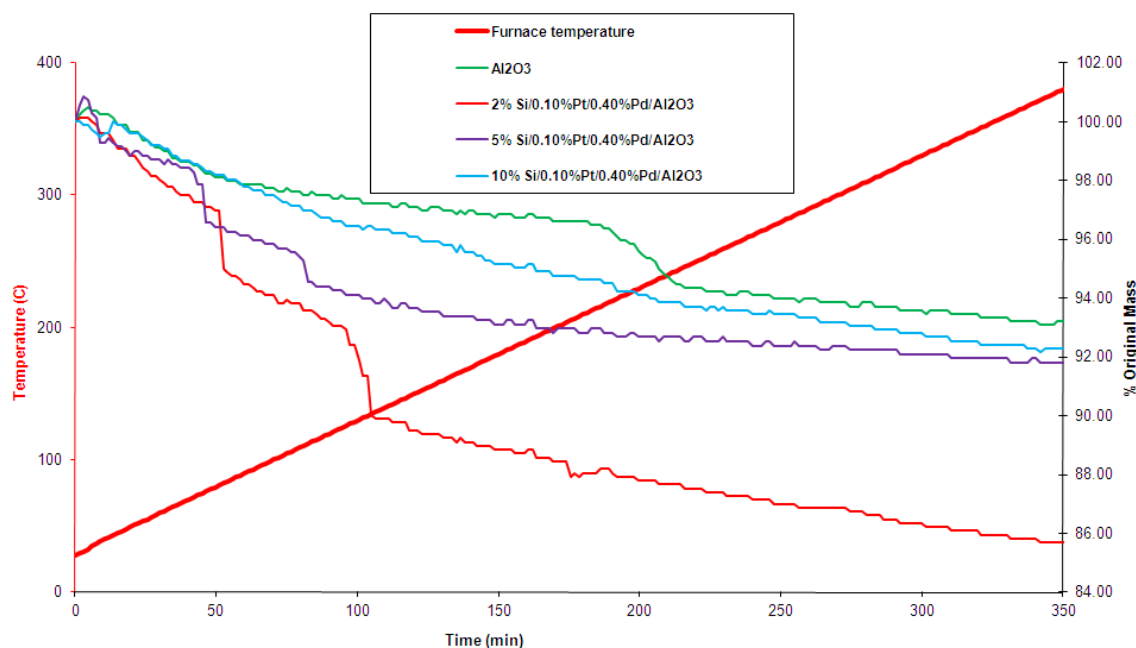


Figure 75 - TGA of Si doped Al₂O₃ spheres

It is demonstrated that silylated alumina behaves significantly differently to the undoped reference. All samples show slow mass loss with time. Some batches display distinct mass losses at certain temperatures. Reference alumina displays one distinct mass loss, at ~200°C. It can be inferred that this is loss of chemisorbed water, as there are no other candidates. At experimental conclusion, the sample has lost ~6.5% of total mass. 2.0% silylated alumina shows two distinct mass losses, at ~80°C and ~130°C. At experimental conclusion, the sample has lost ~14% of total mass. No mass loss is observed at ~200°C. 5.0% silylated alumina also displays two distinct mass losses, at ~75°C and ~110°C. No mass loss is exhibited at 200°C. At experimental conclusion, the sample has lost ~8% of

total mass. 10.0% sited alumina displays no significant mass losses, and at conclusion has lost ~8% of total mass. The distinct mass losses observed in the 2.0% and 5.0% samples suggest that the catalyst is sequentially shedding methyl groups^{17, 18}.

5.4 Discussion

5.4.1 Effective ratio towards synergy between Pt/Pd-Al₂O₃

Pt and Pd were electrostatically adsorbed onto γ -Al₂O₃ spheres. UV-Vis and EDX characterisation support the conclusion that 90-95% the reagent metals are present on the catalyst surface. The exact dispersion and morphology of metal particles was not characterised due to instrumental issues. Comparison of bimetallic activity with the activity of single metal catalysts displays a steady state activity increase. The 0.75%/0.75% catalyst show a superior activity to reference catalysts at all times. The 0.25%/0.25% and 0.50%/0.50% catalysts show an inferior activity at the start of the experiment which rises within 1 h to exceed the reference batches. These changes could be explained by synergetic activity between Pt and Pd, or another interaction.

Experimentally speaking, two non-synergetic conditions could be affecting the bimetallic Pt and Pd synthesis. Considering the two reagents, the interaction of ligand salt ions with the opposite metal is the first possibility. Na⁺ ions are present in the salt solution from the Pd salt, which may have an effect upon PtCl₆²⁻ anions. Na⁺ ions are later introduced into the catalyst via sodium formate, and as such any unique interaction would have to be in the adsorption rather than reduction stage. Sodium chloroplatinate is a known compound, soluble in water to PtCl₆²⁻. As such it would seem unlikely that any Cl ligand exchange to Na had taken place. The effects of the other ions, Cl⁻ and H⁺, can be considered nil, as they are both present in the monometallic catalyst synthesis.

Secondly, a possibility is that Pd and Pt exhibit synergy as they react with a substance that the other reaction considers a poison, or produce a substance the other considers a promoter. This is very unlikely, as the two reactions are so similar as to be considered

identical by some researchers²². Although the reactions are equivalent, it could be theorised that one of the metals is slightly more susceptible to CO/CO₂ self poisoning or H₂O promotion. This could change the reaction concentrations of reagents on the opposite metal. This can be considered to be very unlikely. The concentrations of CO, CO₂ and H₂O over the catalyst are being continually refreshed by the gas stream.

Excluding these possibilities, Pt-Pd synergy can be attributed to morphological or electronic interactions between the metal atoms. Changes in metal dispersion or Pt/Pd alloying are possibilities. Metal dispersion could not be measured due to equipment issues. Bimetallic alloying has been reported by Park and Lee²³ and Kaya and Üner²⁴. Both conclude that Pd will segregate to the surface of Pt:Pd clusters. At low temperatures, the bimetallic particles behaved identically to monometallic Pd. Given that Pd is less active than Pt, EA synthesis was selected to avoid metal alloying. Due to the nature of EA, it is unlikely that two negatively charged metal anions would bond on the catalyst surface to form a bimetallic cluster. The activity data displays a far higher activity than monometallic palladium, which supports the conclusion that significant alloying has not occurred. XPS characterisation of the bimetallic catalysts showed that increasing the weighting on either Pt or Pd did not suppress the signal for the opposite metal. This would indicate that significant surface segregation of Pd or Pt has not occurred. This would be in concordance with the synthesis conditions.

With these morphological possibilities eliminated, the prospect of Pt/Pd electronic interactions must be considered. XPS data indicates that Pt⁰ and Pd⁰ exist on the surface, and are unlikely to have preferential surface segregation of either metal. Veisz *et al.*²⁵ reported Pt/Pd synergy correlating to inhibition of Pd oxidation to PdO by Pt. If Pt/Pd in these catalysts has formed bimetallic clusters, this possibility cannot be ruled out.

It has also been discussed that CO_(ad) on precious metal surface will migrate to immobile O_{2(ad)}. Kaya and Üner²⁴ report that Pd is more tolerant to CO self poisoning than Pt. A possibility in Pt/Pd clusters is excess CO on the surface of Pt migrating to vacant Pd sites. This would raise the CO_(ads) on Pd, which is better suited to coping with excess CO. It

would also relieve Pt active sites of CO, facilitating O₂ adsorption. Competitive CO/O₂ adsorption has been described as the most sensitive condition in CO oxidation²⁶. Without further characterisation, this hypothesis cannot be validated however.

Investigations into effective catalyst Pt/Pd ratio were conducted to shed some light upon the cause of Pt/Pd synergy. Pt and Pd were electrostatically adsorbed onto γ -Al₂O₃ spheres in ratios between 1:1 and 1:10. The data indicates that sequential activity increases are highest when the metal ratio is approximately 1:4. This is demonstrated in Table 32, a compilation of data. Pt/Pd weight ratio compared to the sequential % rise in final activity. 0.10% Pt / 0.50% Pd is excluded as an anomalous result.

Pt % loading	Pd % loading	Pt/Pd	Final Activity %	Activity Rise %
0.1	0.1	1.00	22.9	n/a
0.1	0.2	0.50	32.3	9.4
0.1	0.3	0.33	50	17.7
0.1	0.4	0.25	58.2	8.2
0.1	0.5	0.20	54.1 (anomalous)	n/a
0.1	0.6	0.17	59	0.8
0.1	0.7	0.14	61	2
0.04	0.4	0.1	33.4	n/a
0.08	0.4	0.2	46.4	13
0.12	0.4	0.3	51.4	5
0.16	0.4	0.4	57.4	6

Table 32 – Data for relative activity rises vs. Pt/Pd ratio

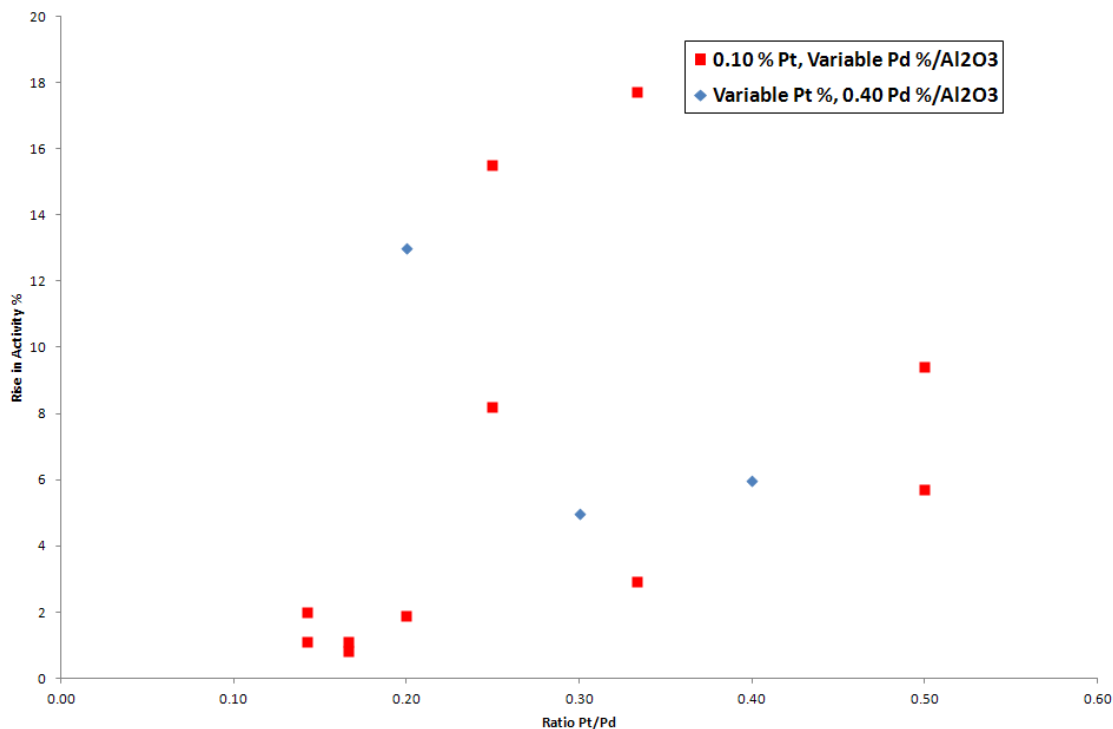


Figure 76 - Pt/Pd ratio vs (% Activity minus % Activity of previous loading)

Figure 76 displays this information in a graphical format (inclusive of repeat experiments). Pt/Pd weight ratio (X-axis) is plotted against the sequential % rise in final activity (Y-axis). It can be observed that the greatest activity rises are correlated to Pt:Pd ratios between approximately 1:5 and 1:3. It has been discussed that Pt and Pd exhibit synergy for ambient temperature CO oxidation. This data appears to support this conclusion, also suggesting that excess Pt or Pd far removed from a 1:4 ratio is less efficient than the synergy presented by closer ratios. It could be inferred that this is due to a lack of sufficient counterpart metal to synergise with. These results are not unprecedented. Parinyaswan *et al.*²⁷ investigated Pt/Pd-CeO₂ ratio for PROX of CO-H₂. He reported a 1:7 ratio was the most active ratio. Yashima *et al.*²⁸ prepared Pt and Pd alloys by reaction in microemulsion followed by deposition upon Al₂O₃. He reports that a 20:80 molar ratio was the most active catalyst. Standard wet-impregnated catalysts were most active at a 50:50 ratio.

5.4.2 Effect of Silicon on CO oxidation over Platinum/Palladium

Alumina spheres were impregnated with a chloro-methyl-silicon compound in toluene. EDX analysis indicates that both silicon and chlorine are present in the catalyst support. The exact morphology and ligands of the silicon is unknown. Possibilities include physisorbed DDMS and/or chemisorbed $\text{Al-O-Si-(CH}_3)_2$ (displayed in Figure 77).

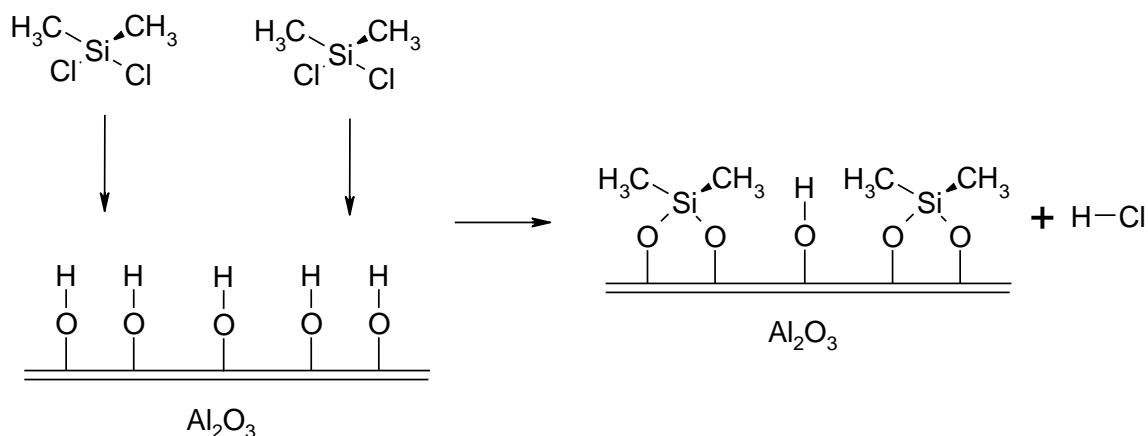


Figure 77 – Theoretical deposition of DDMS onto Al_2O_3 pellets

The characterisation data eliminates neither possibility. Under TPR analysis, silylated alumina displays significantly different behaviour than unmodified alumina. Unmodified alumina shows one distinct mass loss at $\sim 200^\circ\text{C}$. It can be inferred that this is loss of chemisorbed water, as there are no other candidates. Alumina silylated with 2.0% and 5.0% loading shows no sudden mass loss corresponding to the loss of chemisorbed water. They also display two distinct mass losses of equivalent value. Slavov *et al.*²⁰ reports that under increasing temperature, methyl-silylated alumina will sequentially lose methyl groups as methane. Given the equivalent mass of the two TPR losses, it can be inferred that this is loss of the two $\text{Si(CH}_3)_2$ methyl groups. Thus it can be concluded that methylated silicon is present in the catalyst. Its state as a physisorbed or chemisorbed compound is unknown. EDX shows chlorine is present in the catalyst. Slavov¹⁹ reports that chlorine remains bound to the alumina surface after gas phase silylation by chlorotrimethylsilane. Thus Cl could be as a ligand of physisorbed DDMS, or as a chemisorbed chlorine group on the surface. Lack of XPS data precludes further study of

catalyst surface morphology. Slavov's experiments have reported that CH_4 and not HCl is the only gaseous product of silylated alumina combustion. This supports the theory that CH_4 effervescence is preventing the establishment of high vacuum conditions.

The silylated spheres were subsequently impregnated with platinum and palladium (Figure 78). EDX characterisation shows that Pt and Pd are present on the catalyst surface. The reported ratio indicates that substantially more Pd is present than Pt. Chlorine levels have also been reduced. This is not unexpected, as spheres were washed following catalyst reduction. Silicon levels have dropped slightly.

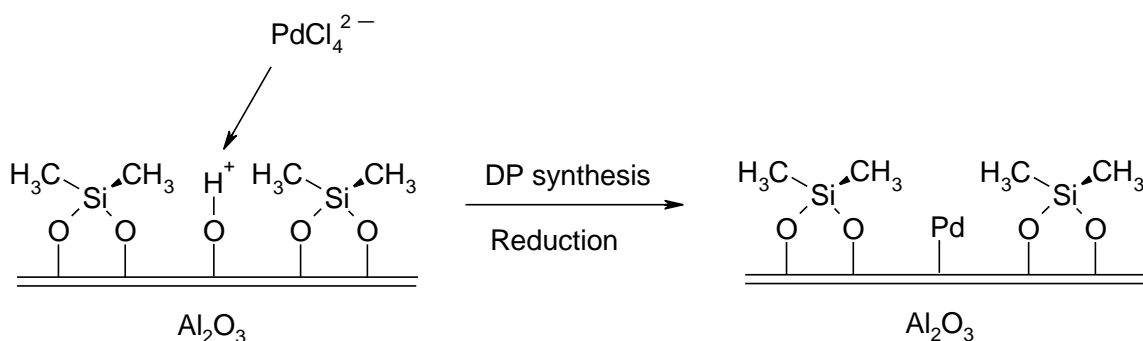


Figure 78 – Electrostatic Adsorption of Pd anions onto Si doped Al_2O_3

The test catalyst activity, all batches were identically impregnated with 0.1%/0.4% Pt/Pd loadings. Two reference batches were prepared. The first, 'solvent reference' was treated with toluene under experimental conditions without any other chemicals added before Pt/Pd adsorption. Activity was increased by ~10%. This increase could be attributed to oxidised residual toluene vaporising as CO_2 . The second, 'solvent and ion' reference was treated with toluene as well as HCl , in quantities identical to the chlorine concentration that would have been introduced by 2.0% DDMS silylation. This catalyst exhibited an activity drop of approx 40% compared to the solvent reference. This supports the hypothesis that the majority of activity loss exhibited by silylation is attributable to chlorine treatment. This is unexpected – the highly active species described in 5.1 and 5.2 are both synthesised from chlorine salts. The 2.0% silyated batch shows an additional 15% activity drop compared to the 'solvent and ion' reference. This is attributable specifically to $\text{Si}(\text{CH}_3)_2$ groups. More heavily silicon weighted catalysts show increasing

deactivation, attributable to either increasing Cl concentration or increasing $\text{Si}(\text{CH}_3)_2$ groups.

The reasons for this deactivation could be interference with Pd/Pt EA, or poisoning of the reaction mechanism. As Cl ions are present during EA, catalyst poisoning by chlorine is unlikely. Oran and Uner²⁹ investigated Pt/ Al_2O_3 and reported that the presence of residual chlorine is unlikely to affect the CO oxidation reaction. They attribute this to Cl occupying active sites not used for CO oxidation reaction. They also report that chlorine can be effectively removed by washing with hot distilled water. This is supported by the EDX chlorine levels of the washed catalysts reported in 5.1 and 5.2, which were 0%.

Catalyst poisoning by silicon is unlikely. Pt/ SiO_2 catalysts are extensively reported as highly active for CO oxidation at all temperatures. Poisoning by CH_3 groups is more likely. Carlsson and Skoglundh³⁰ report that the ignition and extinction processes for competitive CO and CH_4 oxidation occur in different temperature regions. This infers that if CH_4 compounds adsorb onto Pt/Pd surface, they will not dissociate at low temperatures. However, TPR data indicates that CH_3 groups have remained bound to Si atoms either as chemisorbed $\text{Si}(\text{CH}_3)_2$ or physisorbed DDMS. As such, they are unlikely to interact with CO oxidation over Pt/Pd.

If Pt/Pd are not being chemically poisoned by a constituent of the DDMS impregnation, it would infer that deactivation is due to interference with EA. EA of Pt/Pd is known to be affected by the charge and morphology of the alumina surface. Observations of the reference catalysts indicate that both HCl and $\text{Si}(\text{CH}_3)_2$ all affect catalyst activity. SiO_2 is of similar chemistry to Al_2O_3 , however $\text{Si}(\text{CH}_3)_2$ is very different. The interactions between organic molecules and the EA procedure have not been previously described. Acidic media from HCl charging the $\text{Si}(\text{CH}_3)_2$ group to $\text{Si}^+ + \text{CH}_4$ or $\text{Si}(\text{CH}_2)^+$ is possible. It could also be postulated that DDMS will have blocked sites which are then unusable by Pt and Pd. The exact surface change involved is unknown without XPS and dispersion characterisation.

5.5 Conclusions

Platinum and Palladium adsorbed onto Al_2O_3 via electrostatic adsorption show synergy for CO oxidation at ambient temperature. This synergy is likely electronic or morphological due to elimination of other possibilities. Further studies into metal dispersion could resolve this issue.

It has been discovered that the best Pt:Pd ratio to take advantage of this synergetic effect is 1:4. The reasons for this are unclear, but increasing either Pt or Pd levels past this point shows diminishing returns in regard to activity.

Experiments attempting to influence catalyst hydrophobicity have displayed that adsorption of DDMS onto the catalyst surface acts as a catalyst poison. The state of DDMS as chemi or physisorbed remains unknown. This effect can be at least partially attributed to treatment by Cl^- . An unexpected result displayed that treatment of $\gamma\text{-Al}_2\text{O}_3$ by toluene prior to Pt/Pd EA results in a more active catalyst. This phenomenon could be an area for further investigation.

5.6 Chapter 5 References

1. A. S. Ivanova, E. M. Slavinskaya, R. V. Gulyaev, V. I. Zaikovskii, O. A. Stonkus, I. G. Danilova, L. M. Plyasova, I. A. Polukhina and A. I. Boronin, *Applied Catalysis B-Environmental*, 2010, **97**, 57-71.
2. S. Royer and D. Duprez, *Chemcatchem*, 2011, **3**, 24-65.
3. S. C. Kim, H. H. Park and D. K. Lee, *Catalysis Today*, 2003, **87**, 51-57.
4. K. Ito, K. Satoh, T. Tomino, M. Miyake, M. Ohshima, H. Kurokawa, K. Sugiyama and H. Miura, *Journal of the Japan Petroleum Institute*, 2003, **46**, 315-321.
5. J. L. Rousset, L. Stievano, F. Aires, C. Geantet, A. J. Renouprez and M. Pellarin, *Journal of Catalysis*, 2001, **197**, 335-343.
6. P. K. Babu, H. S. Kim, J. H. Chung, E. Oldfield and A. Wieckowski, *Journal of Physical Chemistry B*, 2004, **108**, 20228-20232.
7. H. Muraki, S. Matunaga, H. Shinjoh, M. S. Wainwright and D. L. Trimm, *Journal of Chemical Technology and Biotechnology*, 1991, **52**, 415-424.
8. K. Fuwa and B. L. Vallee, *Analytical Chemistry*, 1963, **35**, 942
9. J. Regalbuto, *Catalyst Preparation*, CRC Press, Taylor and Francis Group, 2007.
10. C. D. Tait, D. R. Janecky and P. S. Z. Rogers, *Geochimica Et Cosmochimica Acta*, 1991, **55**, 1253-1264.
11. G. Duyckaerts, *Spectrophotometric data for colorimetric analysis*, BUTTERWOTHS SCIENTIFIC PUBLICATIONS, LONDON, 1963.
12. T. Harada, S. Ikeda, M. Miyazaki, T. Sakata, H. Mori and M. Matsumura, *Journal of Molecular Catalysis a-Chemical*, 2007, **268**, 59-64.
13. J. Matthey, *Platinum Today*, <http://www.platinum.matthey.com/>, Accessed 20/12/2010.
14. K. Persson, A. Ersson, K. Jansson, J. L. G. Fierro and S. G. Jaras, *Journal of Catalysis*, 2006, **243**, 14-24.
15. P. Castellazzi, G. Groppi and P. Forzatti, *Applied Catalysis B-Environmental*, 2010, **95**, 303-311.
16. S. Kaya, E. Erunal, R. Shaltaf, S. Ellialtioglu and D. Uner, *Turkish Journal of Chemistry*, 2009, **33**, 11-21.
17. A. Quintanilla, J. J. W. Bakker, M. T. Kreutzer, J. A. Moulijn and F. Kapteijn, *Journal of Catalysis*, 2008, **257**, 55-63.
18. F. Omota, A. C. Dimian and A. Bliet, *Applied Catalysis a-General*, 2005, **294**, 121-130.
19. S. V. Slavov, K. T. Chuang and A. R. Sanger, *Langmuir*, 1995, **11**, 3607-3609.
20. S. V. Slavov, K. T. Chuang and A. R. Sanger, *Journal of Physical Chemistry*, 1995, **99**, 17019-17027.
21. S. V. Slavov, A. R. Sanger and K. T. Chuang, *Journal of Physical Chemistry B*, 1998, **102**, 5475-5482.
22. K. Grass and H. G. Lintz, *Journal of Catalysis*, 1997, **172**, 446-452.
23. B. Park and H. Lee, *Journal of Materials Research*, 1999, **14**, 281-285.
24. S. Kaya and D. Uner, *Turkish Journal of Chemistry*, 2008, **32**, 645-652.
25. B. Veisz, L. Toth, D. Teschner, Z. Paal, N. Gyorffy, U. Wild and R. Schlogl, *Journal of Molecular Catalysis a-Chemical*, 2005, **238**, 56-62.

26. J. Szanyi, W. K. Kuhn and D. W. Goodman, *Journal of Physical Chemistry*, 1994, **98**, 2978-2981.
27. A. Parinyaswan, S. Pongstabodee and A. Luengnaruemitchai, *International Journal of Hydrogen Energy*, 2006, **31**, 1942-1949.
28. M. Yashima, L. K. L. Falk, A. E. C. Palmqvist and K. Holmberg, *Journal of Colloid and Interface Science*, 2003, **268**, 348-356.
29. U. Oran and D. Uner, *Applied Catalysis B-Environmental*, 2004, **54**, 183-191.
30. P. A. Carlsson and M. Skoglundh, *Applied Catalysis B-Environmental*, 2011, **101**, 669-675.

6

Noble Metal Doped γ -Alumina/Tin Oxide

At ambient temperature, stannic oxide is unable to chemisorb CO and is not active for CO oxidation. At the same temperature, Pt⁰ is active but is hindered by CO self-poisoning. However, Pt⁰ supported on SnO₂ exhibits synergy and is active at ambient temperature. Synergy between SnO₂ and Pt has been reported by several researchers¹⁻⁴. Grass and Lintz^{5, 6} report that O₂ migration from SnO₂ to Pt is the rate determining step of the reaction. They propose oxygen adsorbed on SnO₂ migrates to Pt surface, and reacts with excess CO. Tin Oxide/Pt catalysts are widely used, and are commonly synthesised by impregnation of stannic oxide powder (obtained from reduction followed by oxidation of the raw mineral form). In an attempt to reduce the high cost of tin, commercial catalysts are occasionally synthesised by impregnation of alumina with tin salts such as Na₂SnO₃. Many of these are detailed in a thorough study by Hagemeyer *et al.*⁷, who investigated synthesising high surface area tin oxide from over 100 different reagents. These synthesis methods produce hazardous waste products which must be rendered harmless. In an attempt to devise an atom efficient process for the production of tin oxide catalysts, a novel method using tin oxalate will be investigated in this chapter. Tin oxalate dissolves into a viscous liquid in weak hydrogen peroxide. Combustion of this adhesive liquid removes C, H and O atoms as gases leaving pure tin oxide. The lack of other elements results on no waste stream. This synthesis will be compared with two existing tin oxide synthesis methods, firstly using unmodified stannic oxide, and secondly using sodium stannate. All three methods will attempt to impregnate an egg shell coating of tin onto 2-3mm γ -alumina spheres, to reduce cost and improve durability. These spheres will be subsequently impregnated with Pt and Pd using an EA procedure.

6.1 Preparation of Pt/Pd/Sn/Al₂O₃ spheres from SnO₂

γ -Al₂O₃ spheres were coated with aqueous SnO₂ slurry corresponding to 0.5, 1.0, 2.0, 4.0, 8.0 and 16.0% weight tin loading. After calcination, the spheres were treated with a 0.10%, 0.40% Pt/Pd EA procedure followed by a reduction by sodium formate. The exact preparation method is detailed in Chapter 2.

6.1.1 CO Oxidation Activity

The activities of Sn/Pt/Pd/Al₂O₃ catalysts synthesised from SnO₂ are shown in Figure 79. Displayed is the evidence that no strong correlation exists between SnO₂ loading and catalyst activity.

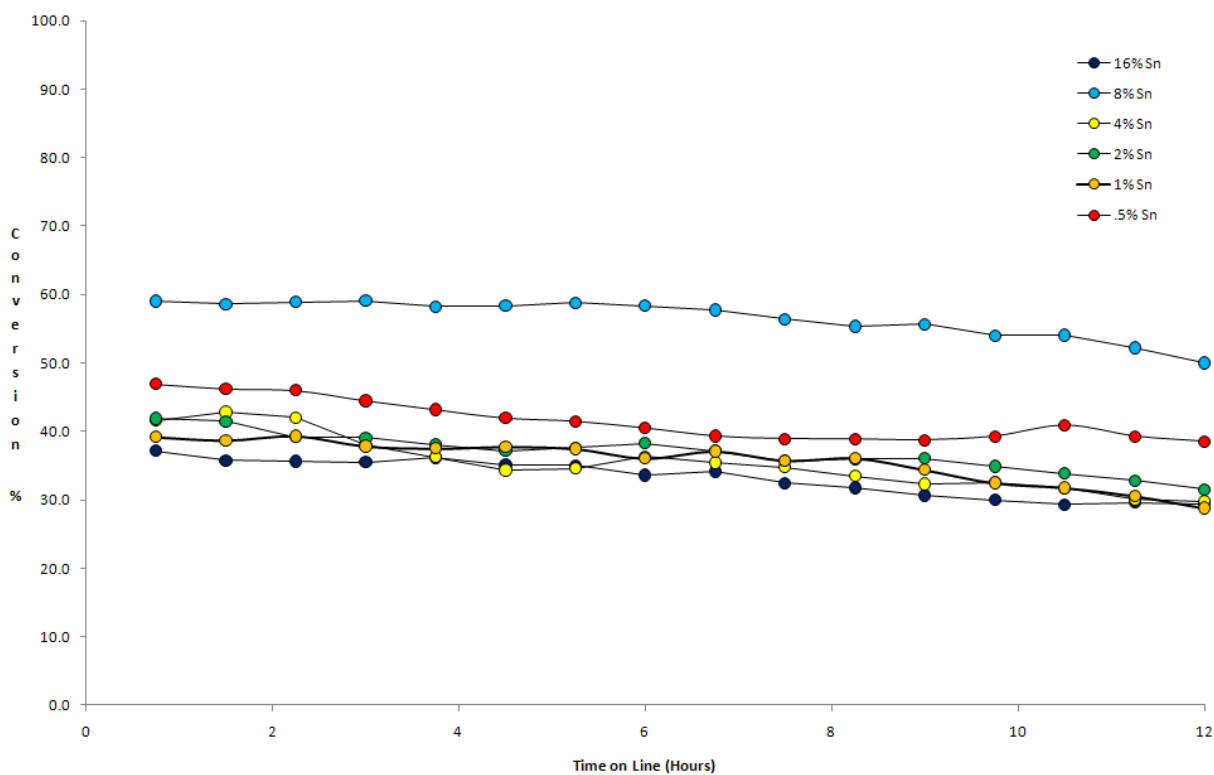


Figure 79 – CO Oxidation Activity – Pt/Pd/SnO₂/Al₂O₃

In all cases, activity curves are uniform. All catalysts display a slow, very shallow deactivation from their initial activity over 12 h. Activity levels are equivalent at ~33% for 1.0, 2.0, 4.0 and

16.0% loadings. 0.5% tin loading shows a slight activity increase to 40%. 8.0% tin loading shows an activity of ~52%.

6.1.2 X-Ray Photoelectron Spectroscopy

Expanded XPS spectra of the most active (8.0% Sn) and the least active (1.0% Sn) catalysts are displayed in Figures 80 and 81. In both cases, the Sn 3d peak at 487.5eV corresponds to the presence of SnO₂, which is not unexpected. These doublet peaks are displaced up the scale, surface charging is a likely candidate. Al 2s peak (not shown) at 119eV shows surface Al appears to be present at Al₂O₃, this is expected.

Pd 3d peaks at 335eV are ~3.8 eV too low to correspond to Pd⁰, but are even further removed from Pd oxides. This could be an evidence of Pt/Pd alloying. In both samples, Pt 4f peak at 71eV corresponds to metallic Pt⁰.

Comparing the two samples, the more active 8.0% Sn sample appears to have a surface impurity attributable to metallic calcium at 345.9eV. This may explain its unusually high reactivity – alkali metals are known catalytic promoters for CO oxidation⁸. The 1% SnO₂ sample shows split peaks emerging above Pd 3d and Sn 3d - this normally indicates the presence of another oxide species or alloying. SnO is a likely candidate for the Sn 3d split. Pd may have formed oxide PdO, this is expected. PdO has been reported as less active for CO oxidation than Pd, which could explain some of the loss in activity.

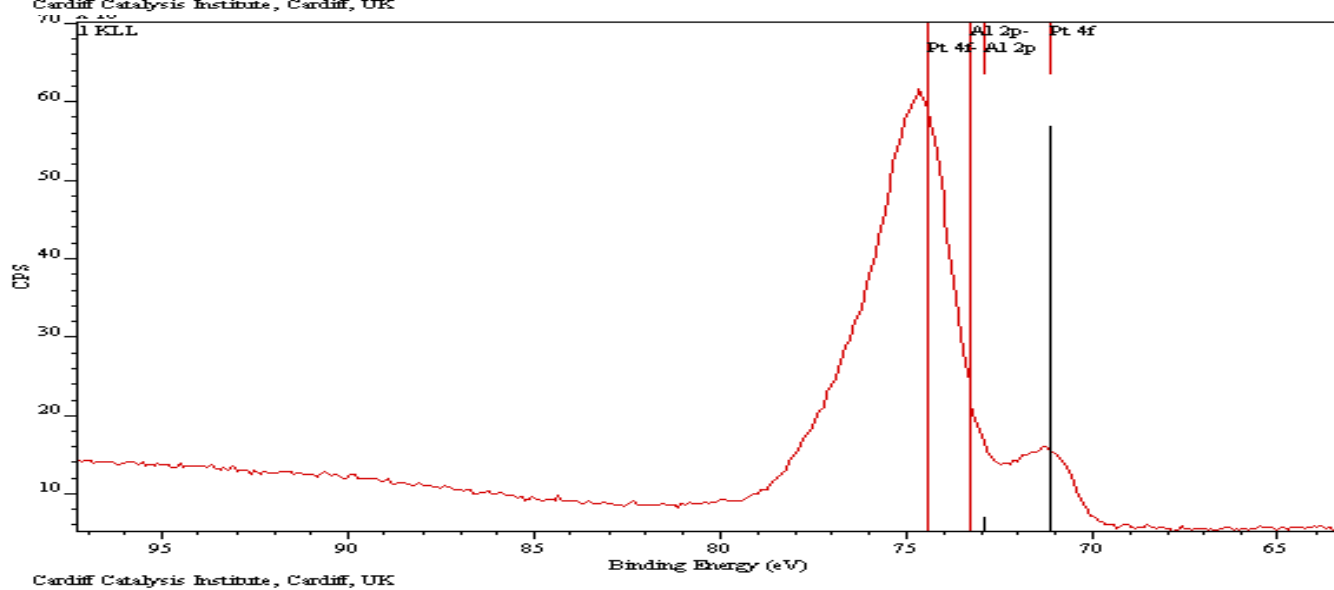
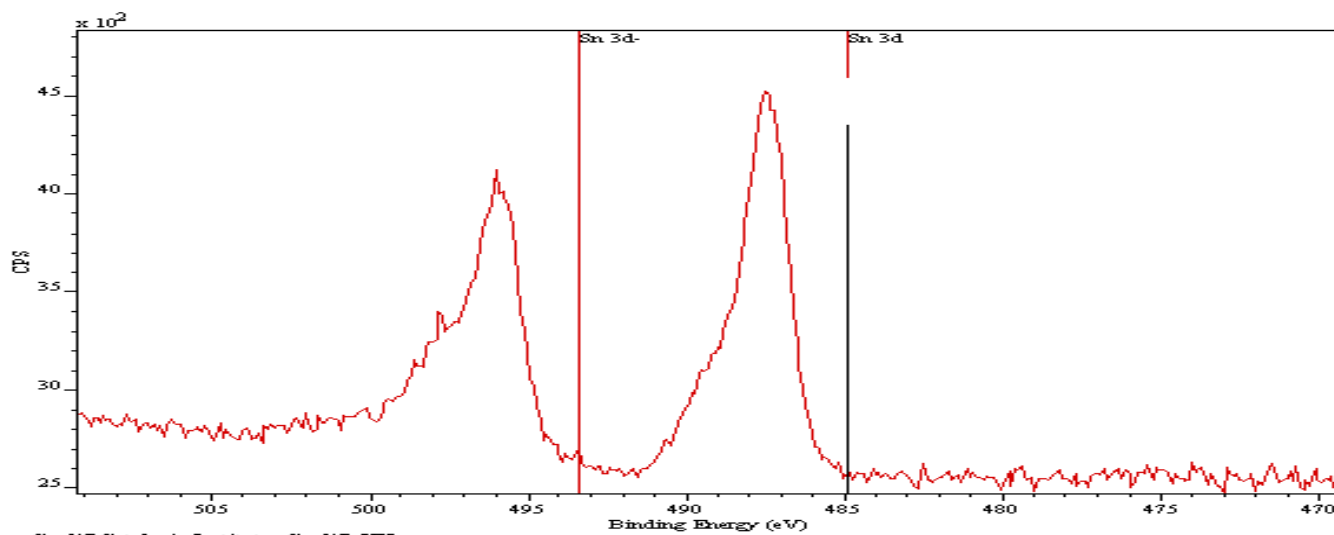
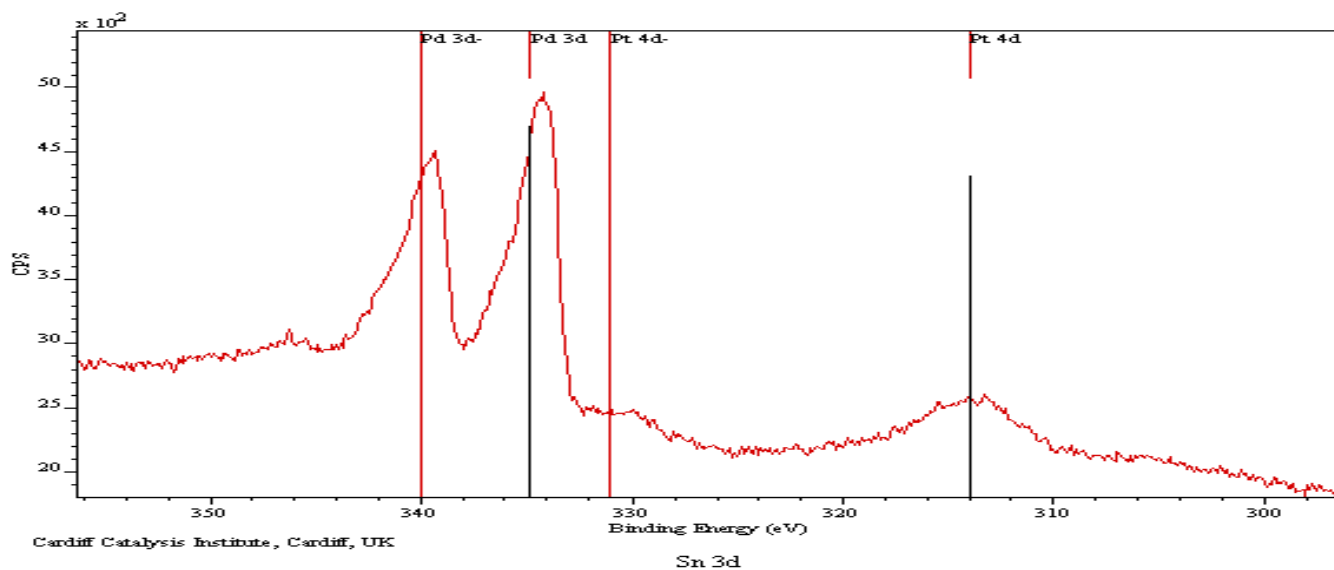


Figure 80 – XPS Spectra, 1.0% SnO₂/Pt/Pd/Al₂O₃

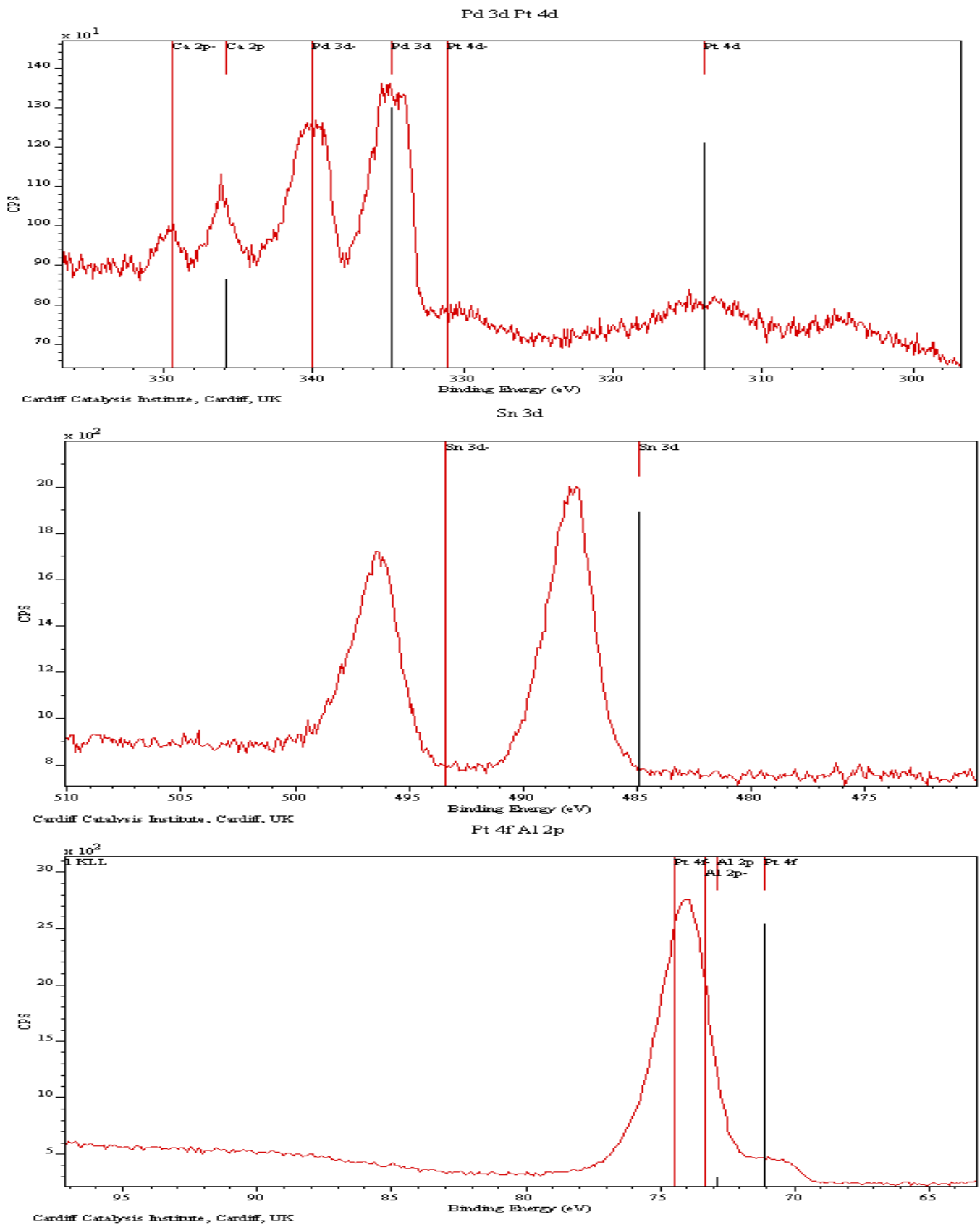


Figure 81 – XPS Spectra, 8.0% $\text{SnO}_2/\text{Pt}/\text{Pd}/\text{Al}_2\text{O}_3$

6.1.3 EDX Molar Ratio

The Sn, Pt and Pd weight % content of the most active (8.0% Sn) and the least active (1.0% Sn) samples defined by EDX spectroscopy are displayed in Table 33. The EDX method is described in more detail in Chapter 2. This data shows that Pt and Pd are present in the sample, within experimental error of the reagent quantities. Tin loadings are not representative of reagent weightings. Sodium and chlorine are not detected.

	CO conversion	Pellet No.	EDX Percentage						
			O	Al	Sn	Pt	Pd	Na	Cl
SNO ₂ (1%)		1	72.15	25.39	2.46				
		2	72.13	26.02	1.85				
		3	73.59	22.85	3.56				
SNO ₂ (1%) .1,.4;Pt,Pd	29%	1	70.64	26.80	2.16	0.12	0.28		
		2	71.98	25.28	2.34	0.09	0.31		
		3	70.90	25.92	2.84	0.04	0.30		
SNO ₂ (8%)		1	73.65	23.68	2.67				
		2	72.76	24.83	2.41				
		3	74.02	23.39	2.59				
SNO ₂ (8%) .1,.4;Pt,Pd	50%	1	73.90	23.83	1.97	0.04	0.26		
		2	76.15	22.47	1.02	0.05	0.31		
		3	73.12	23.77	2.72	0.07	0.32		

Table 33 – EDX data, Pt/Pd/SnO₂/Al₂O₃

6.2 Preparation of Pt/Pd/Sn/Al₂O₃ spheres from Na₂SnO₃

γ -Al₂O₃ spheres were coated with Na₂SnO_{3(aq)} solution corresponding to 0.5, 1.0, 2.0, 4.0, 8.0 and 16.0% tin loading. After calcination, spheres were treated with a 0.10%, 0.40% Pt/Pd EA procedure followed by sodium formate reduction. The exact preparation method is detailed in Chapter 2.

6.2.1 CO Oxidation Activity

The activities of Sn/Pt/Pd/Al₂O₃ catalysts synthesised from Na₂SnO_{3(aq)} are shown in Figure 82

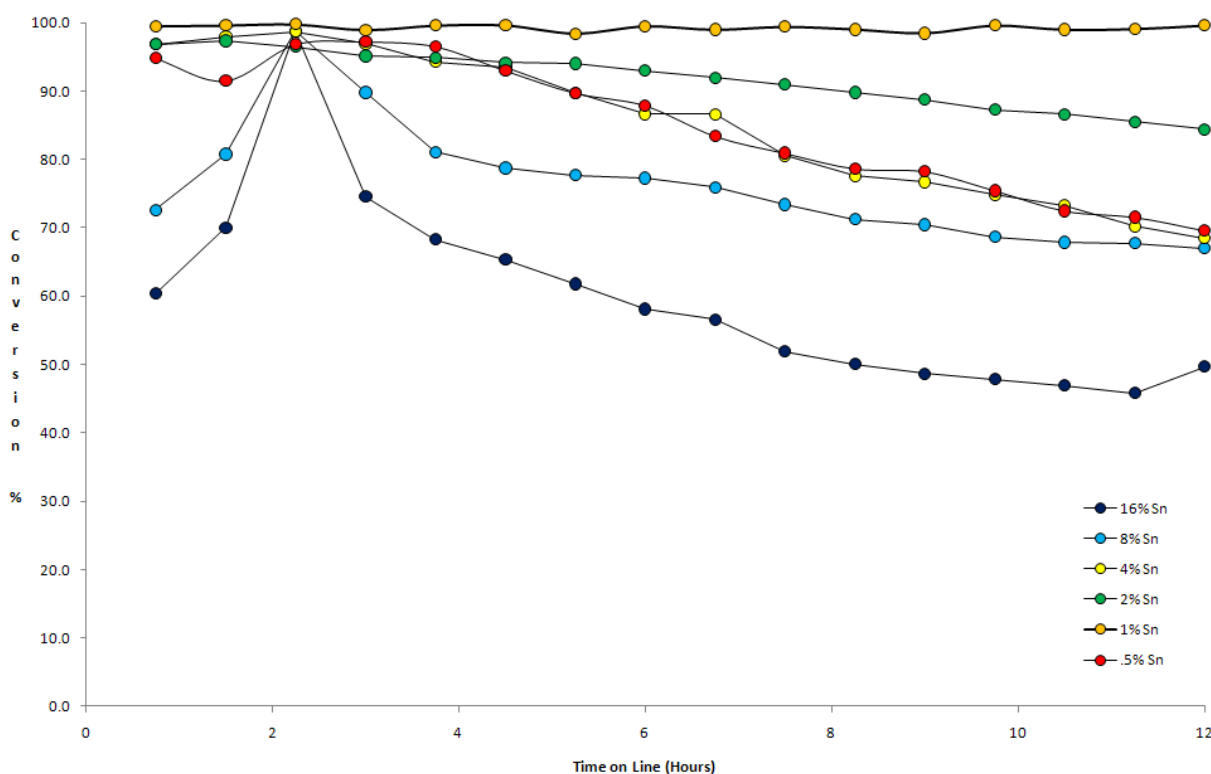


Figure 82 – CO oxidation activity – Pt/Pd/Na₂SnO₃/Al₂O₃

The 1.0% Sn catalyst is the most active, with a steady ~100% conversion for 12 h. The 2.0% loaded catalyst is slightly less active, at ~95% for 4 h and then steadily deactivating to ~88%. The 0.5% and 4.0% weighted catalysts show equivalent activity, at approximately 95% for 4 h and then steadily deactivating to ~75% at 12 h. The 8.0% loaded catalyst displays an initial activity spike, beginning at ~72%, rising to ~100% at 2.5 h, then quickly deactivating to ~75%, equivalent to the 0.5% and 4.0% catalysts. The 16.0% weighted catalysts show a much lower

initial activity, beginning at ~60% , peaking at ~100% after 2.5 h, and deactivating to ~52% at 12 h .

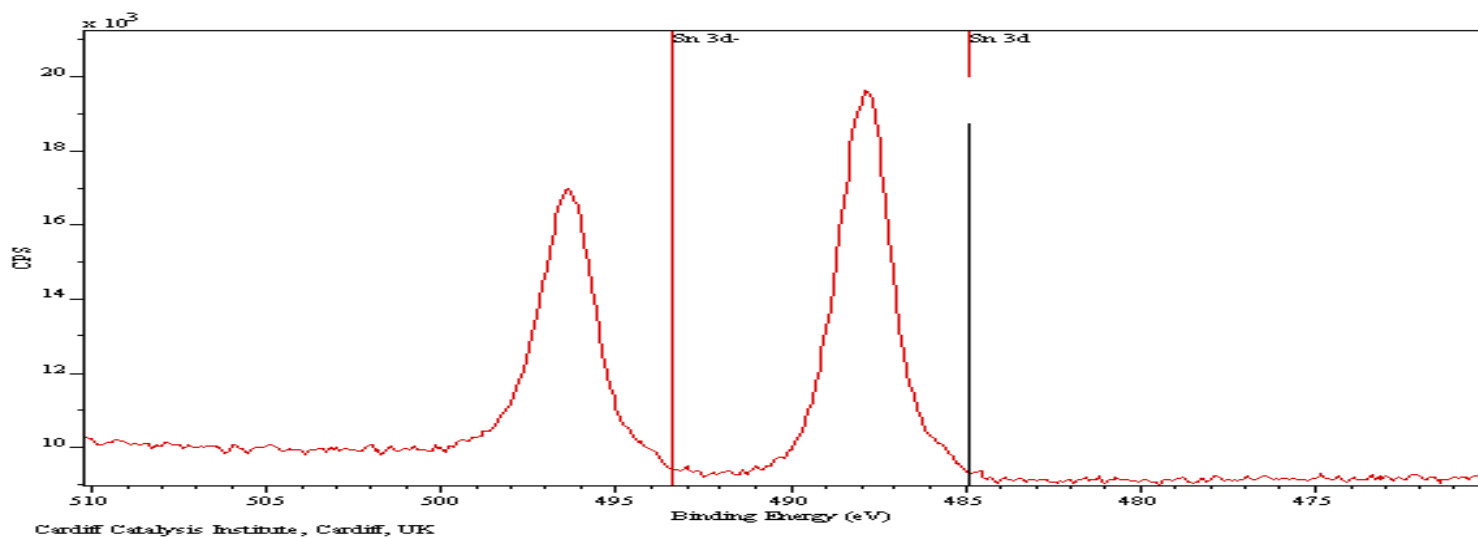
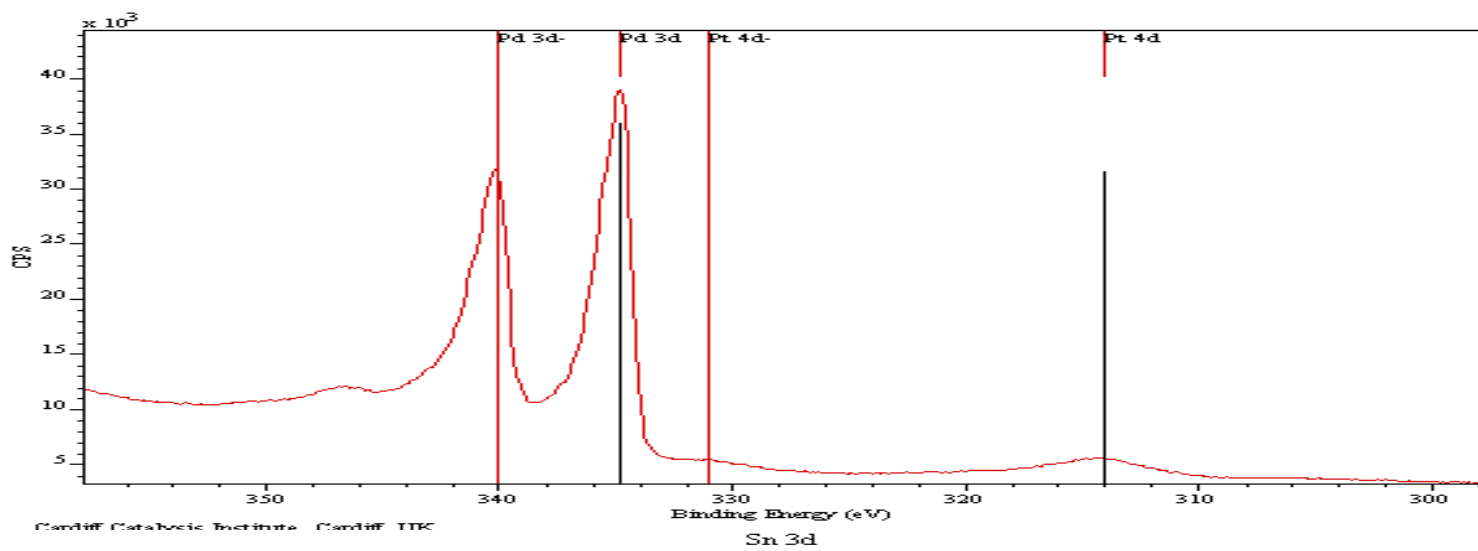
6.2.2 X-Ray Photoelectron Spectroscopy

Expanded XPS spectra of the most active (1.0% Sn) and the least active (16.0% Sn) catalysts are displayed in Figures 83 and 84. The XPS technique is described in more detail in Chapter 2. In both cases, Sn 3d peak at 487.5eV correspond to the presence of SnO₂. These doublet peaks are displaced up the scale, surface charging is a likely candidate. Al 2s peak (not shown) at 119eV shows surface Al appears to be present as Al₂O₃.

Pd 3d peaks at 335eV are ~3.8 eV too low to correspond to Pd⁰, but are even further removed from Pd oxides. This could be an evidence of Pt/Pd alloying. In both samples, Pt 4f peak at 71eV corresponds to metallic Pt⁰. Neither Cl nor Na atoms were detected by this analysis on either sample.

The 16% SnO₂ sample shows split peaks emerging above Pd 3d and Sn 3d - this normally indicates the presence of another oxide species or alloying. Pd may have formed oxide PdO, this is expected. PdO has been reported as less active for CO oxidation than Pd, which could explain some of the loss in activity. SnO is a likely candidate for the Sn 3d split.

Pd 3d Pt 4d



Pt 4f Al 2p

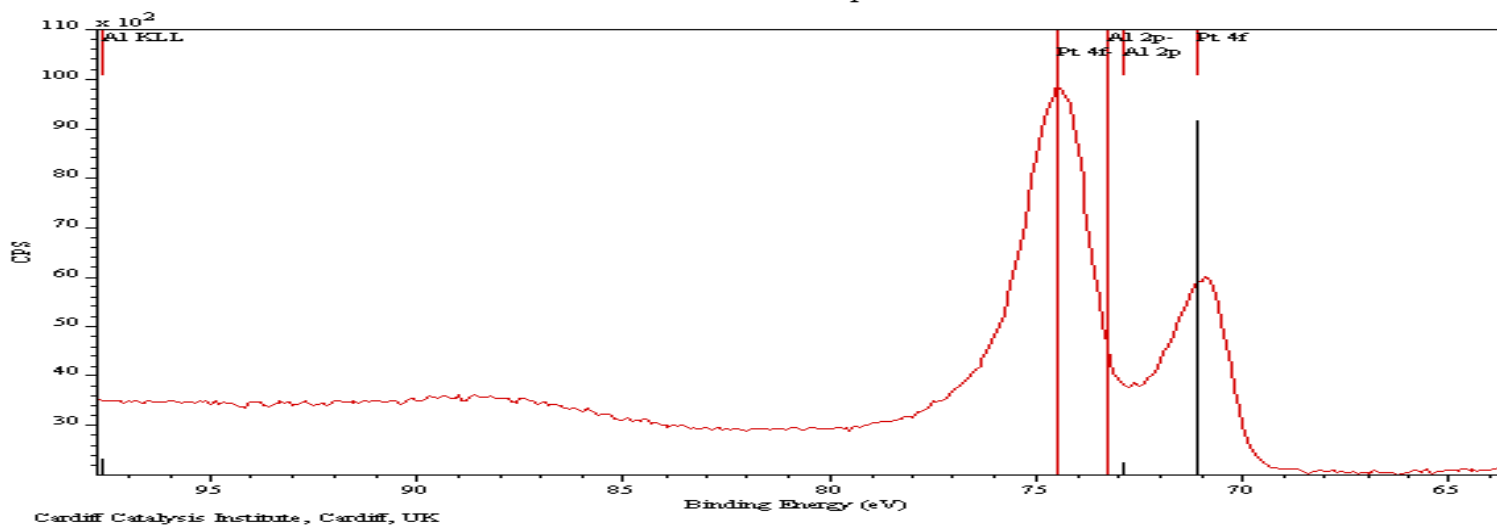


Figure 83 - XPS spectra – 1.0% Pt/Pd/ $\text{Na}_2\text{SnO}_3/\text{Al}_2\text{O}_3$

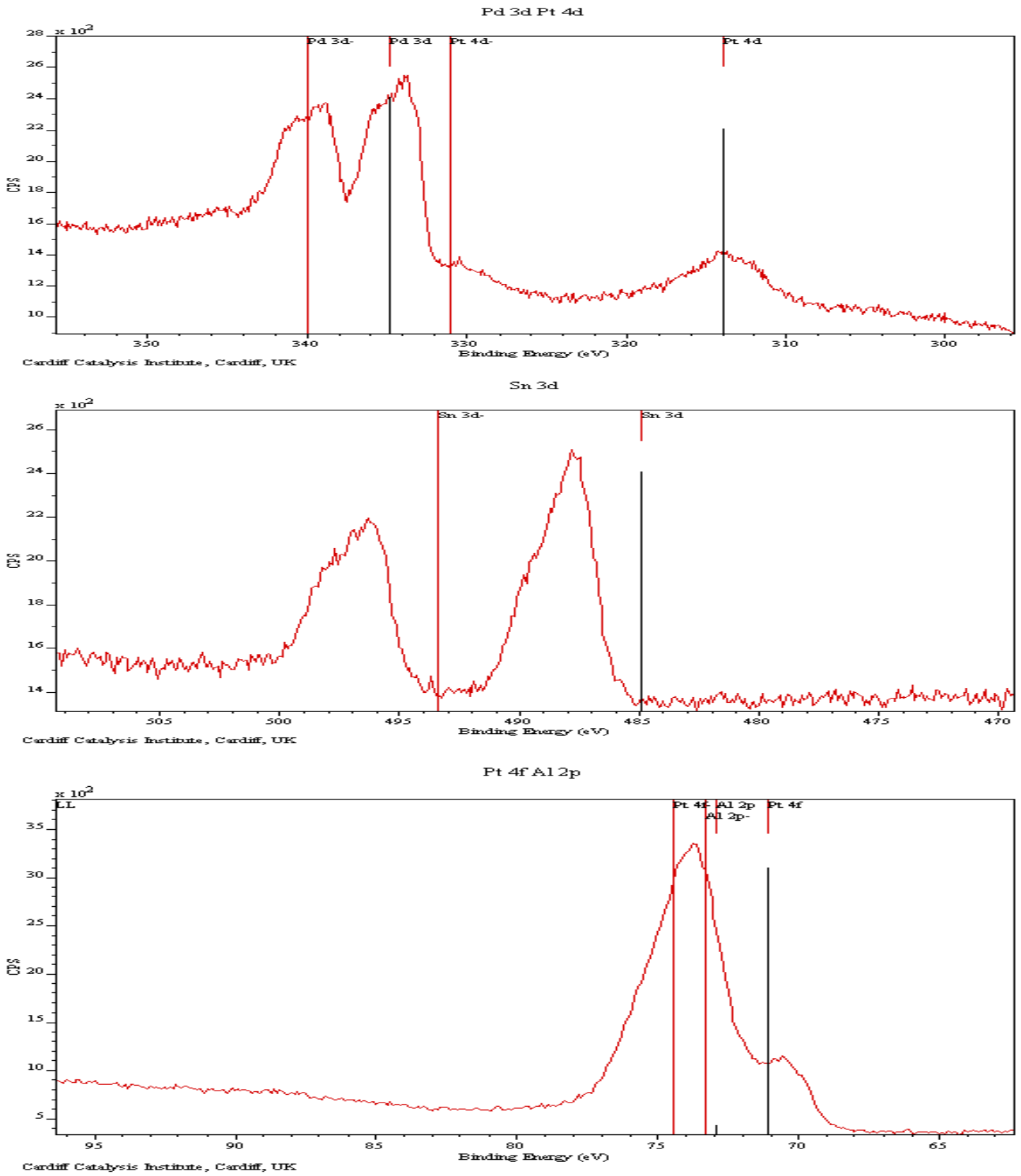


Figure 84 - XPS spectra – 16.0% Pt/Pd/ $\text{Na}_2\text{SnO}_3/\text{Al}_2\text{O}_3$

6.2.3 EDX Molar Ratio

The Na, Sn, Cl, Pt and Pd weight % content of the most active (1.0% Sn) and the least active (16.0% Sn) samples defined by EDX spectroscopy are displayed in Table 34. The EDX method is described in more detail in Chapter 2. This data shows that Pt and Pd are present in the sample, within experimental error of the reagent quantities. Tin loadings are not representative of reagent weightings. Residual sodium is also present in all four catalysts. As expected, the 16.0% catalyst shows far higher levels of Na than the 1.0% catalyst. The Pd/Pt catalysts show reduced sodium levels compared to the references. Low residual chlorine levels are present in the 16.0% catalyst.

	CO Conversion	Sphere No.	EDX Percentage						
			O	Al	Sn	Pt	Pd	Na	Cl
NA ₂ SnO ₃ (1%)		1	69.67	28.84	1.00			0.49	
		2	72.90	25.78	0.77			0.55	
		3	73.60	25.10	0.84			0.55	
NA ₂ SnO ₃ (1%) .1,.4;Pt,Pd	100%	1	68.28	28.24	0.95	0.18	1.99	0.36	
		2	72.10	25.57	0.83	0.14	1.00	0.37	
		3	71.56	26.14	0.80	0.10	0.90	0.49	
NA ₂ SnO ₃ (16%)		1	71.65	24.34	1.40			2.61	
		2	72.09	22.71	1.76			3.44	
		3	70.99	24.18	1.91			2.92	
NA ₂ SnO ₃ (16%) .1,.4;Pt,Pd	52%	1	70.04	26.29	1.99	0.07	0.70	0.79	0.12
		2	69.91	26.15	1.94	0.10	0.82	0.91	0.17
		3	67.57	27.19	1.80	0.66	1.73	0.84	0.20

Table 34 – CO oxidation activity – Pt/Pd/Na₂SnO₃/Al₂O₃

6.3 Preparation of Pt/Pd/Sn/ Al_2O_3 spheres from $\text{Sn}(\text{C}_2\text{O}_4)$

Spheres of γ - Al_2O_3 were coated with a $\text{Sn}(\text{C}_2\text{O}_4)$ solution in H_2O_2 corresponding to 0.5, 1.0, 2.0, 4.0, 8.0 and 16.0% tin loading. After calcination, the spheres were treated with a 0.10% : 0.40% Pt & Pd EA procedure followed by a reduction by sodium formate. The exact preparation method is detailed in Chapter 2.

6.3.1 CO Oxidation Activity

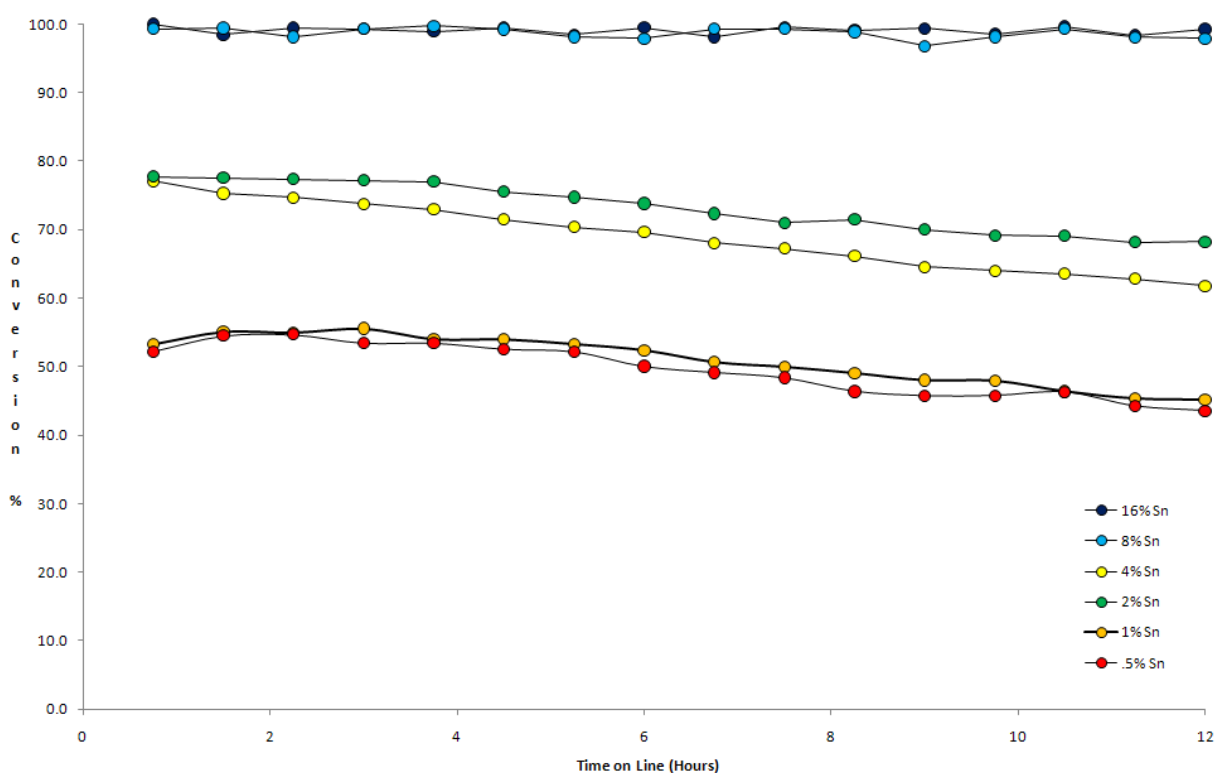


Figure 85 – CO oxidation activity – Pt/Pd/Sn C_2O_4 / Al_2O_3

From the data displayed in Figure 85 it can be concluded that there is a direct correlation between rising catalyst tin loading and rising activity. The 8.0% and 16.0% Sn catalysts are the most active, with a steady ~100% conversion for 12 h. The 2.0% and 4.0% loaded catalysts are slightly less active, beginning at ~78% and steadily deactivating to ~71% and ~63% respectively. The 1.0% and 0.5% weighted catalysts show equivalent activity, at approximately ~54% for 6 h and then steadily deactivating to ~47% at 12 h.

6.3.2 Thermogravimetric Analysis

In a reference experiment, $\text{Sn}(\text{C}_2\text{O}_4)/\text{H}_2\text{O}_2$ slurry was treated with the same conditions as the experimental spheres was prepared to establish the chemistry of $\text{Sn}(\text{C}_2\text{O}_4)/\text{H}_2\text{O}_2$ decomposition. The TGA data for this compound is displayed in Figure 86. TGA is described as a technique in Chapter 2. The data shows that $\text{Sn}(\text{C}_2\text{O}_4)$ loses $\sim 32\%$ of initial mass under calcination. This corresponds exactly to the atomic mass difference between $\text{Sn}(\text{C}_2\text{O}_4)$ and SnO_2 .

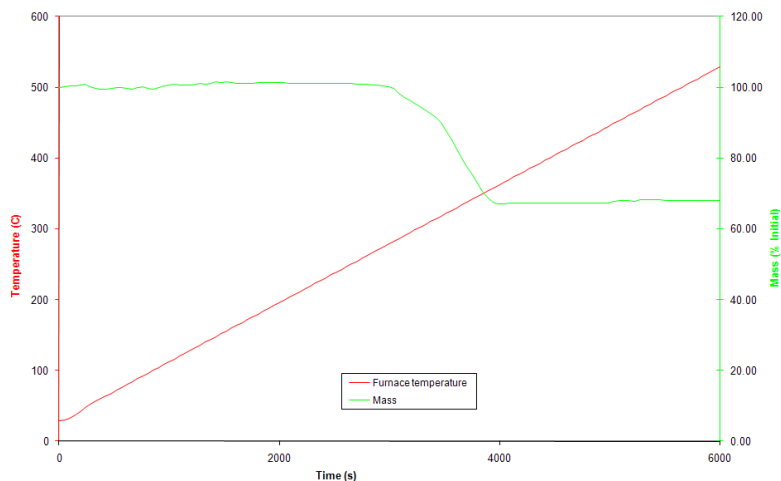


Figure 86 - TGA data of $\text{Sn}(\text{C}_2\text{O}_4)$

6.3.3 X-Ray Diffraction

In a reference experiment, $\text{Sn}(\text{C}_2\text{O}_4)$ powder was treated and calcined with the same conditions as the experimental spheres. This calcined powder and the initial reagent was tested in an XRD diffractometer. This data is displayed in Figure 87. The reagent pattern can be unambiguously described as near pure $\text{Sn}(\text{C}_2\text{O}_4)$. The product pattern corresponds almost exactly to documented SnO_2 pattern, with the exception of a small uncharacterised peak at 2θ ca. 29° .

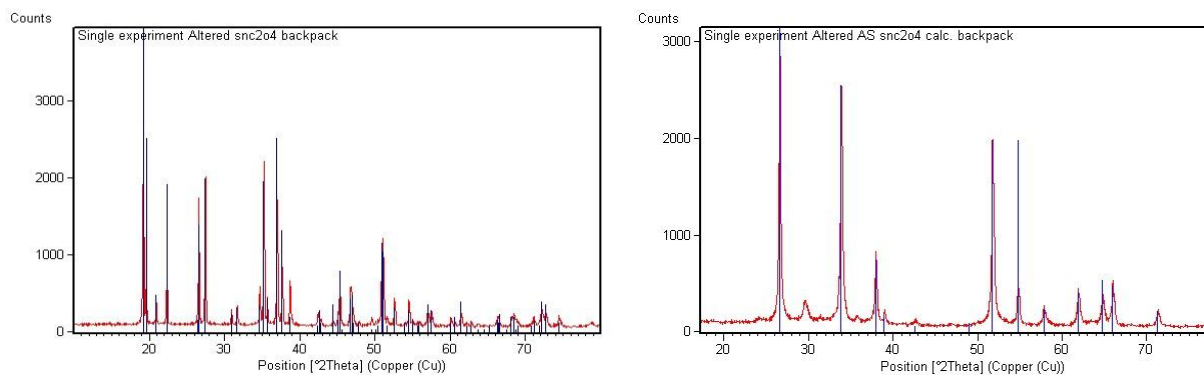


Figure 87 – XRD patterns, $\text{Sn}(\text{C}_2\text{O}_4)$ (left) and calcined at 350°C 1 h (right)

6.3.4 X-Ray Photoelectron Spectroscopy

Expanded XPS spectra of the most active (16.0% Sn) and the least active (0.5% Sn) catalysts are displayed in Figures 88 and 89. The XPS technique is described in more detail in Chapter 2. In both cases, Sn 3d peak at 487.5eV correspond to the presence of SnO₂. These doublet peaks are displaced up the scale, surface charging is a likely candidate. Al 2s peak (not shown) at 119eV shows surface Al appears to be present as Al₂O₃. Pd 3d peaks at 335eV correspond to Pd⁰. The slight change in eV displayed in parts 6.1 and 6.2 was not present on this sample.

Pt 4f peak at 71eV corresponds to metallic Pt⁰. Neither Cl nor Na atoms were detected by this analysis on either sample. Analysis of carbon state could not be attempted as the technique uses the only carbon peak (1s) as a calibration standard, and it will be detected regardless of sample composition. Hydrogen cannot be detected by XPS due to its small radius.

The 16% SnO₂ sample shows split peaks emerging above Pd 3d and Sn 3d - this normally indicates the presence of another oxide species or alloying. SnO is a likely candidate for the Sn 3d split. Pd may have formed oxide PdO, this is expected. Although PdO has been reported as less active for CO oxidation than Pd, the 16% Sn sample is more active than the 0.5% sample. This is in direct contrast to the data in Parts 6.1 and 6.2, where the less active catalysts displayed splitting in the Pd signal.

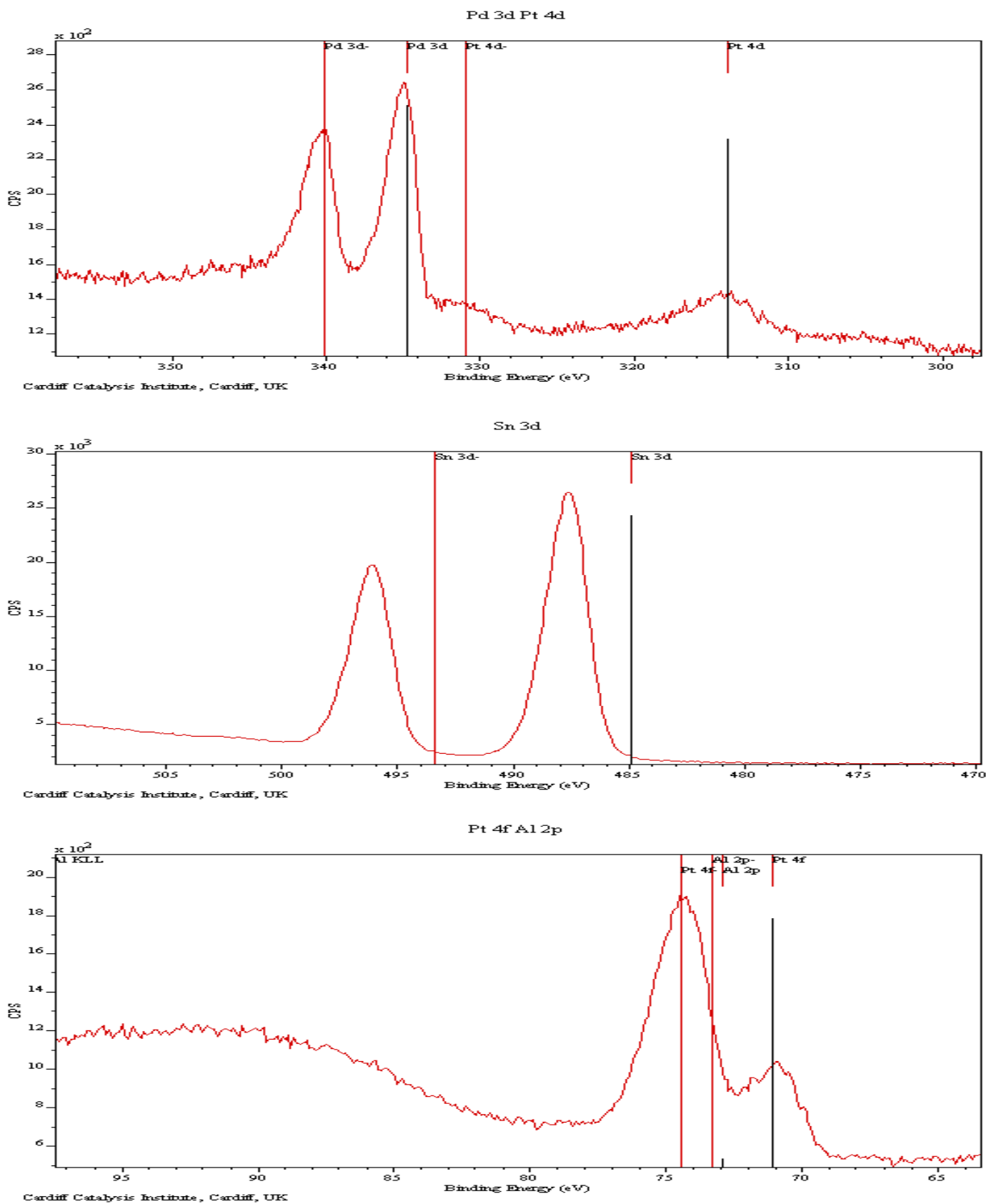


Figure 88 – XPS spectra, 0.5% Pt/Pd/SnC₂O₄/Al₂O₃

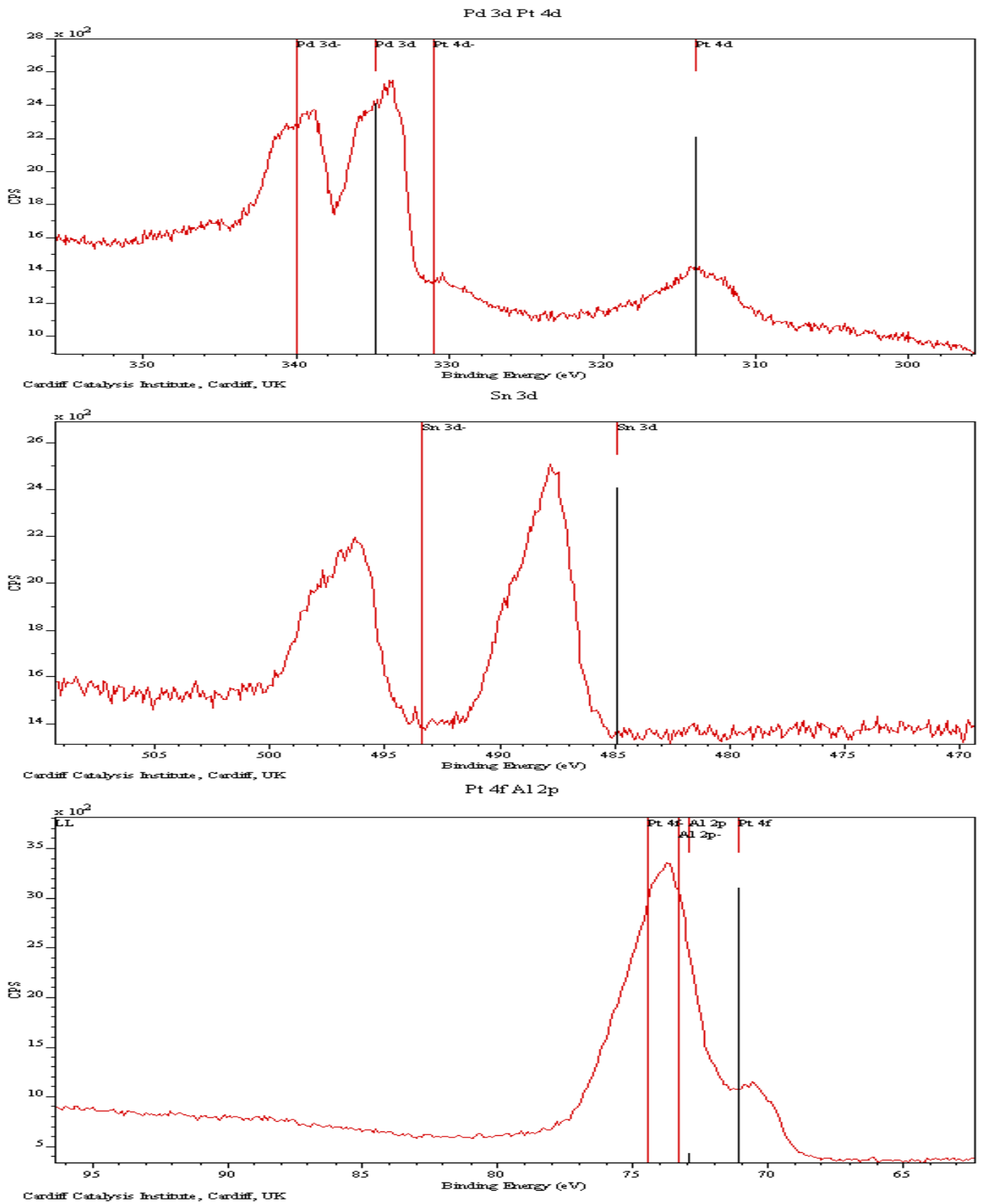


Figure 89 – XPS spectra, 16.0% Pt/Pd/SnC₂O₄/Al₂O₃

6.3.5 EDX Molar Ratio

The Sn, Pt and Pd weight % content of the most active (16.0% Sn) and the least active (0.5% Sn) samples defined by EDX spectroscopy are displayed in Table 35. The EDX method is described in more detail in Chapter 2. This data shows that Pt and Pd are present in the sample, within experimental error of the reagent ratio. Tin is also present. Impurities were not detected. As a bulk technique, ‘true’ loadings cannot be determined by this method.

	CO conversion	Pellet No.	EDX Percentage						
			O	Al	Sn	Pt	Pd	Na	Cl
SNC ₂ O ₄ (.5%)		1	71.78	26.48	1.73				
		2	74.06	23.70	2.24				
		3	73.08	25.48	1.44				
SNC ₂ O ₄ (.5%) .1%,.4%;Pt,Pd	43.5%	1	70.77	26.84	1.94	0.14	0.32		
		2	72.84	25.66	1.16	0.08	0.26		
		3	72.03	26.48	1.73	0.06	0.23		
SNC ₂ O ₄ (16%)		1	76.20	21.00	2.80				
		2	76.20	19.94	3.18				
		3	75.96	21.83	2.22				
SNC ₂ O ₄ (16%) .1%,.4%;Pt,Pd	97%	1	75.26	22.87	1.61	0.03	0.23		
		2	75.00	22.89	1.78	0.03	0.29		
		3	76.90	21.28	1.51	0.00	0.31		

Table 35 – EDX data, Pt/Pd/SnC₂O₄/Al₂O₃

6.4 Discussion

A comparison of the activity at 12 h for all batches is displayed in Figure 90. It is shown that for Sn loadings below $\sim 3.7\%$, synthesis from Na_2SnO_3 results in the most active catalyst. Above $\sim 3.7\%$ Sn loading, synthesis from $\text{Sn}(\text{C}_2\text{O}_4)$ is more active. Catalysts synthesised from powder SnO_2 slurry display inferior activity to the other batches.

XPS characterisation common to all batches records Sn 3d peaks at 488eV. This corresponds to the presence of surface SnO_2 ⁹. Al shows surface presence as Al_2O_3 . Pt is present as Pt^0 . A Pd 3d peak at $\sim 335\text{eV}$ is a reproducible result. An equivalent Pd eV measurement of ~ 335.5 was recorded in Chapter 5 on a reduced Pd/ Al_2O_3 catalyst. Pd metal registers binding energy at $\sim 339+$ eV. As XPS peaks are never lower than their reported ground state values, it could be deduced that this is a Pd alloy. Across three of the six samples, observed peak splittings of Pd 3d and Sn 3d is of evidence of differences in oxidation state. However, there is no correlation between activity and pure state catalysts. It is likely that other factors are affecting catalyst activity.

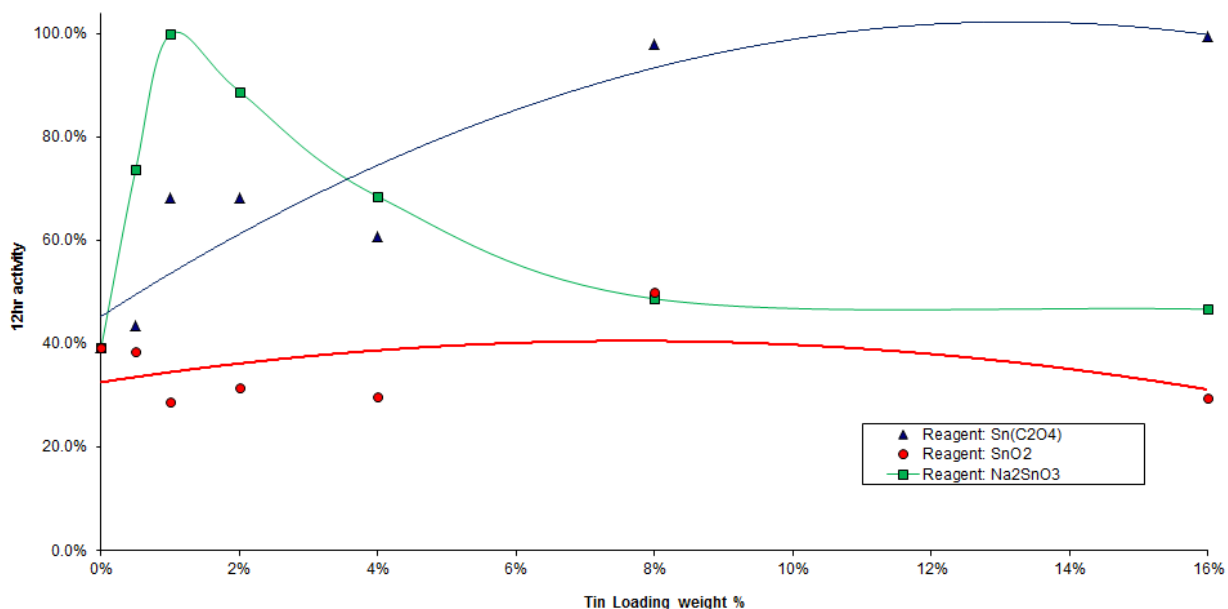


Figure 90 – Pt/Pd/Sn/ Al_2O_3 activity at 12 h vs. Sn Loading

XPS characterisation of the reagent-SnO₂ batches showed only one qualitative difference between the highest and lowest activity catalyst. The high activity catalyst contains residual surface calcium metal. Bulk analysis by EDX did not detect Ca, indicating that this element is a surface impurity. The specific effect of Ca on Pt/Al₂O₃ CO oxidation has not been previously reported. Alkali metals are known catalytic promoters; Mirkelamoglu *et al.*¹⁰ postulates that Na promoted SnO₂ displays increased oxygen affinity. As oxygen migration from Sn to Pt/Pd has been described as the rate limiting step of this reaction^{5, 6}, calcium promotion is a likely candidate for the increased activity of the 8.0% doped batch. The universal low activity of the reagent-SnO₂ spheres was not explained by characterisation data. However, in regard to synthesis and experimental observations, surface powder was observed to be eroding from the spheres surface with even the most sensitive handling. This would reduce tin loading on the sphere. After Pt/Pd EA, this would also remove precious metal loadings. This would undoubtedly reduce activity levels, which could account for the low activity of reagent-SnO₂ batches.

Characterisation of the reagent-Na₂SnO₃ spheres showed significant differences between the highest and lowest activity batches. EDX characterisation of the high activity 1.0% Sn batch shows residual sodium only. EDX of the low activity 16.0% Sn batch shows higher levels of residual sodium and residual chlorine. XPS characterisation detected neither chlorine nor sodium on the catalyst surface. As EDX is bulk sensitive, it may be that residual Na and Cl are present in the catalyst pores, having been removed from the surface by careful washing. These results are not unexpected, as they mirror the concentrations of reagents the two batches were exposed to. The 16.0% catalyst would have been exposed to 16 times the concentration of sodium from the tin salt than the 1.0% catalyst. This would correspond to an increase in Cl⁻ ion concentration introduced to pH control the EA procedure. In regard to chlorine, residual Cl has been described at a catalytic poison for Pt/CeO₂/Al₂O₃ catalysts by Oran and Uner¹¹ via a site blocking mechanism. It could be postulated that the relative inactivity of higher tin loadings during this procedure is due to a poisoning effect from increasing residual Cl ions. Sodium has been described as a catalytic promoter of PdO/SnO₂¹⁰. EDX indicates that levels of bulk sodium in the more active 1.0% catalyst are half that of the less active 16.0% catalyst, despite a 16-fold reduction in reagent ions. It could be postulated that the more active catalyst is being promoted

by Na, and as the reagent quantities increase the increasing Cl concentration outcompetes this gain resulting in activity loss. The 0.5% catalyst would show lower activity compared to 1.0% due to low Na concentration rather than Cl poisoning.

Characterisation of the reagent $\text{Sn}(\text{C}_2\text{O}_4)$ batches is unambiguous. Reference TGA and XRD measurements have shown that $\text{Sn}(\text{C}_2\text{O}_4)$, treated with H_2O_2 , decomposes to SnO_2 . This is further verified by the XPS spectra, Sn 3d peaks are characterised as SnO_2 . Bulk EDX analysis shows no residual ions. Activity rises in correlation with rising tin loading. This is in agreement with the literature, which describes Sn-Pt⁵ and Sn/Pd¹² synergy. The chemistry of this catalyst is unlikely to be different from existing Sn-Pt or Sn-Pd catalysts due to a lack of interference by residual ions. From this data, it can be concluded it is likely that activity is directly related to tin oxide loading. This conclusion is not unexpected or groundbreaking, the purpose of this experiment was to synthesise an active catalyst without producing a liquid waste stream. The catalyst performs very well compared to the two references, although the cost of the 8.0% tin loading to reach the same activity as the 1.0% Na_2SnO_3 catalyst is an economical issue.

6.5 Conclusions

The exact synergy of Pt/Pd/ SnO_2 / Al_2O_3 catalysts was not discovered due to characterisation problems. However, it can be concluded that efficient SnO_2 catalysts can be synthesised using a combination of tin oxalate and hydrogen peroxide reagents. This allows some interesting and novel concepts to be explored in regard to both environmental concerns and clean catalyst synthesis.

Calcium may be a catalytic promoter for Pt/Pd/ SnO_2 / Al_2O_3 catalysts, and chlorine may be a poison. Both elements will need further investigation before anything conclusive can be proven however.

6.6 References

1. N. D. Gangal, N. M. Gupta and R. M. Iyer, *Journal of Catalysis*, 1990, **126**, 13-25.
2. G. C. Bond, L. R. Molloy and M. J. Fuller, *Journal of the Chemical Society-Chemical Communications*, 1975, 796-797.
3. M. Sheintuch, J. Schmidt, Y. Lechthman and G. Yahav, *Applied Catalysis*, 1989, **49**, 55-65.
4. D. R. Schryer, B. T. Upchurch, B. D. Sidney, K. G. Brown, G. B. Hoflund and R. K. Herz, *Journal of Catalysis*, 1991, **130**, 314-317.
5. K. Grass and H. G. Lintz, *Journal of Catalysis*, 1997, **172**, 446-452.
6. K. Grass and H. G. Lintz, *Preparation of Catalysts Vi*, 1995, **91**, 1111-1119.
7. A. Hagemeyer, Z. Hogan, M. Schlichter, B. Smaka, G. Streukens, H. Turner, A. Volpe, H. Weinberg and K. Yaccato, *Applied Catalysis a-General*, 2007, **317**, 139-148.
8. M. Bowker, *The Basis and Applications of Heterogeneous Catalysis*, Oxford University Press, United States, 1998.
9. *NIST X-ray Photoelectron Spectroscopy Database*, <http://srdata.nist.gov/xps/>, 2011.
10. B. Mirkelamoglu and G. Karakas, *Applied Catalysis a-General*, 2006, **299**, 84-94.
11. U. Oran and D. Uner, *Applied Catalysis B-Environmental*, 2004, **54**, 183-191.

7

Conclusions & Further Work

7.1 Hopcalite Modification

Doping of CuMn_2O_4 with transition metals Ce, V, and Pd was ultimately unsuccessful in promoting CO oxidation activity. Introduction of increasing loadings of all the elements were correlated to poisoning of the $\text{Cu} \leftrightarrow \text{Mn}$ redox mechanism. However, the catalysts synthesised with low transition metal loadings (1% and below) showed increased surface area and reduced poisoning effect. In the case of 1.0% V-doped $\text{Cu}_{1-x}\text{Mn}_2\text{V}_x\text{O}_4$ and 0.25%, 0.50% and 1.0% Pd doped catalysts, this surface area increase was able to more than compensate for the poisoning effect and increase overall activity. Previous work done on hopcalite doping by Jones¹ and Cole² have ranged between higher 1% and 25% weight dopings. This would indicate that doping very low levels of transition metals into hopcalite (0.10%, 0.25% etc) could take maximum advantage of this effect. Veprek³ theorises that dopant ionic radius can influence surface segregation. Careful selection of dopant element alongside low loadings could minimise $\text{Cu} \leftrightarrow \text{Mn}$ redox mechanism interaction while promoting catalyst surface area. A notable omission from this thesis was TPR and XPS data of hopcalite catalysts, due to equipment issues. Surface segregation and chemical state of dopant metals could be measured by these techniques.

In regard to the selection of dopant metals, the selection process detailed in Chapter 1 would indicate that Ni, Ag, Co, Fe and Zn are the most promising candidates. These elements were previously studied by Jones and Cole with some success. The elements studied in this thesis, Ce, V, Pd and Si were of interest but were theoretically less likely to be good dopants. The results indicate that Ce and V, Si and Pd are catalytic poisons, while Pd is also a structural promoter. It

seems likely that elements even further removed from the theoretical ideal selection would be poor dopants.

A theoretically promising candidate for further work is mercury doping. Hg is theoretically an exceptional replacement for Cu in the hopcalite lattice. Mercury has an identical oxidation state (+1 and +2) to Cu, ionisation energies between the values of Ni/Zn and Cu, and an ionic radius similar to Ag. Mercury nitrate is commercially available. Investigations into mercury doping were not conducted in this thesis due to environmental and safety concerns.

Attempts to improve hopcalite water resistance were made by doping with ‘sacrificial’ silicon oxide, and also by impregnation of Pd and Pt on hopcalite surface. In all cases, catalyst activity with a 4% hydrated gas stream was 0% at 4 min. It could be postulated that attempts to solve hopcalite deactivation by humidity will not be solved by doping or impregnation with these noble metals. Cole² reported increased water resistance with Au impregnated CuMn_2O_4 , which would be the logical choice for further noble metal investigation. Xie et al.⁴ has published describing novel Co_3O_4 nanorods with humidity resistance and high low temperature activity. Studies into a ‘hopcalite nanorod’ with preferential planes exposed could lead to a water resistant catalyst.

Pt/Pd impregnation on CuMn_2O_4 surface caused complete deactivation of noble metals for CO oxidation, even at total 5% weight loading. This is probably due to oxidation of Pd/Pt by Mn in the hopcalite lattice. It could be postulated that for reactions where Pd/Pt oxides are an active catalyst, or Pd/Pt oxidation is the rate limiting step, Pt/Pd/ CuMn_2O_4 would be very efficient.

7.2 Supported Noble Metals on Al₂O₃ and Sn

Pt and Pt supported on Al₂O₃ exhibit synergetic activity compared the monometallic catalysts, and the most efficient Pt:Pd ratio to take advantage of this effect is approximately 1:4. This ratio was used when testing hopcalite and tin oxide supports, although there is no evidence that either synergy or an effective 1:4 ratio is present on these catalysts. This could be a promising future investigation.

In regard to the preparation of SnO₂ catalysts from Sn(C₂O₄), detailed in Chapter 6. Catalysts prepared from reagent tin oxalate are at least as active as those prepared from SnO₂ and sodium stannate. The successful use of tin oxalate precursor highlights opportunities in other areas of catalysis. Most studies on precious metal catalysts use metal salt reagents to form the support or active phase of a catalyst. Studies then attempt to link a phenomena exhibited by that catalyst with a factor in the precious metal or support. However, studies are often complicated by the presence of residual ions which cannot be 100% eliminated. Even ppb quantities of these atoms can influence results. Using an oxalate precursor in hydrogen peroxide followed by a calcination and then hydrogen reduction provides a very atom efficient method for synthesising catalysts without residual salt ions. It would then be possible to compare these ‘clean’ catalysts to the potentially contaminated versions. If both exhibit the same phenomena, it can be said with some confidence that that observation is due to the catalyst itself rather than a residual impurity. This approach could theoretically be applied to Tin Tartrate, SnC₄O₈.

Residual Ca detected by XPS in the most active reagent SnO₂ catalyst could indicate that this is an effective promoter for this reaction. The specific effect of Ca on Pt/Pd/Al₂O₃ CO oxidation has not been previously reported.

7.3 References

1. C. D. Jones, Cardiff University, 2006.
2. K. J. Cole, Cardiff University, 2008.
3. S. Veprek, D. L. Cocke, S. Kehl and H. R. Oswald, *Journal of Catalysis*, 1986, **100**, 250-263.
4. X. W. Xie, Y. Li, Z. Q. Liu, M. Haruta and W. J. Shen, *Nature*, 2009, **458**, 746-749.